



Evaluation of an Ejector-Powered Engine Simulator at Transonic Mach Numbers

C. E. Robinson, G. D. Smith, and R. J. Matz
ARO, Inc.

July 1979

Final Report for Period October 1, 1977 – September 1, 1978

Approved for public release; distribution unlimited.

**ARNOLD ENGINEERING DEVELOPMENT CENTER
ARNOLD AIR FORCE STATION, TENNESSEE
AIR FORCE SYSTEMS COMMAND
UNITED STATES AIR FORCE**

NOTICES

When U. S. Government drawings, specifications, or other data are used for any purpose other than a definitely related Government procurement operation, the Government thereby incurs no responsibility nor any obligation whatsoever, and the fact that the Government may have formulated, furnished, or in any way supplied the said drawings, specifications, or other data, is not to be regarded by implication or otherwise, or in any manner licensing the holder or any other person or corporation, or conveying any rights or permission to manufacture, use, or sell any patented invention that may in any way be related thereto.

Qualified users may obtain copies of this report from the Defense Documentation Center.

References to named commercial products in this report are not to be considered in any sense as an endorsement of the product by the United States Air Force or the Government.

This report has been reviewed by the Information Office (OI) and is releasable to the National Technical Information Service (NTIS). At NTIS, it will be available to the general public, including foreign nations.

APPROVAL STATEMENT

This report has been reviewed and approved.

Elton R. Thompson
ELTON R. THOMPSON
Project Manager, Research Division
Directorate of Test Engineering

Approved for publication:

FOR THE COMMANDER

Robert W. Crossley
ROBERT W. CROSSLEY, Lt Colonel, USAF
Acting Director of Test Engineering
Deputy for Operations

UNCLASSIFIED

REPORT DOCUMENTATION PAGE		READ INSTRUCTIONS BEFORE COMPLETING FORM
1 REPORT NUMBER AEDC-TR-78-69	12 GOVT ACCESSION NO.	3 RECIPIENT'S CATALOG NUMBER
4 TITLE (and Subtitle) EVALUATION OF AN EJECTOR-POWERED ENGINE SIMULATOR AT TRANSONIC MACH NUMBERS		5 TYPE OF REPORT & PERIOD COVERED Final Report, Oct 1, 1977 - Sept 1, 1978
7 AUTHOR(s) C. E. Robinson, G. D. Smith, and R. J. Matz, ARO, Inc., a Sverdrup Corporation Company		6 PERFORMING ORG. REPORT NUMBER
9 PERFORMING ORGANIZATION NAME AND ADDRESS Arnold Engineering Development Center/DOTR Air Force Systems Command Arnold Air Force Station, Tennessee 37389		10 PROGRAM ELEMENT, PROJECT, TASK AREA & WORK UNIT NUMBERS 65807F
11. CONTROLLING OFFICE NAME AND ADDRESS Arnold Engineering Development Center/OIS Arnold Air Force Station, Tennessee 37389		12 REPORT DATE July 1979
		13 NUMBER OF PAGES 248
14 MONITORING AGENCY NAME & ADDRESS(if different from Controlling Office)		15 SECURITY CLASS. (of this report) UNCLASSIFIED
		15a. DECLASSIFICATION/DOWNGRADING SCHEDULE N/A
16 DISTRIBUTION STATEMENT (of this Report) Approved for public release; distribution unlimited.		
17 DISTRIBUTION STATEMENT (for the abstract entered in Block 20, if different from Report)		
18 SUPPLEMENTARY NOTES Available in DDC		
19 KEY WORDS (Continue on reverse side if necessary and identify by block number) ejectors (air-driven) B-1 aircraft turbofan engines inlets simulators nozzles scale Mach numbers model transonic flow		
20 ABSTRACT (Continue on reverse side if necessary and identify by block number) An experimental program was conducted to evaluate an air-driven ejector for use as a turbo-engine simulator in wind tunnel testing. The use of an engine simulator will provide the capability to simultaneously simulate inlet and afterbody flow fields of a turbo-powered vehicle. The ejector-powered engine simulator (EPES) was fitted to the right-wing nacelle of a 0.06-scale B-1 aircraft model. The B-1 model was chosen for the investigation because of		

UNCLASSIFIED

20. ABSTRACT (Continued)

the availability for comparisons of inlet and nozzle afterbody data previously obtained in the Arnold Engineering Development Center (AEDC) Propulsion Wind Tunnel Facility Propulsion Wind Tunnel (16T) using conventional test techniques. A limited amount of flight data from the B-1 flight to wind tunnel correlation program was also available to aid in determining the effectiveness of the EPES as a wind tunnel test tool. Data were obtained at free-stream Mach numbers 0.60 to 1.20 with inlet mass flow ratio, nozzle pressure ratio, and model angle of attack as primary variables. The pressure distributions measured on both the inlet and nozzle afterbody surfaces using the EPES model were in general agreement with the conventional test techniques data for both the inlet and the nozzle afterbody at Mach numbers 0.85 and 1.20. The integrated axial pressure force coefficient agreed, in general, to within two counts. In comparison to flight vehicle data, both the inlet and nozzle afterbody pressure distributions agreed well at Mach number 0.85. At Mach number 1.20 the inlet pressure distribution agreed with the flight data; however, the agreement of the nozzle afterbody surface data was not as good. The results obtained over the range of conditions investigated demonstrate that the EPES is a viable test tool for wind tunnel applications.

PREFACE

The work reported herein was conducted by the Arnold Engineering Development Center (AEDC), Air Force Systems Command (AFSC), and Elton R. Thompson was the Air Force project manager. The results presented were obtained by ARO, Inc., AEDC Division (a Sverdrup Corporation Company), operating contractor for the AEDC, AFSC, Arnold Air Force Station, Tennessee. The work was conducted under ARO Projects No. P41T-R4A and P32P-R2A, and the data analysis was completed on September 1, 1978. The manuscript was submitted for publication on October 6, 1978.

CONTENTS

	<u>Page</u>
1.0 INTRODUCTION	7
2.0 APPARATUS	
2.1 Test Facility	8
2.2 Test Article Description	8
2.3 Instrumentation	10
3.0 DATA REDUCTION	
3.1 Data Acquisition and Presentation	11
3.2 Data Reduction Equations	11
3.3 Data Uncertainties	13
4.0 RESULTS AND DISCUSSION	
4.1 Ejector-Powered Engine Simulator Performance	13
4.2 Inlet Pressure Distributions	15
4.3 Nozzle Afterbody Pressure Distributions	17
4.4 Off-Design Performance	20
5.0 SUMMARY OF RESULTS	22
REFERENCES	23

ILLUSTRATIONS

Figure

1. Location of Model in Test Section	25
2. 0.06-Scale B-1 Model Installed in Tunnel 16T	26
3. Left-Hand Flow-Through Nacelle	28
4. Ejector-Powered Engine Simulator Right-Hand Nacelle	29
5. Ejector Primary Nozzles, Subsonic Cruise Configuration	30
6. Conventional Test Techniques Nozzle Afterbody Nacelle	31
7. Nozzle Details	32
8. Conventional Test Techniques Inlet Model, 0.07 Scale	33
9. Conventional Test Techniques Inlet Model Installed in Tunnel 16T	34
10. Details of Inlet Model	35
11. Location of Aft-Nacelle Static Pressure Orifices	36
12. Location of Inlet Ramp and Cowl Static Pressure Orifices	37
13. Ejector-Powered Engine Simulator Internal Instrumentation	38
14. Identification of Pressure Rows	39

<u>Figure</u>	<u>Page</u>
15. Repeatability of Pressure Coefficient Measurements, Ejector-Powered Engine Simulator Model	41
16. Repeatability of Pressure Coefficient Measurements, Flight Vehicle	43
17. Typical EPES Inlet Mach Number Distributions Obtained in Tunnel 16T	45
18. Comparison of Mixing Duct Total Pressures from the Station 8 Probes in the Nacelle with Average Nozzle Exit Pressure from the Calibration	47
19. Variation of Mixing Duct Exit Static Pressure with Primary Pressure (Supersonic Dash Ejectors)	48
20. Variation of Inlet Corrected Airflow Parameter with Ejector Pressure	49
21. Effect of Free-Stream Mach Number on EPES Performance	51
22. Effect of Reynolds Number on EPES Performance	53
23. Effect of Angle of Attack on EPES Performance	55
24. Effect of Mass Flow Ratio on Inlet Pressure Distributions, $M = 0.85$	57
25. Effect of Mass Flow Ratio on External Cowl Surface Pressure Distribution	59
26. Effect of Reynolds Number on Inlet Pressure Distributions, $M = 0.85$	60
27. Effect of Angle of Attack on Inlet Pressure Distributions, $M = 0.85$	62
28. Effect of Nozzle Pressure Ratio on Inlet Pressure Distributions, $M = 0.85$	64
29. Comparison of Inlet Pressure Distributions for the EPES and 0.07-Scale Models, $M = 0.85, \alpha = 1$ deg	66
30. Comparison of Inlet Pressure Distributions for the EPES and 0.07-Scale Models, $M = 0.85, \alpha = 4$ deg	68
31. Comparison of Inlet Pressure Distributions for the EPES and 0.07-Scale Models, $M = 1.20, \alpha = 0$	70
32. Comparison of Inlet Pressure Distributions for the EPES, 0.07-Scale and the Flight Vehicle, $M = 0.85, \alpha = 0.84$ deg	72
33. Comparison of Inlet Pressure Distributions for the EPES Model and the Flight Vehicle, $M = 1.20, \alpha = 2.8$ deg	74
34. Effect of Mass Flow Ratio on Nozzle Afterbody Pressure Distribution, $M = 0.85, \alpha = 0$	76
35. Effect of Reynolds Number on Nozzle Afterbody Pressure Distribution, $M = 0.85, \alpha = 0$	86
36. Effect of Angle of Attack on Nozzle Afterbody Pressure Distributions, $M = 0.85$	96
37. Effect of Nozzle Pressure Ratio on Nozzle Afterbody Pressure Distribution, $M = 0.85, \alpha = 0$	106
38. Effect of Nozzle Pressure Ratio on Nozzle Afterbody Pressure Distribution, $M = 1.20, \alpha = 0$	116

<u>Figure</u>	<u>Page</u>
39. Comparison of Nozzle Afterbody Pressure Distribution for the EPES and NAB Models, $M = 0.85, \alpha = 0$	126
40. Comparison of Nozzle Afterbody Pressure Distributions for the EPES and NAB Models, $M = 1.20, \alpha = 0$	136
41. Comparison of Nozzle Afterbody Pressure Distributions for the EPES and NAB Models and the Flight Vehicle, $M = 0.85, \alpha = 3.45 \text{ deg}$	146
42. Comparison of Nozzle Afterbody Pressure Distributions for the EPES and NAB Models and the Flight Vehicle, $M = 1.20, \alpha = 2.8 \text{ deg}$	156
43. Left-Hand Nacelle Inlets Plugged with Wood Inserts	166
44. Effect of Spillage from the Opposite Nacelle on the Nozzle Afterbody Flow Field, $M = 0.85$	167
45. Effect of Spillage from the Opposite Nacelle on the Nozzle Afterbody Flow Field, $M = 1.20$	177
46. Comparison of Inlet Pressure Distributions of the EPES and 0.07-Scale Models, $M = 0.80$	187
47. Comparison of Inlet Pressure Distributions of the EPES and 0.07-Scale Models, $M = 0.60$	189
48. Comparison of Nozzle Afterbody Pressure Distributions for the EPES and NAB Models, $M = 0.80$	191
49. Comparison of Nozzle Afterbody Pressure Distributions for the EPES and the NAB Models, $M = 0.90$	201
50. Comparison of Axial Force Coefficient for EPES and NAB Models and Flight Vehicle	211
TABLES	
1. Summary of Test Conditions	212
2. Measurement Uncertainties	213
APPENDIX	
A. DESIGN AND CALIBRATION OF EJECTOR-POWERED ENGINE SIMULATORS FOR THE B-1 MODEL	215
NOMENCLATURE	246

1.0 INTRODUCTION

The extension of aircraft model performance data obtained in a wind tunnel to the performance of a flight vehicle is, at present, done with guarded optimism. There are many assumptions which are necessary because it is not possible to duplicate the true aircraft flow field in the wind tunnel. Problems such as model fidelity, the mismatch of Reynolds number, tunnel wall interference, exhaust jet simulation technique, and model support influences have been and will continue to be the subject of intensive investigations in order to improve the techniques used to relate model data to a full-scale vehicle. Engine-induced interactions with the airframe is another area in which uncertainties in the application of wind tunnel data to full scale exist. The present technique used to obtain engine-induced effects requires three models, a complex drag accounting system, and the assumption that the engine-induced drag increments can be applied by superposition throughout the aircraft operating envelope (Ref. 1). The three models required include (1) an aircraft force and moments model to measure the reference performance for the unpowered configuration performance, (2) a jet-effects model with faired-over inlets to measure the nozzle afterbody drag increments, and (3) an inlet model to measure the inlet drag increments. This technique does not include possible interactions between the nacelle inlet and the nozzle afterbody flow fields.

In recent years, a wide variety of wind tunnel techniques has been proposed to obtain coupled engine-airframe performance (Ref. 2). One method proposed is to use an engine simulator installed in the model which is capable of providing simultaneously both inlet and nozzle afterbody flow fields. If successful, this method would reduce the requirement for those models to two by eliminating the need for both inlet and jet-effects models. The results of a test research conducted in the Arnold Engineering Development Center (AEDC) Propulsion Wind Tunnel (16T) (Tunnel 16T) to evaluate the air-driven ejector as an engine simulator are described herein.

The ejector-powered engine simulator (EPES) was designed to match the nacelle of a 0.06-scale model of the B-1 aircraft. The B-1 model was chosen because of the availability of conventional test techniques data on both the inlet and nozzle afterbody for comparison with the EPES results and the availability of flight data from a fully instrumented B-1 aircraft. The B-1 model was also chosen because the short nacelle length-to-diameter ratio represents a more difficult problem for the EPES than would a fighter with fuselage-mounted engines.

2.0 APPARATUS

2.1 TEST FACILITY

The AEDC Tunnel 16T is a variable density, continuous flow tunnel capable of being operated at Mach numbers from 0.20 to 1.60 and stagnation pressures from 120 to 4,000 psfa. The maximum attainable Mach number can vary slightly depending upon the tunnel pressure ratio requirements with a particular test installation. The maximum stagnation pressure attainable is a function of Mach number and available electrical power. The tunnel stagnation temperature can be varied from about 80 to 160°F depending upon the available cooling-water temperature. The test section is 16 ft square by 40 ft long and is enclosed by 60-deg inclined-hole perforated walls of six-percent porosity. The general arrangement of the test section with the model installed is shown in Fig. 1. Additional information about the tunnel, its capabilities, and operating characteristics is presented in Ref. 3.

2.2 TEST ARTICLE DESCRIPTION

The basic model which was used to measure both the EPES and the conventional nozzle afterbody data was a 0.06-scale model of the B-1 aircraft. The model was strut mounted in the inverted position as shown in Fig. 1. Photographs of the model showing front and aft views are presented in Fig. 2. Wing sweep could be manually changed to any of four leading-edge sweep angles (25, 55, 65, and 67.5 deg). For this investigation, a wing sweep angle of 65 deg was used with a wing glove fairing which simulated a 1G wing deflection. The nacelles, shown in Fig. 2, were removable to allow interchangeable nacelle configurations to be tested. The inlet data used for comparison with the EPES results were obtained using a 0.07-scale B-1 inlet model.

2.2.1 Ejector Powered Engine Simulator

A 0.06-scale right-wing nacelle (Fig. 2b), especially designed to accommodate two EPES units, was used to simulate the engine installation. The inlet ramp configuration of this nacelle represented the collapsed ramp contours of the aircraft during subsonic flight. The external contours of the nacelle duplicated those of the flight vehicle, and the aft area was designed to accept the nozzles used on the jet-effects model. The left-hand nacelle was the Rockwell International flow-through configuration with reference nozzles (Fig. 3).

Two sets of EPES units, shown schematically in Fig. 4, were used during the investigation, (1) a subsonic cruise configuration and (2) a supersonic dash configuration. The subsonic cruise configuration had 19 strut-mounted primary nozzles distributed in the

flow duct as shown in Fig. 4 and an exhaust nozzle contraction ratio of 1.19. The supersonic dash configuration had 22 strut-mounted primary nozzles and an exhaust nozzle contraction of 1.1. An outbleed scoop to remove a portion of the inlet airflow was provided for both EPES configurations as shown in Fig. 4. Figure 5 shows the subsonic cruise EPES ejector nozzles with the primary airflow path indicated.

The subsonic cruise EPES consisting of the ejector assembly, the mixing duct, and a duplicate of the internal geometry of the 0.06-scale B-1 Mach number 0.85 cruise nozzle was calibrated in the R-1A-2 test cell. The supersonic dash EPES was also calibrated in the R-1A-2 test cell with the mixing duct and internal nozzle geometry of the 1.2 A/B nozzle. During the wind tunnel program, however, the 1.6 A/B nozzle was used with the supersonic dash ejectors because the external contours were more representative of the flight test configuration. The mixing duct and nozzle throat diameters of the 1.6 A/B configuration were 2.74 and 2.638 in., respectively, compared to 2.808 and 2.678 in. for the 1.2 A/B nozzle configuration. Discussion of the EPES design considerations and calibration tests are presented in Appendix A.

2.2.2 Jet-Effects Model

The jet-effects nacelle (Fig. 6), which was installed on the same 0.06-scale B-1 model used in the simulator tests, had faired-over inlets and was designed to provide nozzle afterbody data using the conventional testing technique. High-pressure air for exhaust plume simulation is introduced into the nacelle through airflow passages internal to the model. The aft portion of the nacelle is designed to allow the mounting of various nozzle afterbodies which represent nozzle contours at different flight conditions. The external contours of the nacelle downstream of the inlet fairing conforms to the contours of the flight vehicle. A more detailed description of the jet-effects nacelle is presented in Ref. 4.

2.2.3 Nozzle Afterbodies

Two nozzle afterbodies representing the external contours of the Mach number 0.85 cruise configuration and the Mach number 1.60 afterburning supersonic dash configuration were used during this program. In addition, the reference nozzles were used on the left-hand flow-through nacelle. The details of the nozzle contours are shown in Fig. 7.

2.2.4 Inlet Model

The inlet data used for comparison with the EPES data were obtained using a 0.07-scale representation of a partial left-side fuselage-wing and left-side dual-inlet nacelle of the B-1

aircraft (Fig. 8). A photograph of the model installed in the wind tunnel is presented in Fig. 9. The external contours of the inlet conform to those of the B-1 aircraft. Each inlet had one fixed 7-deg ramp, two movable ramps, and one movable panel (Fig. 10). The throat lip height was remotely adjustable from 52 to 83 percent of inlet capture height. The inlet mass flow was controlled by using a remotely actuated flow control valve located between the diffuser section and the metering nozzle in each duct. A more detailed description of the inlet model is presented in Ref. 5.

2.2.5 Flight Test Aircraft

The left-hand nacelle of the B-1 No. 2 aircraft was instrumented for pressure measurements as a part of an extensive wind tunnel-to-flight correlation program (Ref. 6). The aircraft is a blended wing-body configuration with variable sweep wings. Four YF-101-68-100 dual-rotor augmented turbofan engines are mounted in the two nacelles which are attached to the underside of the wing. The exhaust nozzles are of a variable area convergent-divergent design; the external compression inlet has a fixed 7-deg first ramp, variable angle second and third ramps, and a variable throat lip height.

2.3 INSTRUMENTATION

The EPES nacelle was instrumented with 274 surface pressure orifices, 228 of which were located on the aft nacelle and nozzle afterbody surfaces as shown in Fig. 11. The remaining 46 orifices were located on the inlet ramp and cowl of the outboard flow duct (Fig. 12). The location of the 228 pressure orifices on the aft nacelle is geometrically the same as those on the 0.06-scale jet-effects model and the flight vehicle. The location of the 46 inlet pressure orifices is geometrically the same as the 0.07-scale inlet model and the flight vehicle; however, both the 0.07-scale inlet and flight vehicle instrumentation was on the left-side nacelle. The static pressures on the model surface were measured with eight Statham transducers connected to eight Scanivalves^{*} mounted in the model. Airflow temperatures were measured using copper-constantan thermocouples.

The internal flow ducts of the EPES nacelle were instrumented with 44 pressures as shown in Fig. 13. The tubing for internal pressures was routed through the support strut and connected to the Tunnel 16T precision pressure balance system (PPB).

For the EPES model, the outbleed flow rate was measured using an airflow venturi. The primary airflow to the ejectors was calculated based on total pressure of the air and the area of the choked primary nozzles. The inlet mass flow rate and the nozzle pressure ratio of the EPES nacelle were calculated from an empirical relationship resulting from pretest calibration of the ejectors (Appendix A).

3.0 DATA REDUCTION

3.1 DATA ACQUISITION AND PRESENTATION

Data were obtained primarily at free-stream Mach numbers of 0.85 and 1.20 which correspond to the design points for the subsonic cruise and supersonic dash EPES. The nozzle pressure ratio (NPR), the mass flow ratio (MFR), and the angle of attack (α) were varied at each condition. The NPR was varied from approximately 1.0 to 4.0 and MFR from 0.38 to 0.48 for the subsonic configuration. Nozzle pressure ratio was varied from approximately 3.0 to 7.0 and MFR from 0.58 to 0.65 for the supersonic configuration. The angle of attack was varied from 0 to 4 deg for both configurations. In addition to these parametric variations, data were obtained at specific values of NPR, MFR, and α corresponding to conditions of the conventional technique test and flight. Limited off-design data were obtained at free-stream Mach numbers 0.60, 0.80, and 0.90 with the subsonic configuration and 0.97, 1.11, 1.15, 1.30, and 1.40 with the supersonic configuration.

The pressure coefficient (C_p) data are presented as a function of nacelle station nondimensionalized by nacelle length. The data are identified by row number with two to four rows presented per page. The location of each row of pressure orifices on the model afterbody and inlet is shown in Fig. 14. A summary of all test conditions for the EPES investigation is presented in Table 1.

3.2 DATA REDUCTION EQUATIONS

The primary data presented in this report are the model pressure coefficient distributions calculated using the following relationship

$$C_{p_i} = \frac{P_i - P_\infty}{q_\infty} \quad (1)$$

The axial pressure drag was calculated for various model components from

$$CD = \sum \frac{C_{p_i} A_i}{AREF} \quad (2)$$

where A_i is the local area assigned to the local C_p and AREF is the reference area based on the wing area (1,946 square feet for the flight vehicle).

The inlet mass flow rates were calculated from pressure measurements in the model. The ejector face flow rate was calculated from

$$W_A = (A_2) (CF_2) (PS_2) \left\{ \frac{\gamma g_c (M_2)^2}{TT_B} \left(1.0 - \frac{\gamma-1}{2} (M_2)^2 \right) \right\}^{1/2} \quad (3)$$

where A_2 is the inlet area at the ejector face, CF_2 is a coefficient equal to 0.9, PS_2 is the measured static pressure, TT is the free-stream total temperature, and M_2 is the local Mach number based on pressure measurements. The bleed flow (WB) was calculated from pressure and temperature measurements in an airflow venturi.

The inlet airflow rate (WI) is the sum of the ejector face flow rate and one-half the bleed flow rate.

$$WI = W_A + 1/2 WB \quad (4)$$

One-half the bleed flow was used under the assumption that the bleed flow was extracted equally from the inboard and outboard flow ducts.

The mass flow ratio (MFR) is defined as

$$MFR = WI/WC \quad (5)$$

where WC is the ideal capture area flow rate obtained from

$$WC = \left(\frac{\gamma g}{R} \right)^{1/2} (P_\infty) (AC) M \left(\frac{1 + \frac{\gamma-1}{2} M^2}{TT} \right)^{-1/2} \quad (6)$$

where AC is the capture area of the inlet.

In the calibration tests, EPES performance was characterized by an inlet corrected airflow parameter (WEC) and an exhaust-to-inlet total-pressure ratio (SPR) where

$$WEC = \frac{WI(A_2)^{1/2}}{(\delta_2) (AEXT)} \quad (7)$$

The wind tunnel and calibration parameters are related by

$$MFR = \frac{(WEC) (AEXT) (\delta_2)}{WC (\delta_2)^{1/2}} \quad (8)$$

and

$$NPR = \frac{(SPR)(PT2A)}{PS_{\infty}} \quad (9)$$

3.3 DATA UNCERTAINTIES

Uncertainties (combinations of systematic and random errors) of the basic tunnel parameters, shown in Table 2, were estimated from repeat calibration of the instrumentation and from the repeatability and uniformity of the test section flow during tunnel calibration. Uncertainties in the instrumentation systems were estimated from repeat calibration of the systems against secondary standards whose uncertainties are traceable to the National Bureau of Standards calibration equipment. The instrument uncertainties are combined using the Taylor series method of error propagation described in Ref. 7 to determine the uncertainties of the reduced parameters shown in Table 2. The uncertainty in C_p (from Table 2) is ± 0.0104 at Mach number 0.85. The repeatability of C_p , however, measured for similar test conditions was ± 0.0029 . Figure 15 presents the C_p distribution for a typical row of pressure orifices on the nozzle and cowl surfaces for two similar test conditions. No error bars are shown on the figures because the uncertainty limits are within the data symbol size. Uncertainties for the jet effects and inlet tests are the same as for the EPES data. The evaluation of data uncertainties for the flight data is not available; however, repeatability of the calculated pressure coefficients C_p 's for the flight data at similar test conditions is shown in Fig. 16 for the same rows of pressure. The repeatability of the flight data is as good as the EPES data.

4.0 RESULTS AND DISCUSSION

4.1 EJECTOR-POWERED ENGINE SIMULATOR PERFORMANCE

Internal flow characteristics obtained with the EPES in the wind tunnel model were compared with calibration results to determine if any significant differences were evident. Effect of free-stream Mach number, Reynolds number, model attitude, and left-hand nacelle geometry on internal performance was also evaluated.

Ejector inlet Mach number distributions (Fig. 17) obtained from the station 2 pitot pressure rakes (Fig. 13) indicated flow nonuniformities in the wind tunnel tests that did not exist in many of the calibrations (Figs. A-4 and A-5). The pressure nonuniformities in both the subsonic cruise and supersonic dash configurations during wind tunnel tests were caused to a large degree by the relative orientation of the outbleed scoops with respect to the station 2 rakes. Scoop wakes produced a low Mach number region near the center of the outboard duct and along the upper portion of the inboard duct. Uniformity of the inboard ejector

inlet flow was improved with outbleed which is consistent with the calibration results (Fig. A-4). The trends and values of inlet Mach numbers indicated in Fig. 17 are representative of results obtained at all wind tunnel test conditions.

Mixing duct flow conditions obtained in the wind tunnel and the calibration tests were generally consistent for the subsonic cruise configurations. However, relatively high mixing duct static pressures, representative of subsonic flow conditions, were maintained at higher ejector pressures and, hence, higher values of NPR in the wind tunnel tests. The calibration results are presented in detail in Appendix A. In the wind tunnel model, the transition from subsonic to supersonic conditions in the mixing duct was delayed because the exhaust nozzle base pressure was from 6 to 13 percent higher in the wind tunnel than the nozzle exit and test cell pressures of the calibration tests. Pitot pressure measurements in the mixing ducts are in good agreement with the average mixing duct total pressures obtained from the calibrations (Fig. 18) for the range of conditions covered in the wind tunnel tests.

Mixing duct static pressures obtained with the inboard and outboard supersonic dash components in the wind tunnel model (Fig. 19) were more consistent than the calibration results. Furthermore, the variation of mixing duct static pressure with ejector pressure obtained in the wind tunnel exhibits a different variation from the calibration results. This difference in the variation is attributed to the differences in mixing ducts and exhaust nozzles discussed in Section 2.2.1. The smaller nozzle throat of the wind tunnel nozzle compared to the calibration nozzle should result in a slightly higher nozzle pressure ratio; however, a recalibration of the EPES using the wind tunnel nozzle would be required to verify this effect.

The variation of inlet corrected airflow with ejector pressure is shown in Fig. 20. Since flow rates in the wind tunnel model nacelles were calculated from an average total pressure obtained from the station 2 rake, they have a higher uncertainty than the calibration flow rates which were obtained with a flow metering venturi. Furthermore, since each of the station 2 probes were equally weighted, the outbleed scoop wakes biased the average ejector inlet pressure and, hence, the flow rate, to a lower-than-actual value, particularly for the inboard units. Considering this effect and the uncertainty in the flow coefficient used at the ejector inlet station for the flow computations (Eq. 3), inlet corrected flow parameters obtained in the nacelle are in reasonable agreement with the calibration results with no outbleed. Choking in the model passages limited the outbleed to about 13 percent and 9 percent for the subsonic cruise and supersonic dash nacelle configurations, respectively.

Variation of SPR with WEC from the nacelle is shown in Figs. 21 through 23. The performance of the subsonic cruise ejectors was measured at free-stream Mach numbers of

0.60, 0.80, and 0.85 (Fig. 21a), Reynolds numbers of 2.5 and 3.6×10^6 per foot (Fig. 22a), and angles of attack of 0 and 4 deg (Fig. 23a). No significant changes in performance were noted at these flow conditions. No changes were noted in the performance of the supersonic dash ejectors as Mach number was varied from 0.97 to 1.40, Reynolds number from 2.5 to 2.9×10^6 per foot, and angles of attack from 0 to 4 deg (Figs. 21b, 22b, and 23b, respectively).

4.2 INLET PRESSURE DISTRIBUTIONS

The pressure distributions measured on the EPES model are compared to the pressure distributions measured on the 0.07-scale inlet test and the B-1 flight vehicle. The pressure orifices for each of these inlets are positioned in geometrically similar locations for all three inlets. There are four variables which are considered to have a potential influence on the inlet performance. The effect of these variables is discussed before direct comparisons of the performance of each inlet are made.

4.2.1 Effect of Mass Flow Ratio

The MFR is defined as the ratio of the actual inlet airflow to the ideal inlet airflow. Inlet spillage, therefore, is one minus the MFR.

The effect of varying MFR on the inlet ramp and cowl pressure distributions is shown in Fig. 24 for the 0.07-scale conventional test techniques model at Mach number 0.85. The pressure distribution shape on the ramp remains generally the same as MFR is increased from 0.504 to 0.700; however, the C_p level decreases with increasing MFR. As a consequence, the axial pressure force on the ramp, also shown in Fig. 24a, decreased six counts as MFR was increased to 0.70. The pressure distribution shape on the cowl changes with increasing MFR as shown in Fig. 24b. The C_p measured at the forward most pressure orifice location increased from -1.25 to 0.30 as MFR increased from 0.504 to 0.70. An explanation for the large effect of MFR on the cowl lip can be shown by considering a typical inlet flow (Fig. 25). At MFR = 1, the incoming stream tube will expand to fill the inlet and stagnation pressure will be measured on the cowl lip. The flow will then accelerate from the stagnation point along the external cowl surface. At an MFR of less than one, the stagnation point will occur further around the cowl lip (toward the inside of the inlet). The external cowl surface will then be influenced by an expansion region in the flow field, as shown in Fig. 25, resulting in low pressure coefficients near the cowl lip. The pressure profiles as a function of MFR observed on the B-1 inlet are consistent with this behavior. The axial force coefficient of the cowl (CDCOWL) increased from -0.0021 to 0 for the pressure distributions shown in Fig. 24b.

4.2.2 Effect of Reynolds Number

The effect of Reynolds number on the inlet ramp and cowl surface pressure distributions for the 0.07-scale inlet is shown in Figs. 26a and b for Mach number 0.85 and Reynolds numbers of 3.5, 4.2, and $5.0 \times 10^6/\text{ft}$. There are only slight differences in the measured pressure coefficients. The axial pressure force coefficients, also presented in Fig. 26, calculated from the C_p profiles were constant for the range of Reynolds number investigated. Therefore, for the purposes of comparing inlet pressure distributions from one model to another, the Reynolds number was not considered to affect the inlet pressure distributions.

4.2.3 Effect of Angle of Attack

The C_p distribution on the ramp surface was affected only slightly (in one pressure orifice row) by varying angle of attack from 0 to 6 deg on the 0.07-scale inlet model (Fig. 27a) at Mach number 0.85. The C_p level on the third ramp pressure orifice row decreased with increasing angle of attack. The axial pressure force was constant to within one count on the ramp. The effect of varying angle of attack on the C_p distribution of the cowl surface was stronger than on the ramp (Fig. 27b). The C_p level increased with increasing angle of attack. Also, the axial pressure force coefficient increased from -0.0028 at $\alpha = 0$ to -0.0024 at $\alpha = 6$ deg.

4.2.4 Effect of Nozzle Pressure Ratio

The effects of NPR on the inlet C_p distributions at $M = 0.85$ are shown in Fig. 28. The C_p data indicate no change for pressure ratios of 1.96 and 3.83. The axial pressure force is also constant on both surfaces for both NPR's. For the extent of this investigation, therefore, it was concluded that the NPR does not affect the inlet C_p distributions.

4.2.5 Comparison of Inlet Pressure Distributions

The 0.06-scale EPES model was tested extensively at Mach numbers 0.85 and 1.20 to allow direct comparisons with data previously obtained on the 0.07-scale inlet model. Also, specific test conditions to match existing flight vehicle data were obtained. A comparison of the inlet ramp and cowl pressure distribution for the EPES and 0.07-scale models is shown in Fig. 29 for Mach number 0.85 and $\alpha =$ approximately 1 deg. The ramp C_p distributions agree closely and the axial pressure force coefficient was constant at 16 counts. The C_p distribution on the cowl surface was similar in shape for both inlets. However, the profile measured on the EPES model displayed an abrupt change in shape at nacelle station (NS)

0.164. This slope change was present in all the data obtained on the EPES model at subsonic Mach numbers and was not evident in the 0.07-scale inlet model data. The cowl lip area was designed to be a gradually curving surface with the slope decreasing with increasing Y/L stations. A posttest inspection of the EPES cowl lip revealed a flat region in the vicinity of station 0.164. This flat region is believed to have caused the change in slope observed in the pressure profile. The surface coordinates of the 0.07-scale inlet were not available for direct contour comparisons. The axial pressure force coefficients for the cowl surfaces were -0.0032 and -0.0040 for the 0.07-scale and EPES models, respectively. The EPES and 0.07-scale pressure distributions are compared in Fig. 30 at Mach number 0.85 and $\alpha = 4$ deg. The agreement of both the ramp and cowl C_p distributions and axial pressure force coefficients is the same as at $\alpha = 1$ deg.

The comparison between the EPES and 0.07-scale inlets at Mach number 1.20 and $\alpha = 0$ is presented in Fig. 31. The ramp C_p distributions measured on both inlets agree closely, and the axial pressure force coefficient for the two models is the same. The C_p distributions on the external cowl again agree in general trend but appear to be affected by the surface irregularity of the EPES model. At Mach number 1.20 the cowl C_p distribution tends to approach a constant value of zero axially down the nacelle for both models. The axial pressure force coefficient for both models was -0.0004.

The range over which MFR could be varied was limited to from 0.38 to 0.48 for a free-stream Mach number of 0.85 (Appendix A). The minimum MFR obtained on the flight vehicle at Mach number 0.85 was 0.66. Therefore, a comparison of inlet C_p distributions at the same MFR was not possible. However, the inlet distributions, both ramp and cowl, measured on all three inlets are presented in Fig. 32 for the test conditions specified in the figure. The disagreement between the profile presented is consistent with the effects of MFR observed in Fig. 24 for the 0.07-scale inlet model. For this reason, it is believed that the C_p distributions measured on the EPES model would agree reasonably well with flight data if MFR could be matched. A comparison between the EPES and flight inlet pressure distributions measured at a free-stream Mach number of 1.20 is shown in Fig. 33. The C_p profiles on the ramp are in good agreement and the integrated axial pressure force is 20 counts for both data sets. The agreement of the distributions measured on the cowl is not as good as those on the ramp, although the axial pressure force difference is only four counts.

4.3 NOZZLE AFTERBODY PRESSURE DISTRIBUTIONS

4.3.1 Effect of Mass Flow Ratio

The effect of varying MFR from 0.423 to 0.480 on the nozzle afterbody C_p distributions at Mach number 0.85 and an NPR of 2.88 is shown in Fig. 34. No effect is evident for this

MFR variation. However, no general conclusion can be reached regarding the effect of MFR on the afterbody flow fields based only on this limited information. The ability to vary MFR was limited by model constraints discussed in Appendix A.

4.3.2 Effect of Reynolds Number

The effects of varying unit Reynolds number from 2.54 to 3.61×10^6 per foot on the nozzle afterbody pressure distribution are shown in Fig. 35. The higher Reynolds number, in general, resulted in a lower level of C_p on the nozzle afterbody surface. The regions most strongly influenced by the Reynolds number change were the areas of the underwing fairing (rows 1 and 2), the inside surfaces of the nozzles (row 7), and the inboard nozzle surface (row 9). The axial pressure force of the combined nozzles increased three counts as Reynolds number was increased from 2.54 to 3.61×10^6 per foot. The effect of Reynolds number on the afterbody pressure distributions was larger for the EPES model than was observed on the NAB model (Ref. 4). However, the NAB model data were obtained with grit on a nacelle forward station, whereas the EPES data were obtained without grit.

4.3.3 Effect of Angle of Attack

The effects of varying α from 0 to 4 deg on the nozzle afterbody C_p distribution are shown in Fig. 36 for Mach number 0.85. The region of the afterbodies affected by varying α were, in general, the outboard side of the nacelle (rows 3, 3, 5, and 6). The effect of varying α was to increase C_p with increasing α . However, the maximum increase in C_p with α was only 0.05, whereas the average increase was on the order of 0.005. The axial pressure force on the nozzle was constant (one count) indicating the overall effect of α on the afterbody flow field is extremely small. The effect of varying α from 0 to 4 deg on the aft nacelle for the jet-effects NAB model was to decrease the axial force by 3.4 counts (Ref. 4). However, the EPES model was not instrumented fully in the midnacelle area, and the total axial force reported in Ref. 4 could not be calculated for this model.

4.3.4 Effect of Nozzle Pressure Ratio

The axial pressure force on the nozzle surfaces increased from zero to seven counts as NPR was increased from 1.55 to 4.22 at Mach number 0.85 (Fig. 37). In general, the absolute value of C_p on the nozzle decreased with increasing NPR. The region which was most affected by varying NPR was the region between the two nozzles (row 7) and the areas immediately adjacent to the nozzle exits. The maximum decrease in C_p was on the order of 0.05 on row 7. The decrease in pressure in these regions as NPR was increased is indicative of entrainment effects from the jet exhaust. The effects of NPR on the nozzle surfaces of the EPES model are larger than, but in the same direction as, the effects observed on the NAB

model (Ref. 4) for which the maximum C_p decrease was 0.017 for an NPR change from 2.0 to 3.6. For Mach number 1.2, the combined axial pressure force for the twin nozzles decreased from 20 counts to 16 counts as NPR was increased from 3.30 to 5.46 (Fig. 38). As in the subsonic case, the region most affected was the area between the two nozzles and the area around the nozzle exit. The maximum C_p rise with increasing NPR was 0.12 in row 7. The increasing C_p with increasing NPR is indicative of plume shape effects generated by plume expansion at the higher pressure ratios. The effects of NPR on the nozzle surface C_p distribution for the EPES model is in the same direction as that observed on the NAB conventional test technique jet-effects model. The maximum change in C_p for the NAB model was 0.10 for a change in NPR from 4.02 to 5.02.

4.3.5 Comparison of Nozzle Afterbody Pressure Distributions

The EPES model was tested at specific values of nozzle pressure ratio and angle of attack at Mach numbers 0.85 and 1.20 to enable direct comparisons with the existing jet-effects model data. Both the EPES and the jet-effects (NAB) models used the same nozzles. A comparison of the C_p distributions measured at Mach number 0.85 and $\alpha = 0$ is shown in Fig. 39. In general, the distributions measured for each row of pressure orifices have the same shape for both models. The value of C_p on the underwing fairing (rows 1 through 4) was consistently 0.025 lower on the EPES model than on the NAB model. On the outboard nozzle surfaces (rows 5 and 6), however, the EPES model had C_p 's on the order of 0.025 , higher than was measured on the NAB model. The region between the two nozzles (row 7) essentially measured free-stream pressure for both models. The C_p 's measured on the inboard nozzle (rows 8 and 9) did not have a systematic difference between the two models. One possible reason for the observed differences in the C_p distributions is the effect of inlet spillage.

For the EPES model, spillage was on the order of 50 percent; on the NAB model, spillage was 100 percent. The effect of spillage on the nozzle afterbody flow field of the EPES model was discussed in Section 4.3.1 and was shown to have no discernible effect; however, the range of spillage variation for the EPES model was only eight percent. The combined axial pressure force of the two nozzles was five counts for the EPES model and three counts for the NAB model. At free-stream Mach number 1.20, $\alpha = 0$, the general shape of the measured C_p distributions was the same (Fig. 40); however, the agreement between the C_p values was not as good for the two models as it was at the subsonic Mach number. This disagreement is attributed to the effect of inlet spillage on the afterbody. If inlet spillage (35 percent for the EPES and 100 percent for the NAB models) does generate the measured differences in the C_p distributions, it is felt that the EPES C_p distributions are more representative of the true flow field since 100 percent spillage is totally unrealistic. There was no systematic difference observed in the data from the two models. The region of

the interfairing between the two nozzles and the external nozzle surfaces joining the interfairing (rows 4 and 7, Figs. 40d and g), had the largest differences in C_p (on the order of 0.05). The axial pressure force for the EPES model was 16 counts and 12 counts for the NAB model. For both the subsonic and the supersonic Mach numbers, the EPES model had a higher combined nozzle axial force than the NAB model.

The C_p distributions measured on the EPES model are compared to those measured on the jet-effects NAB model and the flight vehicle at Mach number 0.85 in Fig. 41. The pressure ratio was not matched (2.73, 2.87, and 2.65 for the NAB, EPES, and Flight, respectively); however, the effect of varying NPR was shown to be small in Section 4.3.4. In general, the C_p profiles measured on all three models agree in shape. The largest disagreement observed between the flight vehicle and models was in the region of the wing trailing-edge fairing (rows 1, 2, and 3). The axial pressure force calculated was minus two, plus one, and zero counts for the NAB, EPES, and flight vehicle, respectively.

The agreement between the C_p distributions on the three models at Mach number 1.20, $\alpha = 2.80$ deg is not good (Fig. 42). The worst agreement was observed in the region of the wing trailing-edge fairing (rows 1, 2, and 4), the nozzle interfairing (row 7), and the area adjacent to the nozzle exits. The integrated axial pressure force coefficient was eight counts for the flight vehicle and 15 and 17 counts for the NAB and EPES models, respectively.

4.3.6 Left Nacelle Spillage Effects

In an attempt to assess the effect of spillage from the opposite nacelle on the afterbody flow field, the left-hand flow-through nacelle inlets were plugged to obtain an MFR of zero. The inlet plugs were made of wood and were inserted for a portion of the experimental program. Figure 43 shows a photograph of the left-hand nacelle with the inlet plugs in place. The C_p distributions obtained both at Mach number 0.85 and at Mach number 1.20 with the plugged left nacelle are compared with the C_p distributions obtained with the flow-through left-hand nacelle (Figs. 44 and 45). Only slight differences in the C_p values were observed for both subsonic and supersonic test conditions. The nozzle axial pressure force was constant for both data sets. For the limited data obtained, the spillage from the opposite nacelle does not affect the NAB flow field.

4.4 OFF-DESIGN PERFORMANCE

Each ejector-powered engine simulator is designed for a specific Mach number condition as stated in Appendix A. The two sets of ejectors used during this experimental program were designed for operation at Mach numbers 0.85 and 1.20. A limited amount of data was obtained at off-design Mach numbers to assess the EPES performance at these conditions.

A comparison of the EPES and 0.07-scale inlet C_p distributions is shown in Figs. 46 and 47 for Mach numbers 0.80 and 0.60, respectively. At Mach number 0.80, the EPES ramp C_p distributions agreed with the distributions measured on the 0.07-scale inlet model. The region of the EPES model irregularity on the cowl surface affected the cowl C_p distribution and resulted in the disagreement shown on Fig. 46b. The axial pressure force was constant on the ramp and differed by 12 counts on the cowl surface. At Mach number 0.60, the absolute value of the ramp pressure coefficients for the EPES model was lower by approximately 0.05 than for the 0.07-scale inlet model (Fig. 47a) which is indicative of a higher MFR. The C_p distribution on the cowl (Fig. 47b) also has the general shape observed for a higher MFR than measured. Based on these pressure distributions, the authors suspect that MFR for the EPES model at Mach number 0.60 is low. This can result if the inlet flow coefficient in Eq. (3) is a function of pressure.

The C_p distributions on the nozzle surfaces obtained with the EPES at Mach number 0.80 generally agree with the distributions from the jet-effects NAB model on the rear portion of the nozzle (Fig. 48). However, on the forward section of the nozzles, particularly in the regions exposed to the free stream (rows 5, 6, and 8), the EPES model, in general, produced higher values of C_p , i.e., values closer to zero. The higher pressure coefficients in these regions resulted in a lower axial force coefficient for the EPES model (0.0003 on the EPES compared to 0.0004 on the NAB model). The C_p distributions measured for rows 5, 6, and 8 were also higher on the forward portion of the nozzles on the EPES model than on the NAB at Mach number 0.90 (Fig. 49). This was overshadowed, however, by lower pressure coefficients measured in the region influenced by the wing interfairing (rows 2, 3, 4, and 9) which resulted in an increased axial pressure force coefficient for the EPES model (0.0005 for the EPES model compared to 0.0003 for the NAB model).

The consistently higher C_p 's observed on the EPES compared to the NAB model for rows 5, 6, and 8 at Mach numbers 0.80 and 0.90 were also present at Mach number 0.85 (Fig. 39). This systematic behavior is probably related to the effects of inlet spillage. One can rationalize that the spillage flow in effect results in a thicker equivalent nacelle, compared to the no spillage case, which would cause the flow to expand more resulting in a generally lower pressure. This effect coupled with the fact that grit was used on the NAB nacelle and not on the EPES nacelle resulted in the consistently lower C_p 's on the NAB model (100-percent spillage) in the region of the afterbody not influenced by the wing interfairing or the jet efflux.

At Mach number 0.90, the forward portion of the nozzle afterbody flow field is also affected by the presence of terminal shock waves whose presence are indicated by C_p values below the critical value (-0.20). The location of these shock waves would also be expected to

be influenced by the spillage flow from the inlet. The effects of spillage on the shock locations is believed to have caused the lower C_p 's measured on the EPES model in the region influenced by the wing intersfairing.

A comparison of the axial force coefficient calculated from pressure measurements on the nozzles for both the EPES and NAB models and the flight vehicle is shown in Fig. 50 as a function of free-stream Mach number. At subsonic speeds, the force coefficient is in excellent agreement for all three data sets. At Mach numbers greater than one, however, the flight vehicle data are systematically lower than are the two sets of data obtained on the models. The reason for this discrepancy is under investigation at AEDC as part of a wind tunnel-to-flight correlation study.

The internal performance of the EPES was not affected by the off-design conditions (Section 4.1). At Mach number 0.80, the EPES inlet pressure distributions agreed with those measured on the 0.07-scale inlet model. The pressure distributions measured on the nozzle afterbody were apparently affected by inlet spillage and, therefore, data obtained with the EPES were considered more representative of flight than those measured on the NAB model, even at the EPES off-design conditions.

5.0 SUMMARY OF RESULTS

An experimental program was conducted in Tunnel 16T to evaluate an air-driven ejector as an engine simulator. The ejectors were installed in a 0.06-scale model of the B-1 aircraft. Data obtained on the EPES nacelle were compared with inlet and nozzle afterbody data obtained using conventional wind tunnel test techniques as well as with flight test data. In general, the inlet and nozzle afterbody data obtained using the EPES model agreed well with the data obtained using conventional test techniques and were in fair agreement with the data from the flight test. It is concluded, therefore, that the EPES provides a method to simultaneously obtain both inlet and nozzle afterbody data on a single model. The use of the EPES in future wind tunnel tests will eliminate the requirement for both an inlet model and a jet-effects model. Further studies using a model designed specifically for use with an EPES are desirable, however, to investigate the possibility of increasing the range of mass flow ratio. Mass flow ratio restrictions encountered during this investigation were the result of adapting an existing model rather than designing a new model which would provide the required inlet outbleed capacity.

REFERENCES

1. "AGARD Conference Proceeding No. 150 on Airframe/Propulsion Interference." AGARD-CP-150, March 1975.
2. Smith, G. D., Matz, R. J., and Bauer, R. C. "Analytical and Experimental Investigation of Ejector-Powered Engine Simulators for Wind Tunnel Models." AEDC-TR-76-128 (ADA034725), January 1977.
3. *Test Facilities Handbook* (Tenth Edition). "Propulsion Wind Tunnel Facility, Vol. 4." Arnold Engineering Development Center, May 1974.
4. Price, E. A., Jr. "Analysis of Nacelle Pressure Distributions from a 0.06-Scale B-1 Jet Effects Model at Transonic Mach Numbers." AEDC-TR-78-48.
5. Black, J. A. "A Wind Tunnel Test of a 0.07-Scale Inlet Drag Model of the B-1 Aircraft at Mach Numbers from 0.60 to 1.60." AEDC-TR-73-188 (AD914546L), November 1973.
6. Richey, G. K., Bowers, D. L., Kostin, L. C., and Price, E. A., Jr. "Wind Tunnel/Flight Test Correlation Program on the B-1 Nacelle Afterbody/Nozzle at Transonic Conditions." AIAA Paper 78-989, Presented at the AIAA/SAE 14th Joint Propulsion Conference, Las Vegas, Nevada, July 25-27, 1978.
7. Abernethy, R. B. and Thompson, J. W., Jr. "Handbook - Uncertainty in Gas Turbine Measurements." AEDC-TR-73-5 (AD755356), February 1973.
8. Shapiro, A. H. *The Dynamics and Thermodynamics of Compressible Fluid Flow*. The Ronald Press Company, New York, 1953, Vol. 1, p. 150.

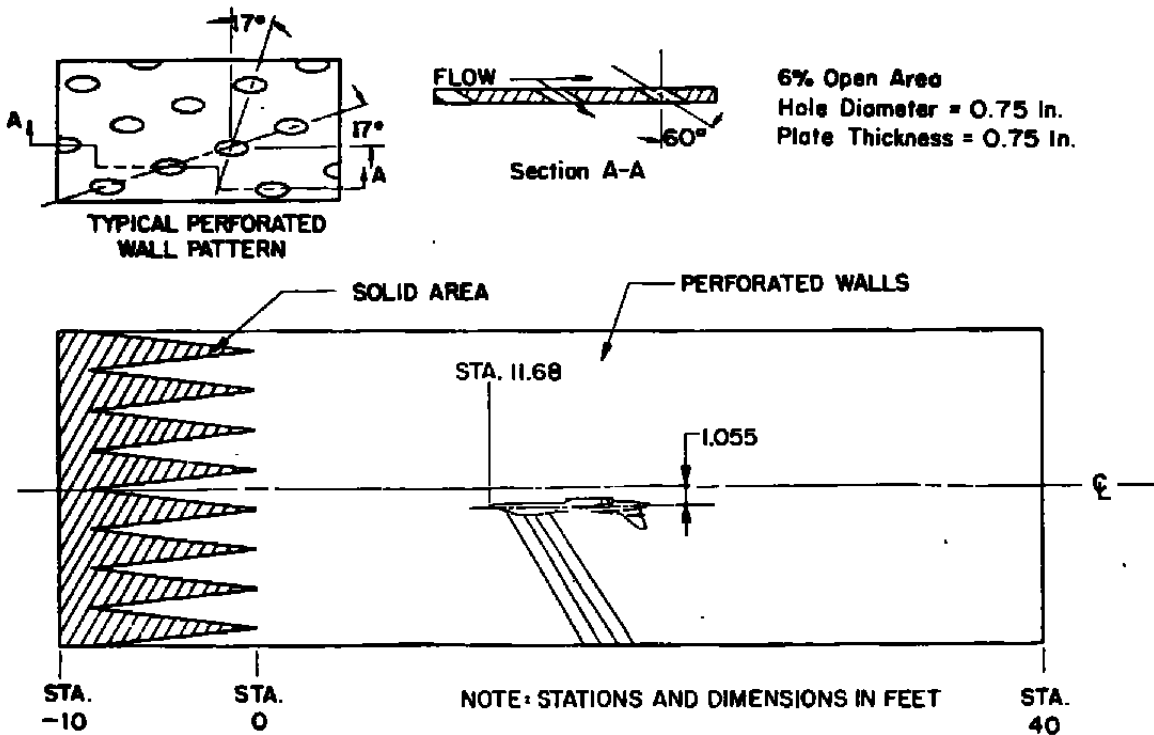
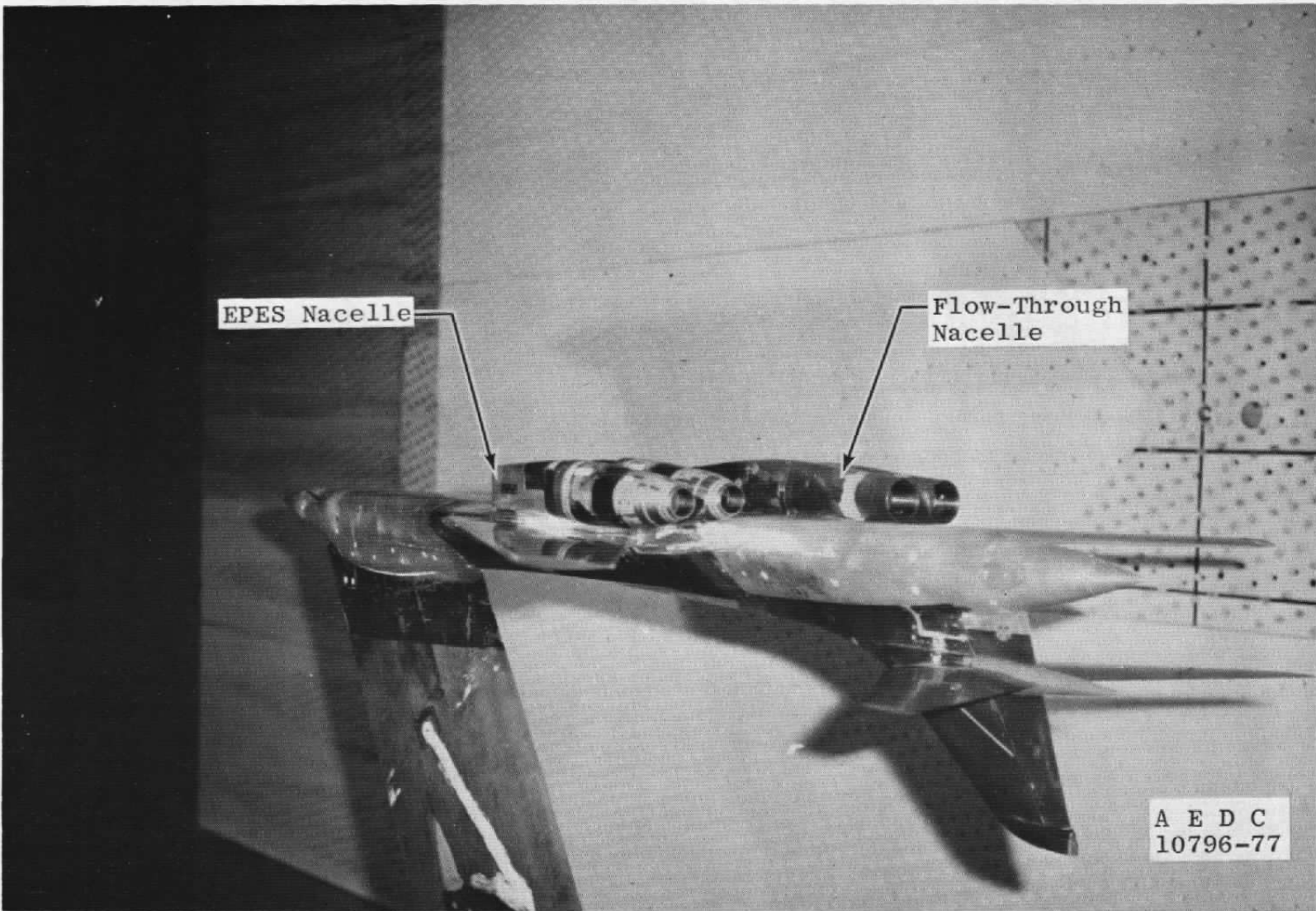


Figure 1. Location of model in test section.



a. View looking downstream
Figure 2. 0.06-scale B-1 model installed in Tunnel 16T.



b. View looking upstream
Figure 2. Concluded.

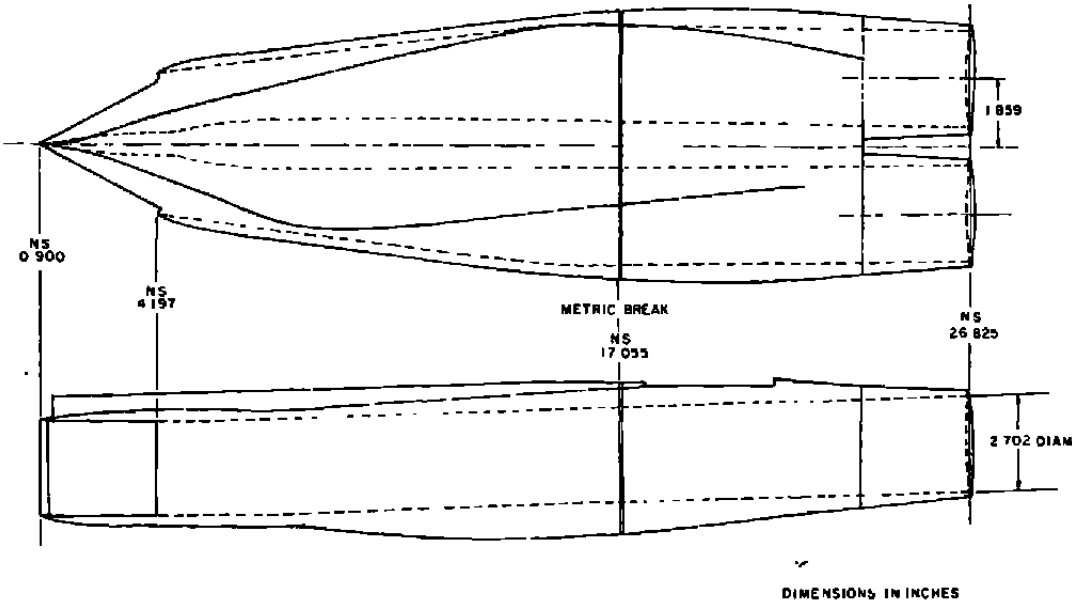


Figure 3. Left-hand flow-through nacelle.

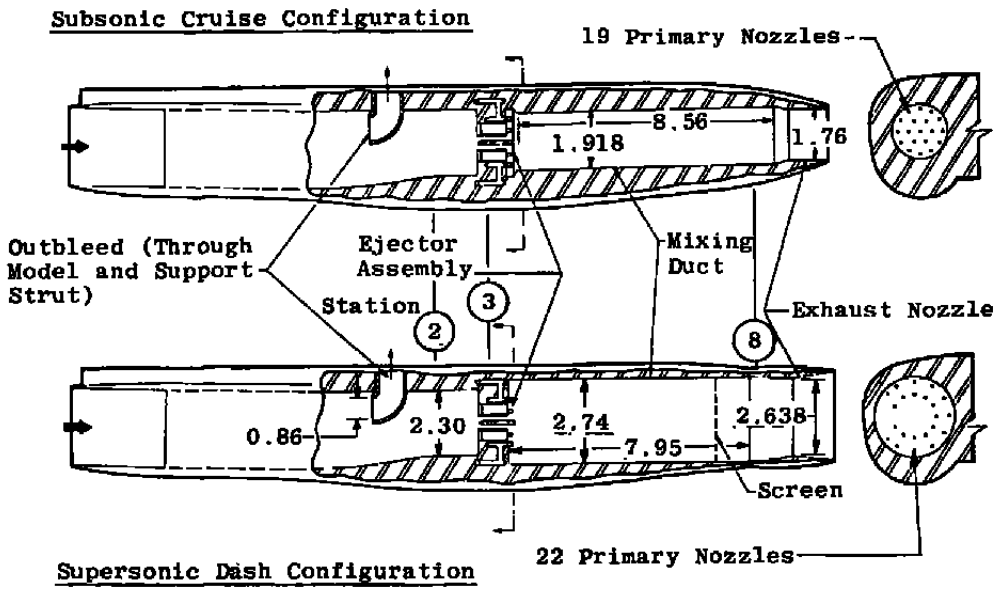


Figure 4. Ejector-powered engine simulator right-hand nacelle.

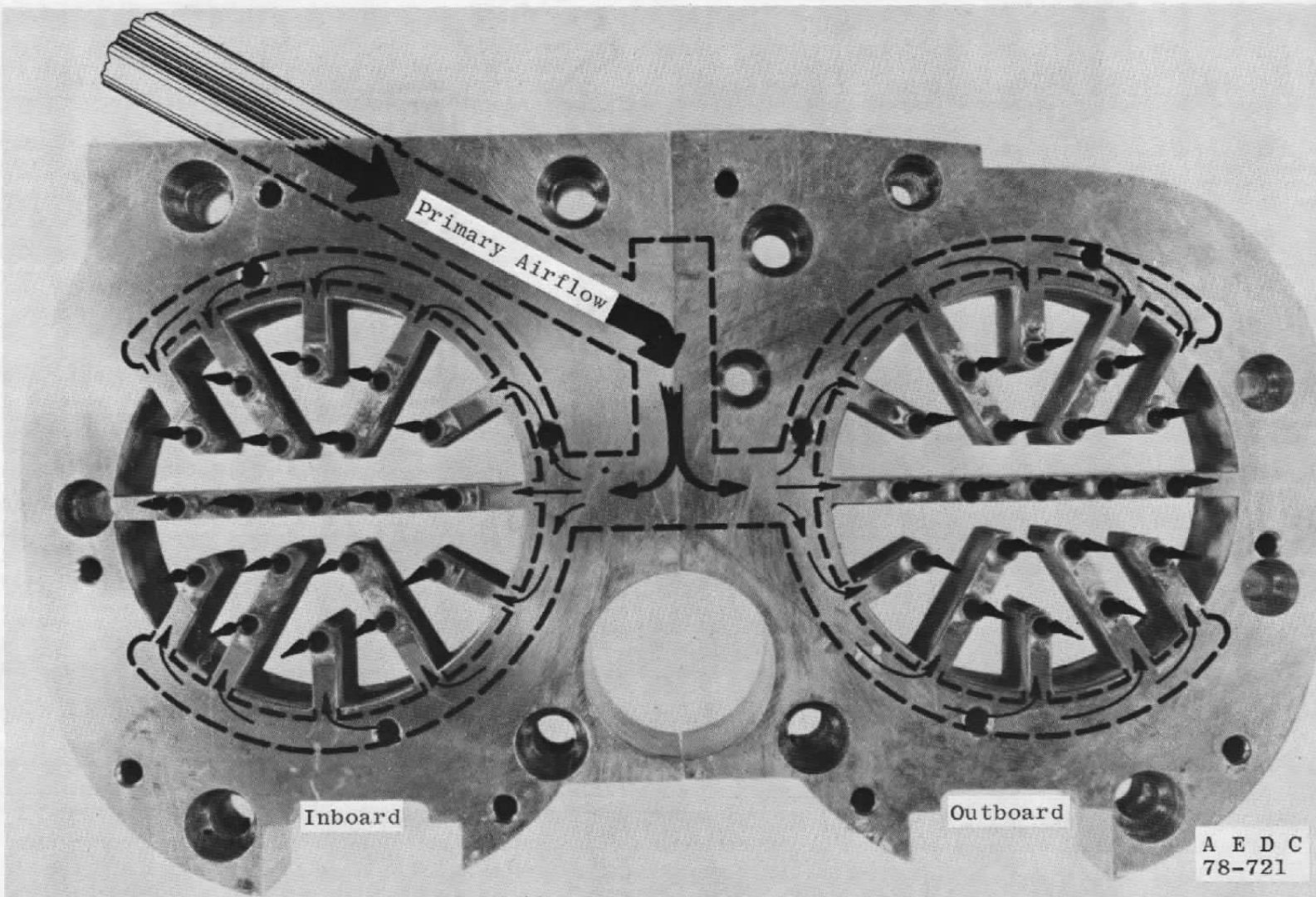


Figure 5. Ejector primary nozzles, subsonic cruise configuration.

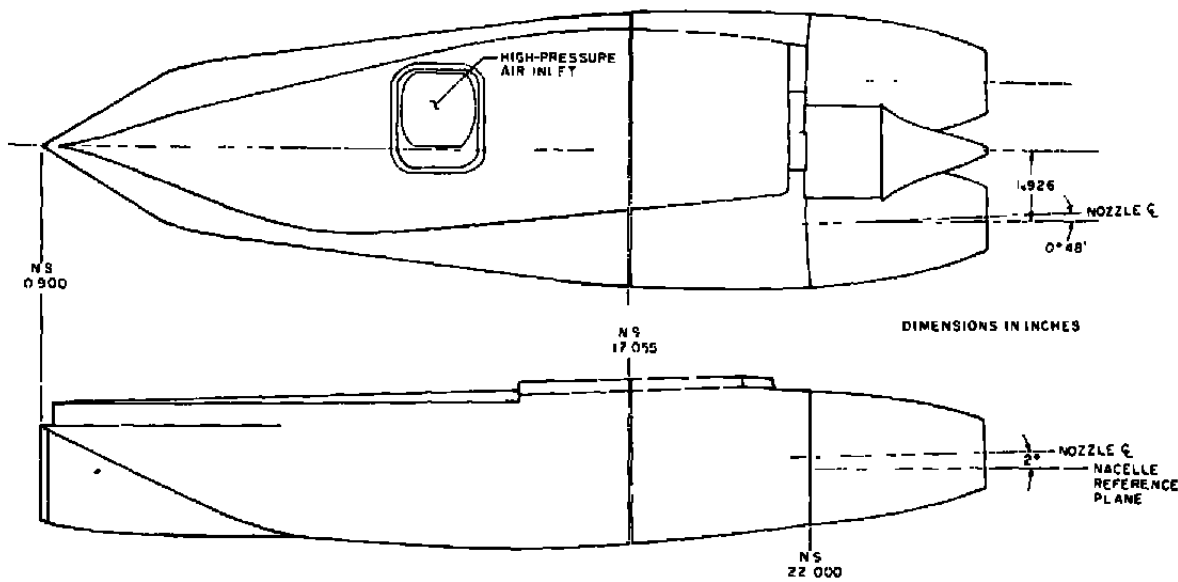
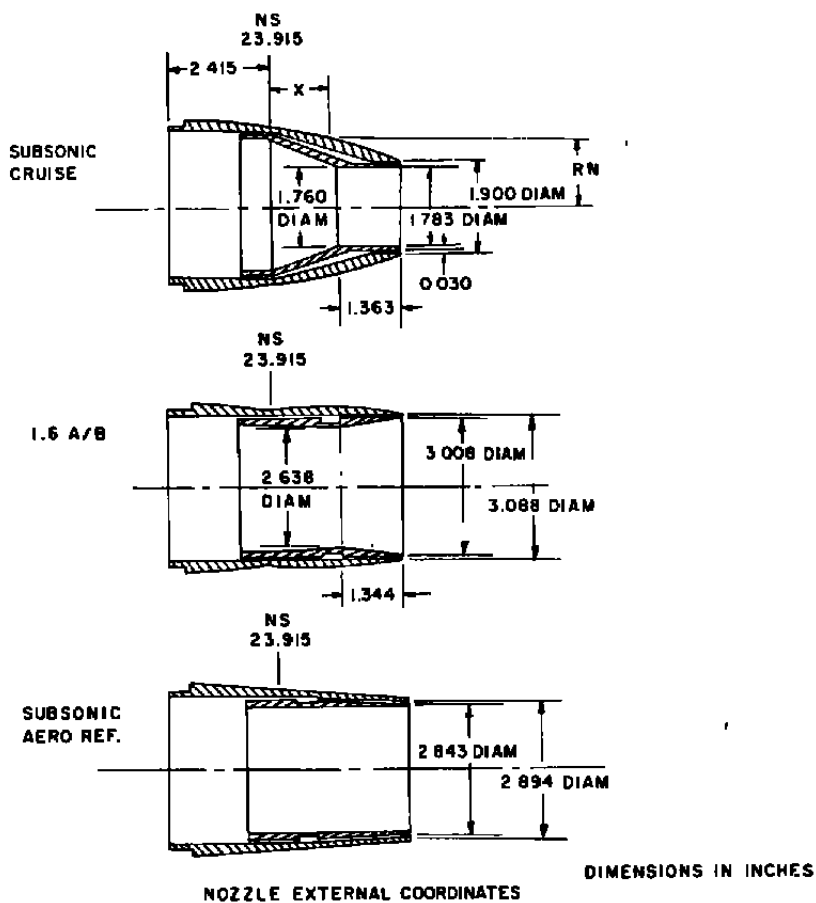


Figure 6. Conventional test techniques nozzle afterbody nacelle.



SUB. CRUISE		1.6 A/B		REF.	
X	RN	X	RN	X	RN
0.000	1.651	0.000	1.651	0.000	1.695
0.300	1.615	0.287	1.676		
0.600	1.569	0.590	1.694		
0.901	1.516	0.859	1.704		
1.201	1.453	1.203	1.705		
1.502	1.381	1.512	1.698		
1.803	1.300	1.823	1.681		
2.104	1.210	2.136	1.655		
2.405	1.110	2.451	1.620		
2.706	1.000	2.768	1.574		
2.832	0.950	2.902	1.552	2.878	1.518

STRAIGHT TAPER

Figure 7. Nozzle details.

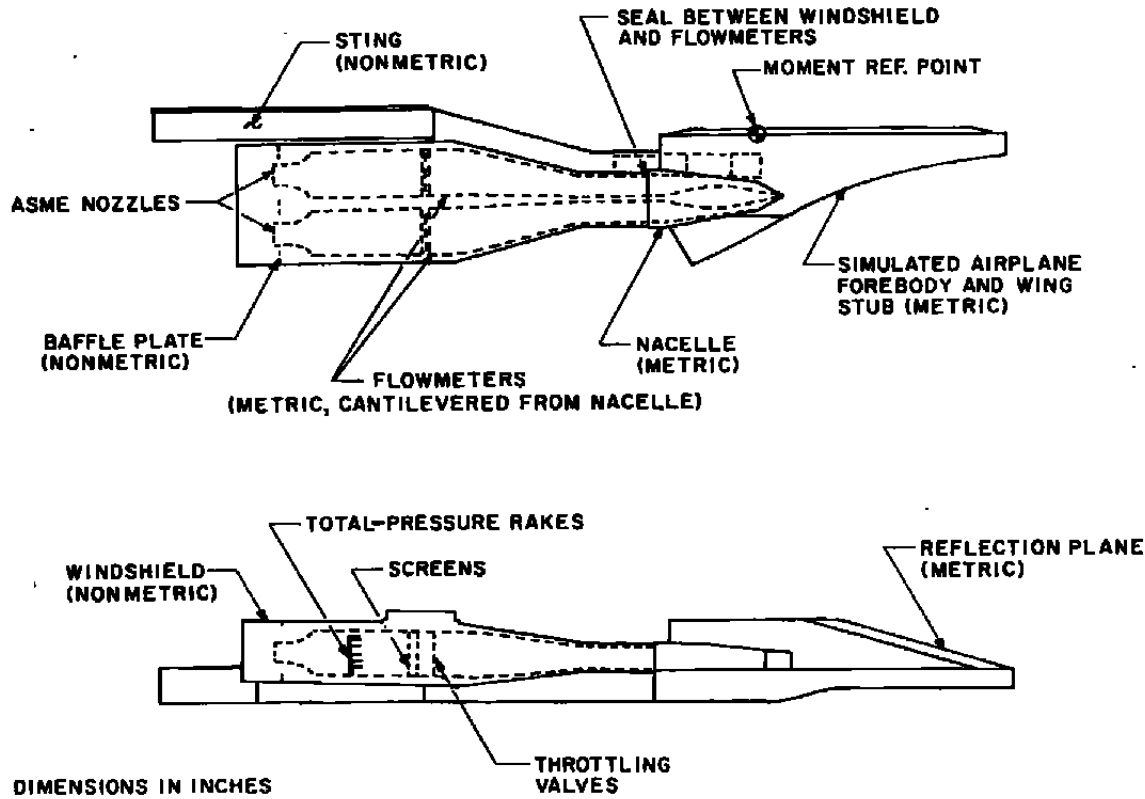
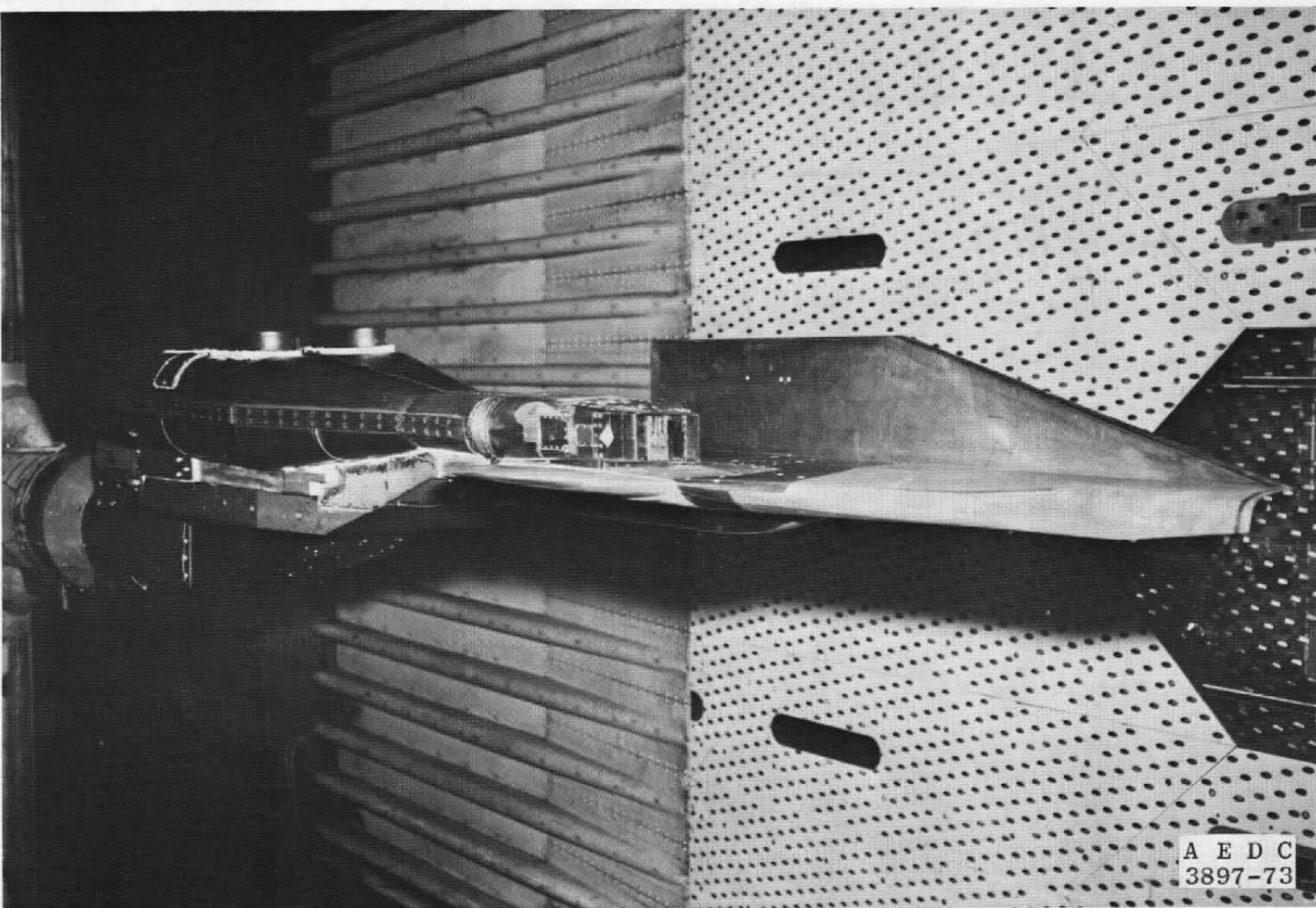


Figure 8. Conventional test techniques inlet model, 0.07 scale.



A E D C
3897-73

Figure 9. Conventional test techniques inlet model installed in Tunnel 16T.

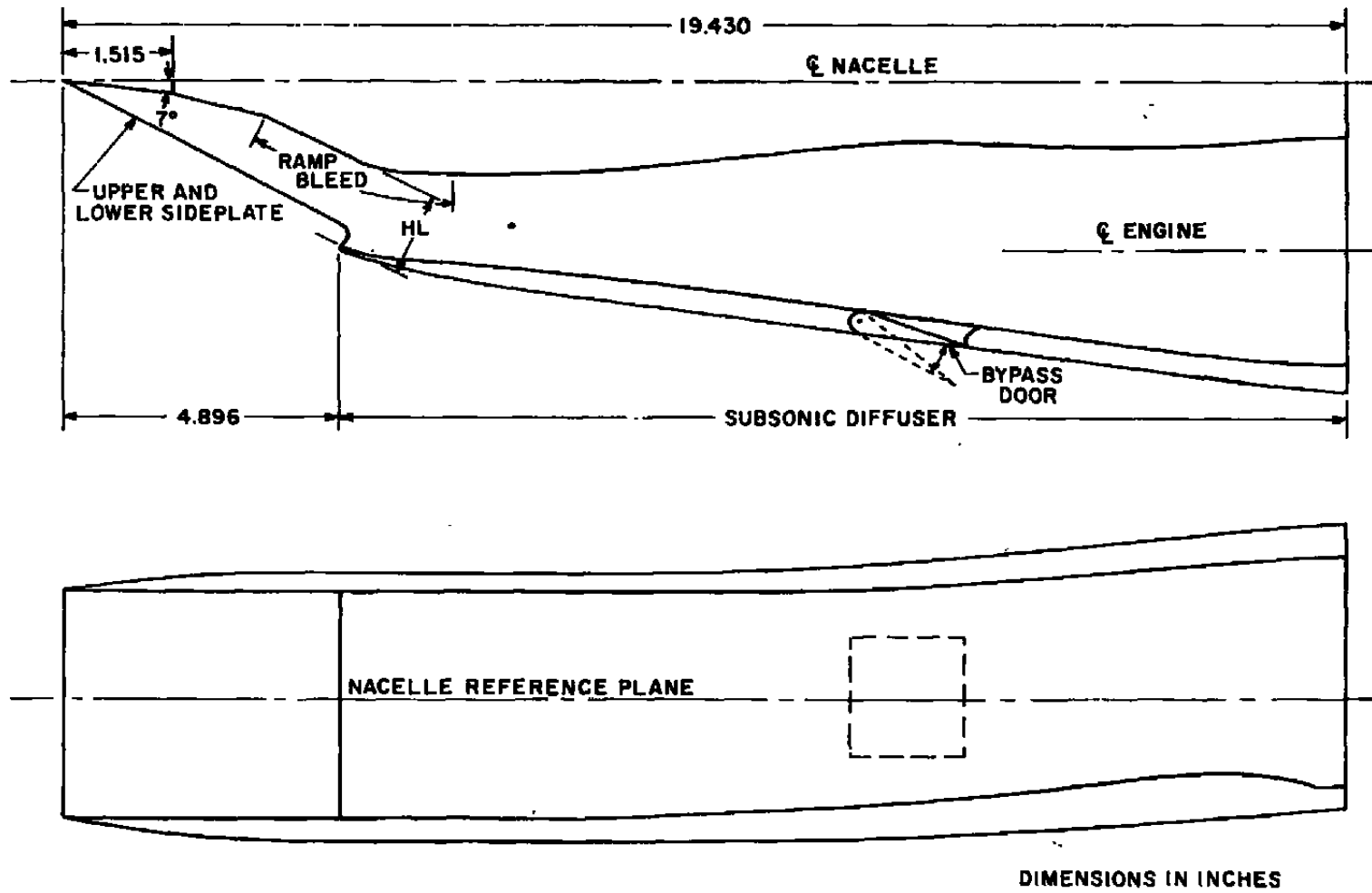


Figure 10. Details of inlet model.

36

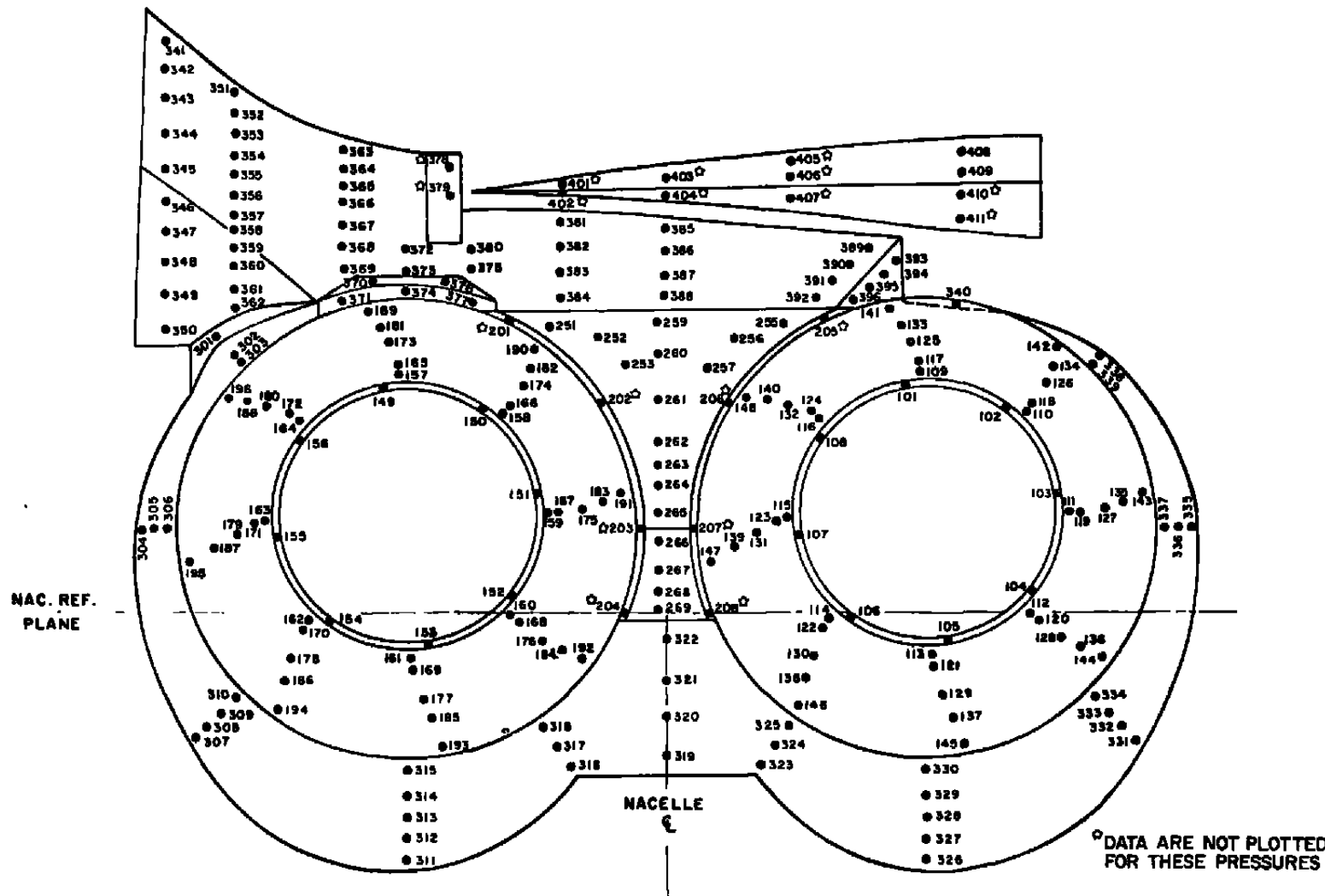


Figure 11. Location of aft-nacelle static pressure orifices.

○ Ramp Block Pressure Orifices
● Cowl Pressure Orifices

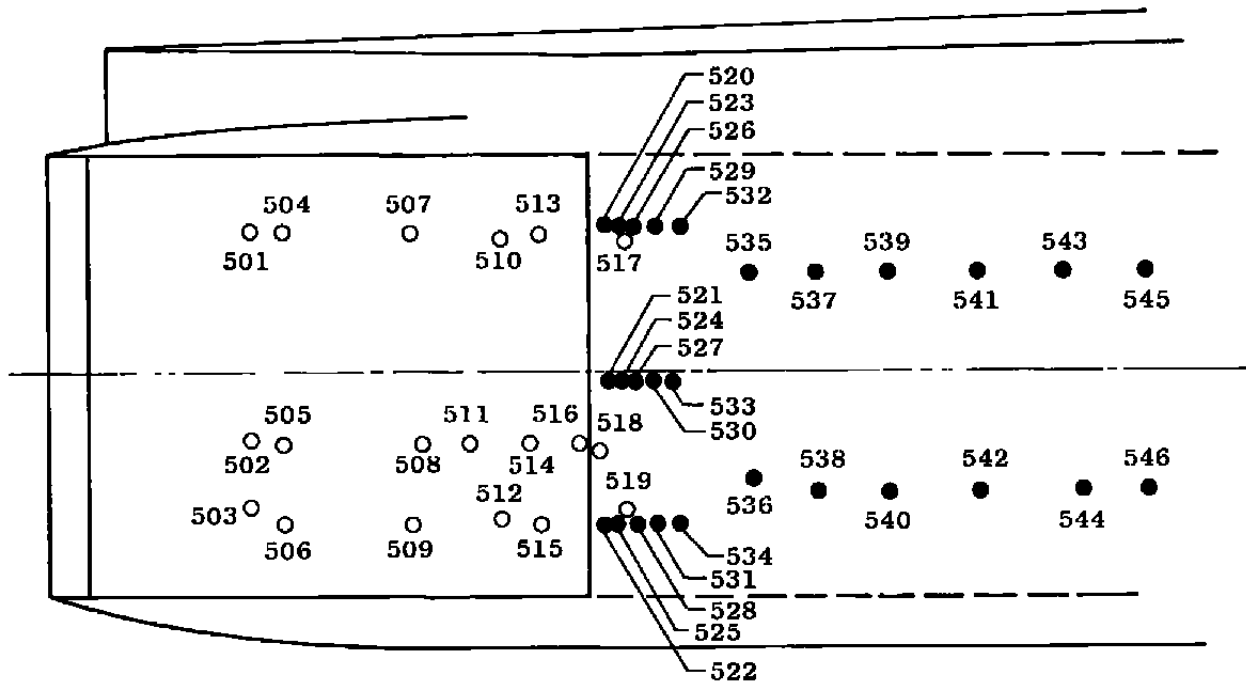
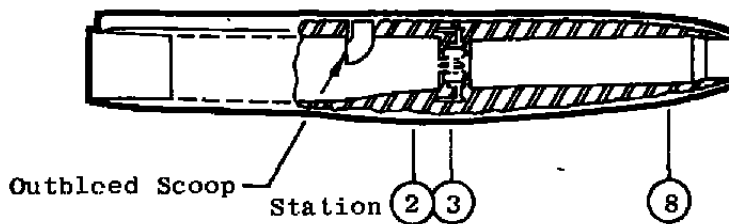


Figure 12. Location of inlet ramp and cowl static pressure orifices.



- Total Pressure
- Static Pressure

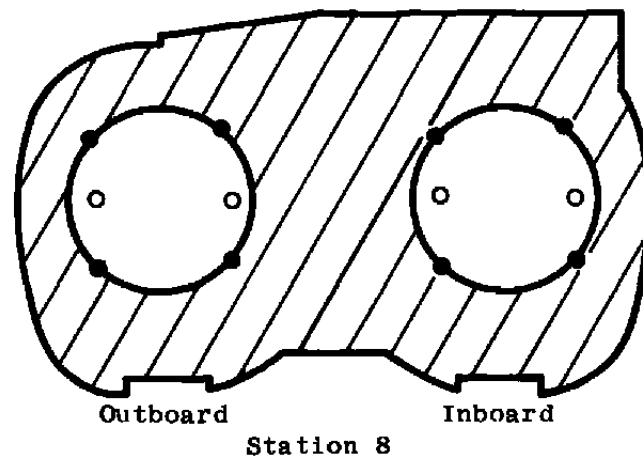
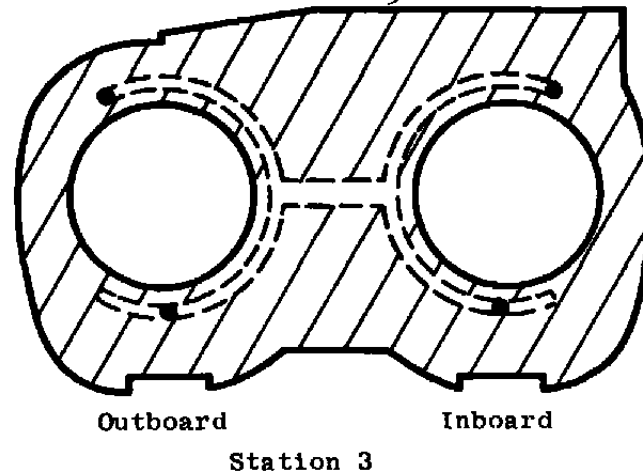
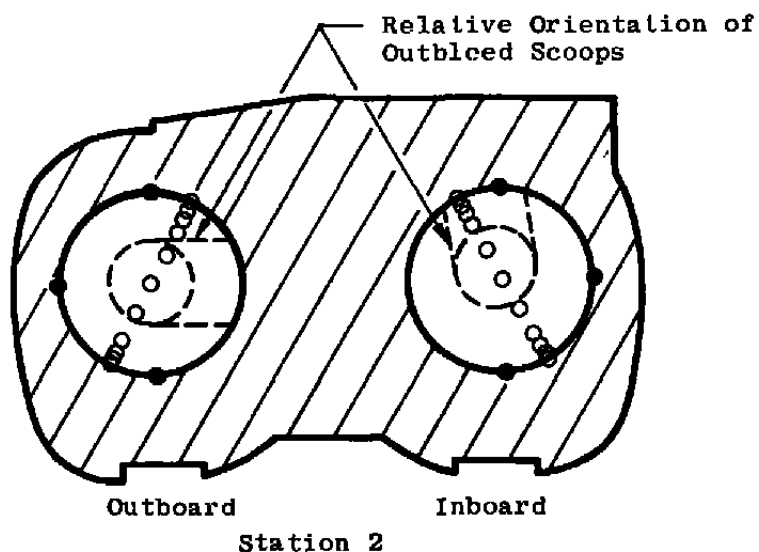
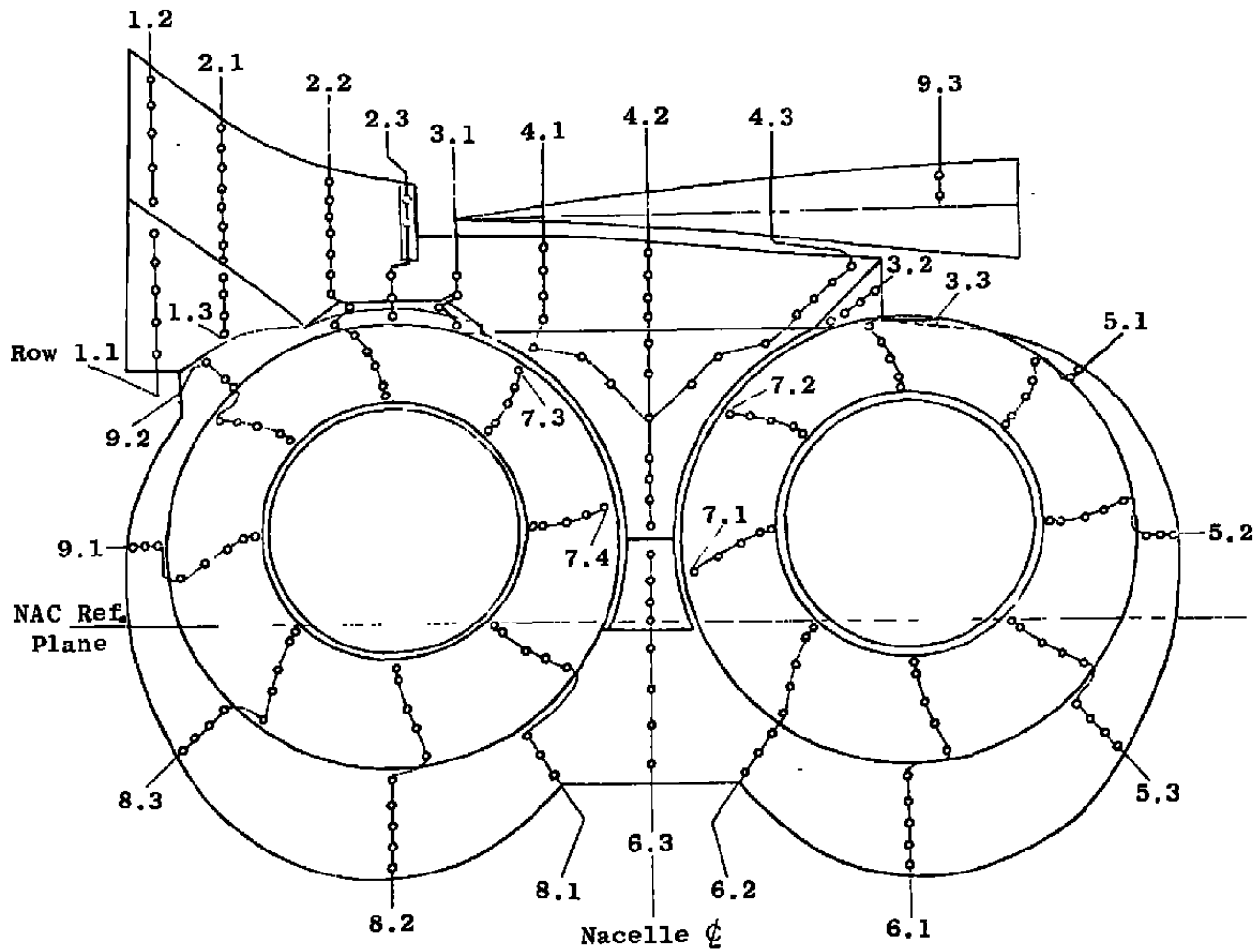


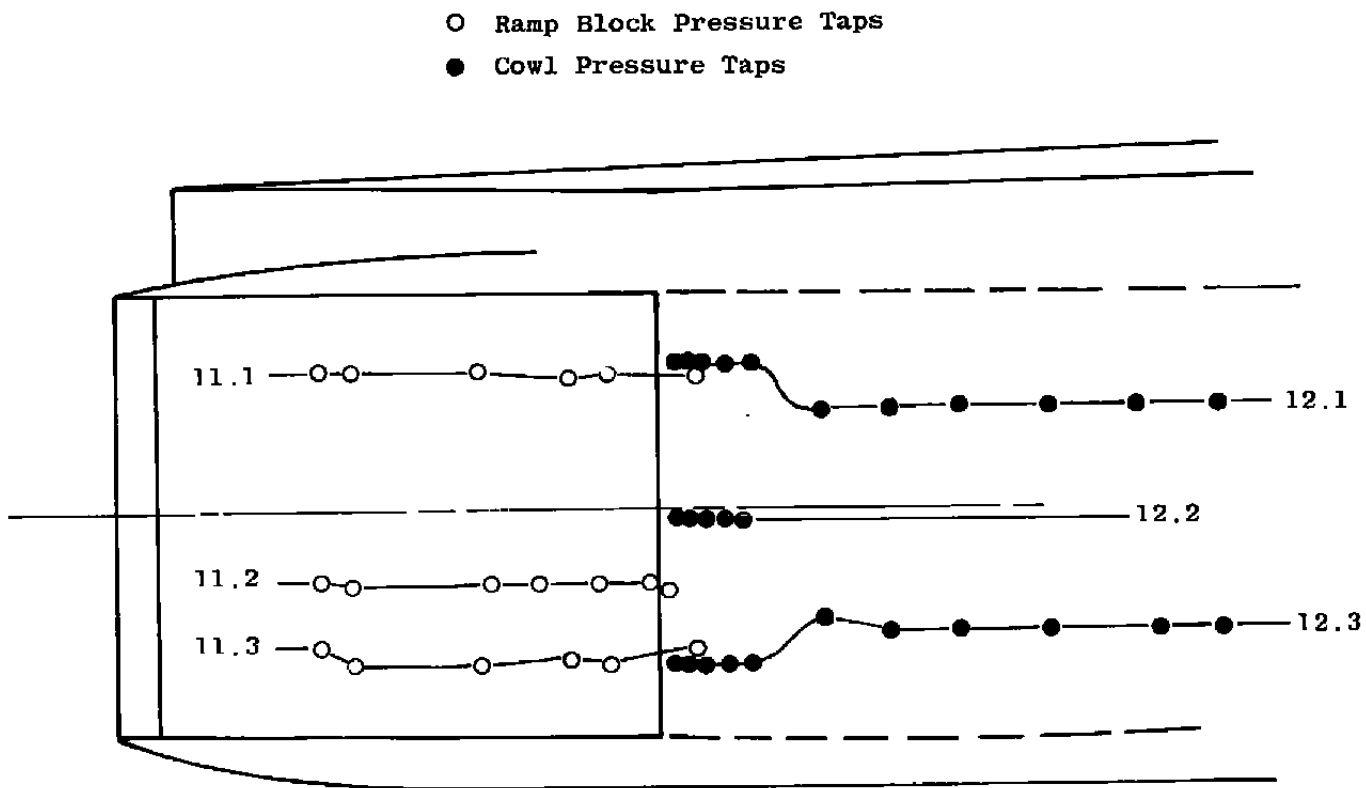
Figure 13. Ejector-powered engine simulator internal instrumentation.



a. Aft nacelle

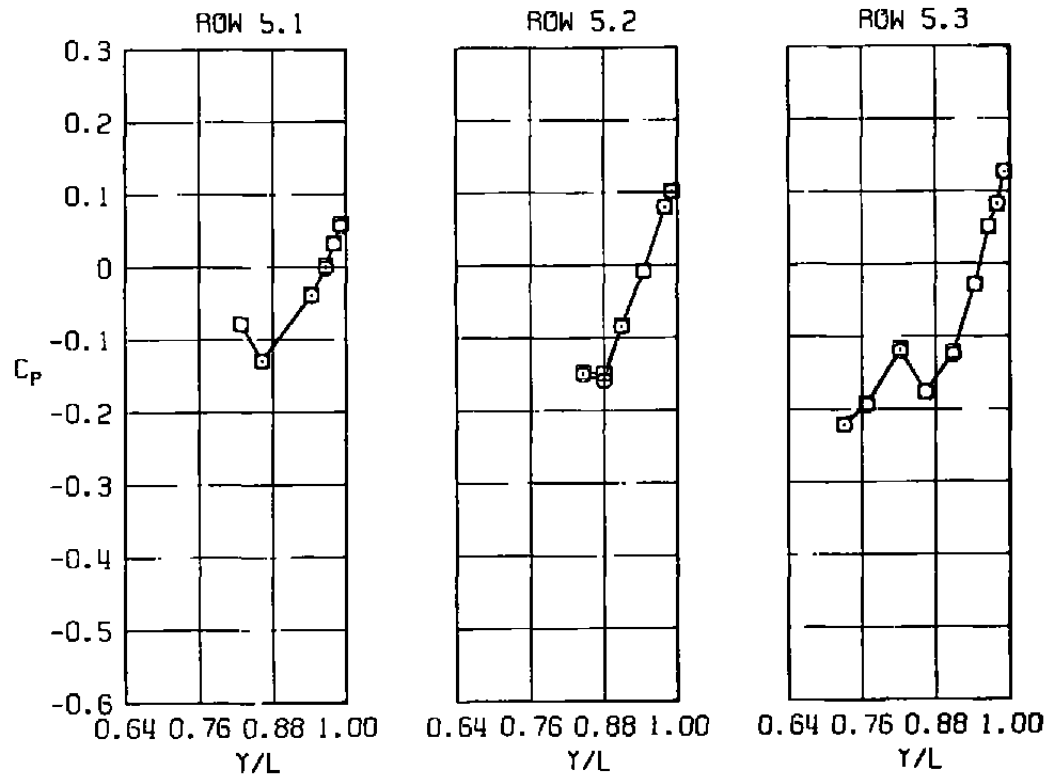
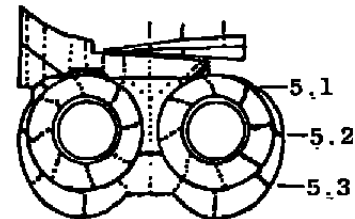
Figure 14. Identification of pressure rows.

40



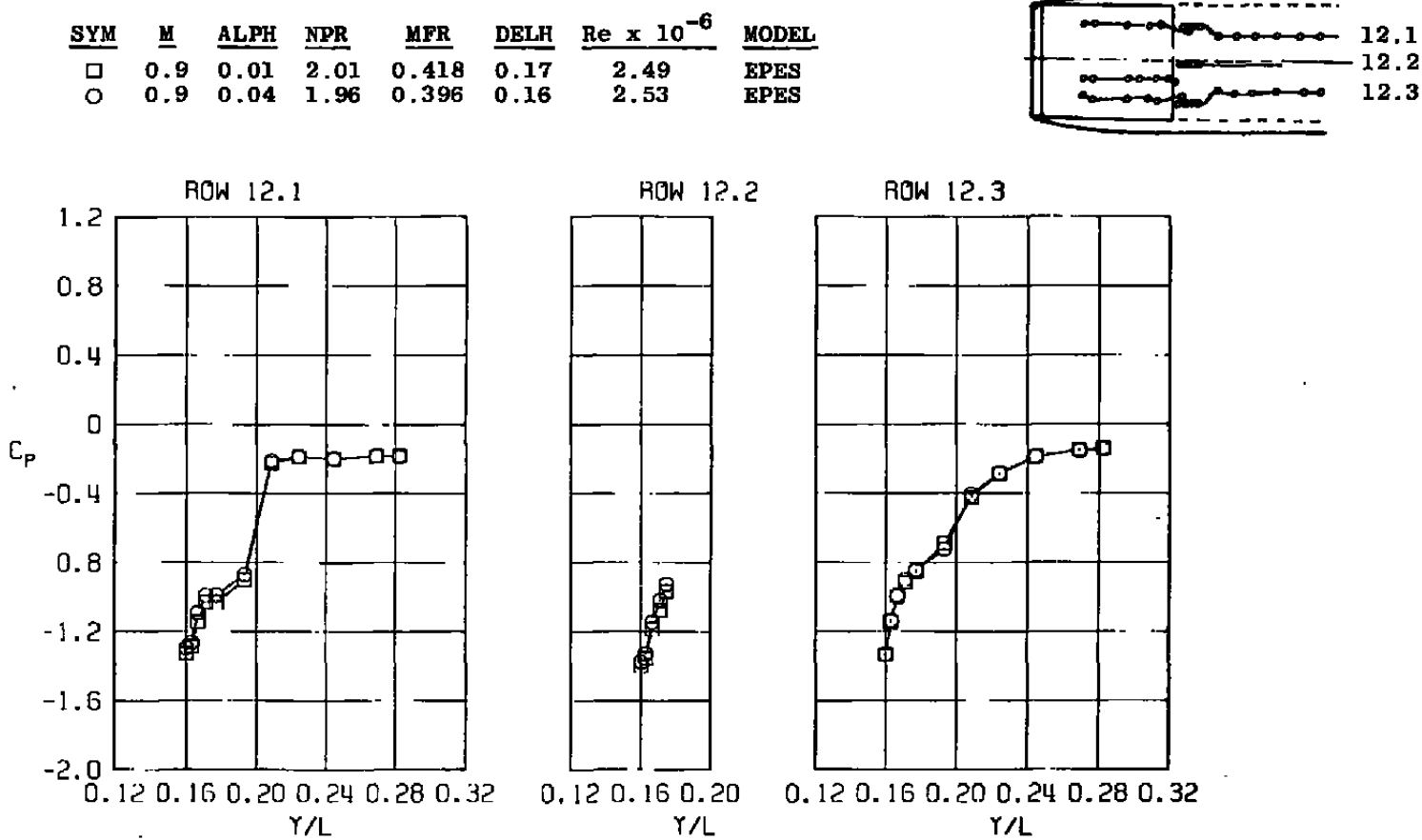
b. Inlet ramp and cowl
Figure 14. Concluded.

<u>SYM</u>	<u>M</u>	<u>ALPH</u>	<u>NPR</u>	<u>MFR</u>	<u>DELT</u> H	<u>Re</u> x 10 ⁻⁶	<u>MODEL</u>
□	0.9	0.01	2.01	0.418	0.17	2.49	EPES
○	0.9	0.04	1.96	0.396	0.16	2.53	EPES



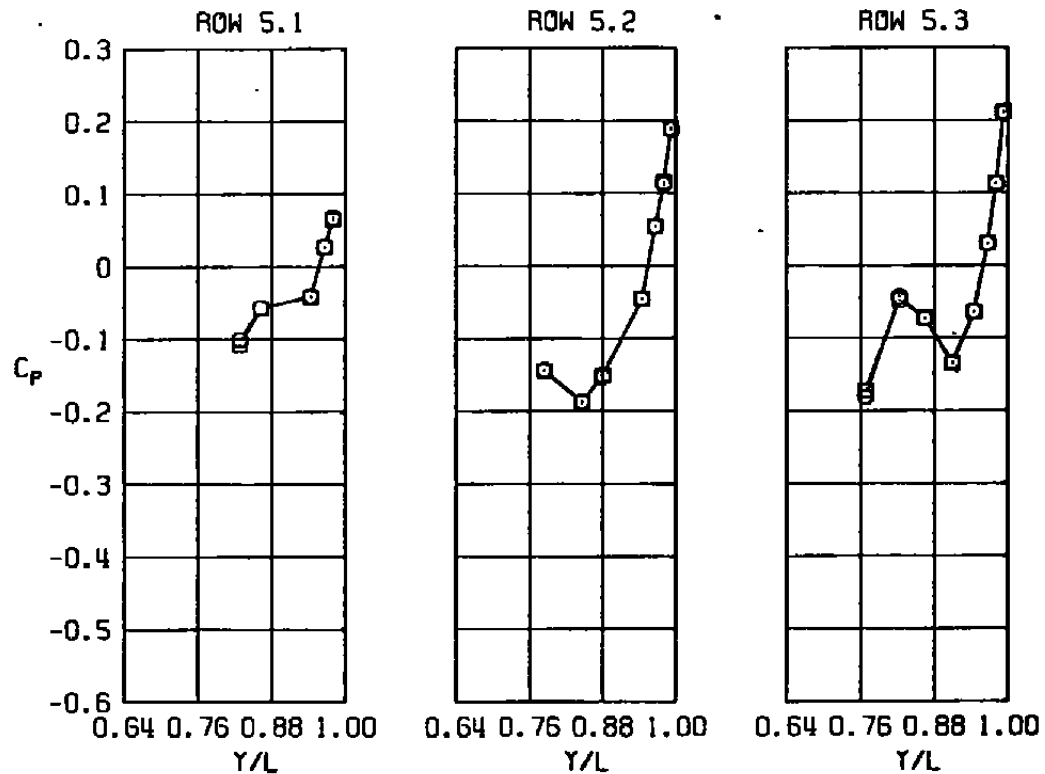
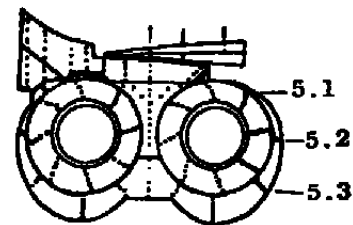
a. NAB

Figure 15. Repeatability of pressure coefficient measurements,
ejector-powered engine simulator model.



b. Cowl
Figure 15. Concluded.

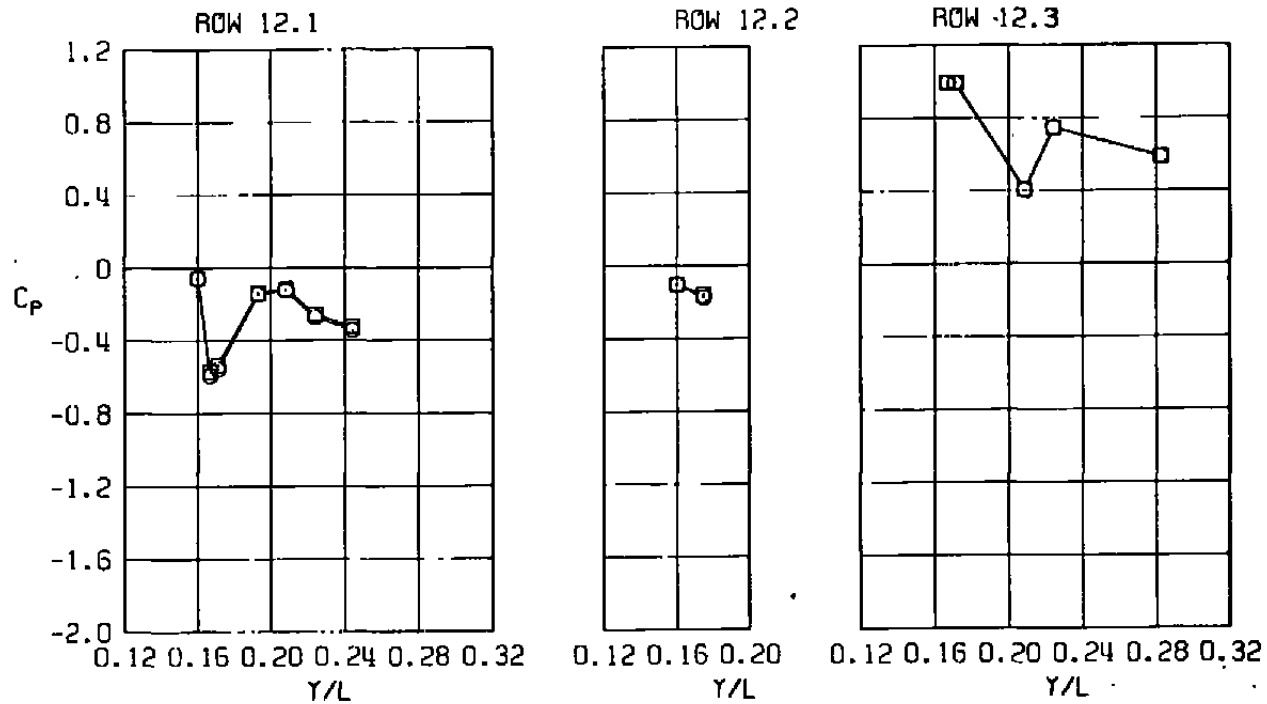
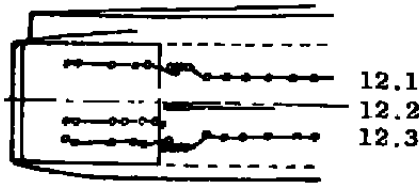
<u>SYM</u>	<u>M</u>	<u>ALPH</u>	<u>NPR</u>	<u>MFR</u>	<u>DELH</u>	<u>Re</u> $\times 10^{-6}$	<u>MODEL</u>
□	0.85	0.90	2.69	0.598	1.82	5.67	FLIGHT
○	0.85	0.87	2.69	0.597	1.77	5.68	FLIGHT



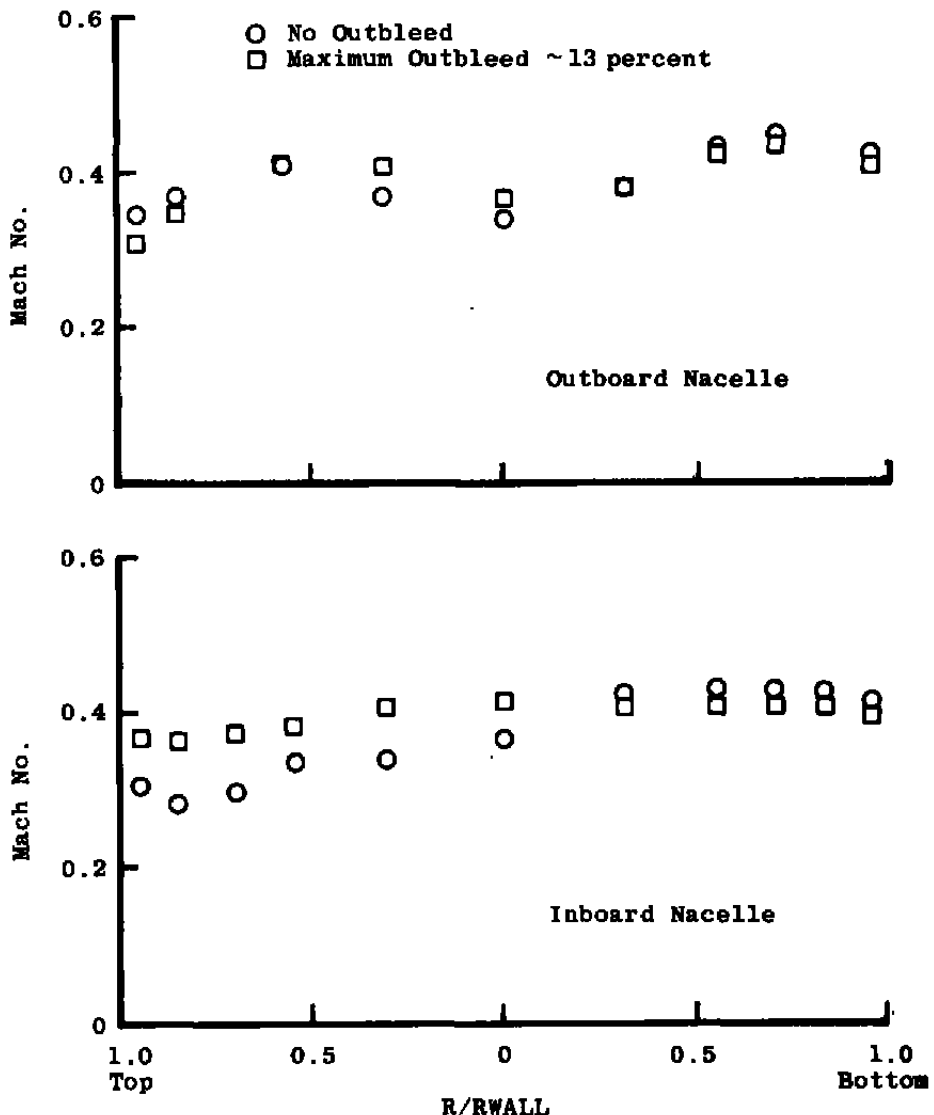
a. NAB

Figure 16. Repeatability of pressure coefficient measurements, flight vehicle.

<u>SYM</u>	<u>M</u>	<u>ALPH</u>	<u>NPR</u>	<u>MFR</u>	<u>DElh</u>	<u>Re x 10⁻⁶</u>	<u>MODEL</u>
□	0.85	0.90	2.69	0.598	1.82	5.67	FLIGHT
○	0.85	0.87	2.69	0.597	1.77	5.68	FLIGHT

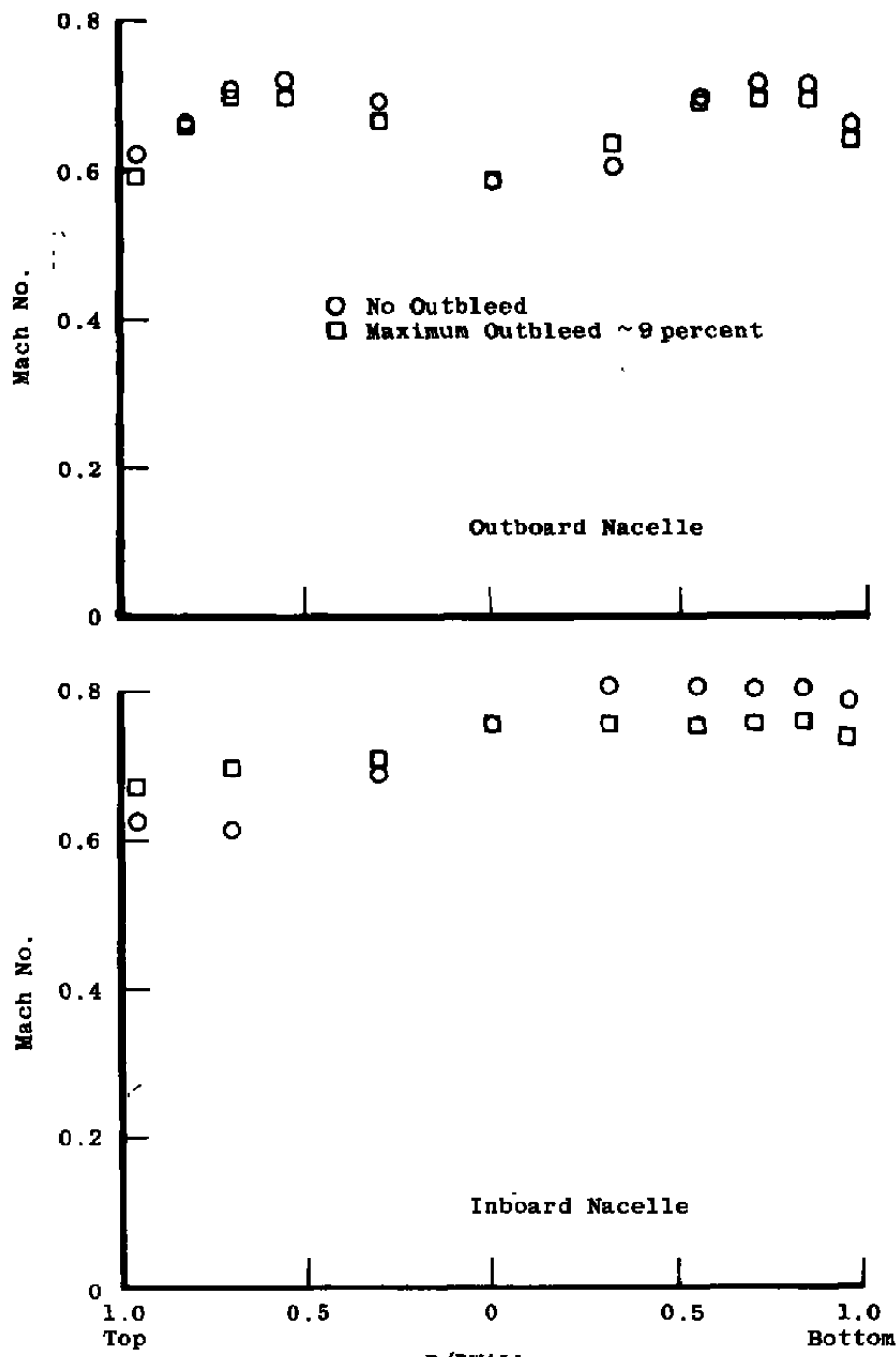


b. Cowl
Figure 16. Concluded.



a. Subsonic cruise

Figure 17. Typical EPES inlet Mach number distributions obtained in Tunnel 16T.



b. Supersonic dash
Figure 17. Concluded.

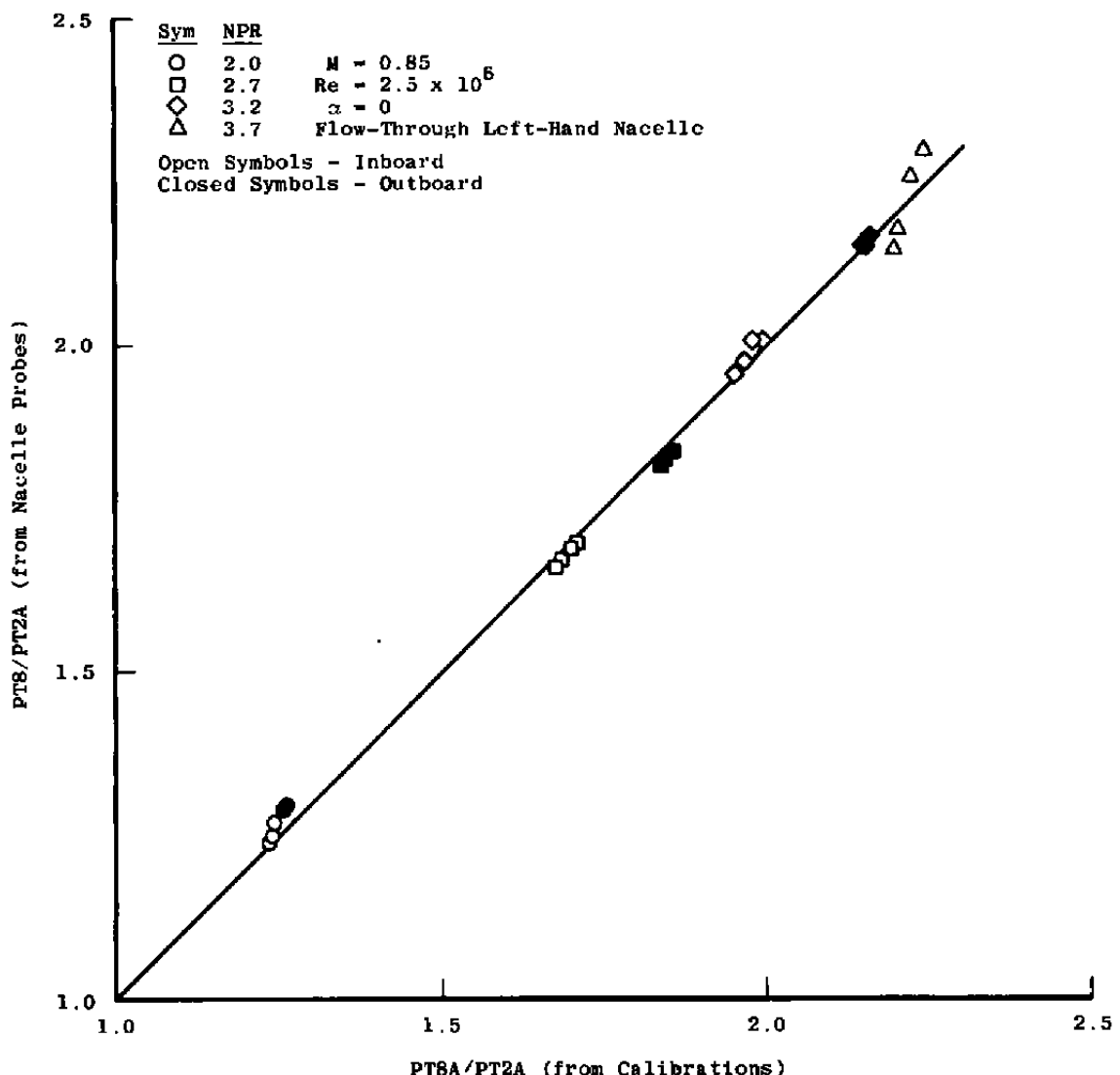


Figure 18. Comparison of mixing duct total pressures from the Station 8 probes in the nacelle with average nozzle exit pressure from the calibration.

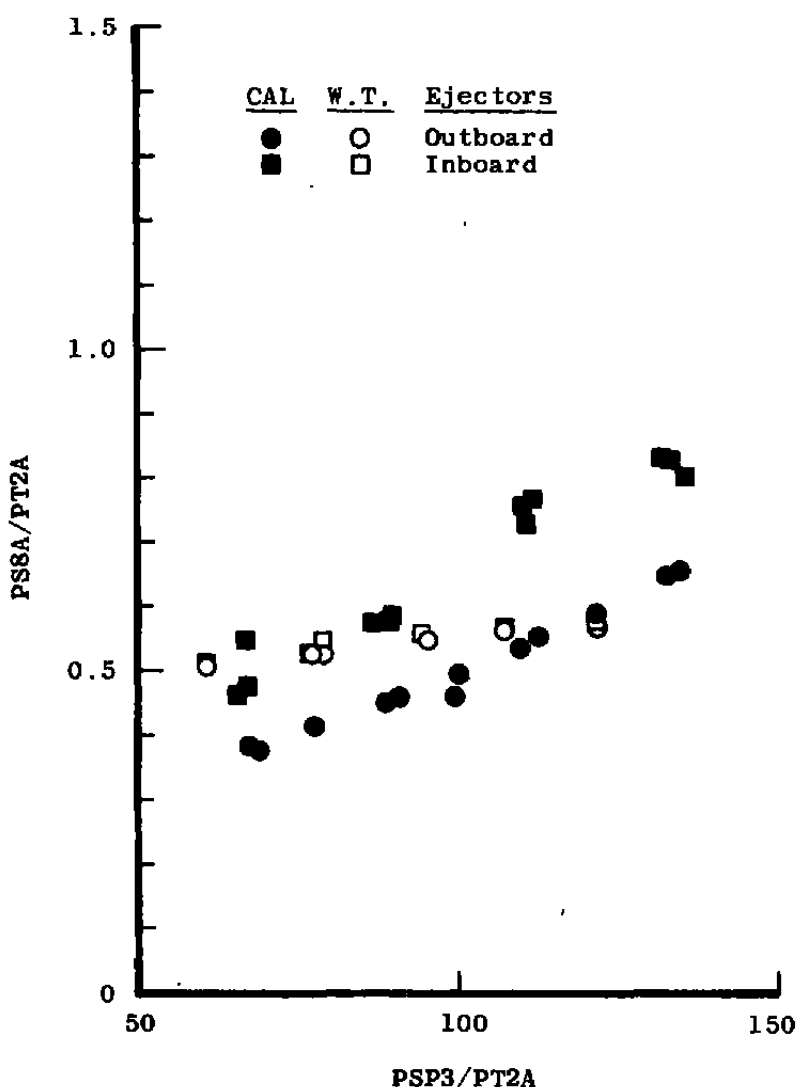
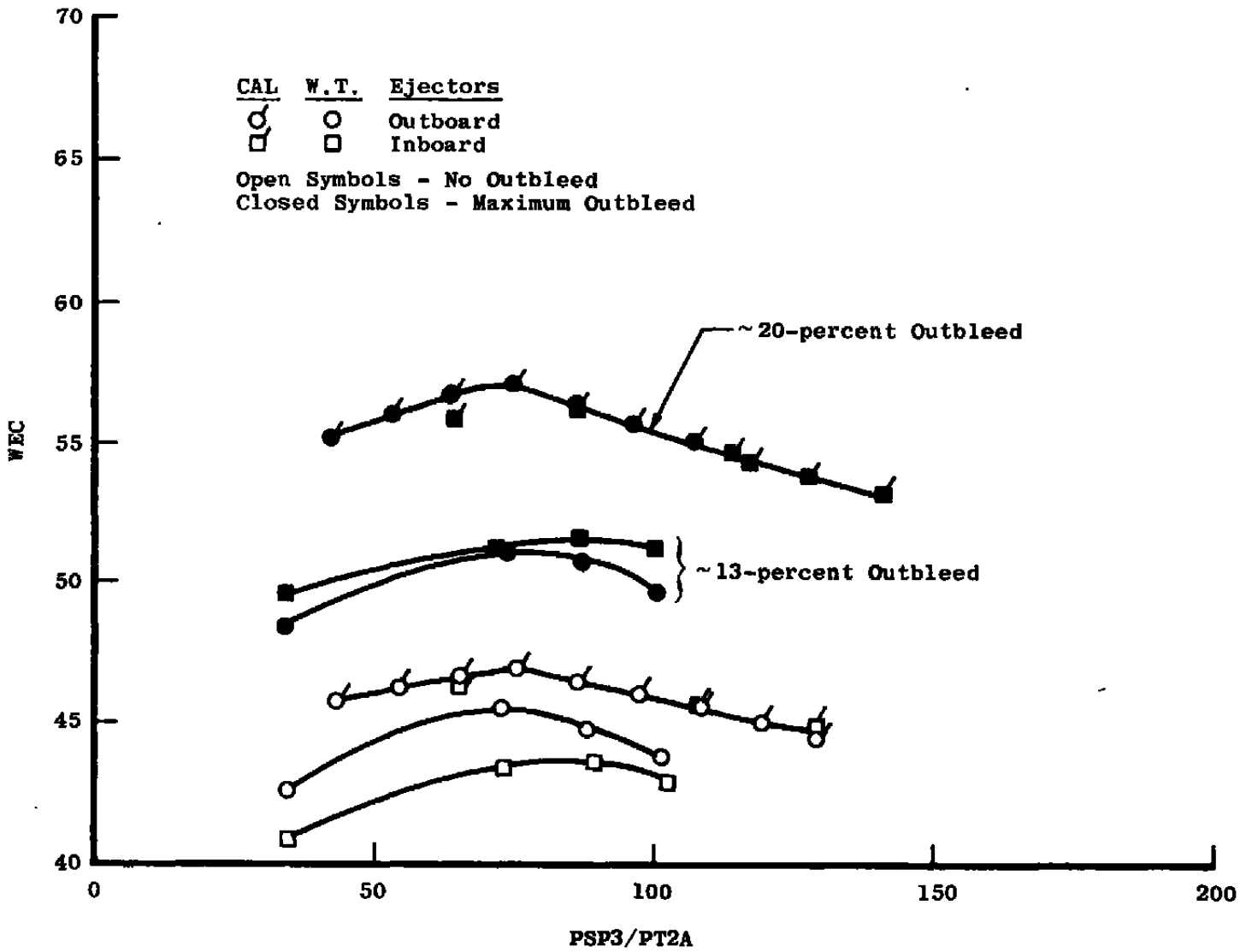
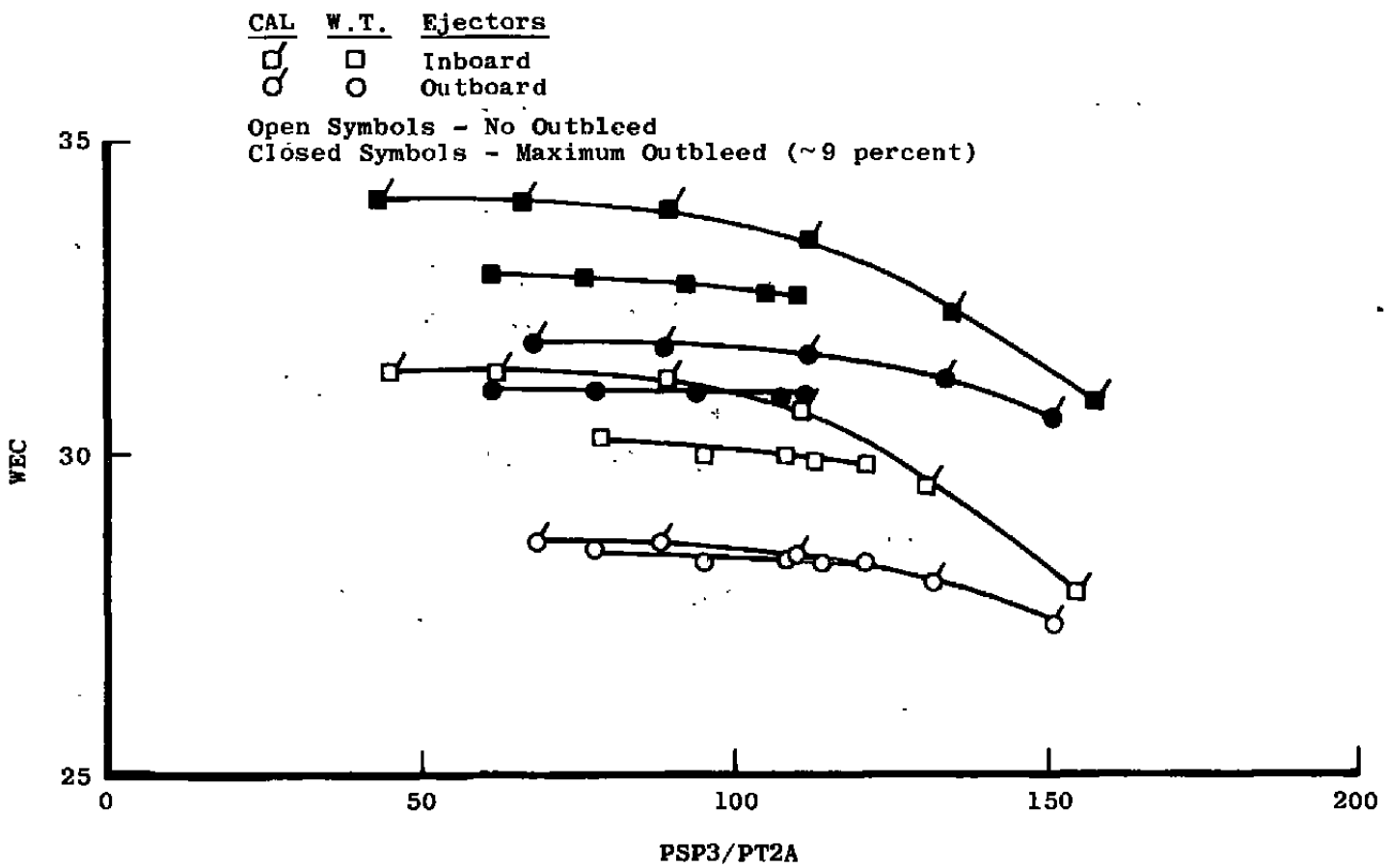


Figure 19. Variation of mixing duct exit static pressure with primary pressure (supersonic dash ejectors).

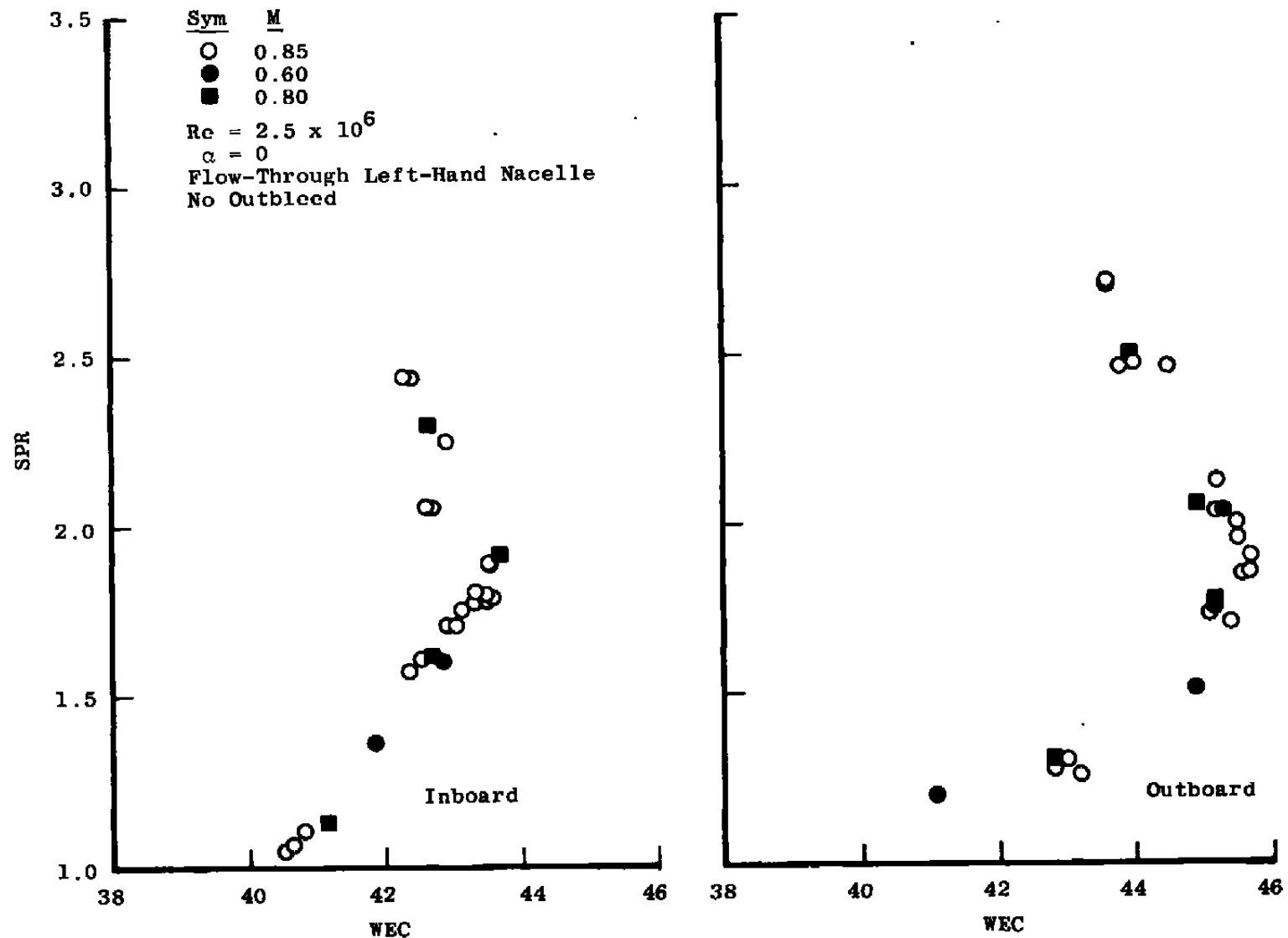


a. Subsonic cruise ejectors

Figure 20. Variation of inlet corrected airflow parameter with ejector pressure.

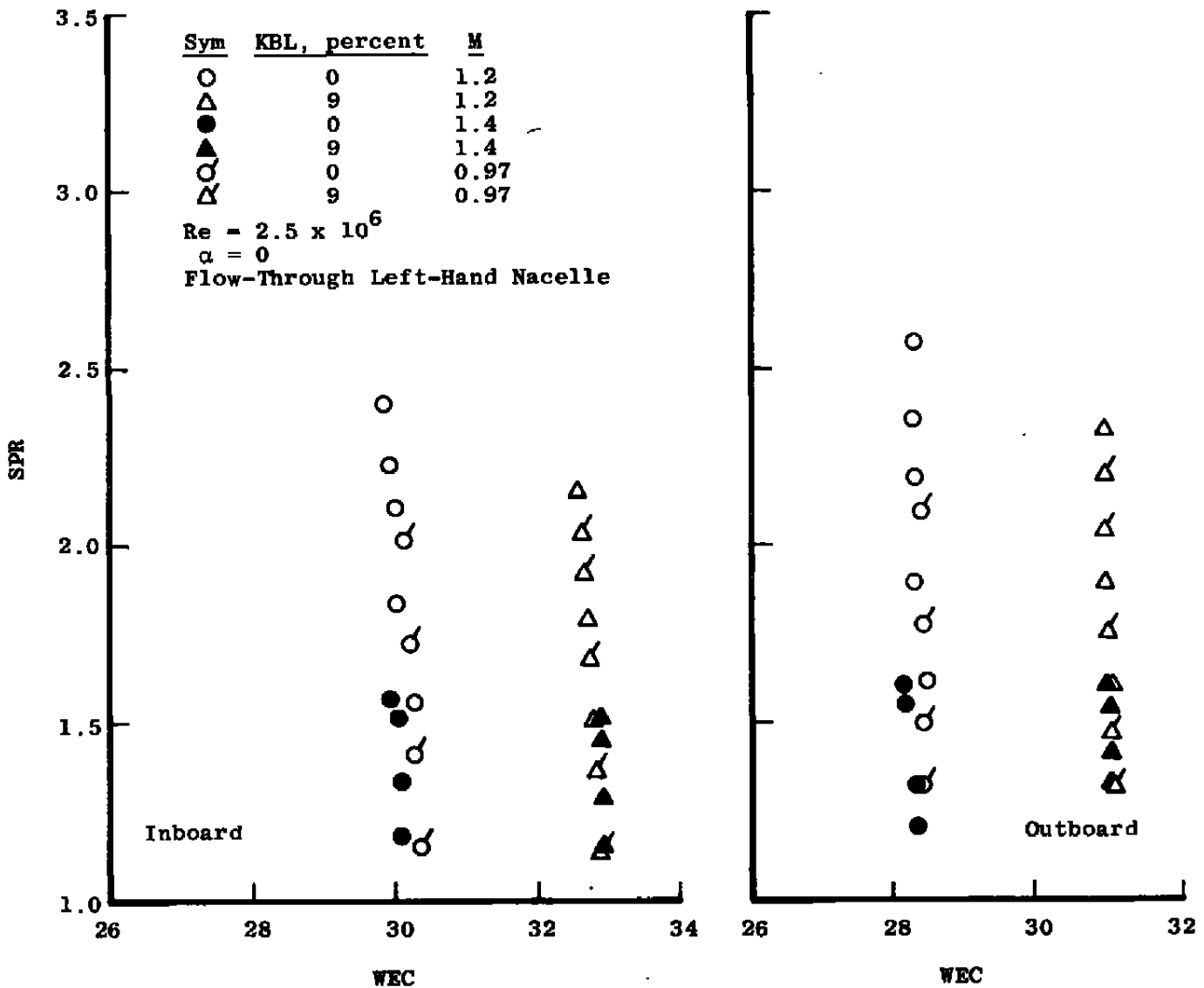


b. Supersonic dash ejectors
Figure 20. Concluded.



a. Subsonic cruise

Figure 21. Effect of free-stream Mach number on EPES performance.



b. Supersonic dash
Figure 21. Concluded.

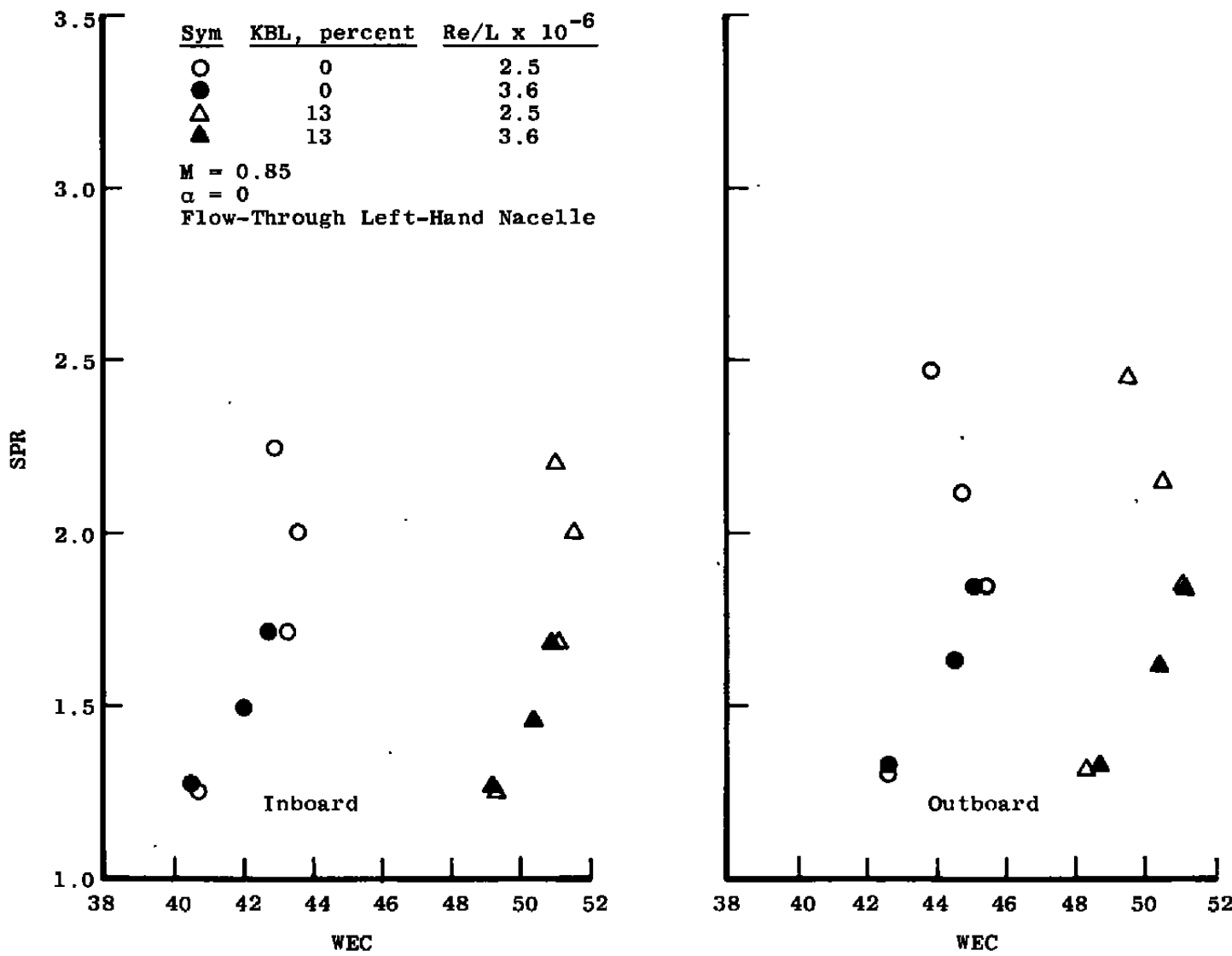
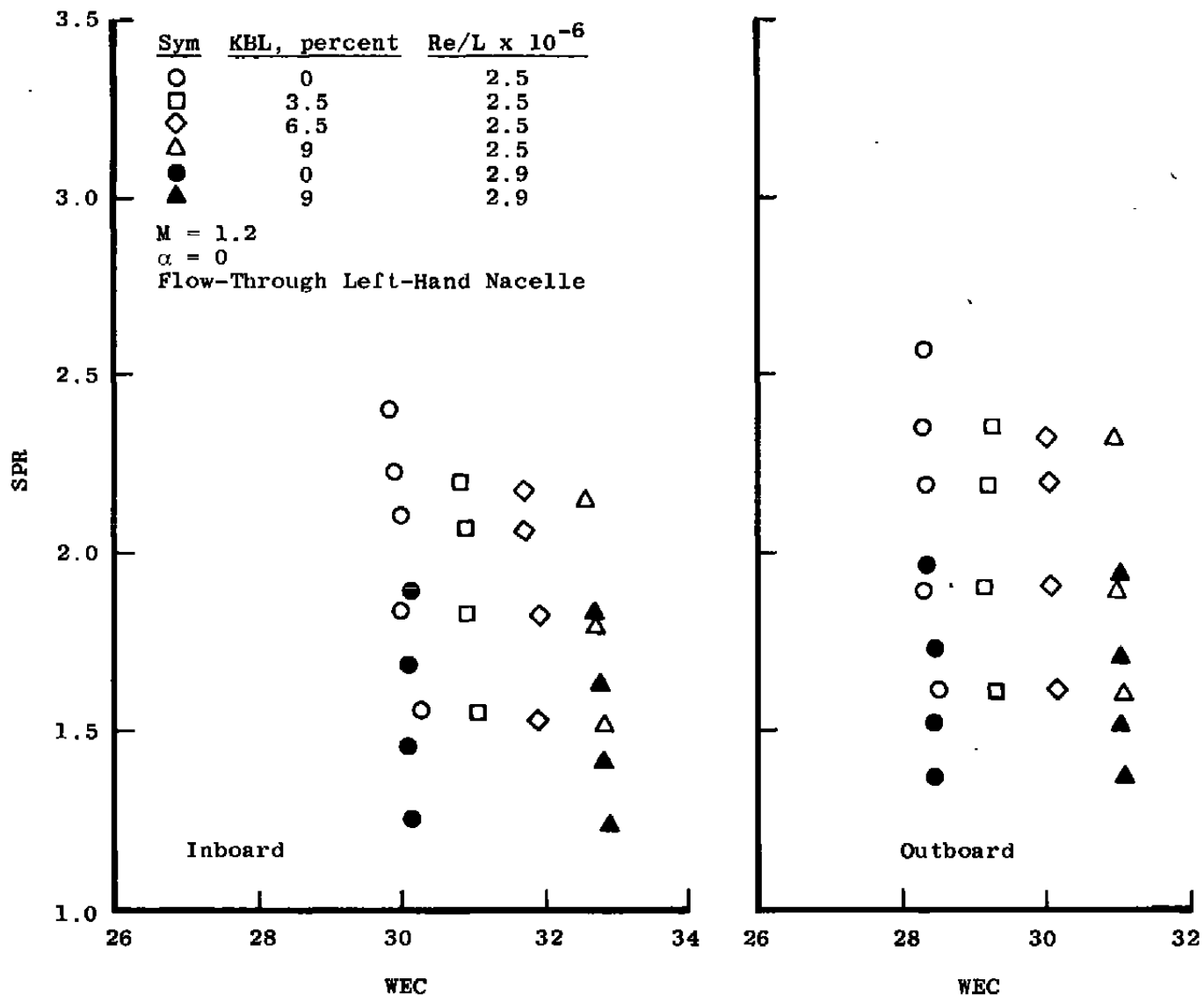
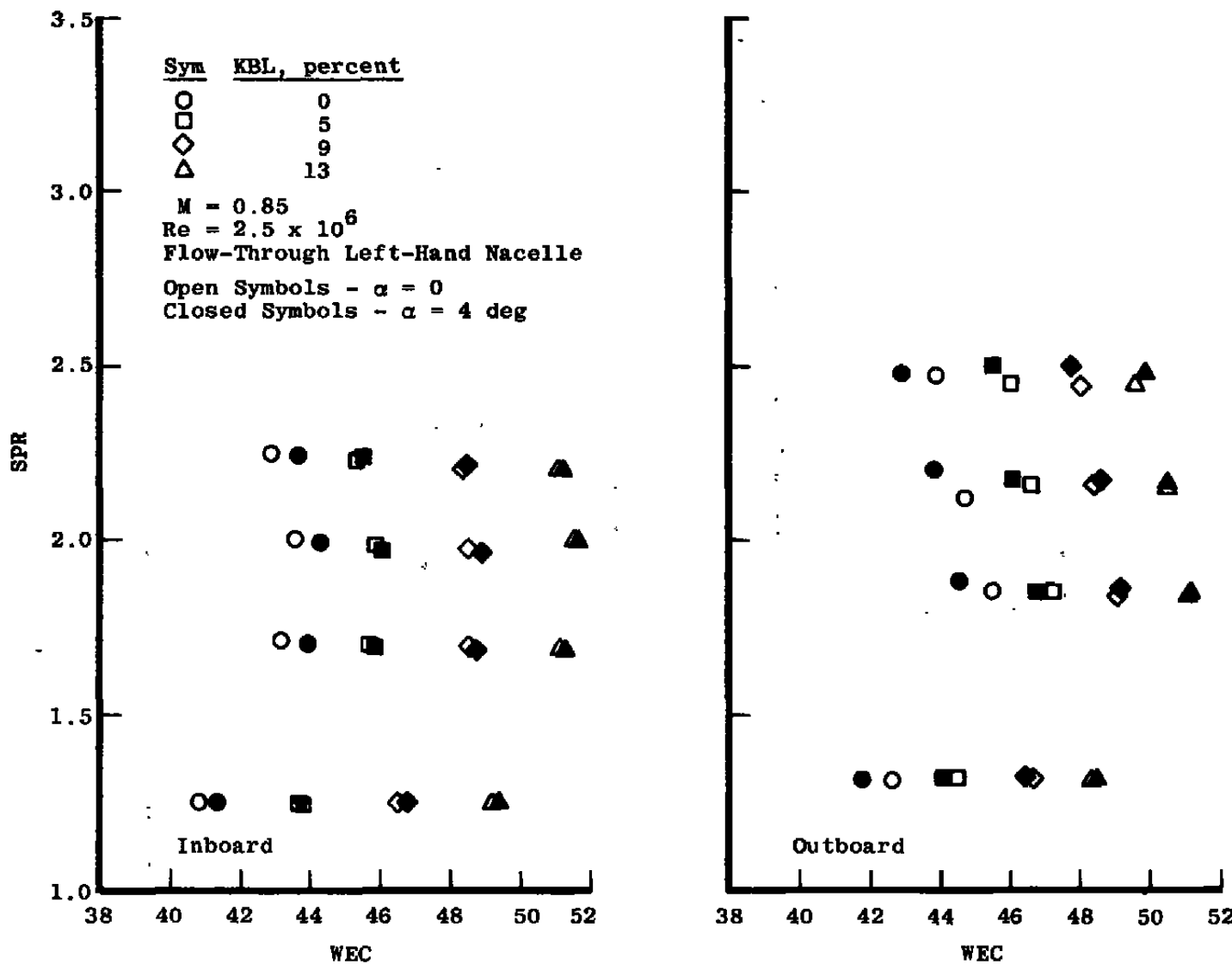


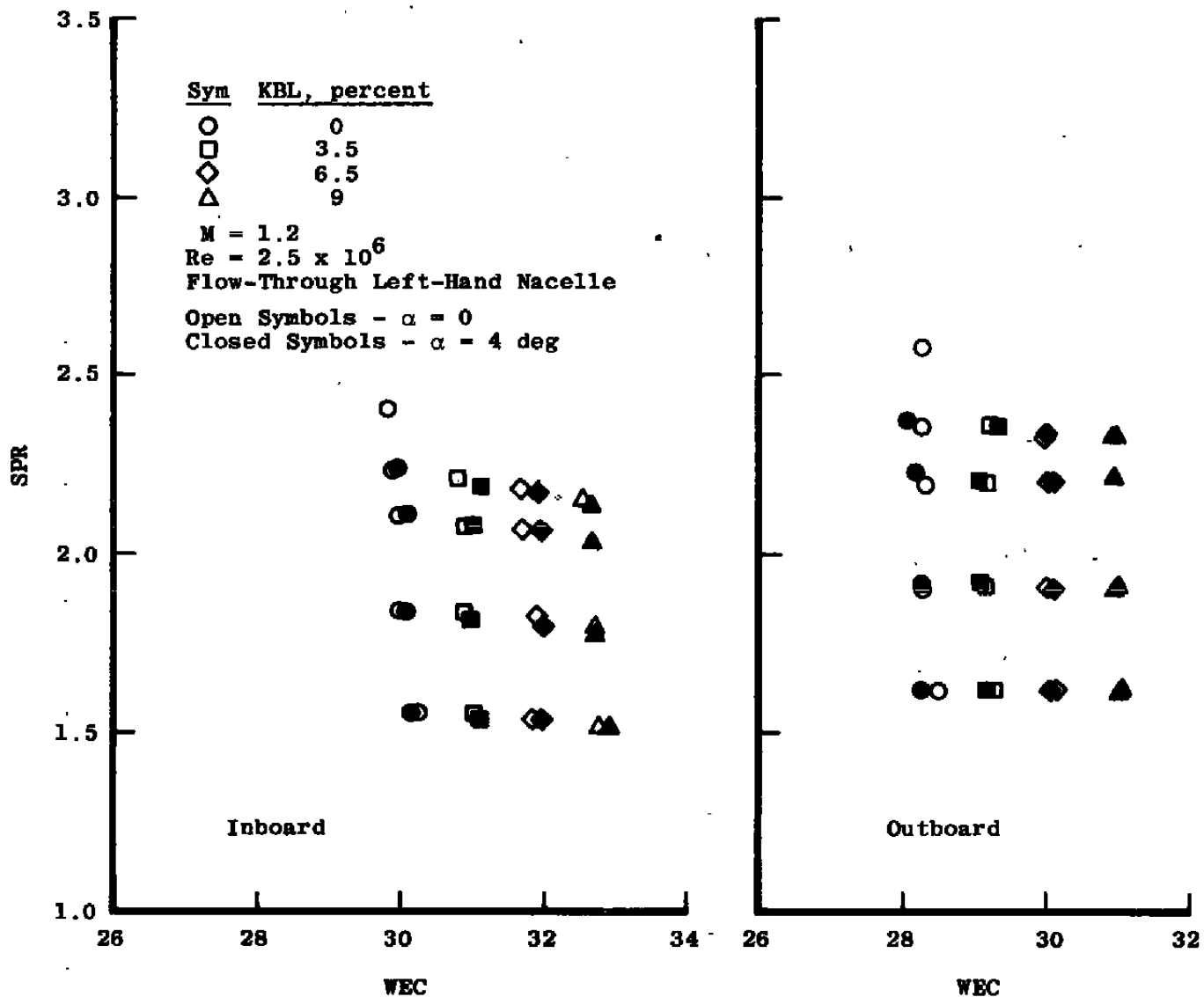
Figure 22. Effect of Reynolds number on EPES performance.



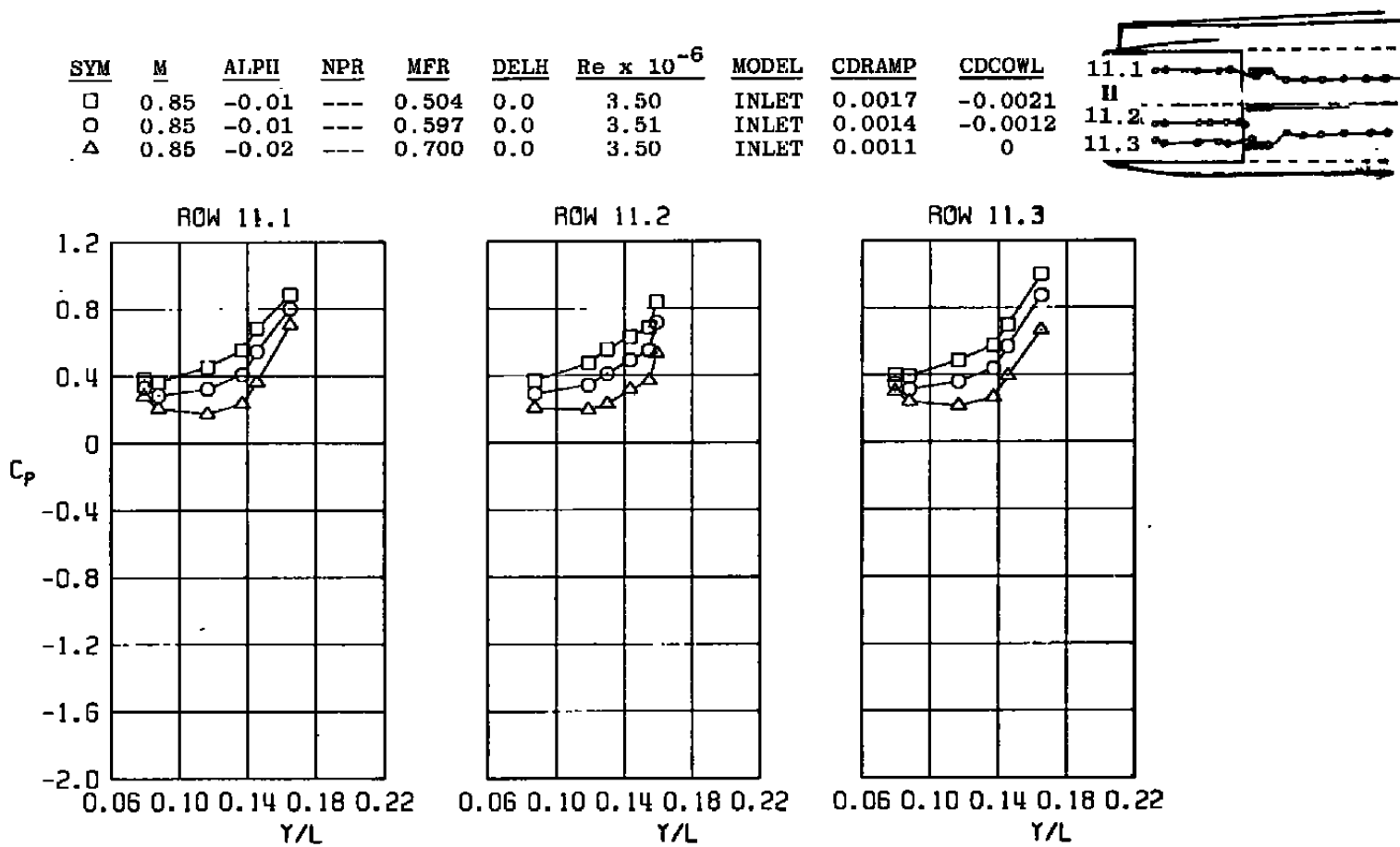
b. Supersonic dash
Figure 22. Concluded.



a. Subsonic cruise
Figure 23. Effect of angle of attack on EPES performance.

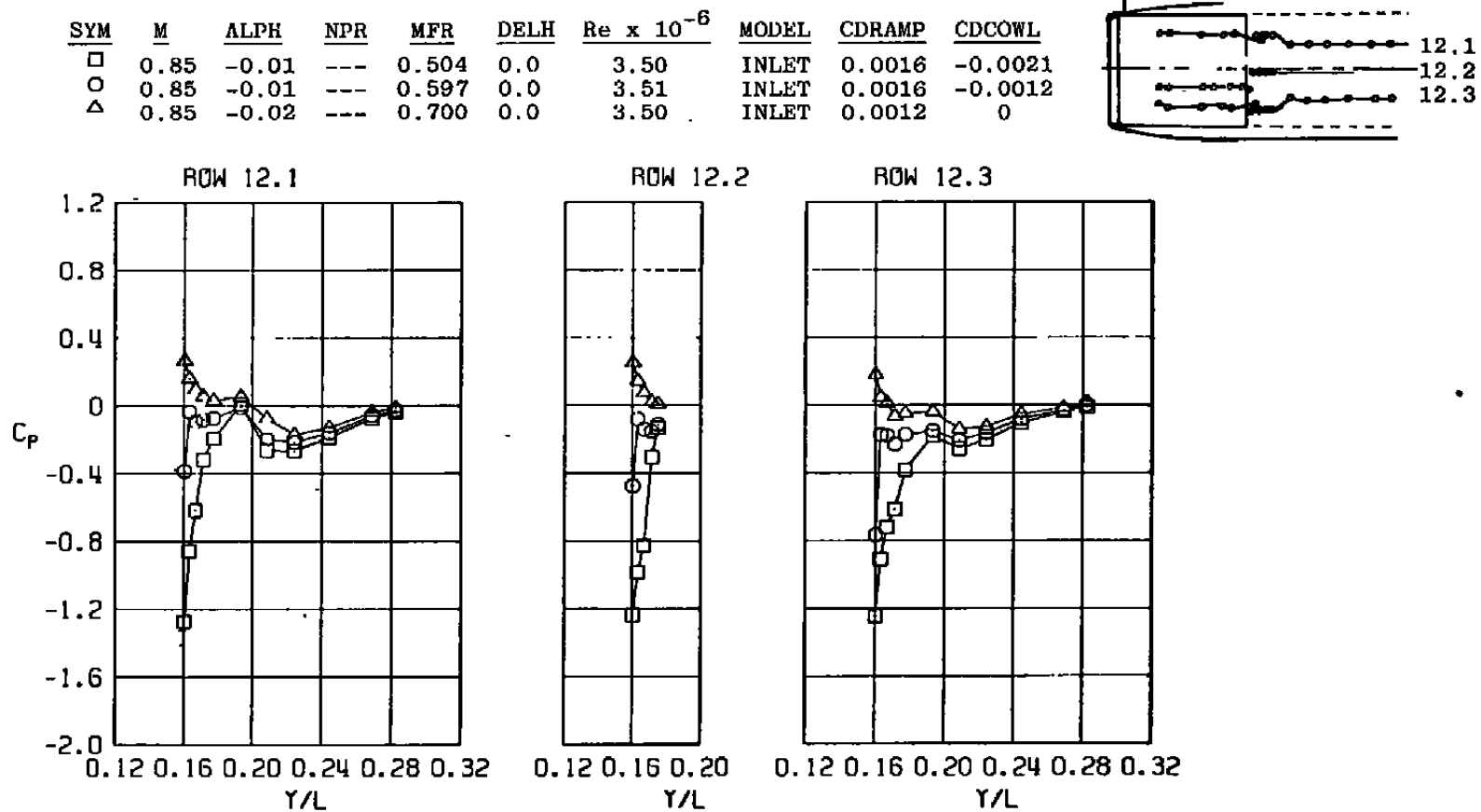


b. Supersonic dash
Figure 23. Concluded.



a. Ramp

Figure 24. Effect of mass flow ratio on inlet pressure distributions,
 $M = 0.85$.



b. Cowl
Figure 24. Concluded.

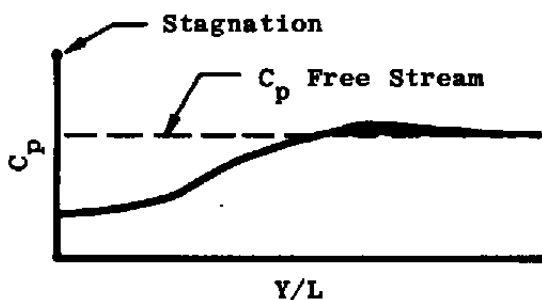
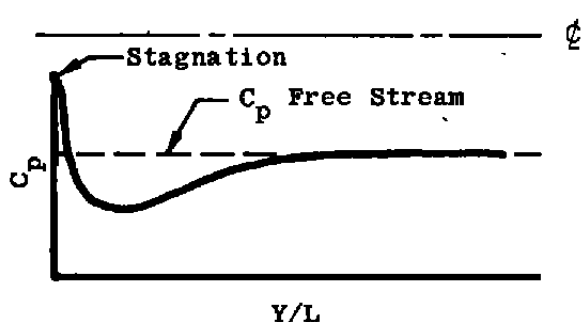
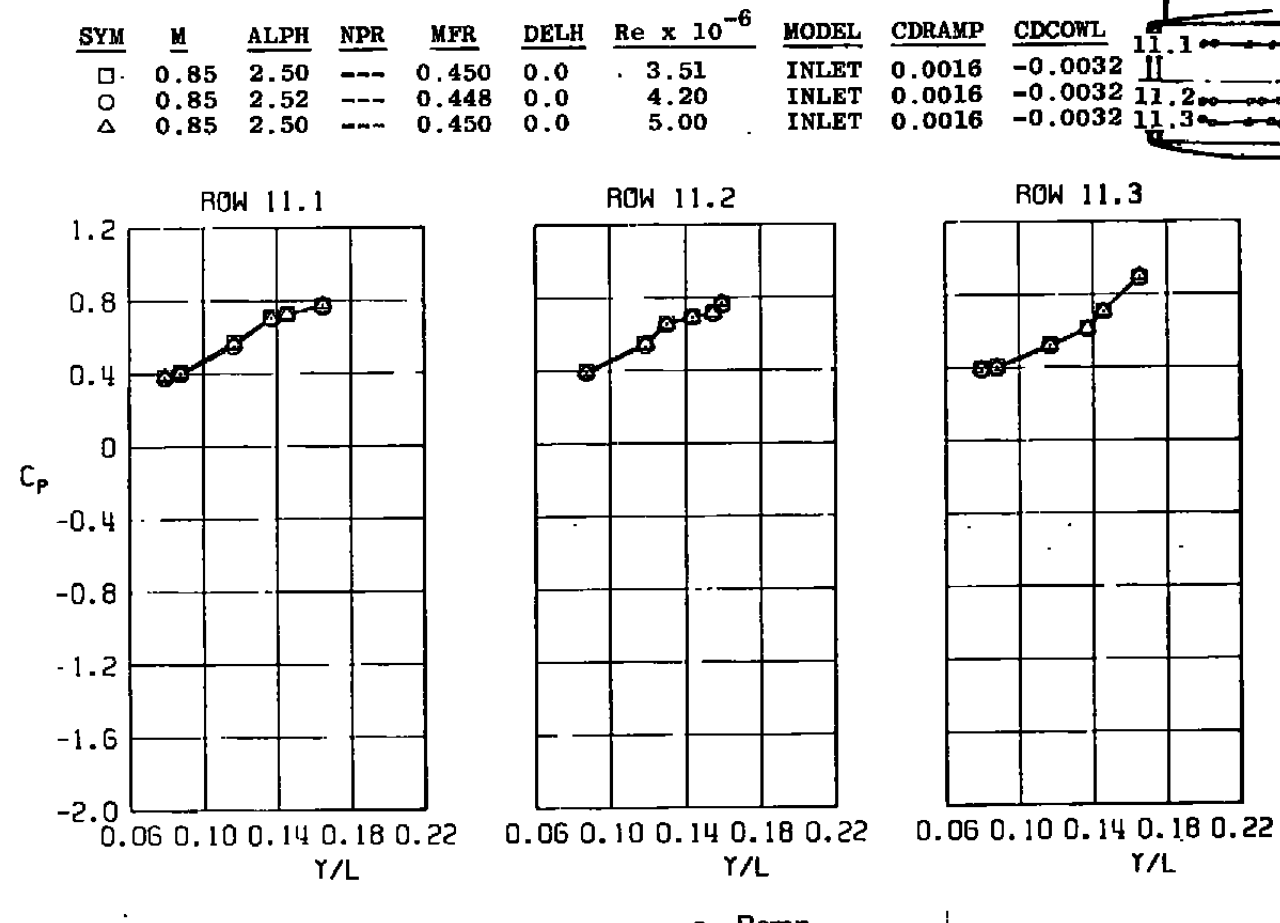
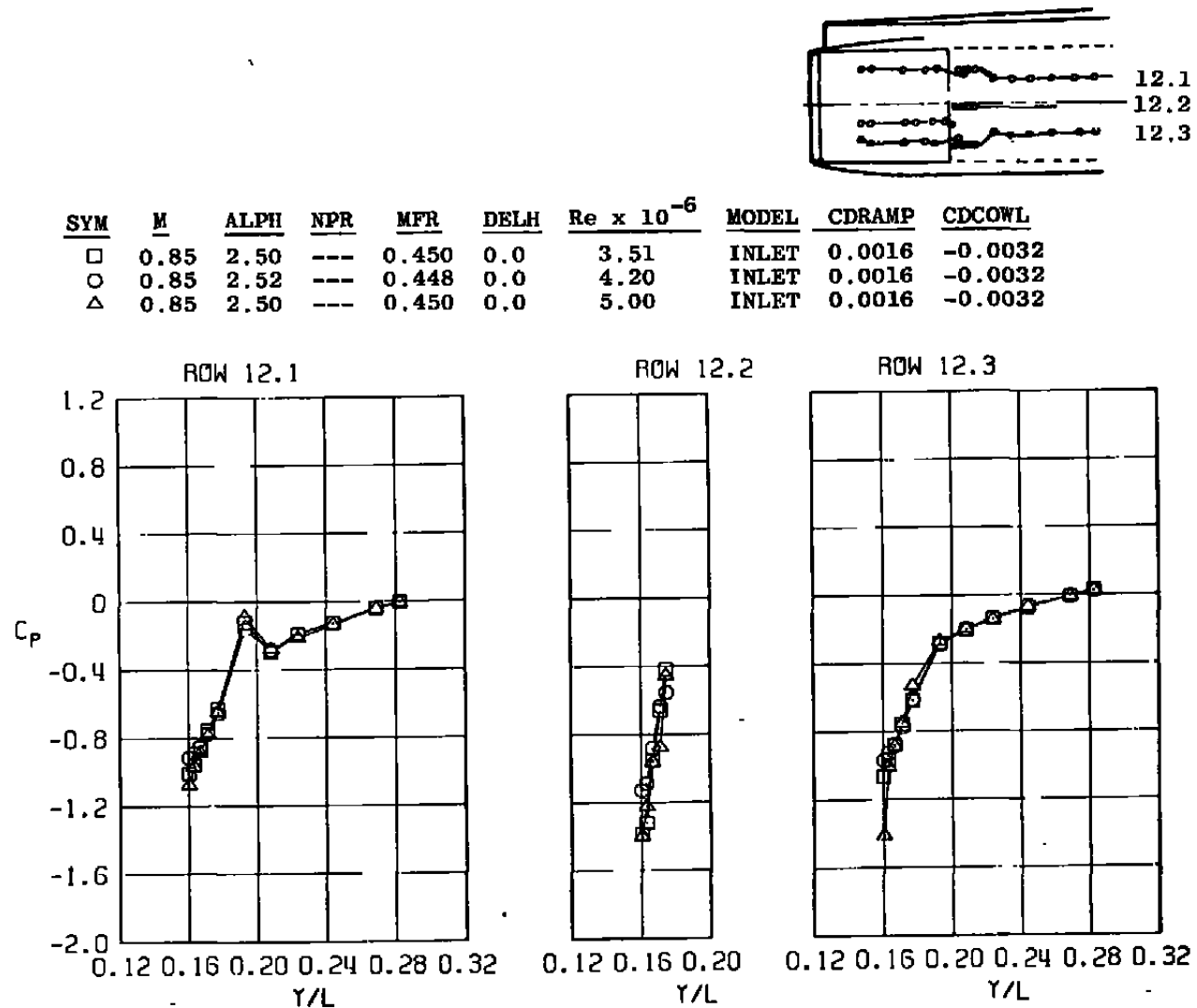


Figure 25. Effect of mass flow ratio on external cowl surface pressure distribution.

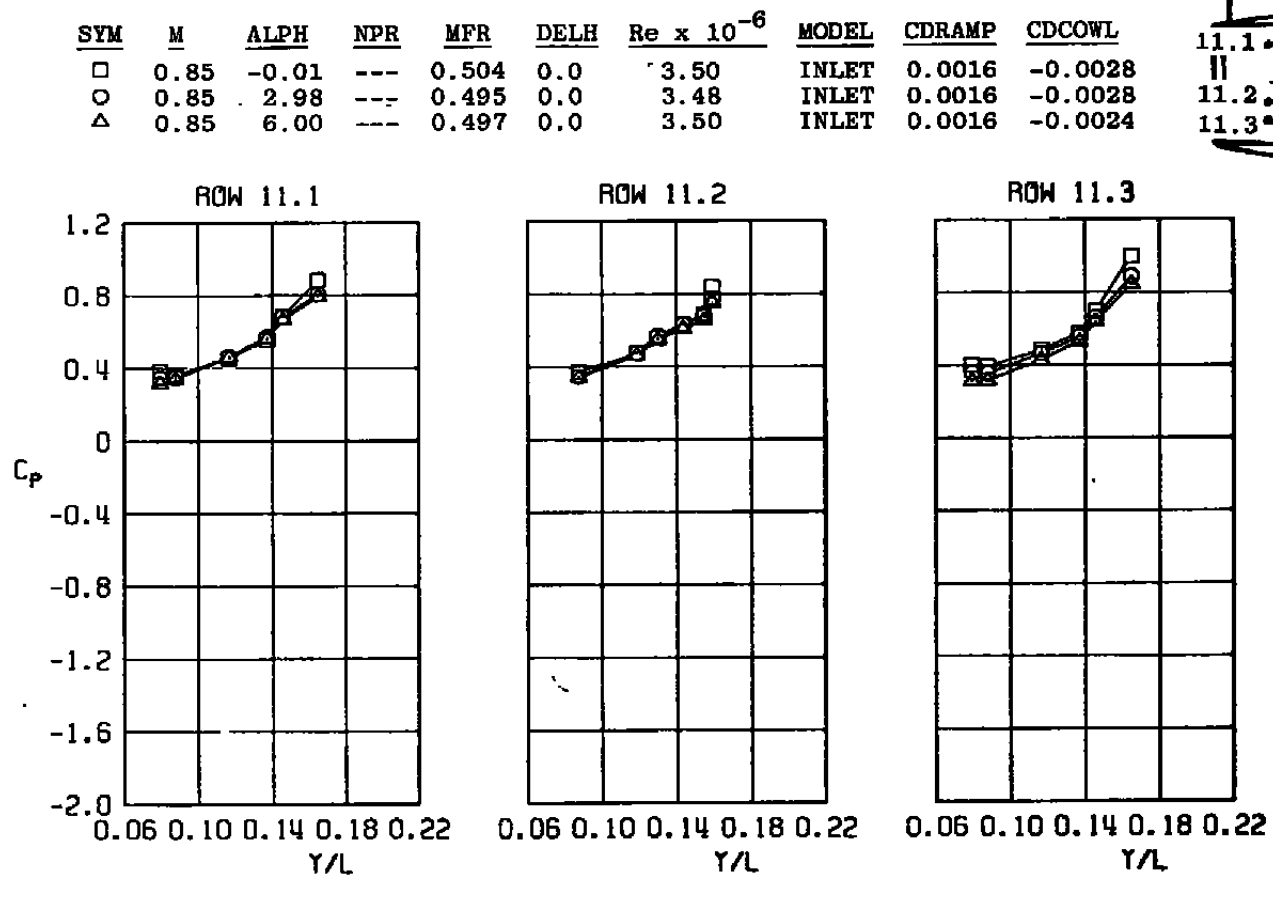


a. Ramp

Figure 26. Effect of Reynolds number on inlet pressure distributions,
M = 0.85.

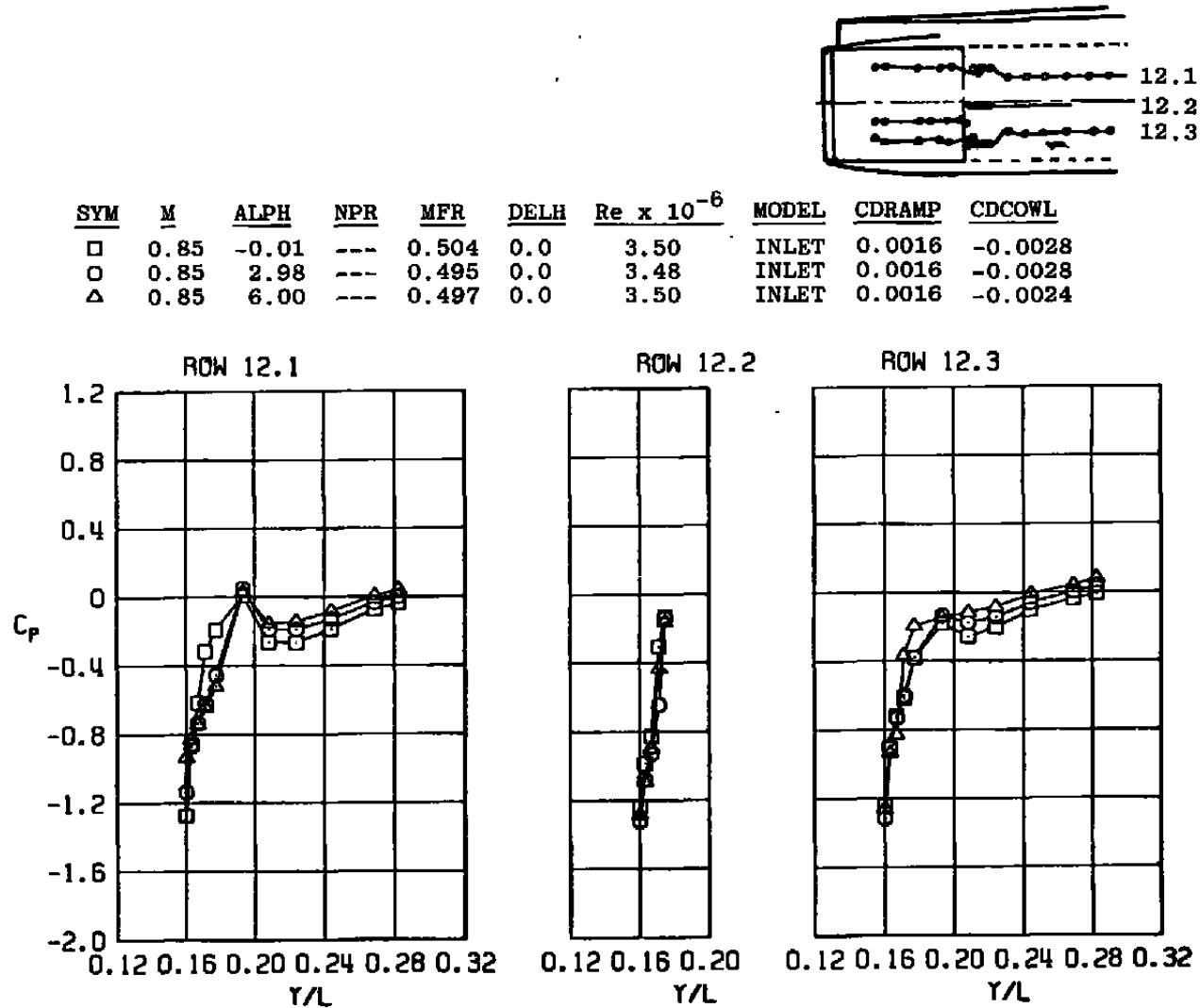


b. Cowl
Figure 26. Concluded.



a. Ramp

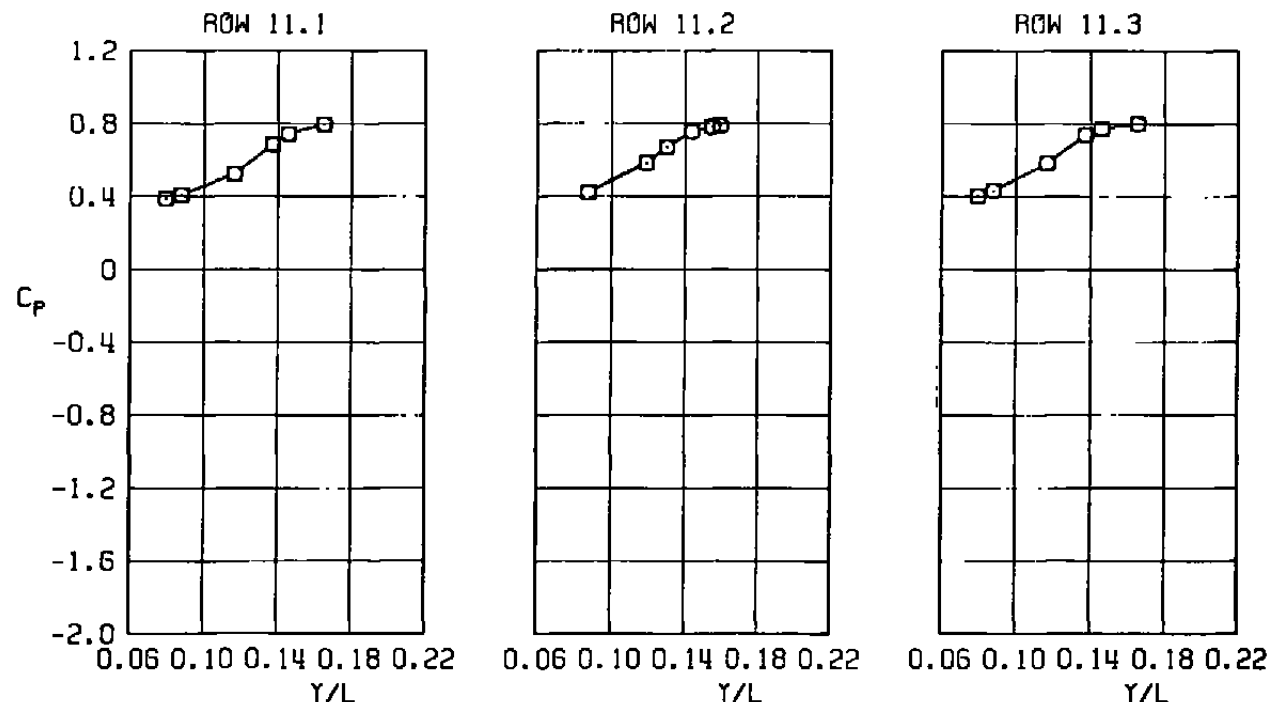
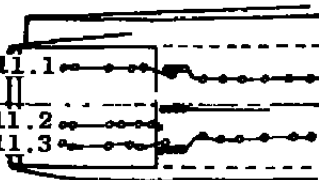
Figure 27. Effect of angle of attack on inlet pressure distributions,
 $M = 0.85$.



b. Cowl
Figure 27. Concluded.

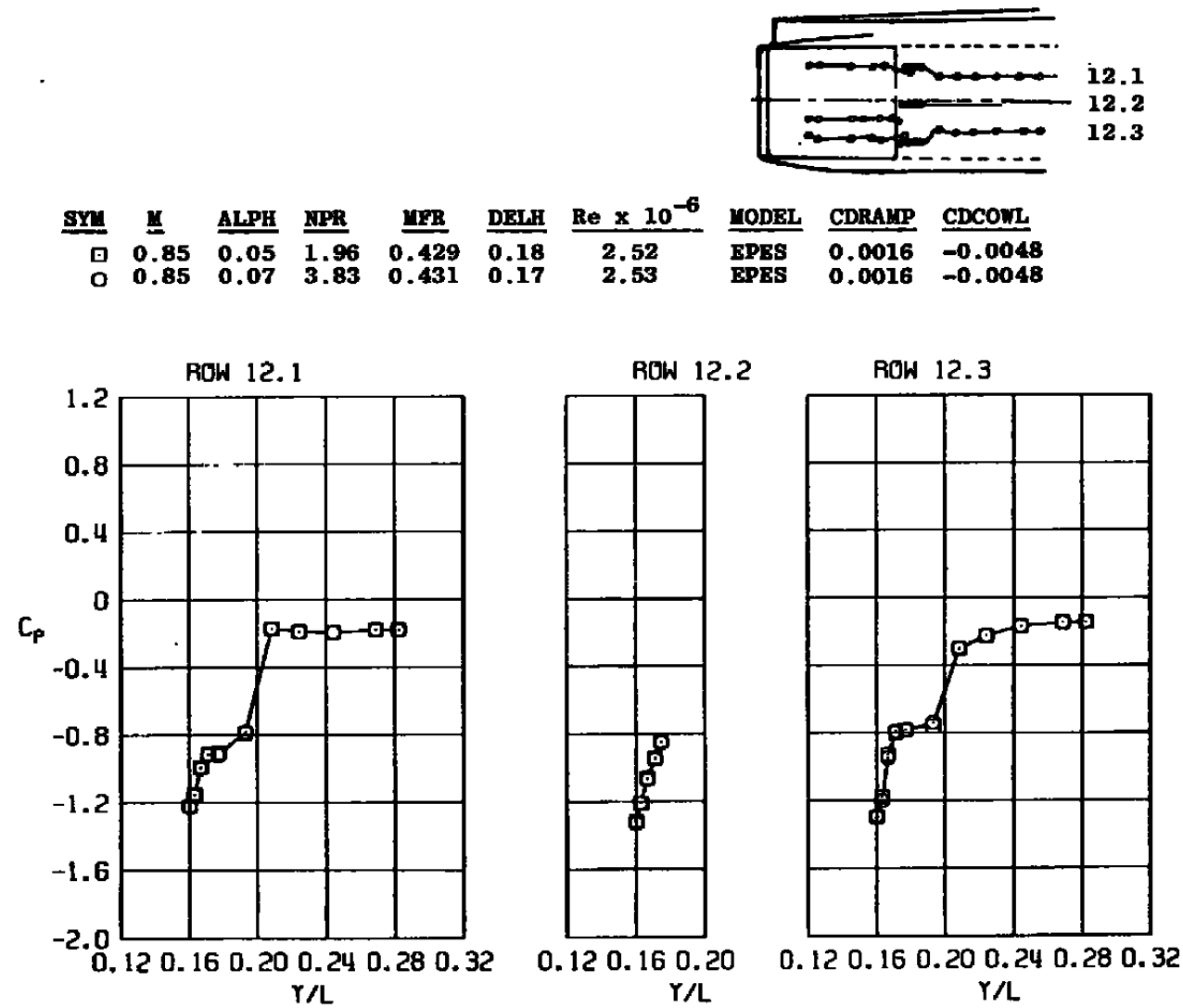
SYM	M	ALPH	NPR	MFR	DELH	$Re \times 10^{-6}$
□	0.85	0.05	1.96	0.429	0.18	2.52
○	0.85	0.07	3.83	0.431	0.17	2.53

MODEL	CDRAMP	CDCOWL
EPES	0.0016	-0.0048
EPES	0.0016	-0.0048

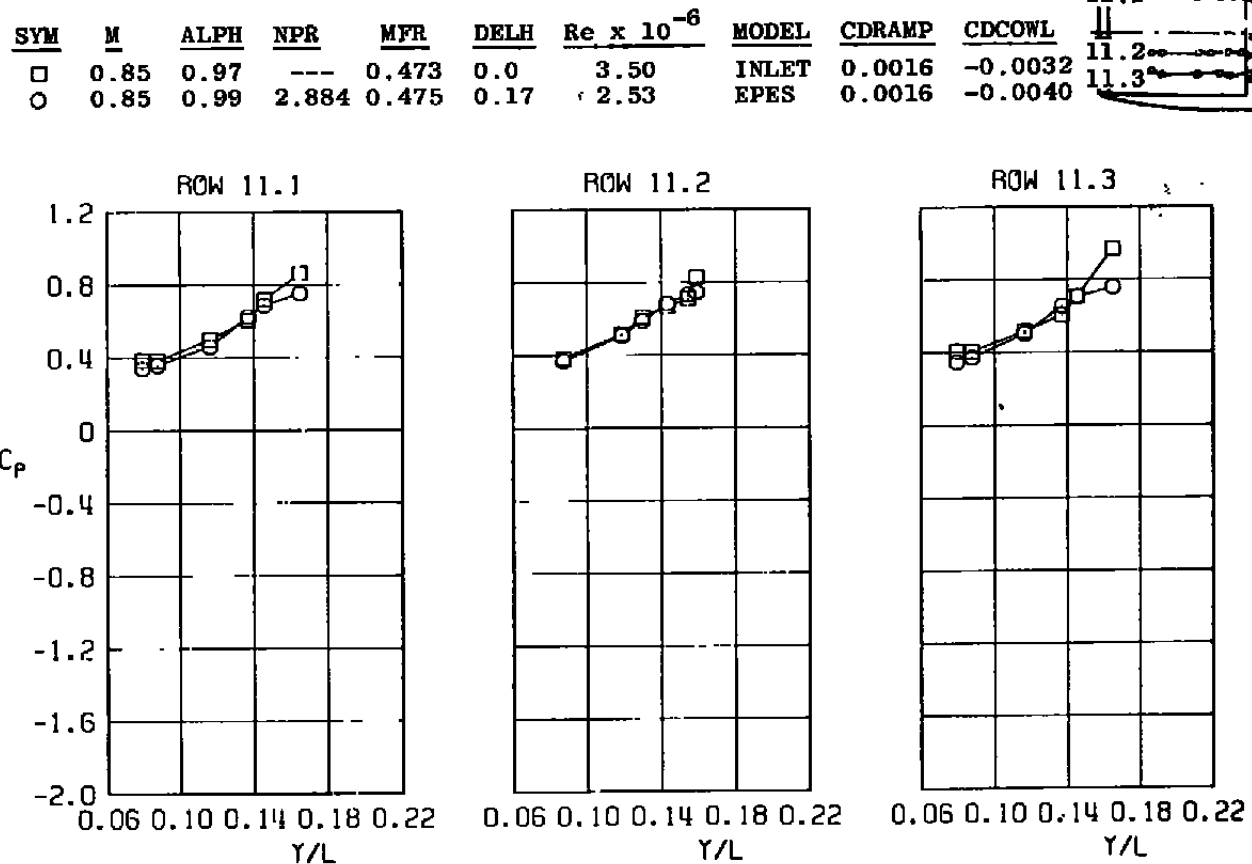


a. Ramp

Figure 28. Effect of nozzle pressure ratio on inlet pressure distributions, $M = 0.85$.

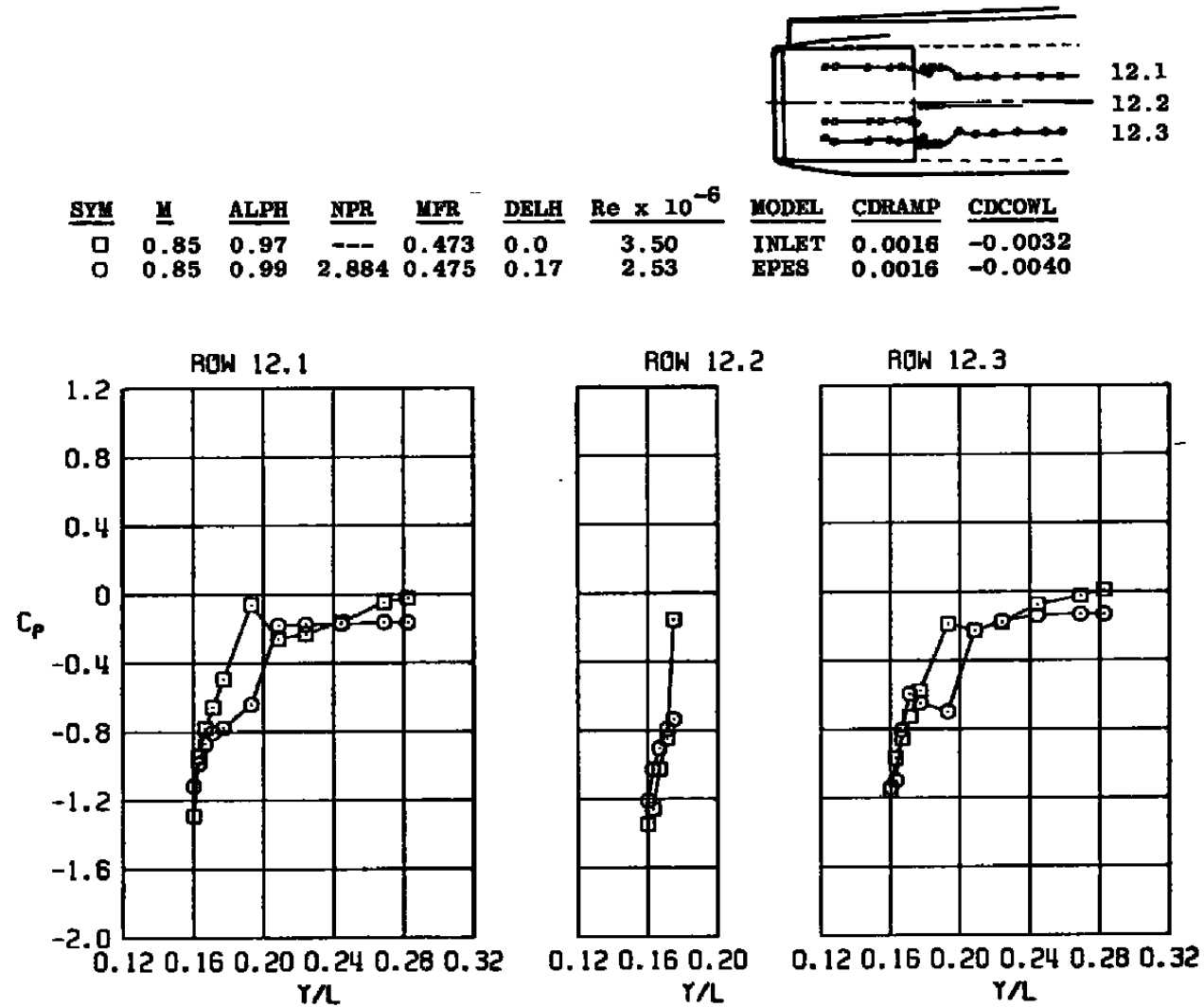


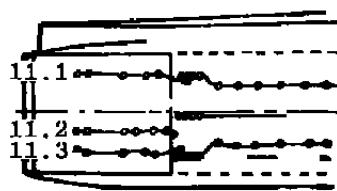
b. Cowl
Figure 28. Concluded.



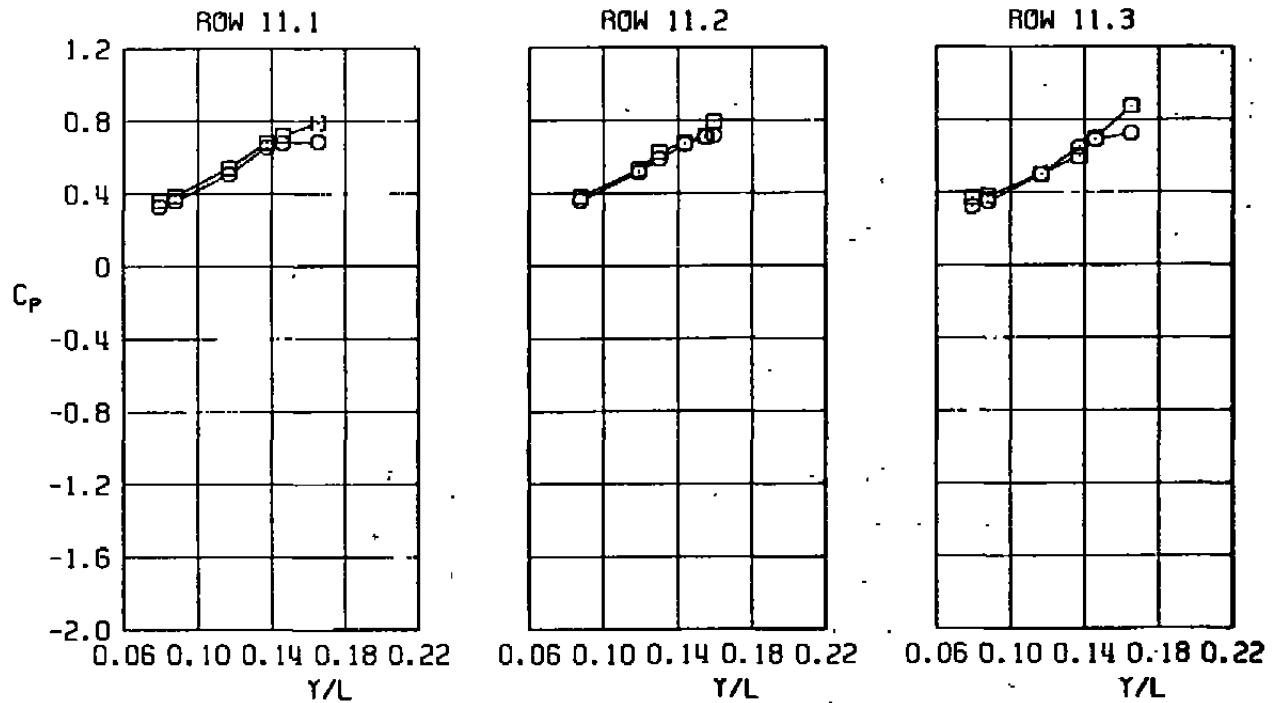
a. Ramp

Figure 29. Comparison of inlet pressure distributions for the EPES and 0.07-scale models, $M = 0.85$, $\alpha = 1$ deg.



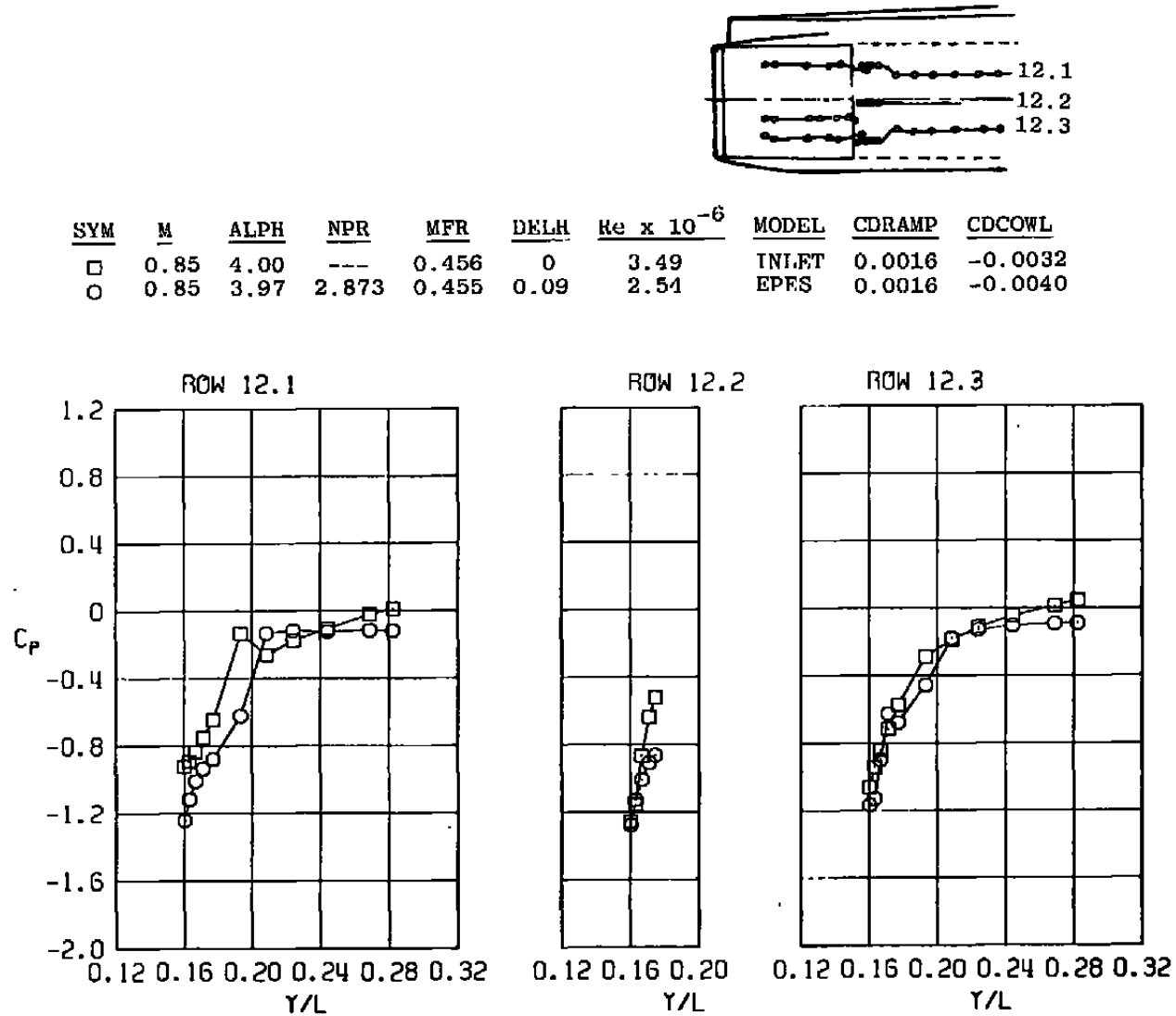


SYM	M	ALPH	NPR	MFR	DElh	$Re \times 10^{-6}$	MODEL	CDRAMP	CDCOWL
□	0.85	4.00	---	0.456	0	3.49	INLET	0.0016	-0.0032
○	0.85	3.97	2.873	0.455	0.09	2.54	EPES	0.0016	-0.0040



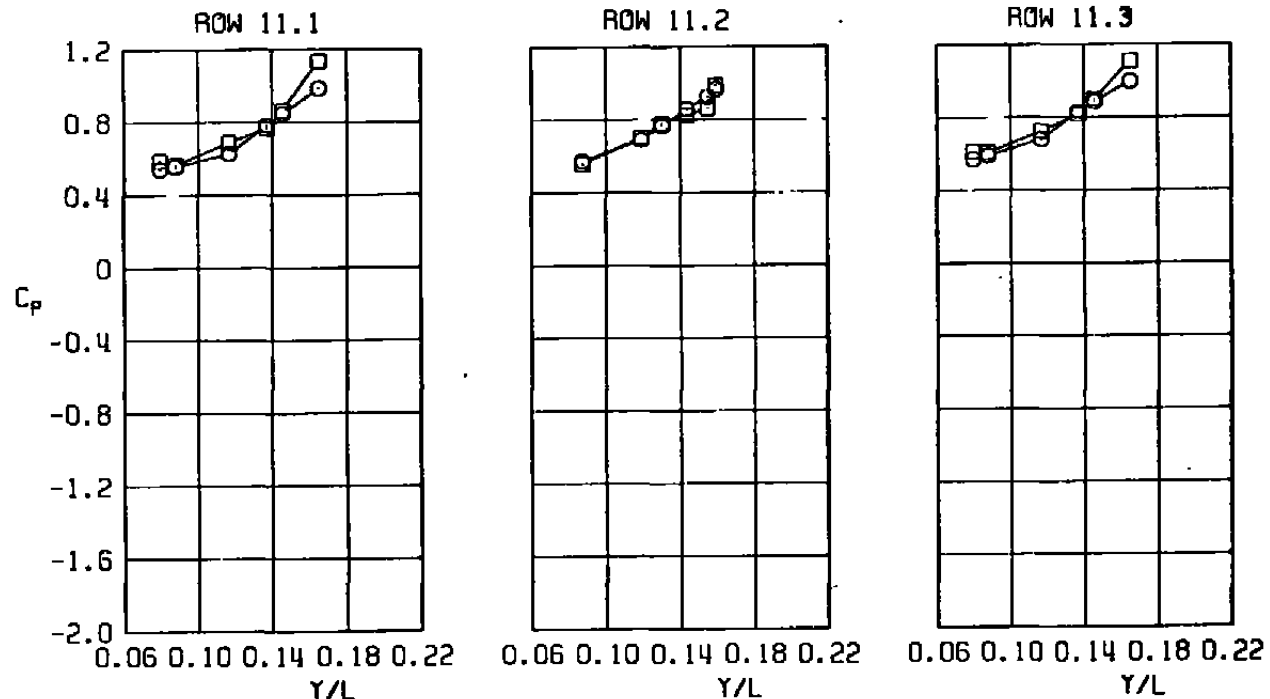
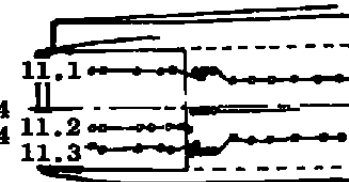
a. Ramp

Figure 30. Comparison of inlet pressure distributions for the EPES and 0.07-scale models, $M = 0.85$, $\alpha = 4$ deg.



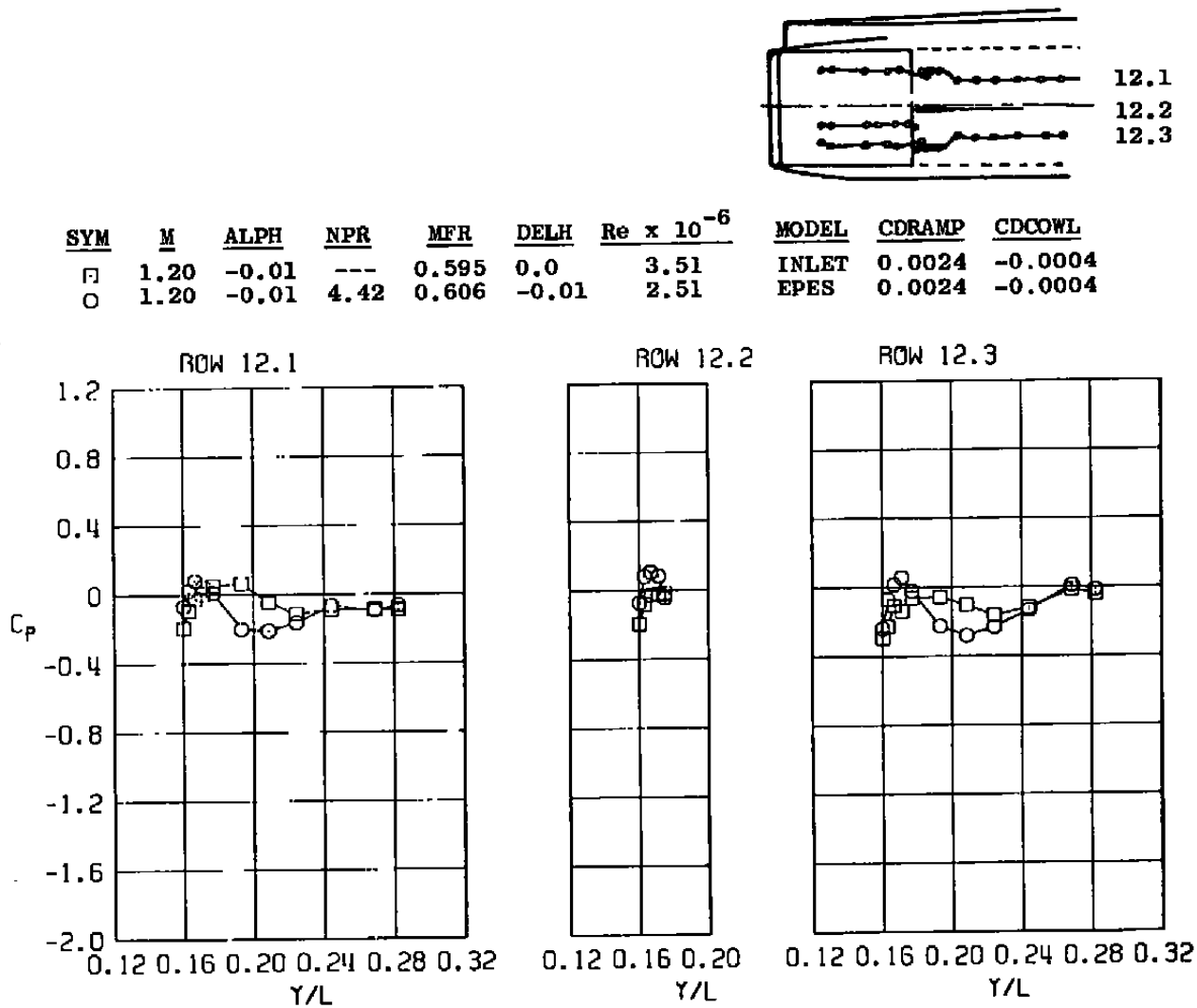
b. cowl
Figure 30. Concluded.

<u>SYM</u>	<u>M</u>	<u>ALPH</u>	<u>NPR</u>	<u>MFR</u>	<u>DElh</u>	<u>Re x 10⁻⁶</u>	<u>MODEL</u>
□	1.20	-0.01	---	0.595	0.0	3.51	INLET
○	1.20	-0.01	4.42	0.606	-0.01	2.51	EPES

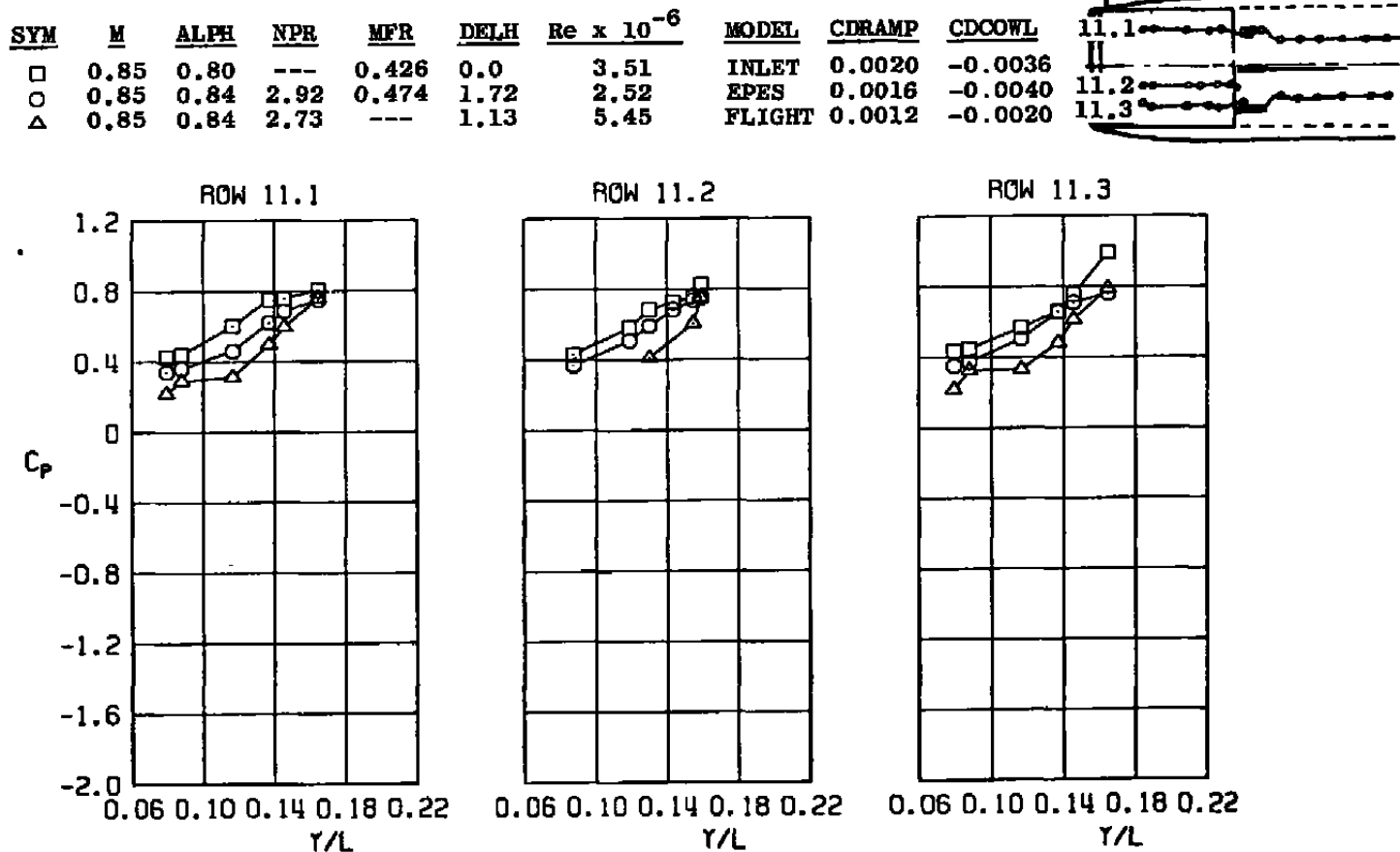


a. Ramp

Figure 31. Comparison of inlet pressure distributions for the EPES and 0.07-scale models, $M = 1.20$, $a = 0$.

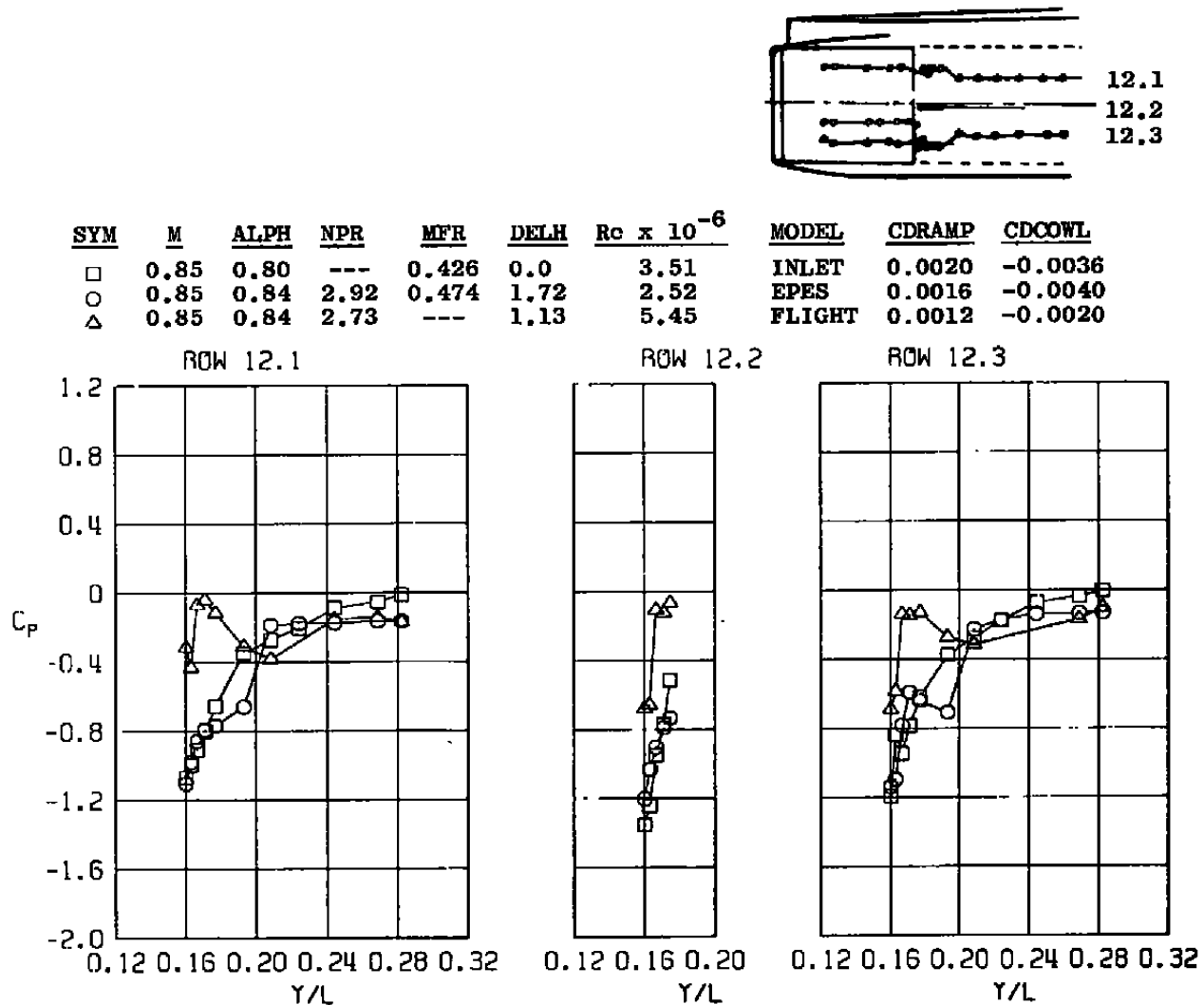


b. Cowl
Figure 31. Concluded.



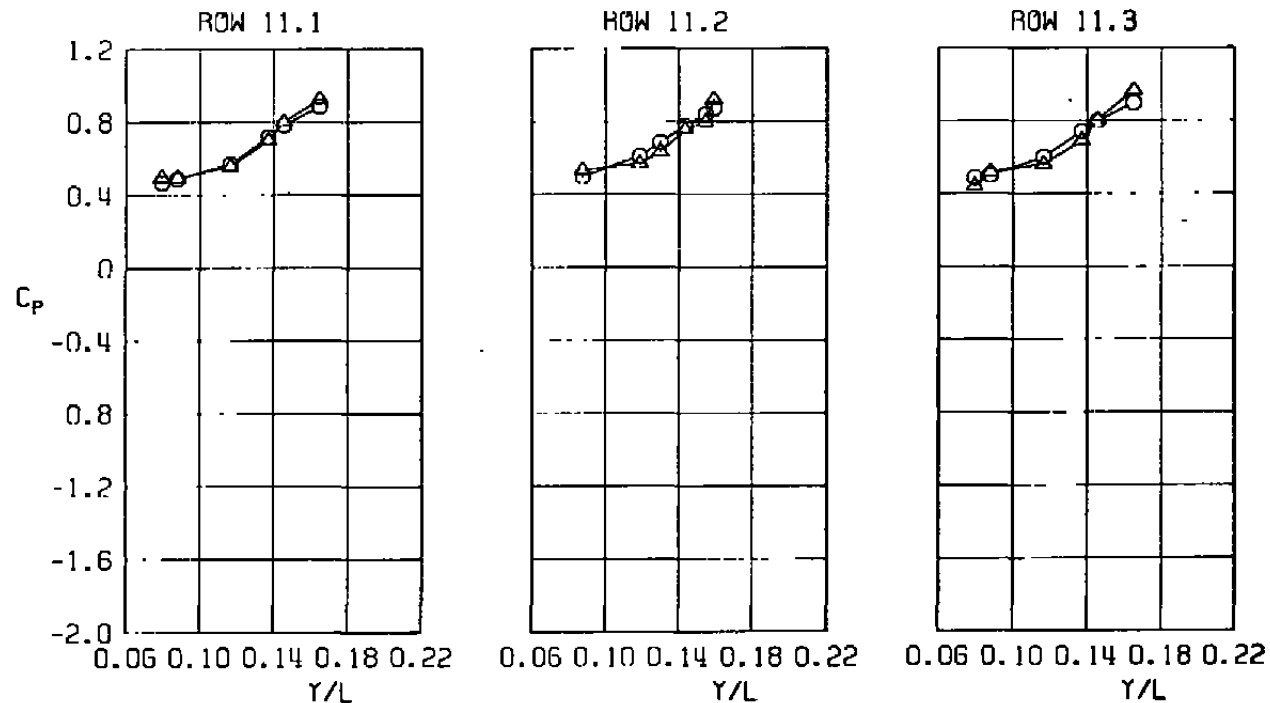
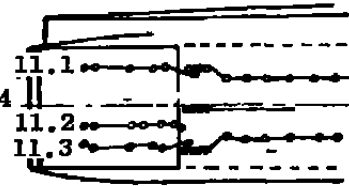
a. Ramp

Figure 32. Comparison of inlet pressure distributions for the EPES, 0.07-scale and the flight vehicle, $M = 0.85$, $\alpha = 0.84$ deg.



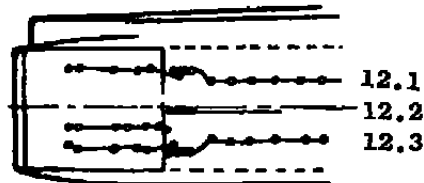
b. Cowl
Figure 32. Concluded.

<u>SYM</u>	<u>M</u>	<u>ALPH</u>	<u>NPR</u>	<u>MFR</u>	<u>DELH</u>	<u>Re x 10⁻⁶</u>	<u>MODEL</u>	<u>CDRAMP</u>	<u>CDCOWL</u>
○	1.20	2.79	4.76	0.641	0.29	2.52	EPES	0.0020	-0.0004
△	1.20	2.82	4.28	0.645	0.23	3.22	FLIGHT	0.0020	0

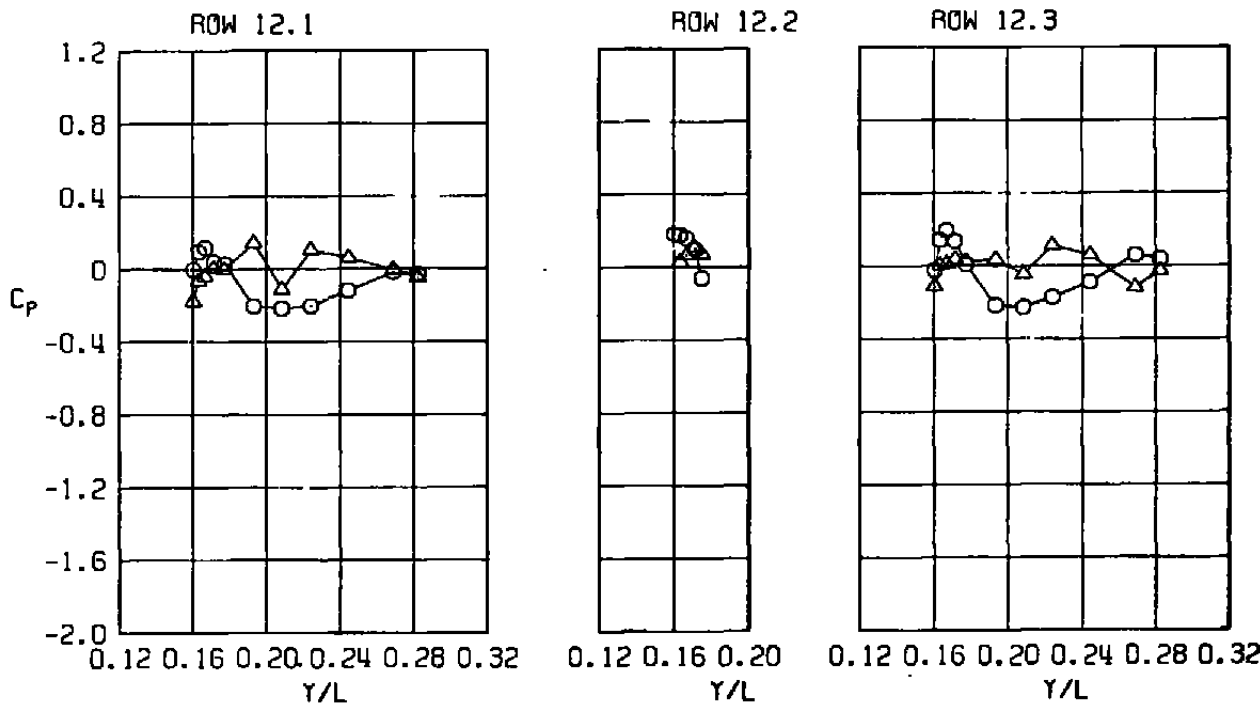


a. Ramp

Figure 33. Comparison of inlet pressure distributions for the EPES model and the flight vehicle, $M = 1.20$, $\alpha = 2.8$ deg.

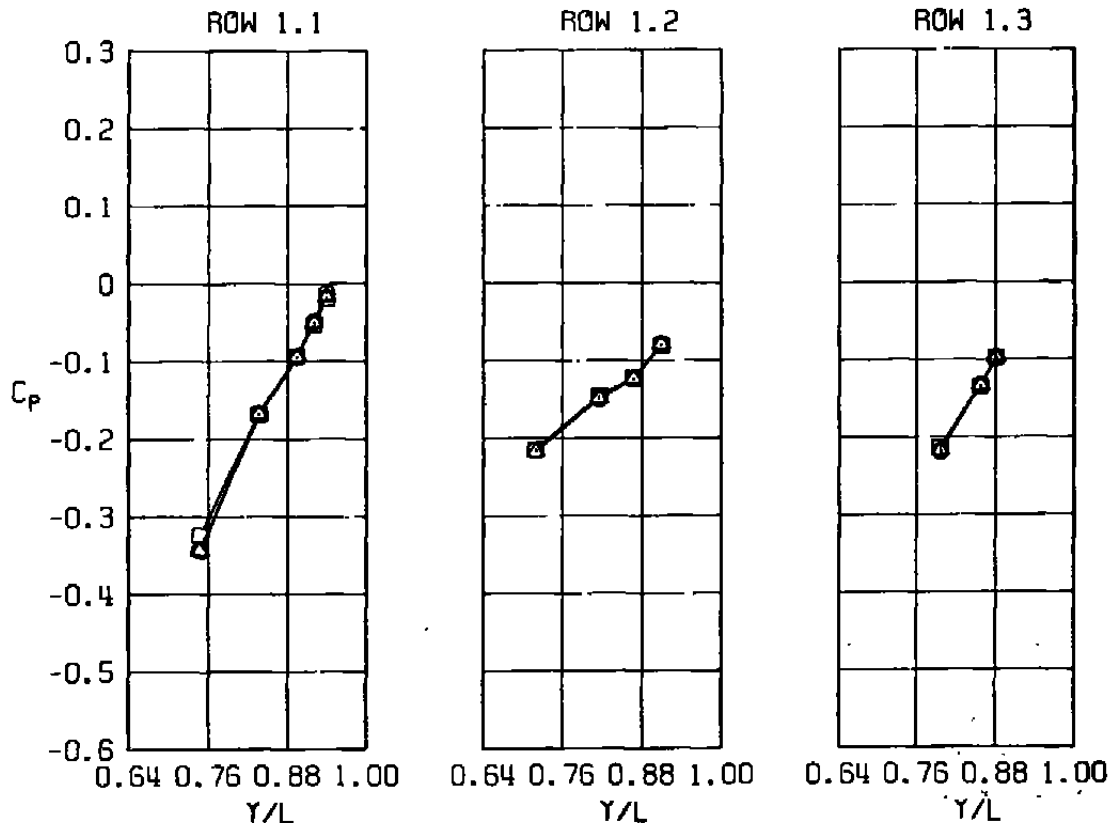
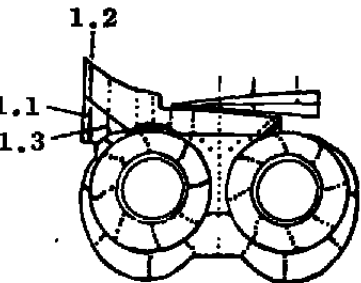


<u>SYM</u>	<u>M</u>	<u>ALPH</u>	<u>NPR</u>	<u>MFR</u>	<u>DElh</u>	<u>Re x 10⁻⁶</u>	<u>MODEL</u>	<u>CDRAMP</u>	<u>CDCOWL</u>
○	1.20	2.79	4.76	0.641	0.29	2.52	EPES	0.0020	-0.0004
△	1.20	2.82	4.28	0.645	0.23	3.22	FLIGHT	0.0020	0



b. Cowl
Figure 33. Concluded.

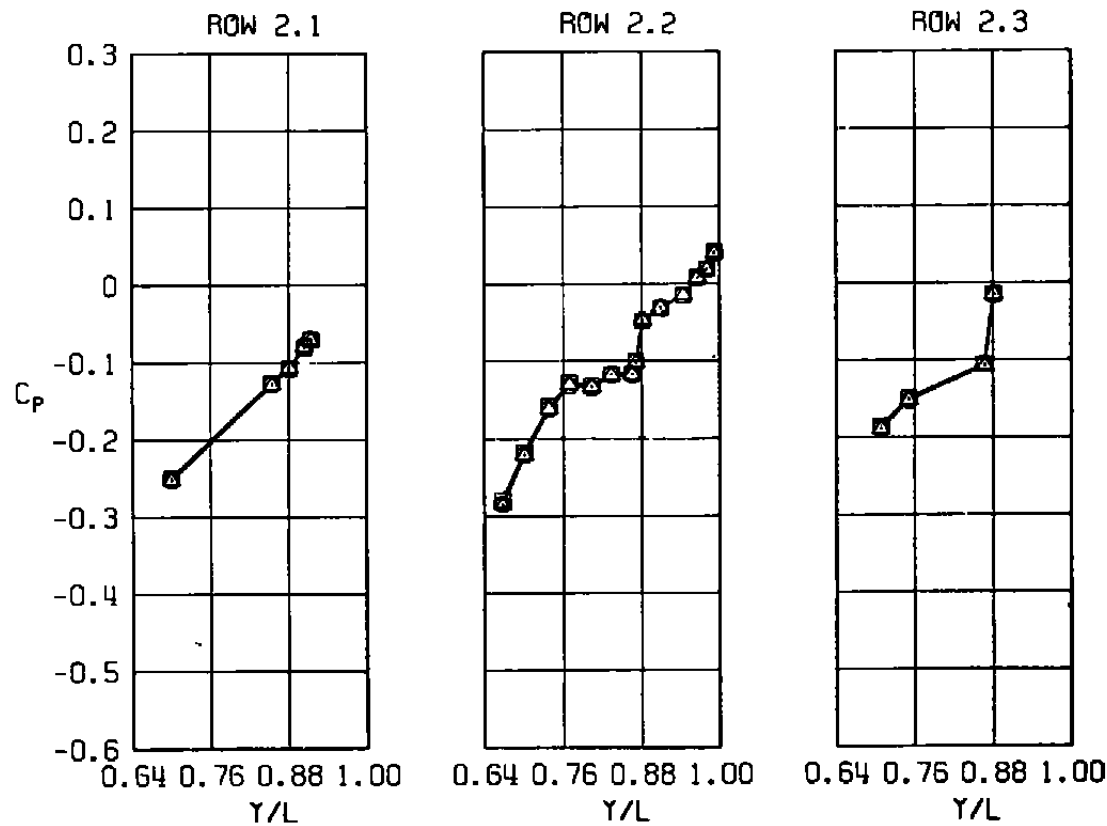
<u>SYM</u>	<u>M</u>	<u>ALPH</u>	<u>NPR</u>	<u>MFR</u>	<u>DElh</u>	<u>Re</u> $\times 10^{-6}$	<u>MODEL</u>	<u>CDNOZ</u>
□	0.85	0.06	2.88	0.423	0.17	2.53	EPES	0.0001
○	0.85	0.06	2.89	0.460	0.17	2.53	EPES	0.0002
△	0.85	0.06	2.88	0.480	0.17	2.53	EPES	0.0002



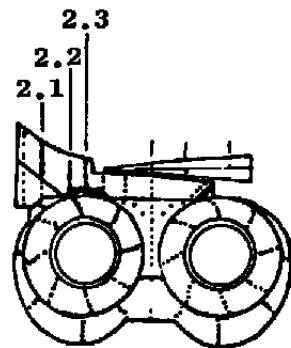
a. Row 1

Figure 34. Effect on mass flow ratio on nozzle afterbody pressure distribution. $M = 0.85$, $\alpha = 0$.

<u>SYM</u>	<u>M</u>	<u>ALPH</u>	<u>NPR</u>	<u>MFR</u>	<u>DELH</u>	<u>Re x 10⁻⁶</u>	<u>MODEL</u>	<u>CDNOZ</u>
□	0.85	0.06	2.88	0.423	0.17	2.53	EPES	0.0001
○	0.85	0.06	2.89	0.460	0.17	2.53	EPES	0.0002
△	0.85	0.06	2.88	0.480	0.17	2.53	EPES	0.0002

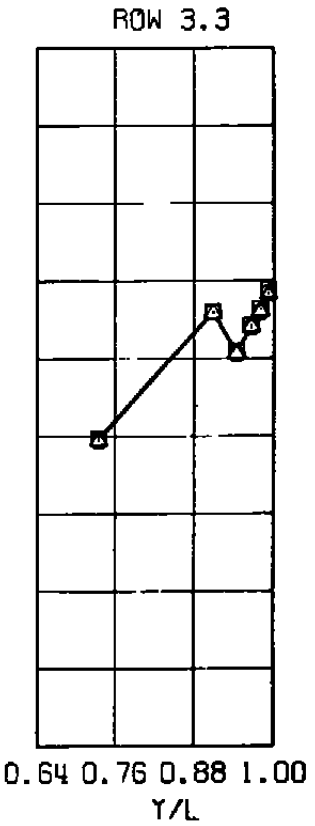
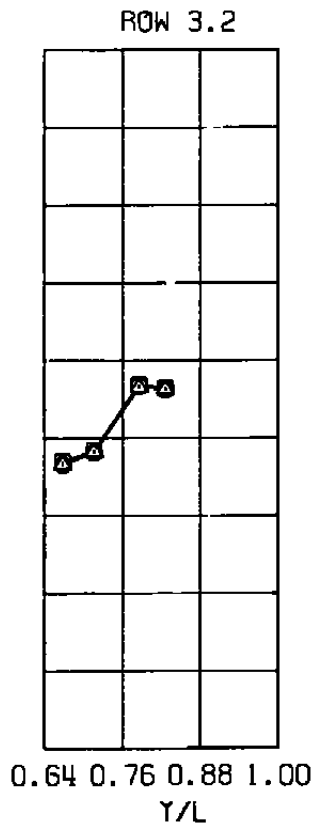
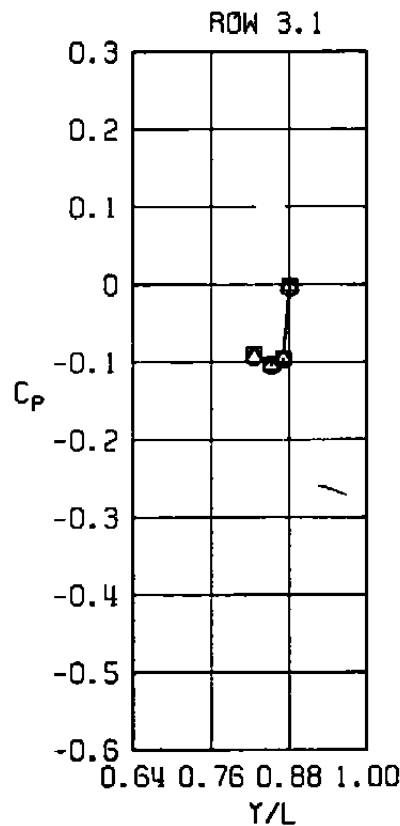
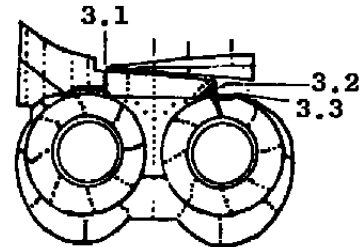


b. Row 2
Figure 34. Continued.



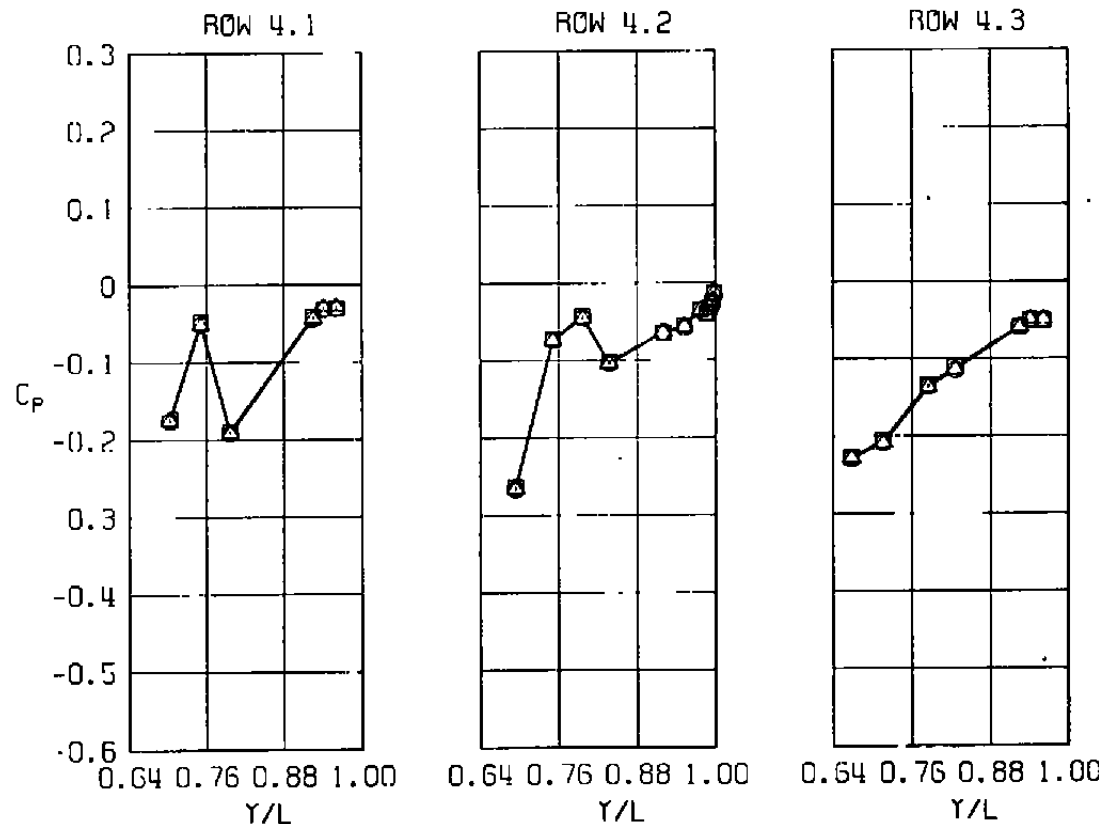
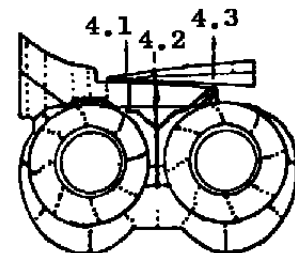
<u>SYM</u>	<u>M</u>	<u>ALPH</u>	<u>NPR</u>	<u>MFR</u>	<u>DELH</u>	<u>Re</u> $\times 10^{-6}$
□	0.85	0.06	2.88	0.423	0.17	2.53
○	0.85	0.06	2.89	0.460	0.17	2.53
△	0.85	0.06	2.88	0.480	0.17	2.53

<u>MODEL</u>	<u>CDNOZ</u>
EPES	0.0001
EPES	0.0002
EPES	0.0002



c. Row 3
Figure 34. Continued.

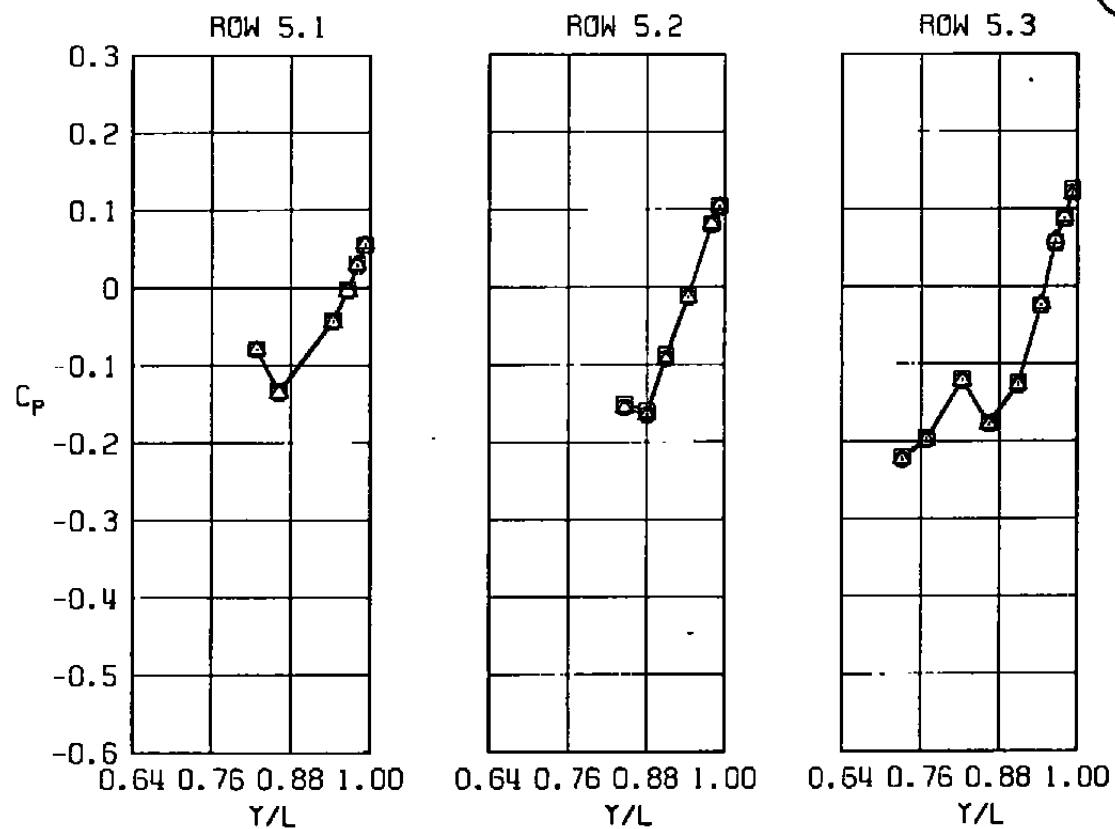
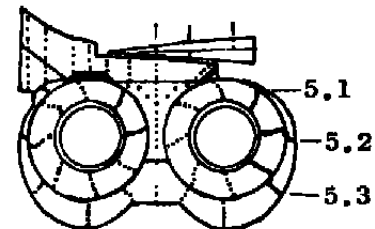
<u>SYM</u>	<u>M</u>	<u>ALPH</u>	<u>NPR</u>	<u>MFR</u>	<u>DELH</u>	<u>Re</u> $\times 10^{-6}$	<u>MODEL</u>	<u>CDNOZ</u>
□	0.85	0.06	2.88	0.423	0.17	2.53	EPES	0.0001
○	0.85	0.06	2.89	0.460	0.17	2.53	EPES	0.0002
△	0.85	0.06	2.88	0.480	0.17	2.53	EPES	0.0002



d. Row 4
Figure 34. Continued.

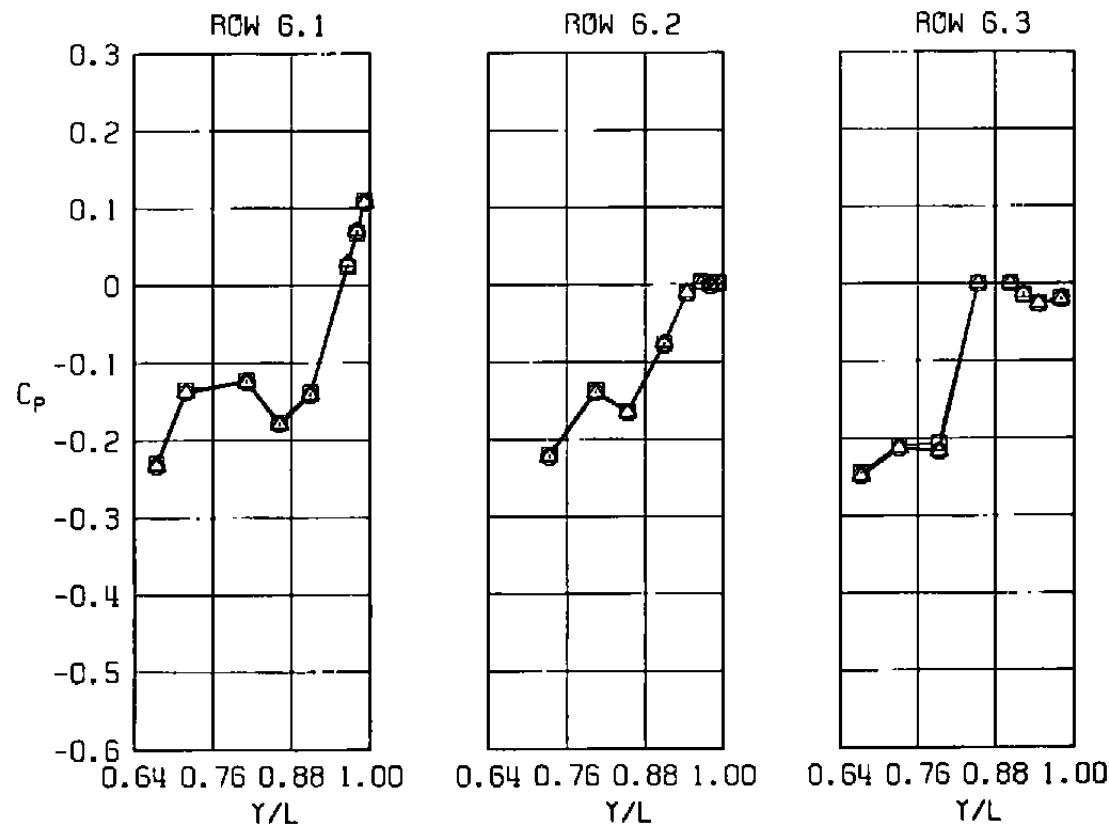
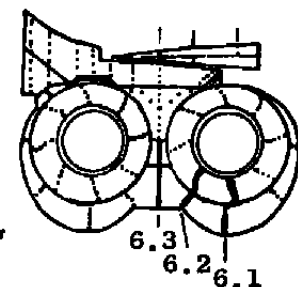
<u>SYM</u>	<u>M</u>	<u>ALPH</u>	<u>NPR</u>	<u>MFR</u>	<u>DELM</u>	<u>Re x 10⁻⁶</u>
□	0.85	0.06	2.88	0.423	0.17	2.53
○	0.85	0.06	2.89	0.460	0.17	2.53
△	0.85	0.06	2.88	0.480	0.17	2.53

<u>MODEL</u>	<u>CDNOZ</u>
EPES	0.0001
EPES	0.0002
EPES	0.0002

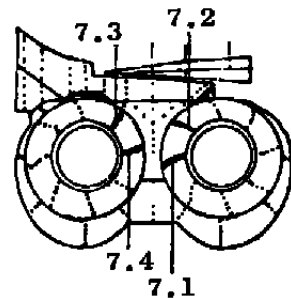
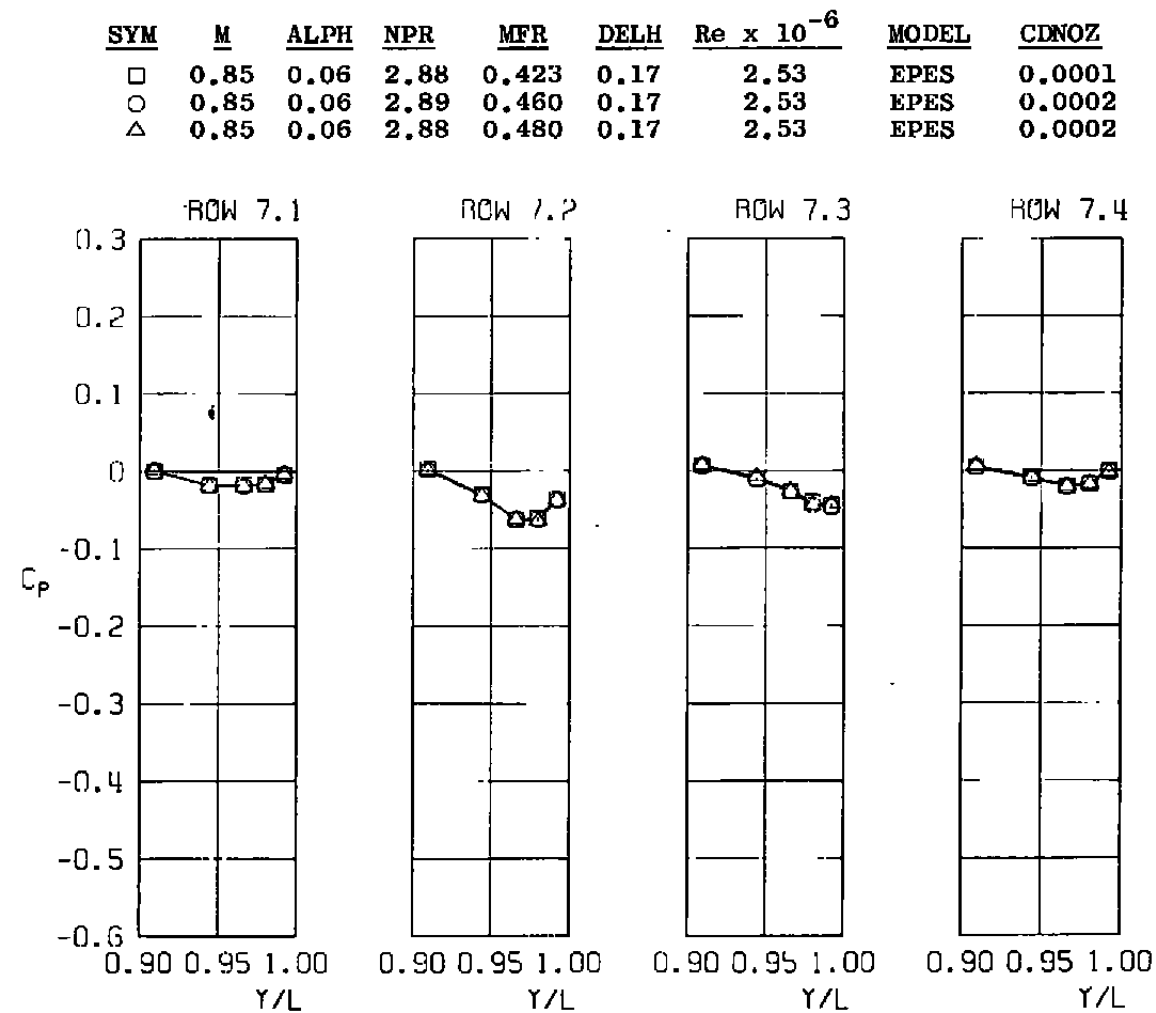


e. Row 5
Figure 34. Continued.

<u>SYM</u>	<u>M</u>	<u>ALPH</u>	<u>NPR</u>	<u>MFR</u>	<u>DELH</u>	<u>Re</u> $\times 10^{-6}$	<u>MODEL</u>	<u>CDNOZ</u>
□	0.85	0.06	2.88	0.423	0.17	2.53	EPES	0.0001
C	0.85	0.06	2.89	0.460	0.17	2.53	EPES	0.0002
△	0.85	0.06	2.88	0.480	0.17	2.53	EPES	0.0002

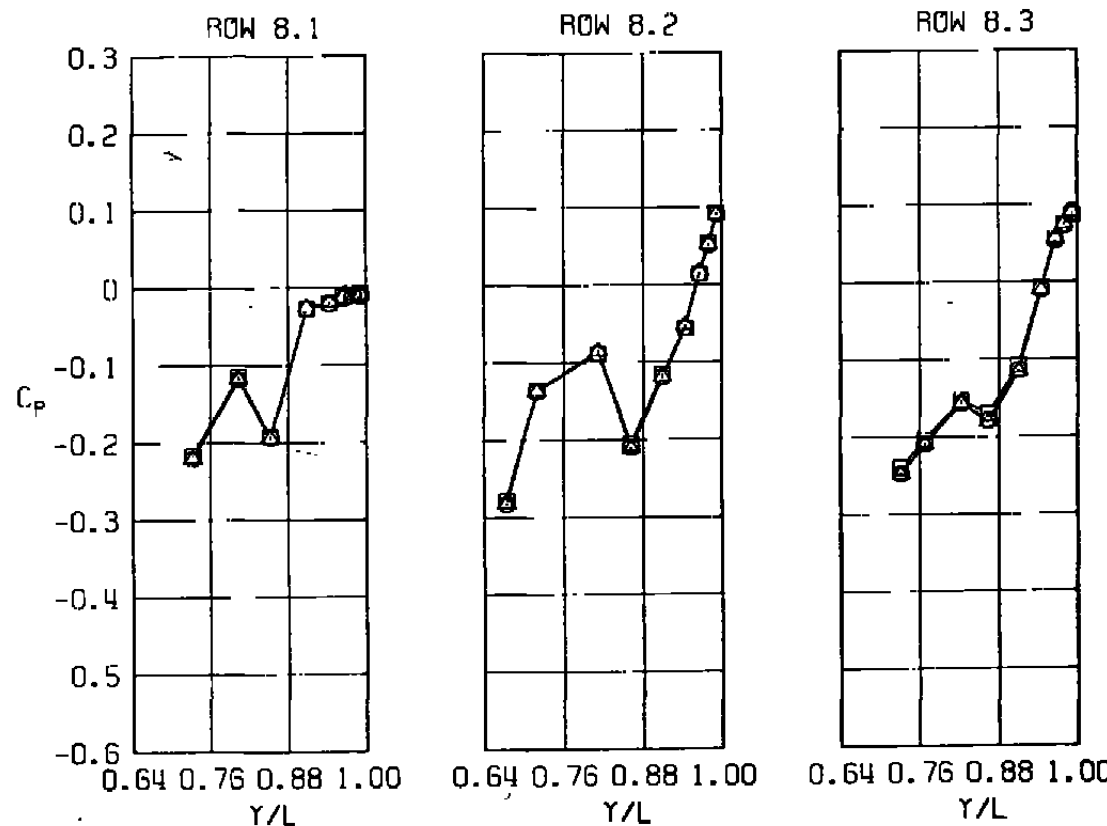
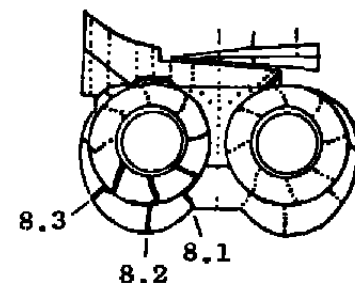


f. Row 6
Figure 34. Continued.



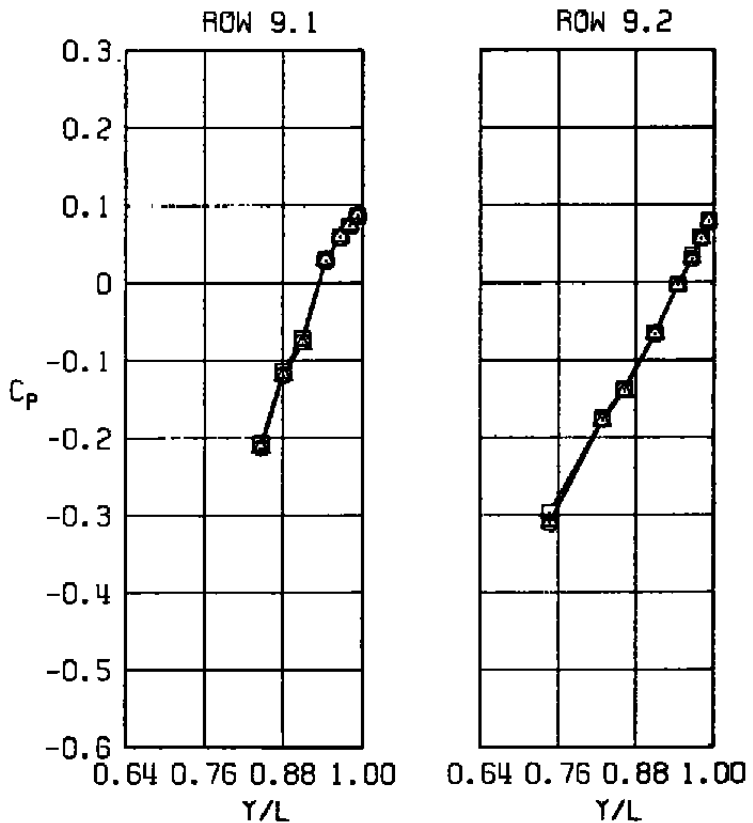
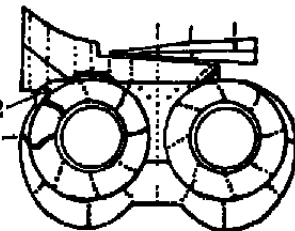
g. Row 7
Figure 34. Continued.

<u>SYM</u>	<u>M</u>	<u>ALPH</u>	<u>NPR</u>	<u>MFR</u>	<u>DELH</u>	<u>Re</u> $\times 10^{-6}$	<u>MODEL</u>	<u>CDNOZ</u>
□	0.85	0.06	2.88	0.423	0.17	2.53	EPES	0.0001
○	0.85	0.06	2.89	0.460	0.17	2.53	EPES	0.0002
△	0.85	0.06	2.88	0.480	0.17	2.53	EPES	0.0002



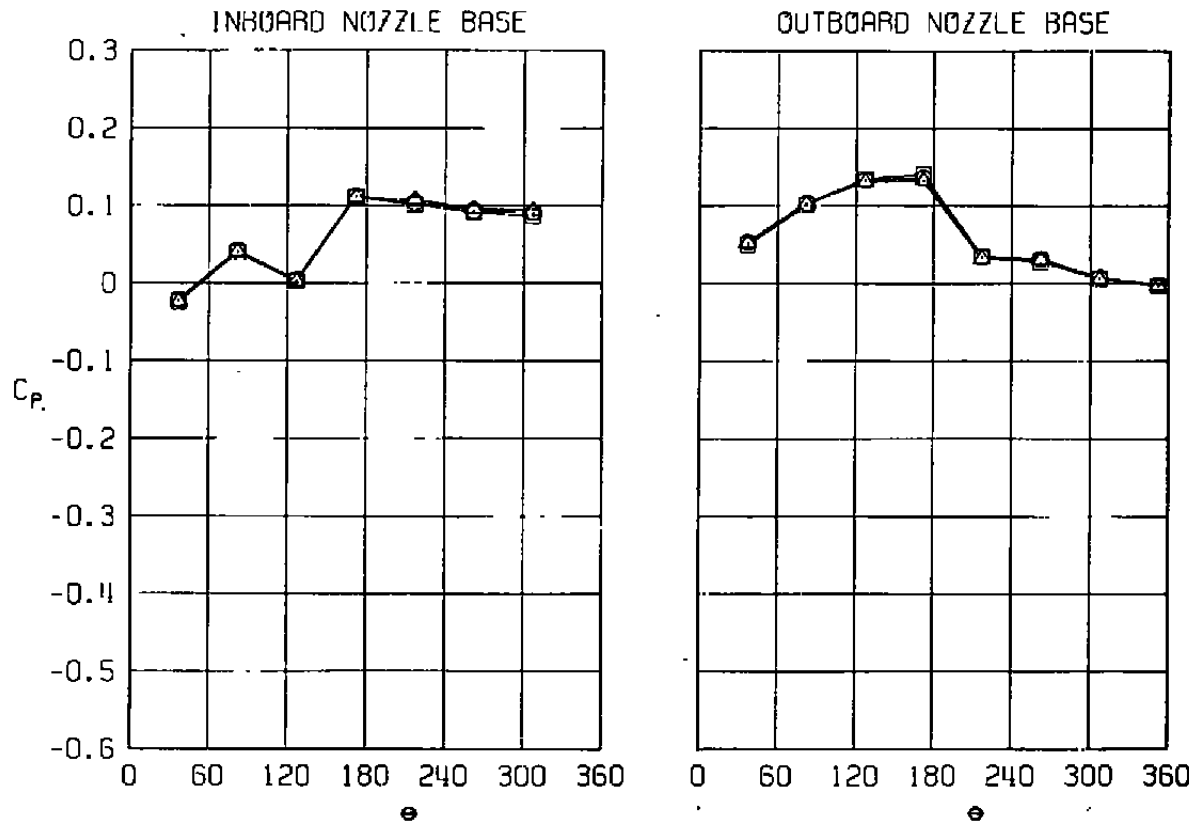
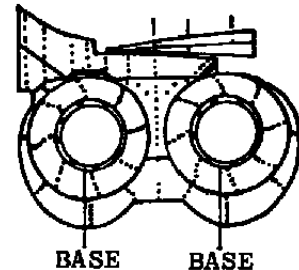
h. Row 8
Figure 34. Continued.

<u>SYM</u>	<u>M</u>	<u>ALPH</u>	<u>NPR</u>	<u>MFR</u>	<u>DELT</u> H	<u>Re</u> $\times 10^{-6}$	<u>MODEL</u>	<u>CDNOZ</u>
□	0.85	0.06	2.88	0.423	0.17	2.53	EPES	0.0001
○	0.85	0.06	2.89	0.460	0.17	2.53	EPES	0.0002
△	0.85	0.06	2.88	0.480	0.17	2.53	EPES	0.0002



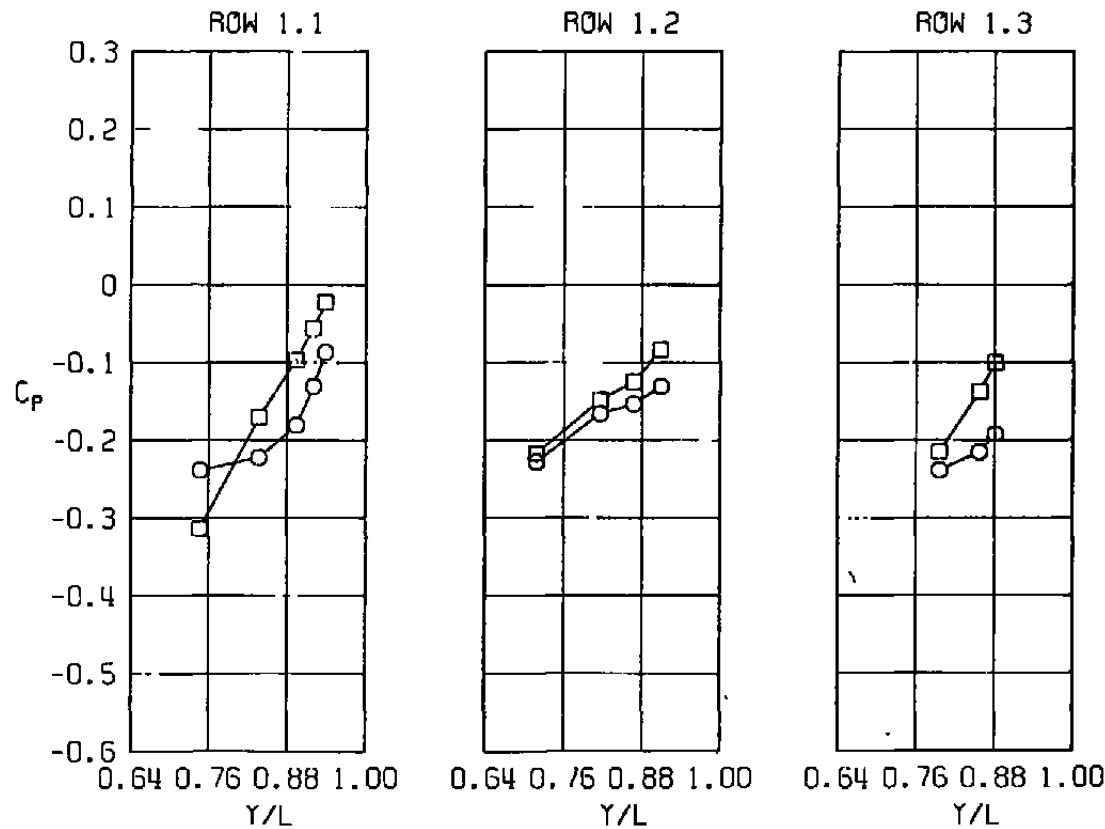
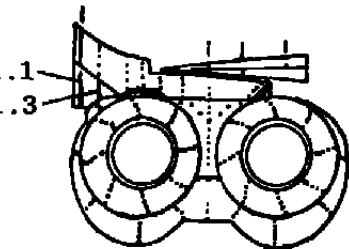
i. Row 9
Figure 34. Continued.

<u>SYM</u>	<u>M</u>	<u>ALPH</u>	<u>NPR</u>	<u>MFR</u>	<u>DELH</u>	<u>Re</u> $\times 10^{-6}$	<u>MODEL</u>	<u>CDNOZ</u>
□	0.85	0.06	2.88	0.423	0.17	2.53	EPES	0.0001
○	0.85	0.06	2.89	0.460	0.17	2.53	EPES	0.0002
△	0.85	0.06	2.88	0.480	0.17	2.53	EPES	0.0002



j. Nozzle base
Figure 34. Concluded.

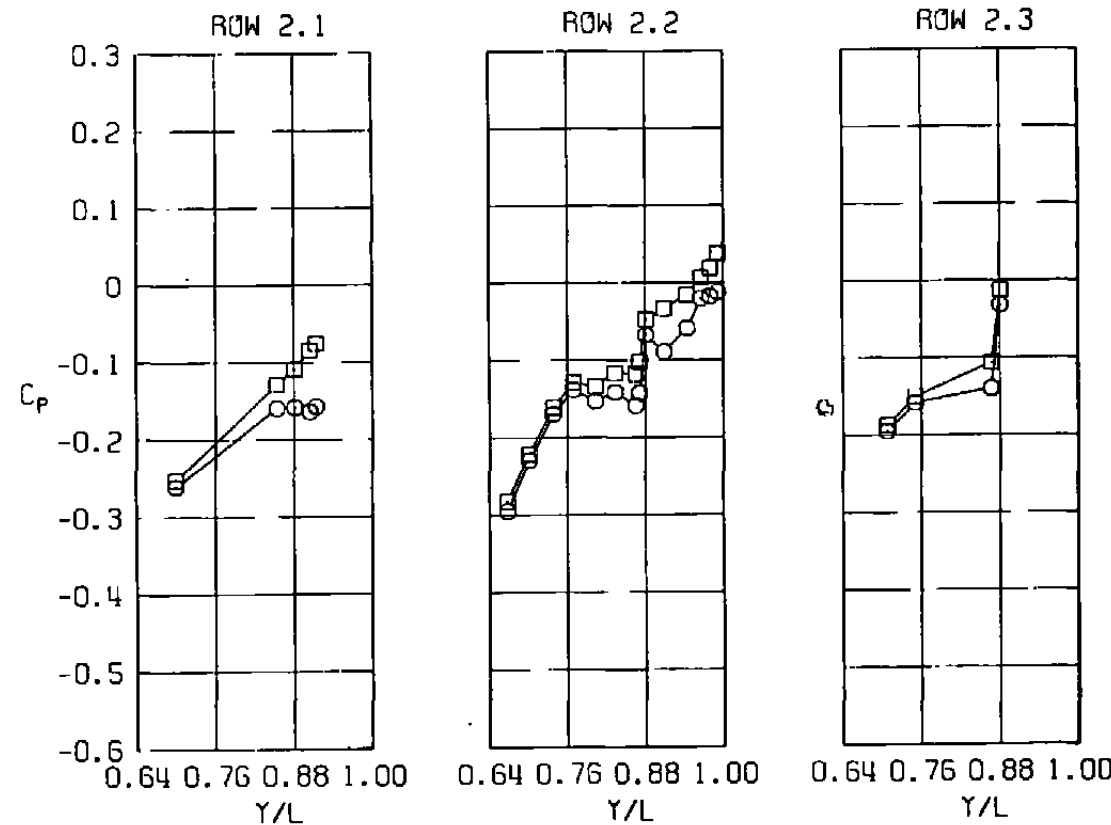
<u>SYM</u>	<u>M</u>	<u>ALPH</u>	<u>NPR</u>	<u>MFR</u>	<u>DElh</u>	<u>Re x 10⁻⁶</u>	<u>MODEL</u>	<u>CDNOZ</u>
□	0.85	0.04	1.96	0.396	0.16	2.53	EPES	0.0001
○	0.85	-0.01	2.00	0.397	0.08	3.61	EPES	0.0004



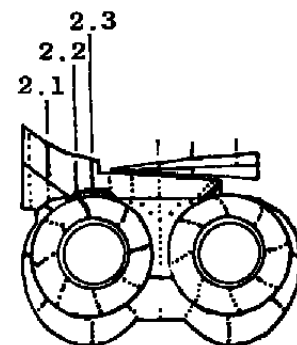
a. Row 1

Figure 35. Effect of Reynolds number on nozzle afterbody pressure distribution, $M = 0.85$, $\alpha = 0$.

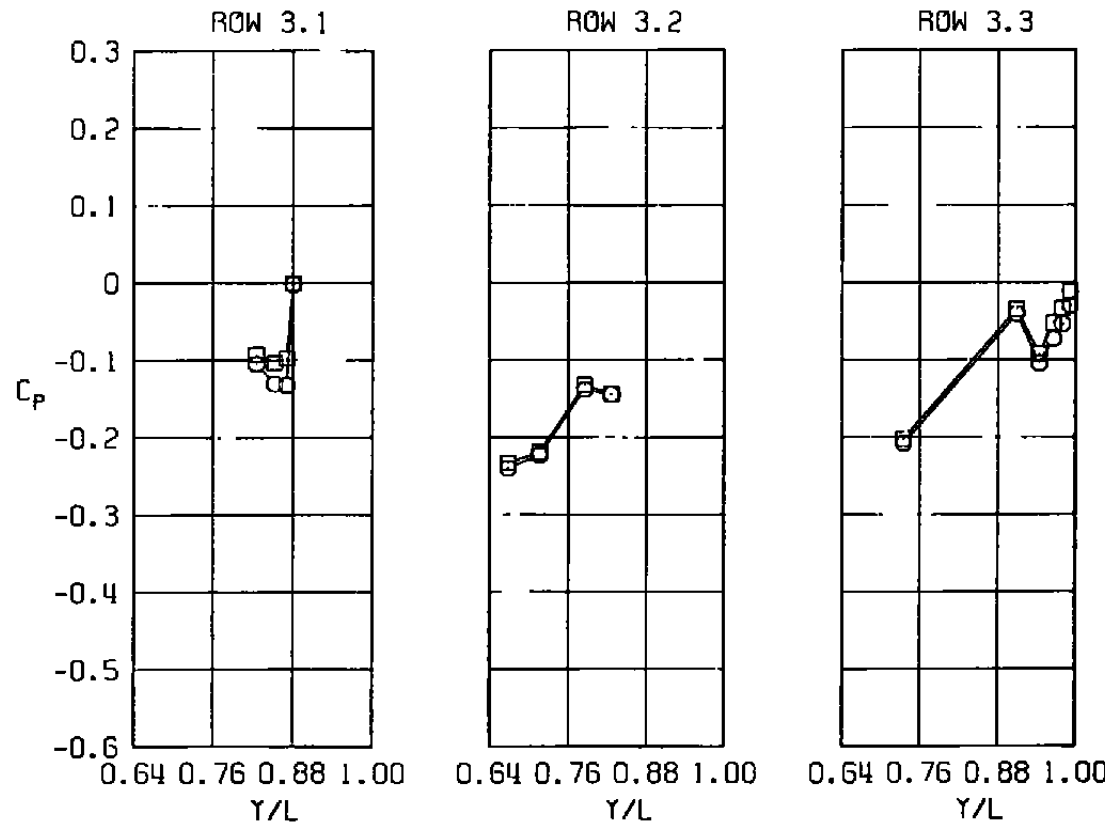
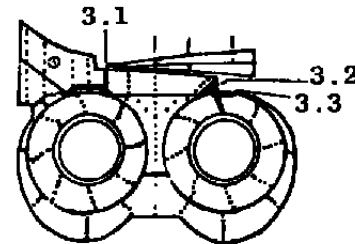
<u>SYM</u>	<u>M.</u>	<u>ALPH</u>	<u>NPR</u>	<u>MFR</u>	<u>DELH</u>	<u>Re x 10⁻⁶</u>	<u>MODEL</u>	<u>CDNOZ</u>
□	0.85	0.04	1.96	0.396	0.16	2.53	EPES	0.0001
○	0.85	-0.01	2.00	0.397	0.08	3.61	EPES	0.0004



b. Row 2
Figure 35. Continued.

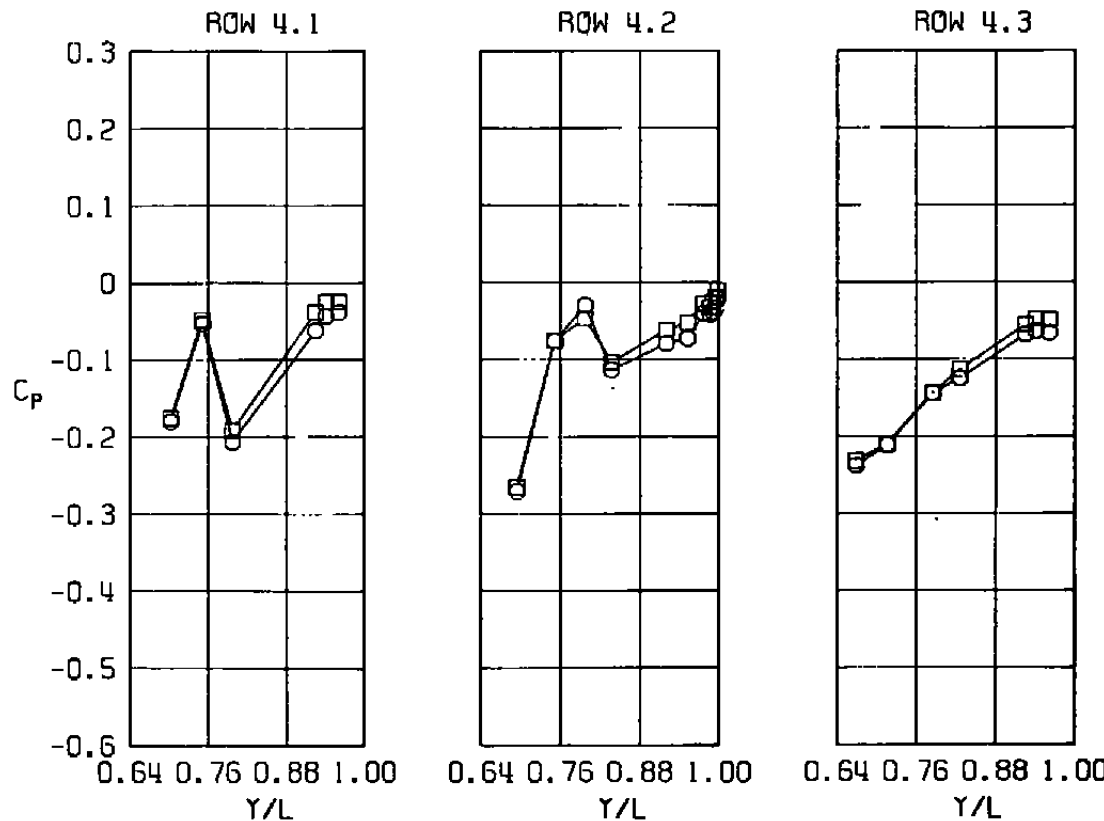
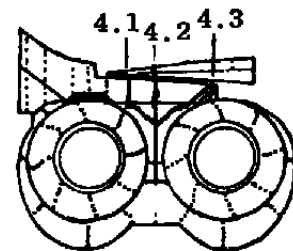


<u>SYM</u>	<u>M</u>	<u>ALPH</u>	<u>NPR</u>	<u>MFR</u>	<u>DELH</u>	<u>Re x 10⁻⁶</u>	<u>MODEL</u>	<u>CDNOZ</u>
□	0.85	0.04	1.96	0.396	0.16	2.53	EPES	0.0001
○	0.85	-0.01	2.00	0.397	0.08	3.61	EPES	0.0004



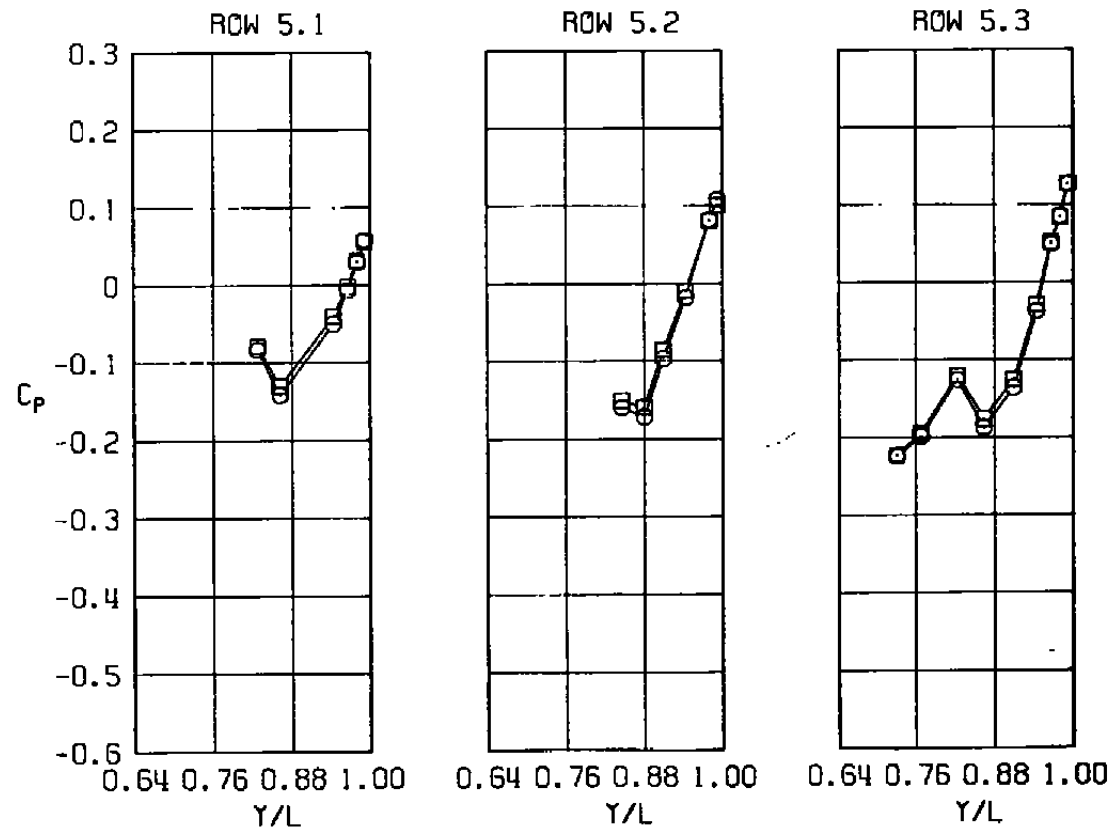
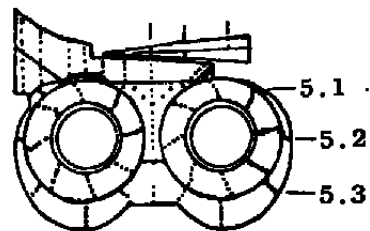
c. Row 3
Figure 35. Continued.

<u>SYM</u>	<u>M</u>	<u>ALPH</u>	<u>NPR</u>	<u>MFR</u>	<u>DELH</u>	<u>Re x 10⁻⁶</u>	<u>MODEL</u>	<u>CDNOZ</u>
□	0.85	0.04	1.96	0.396	0.16	2.53	EPES	0.0001
○	0.85	-0.01	2.00	0.397	0.08	3.61	EPES	0.0004



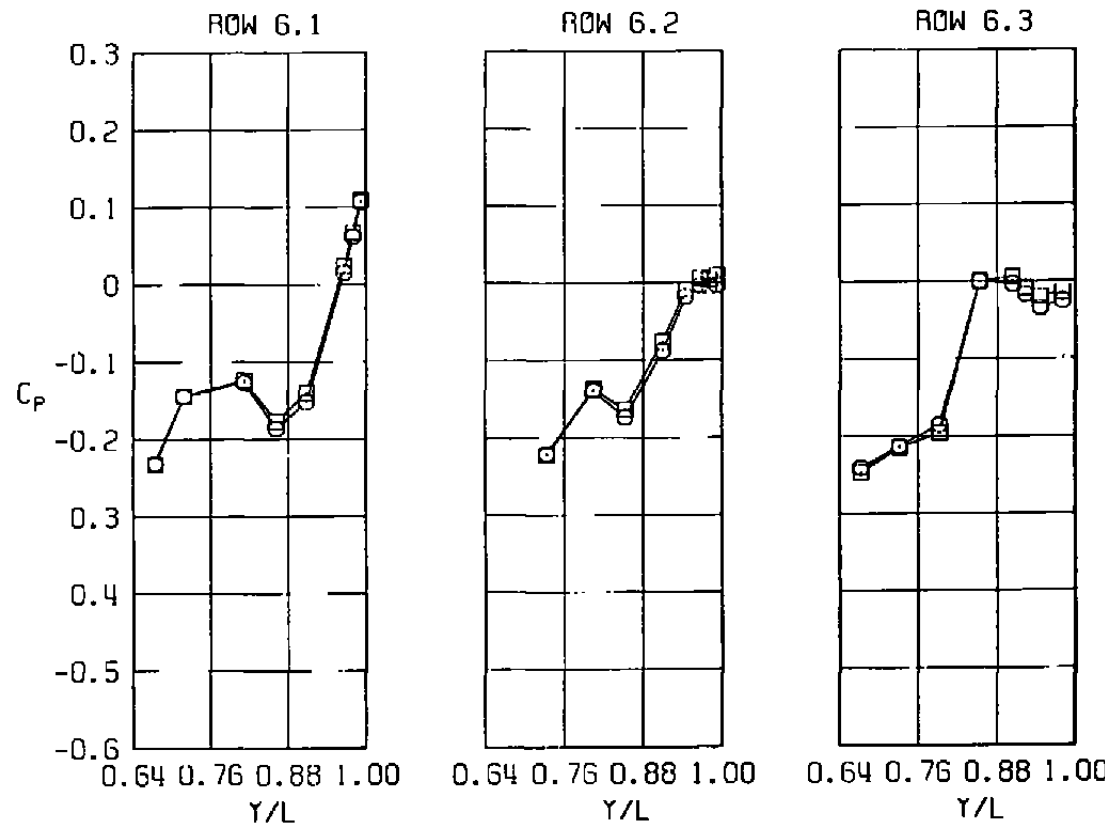
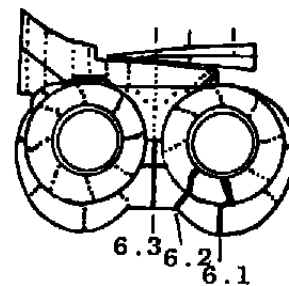
d. Row 4
Figure 35. Continued.

<u>SYM</u>	<u>M</u>	<u>ALPH</u>	<u>NPR</u>	<u>MFR</u>	<u>DELH</u>	<u>Re</u> $\times 10^{-6}$	<u>MODEL</u>	<u>CDNOZ</u>
□	0.85	0.04	1.96	0.396	0.16	2.53	EPES	0.0001
○	0.85	-0.01	2.00	0.397	0.08	3.61	EPES	0.0004



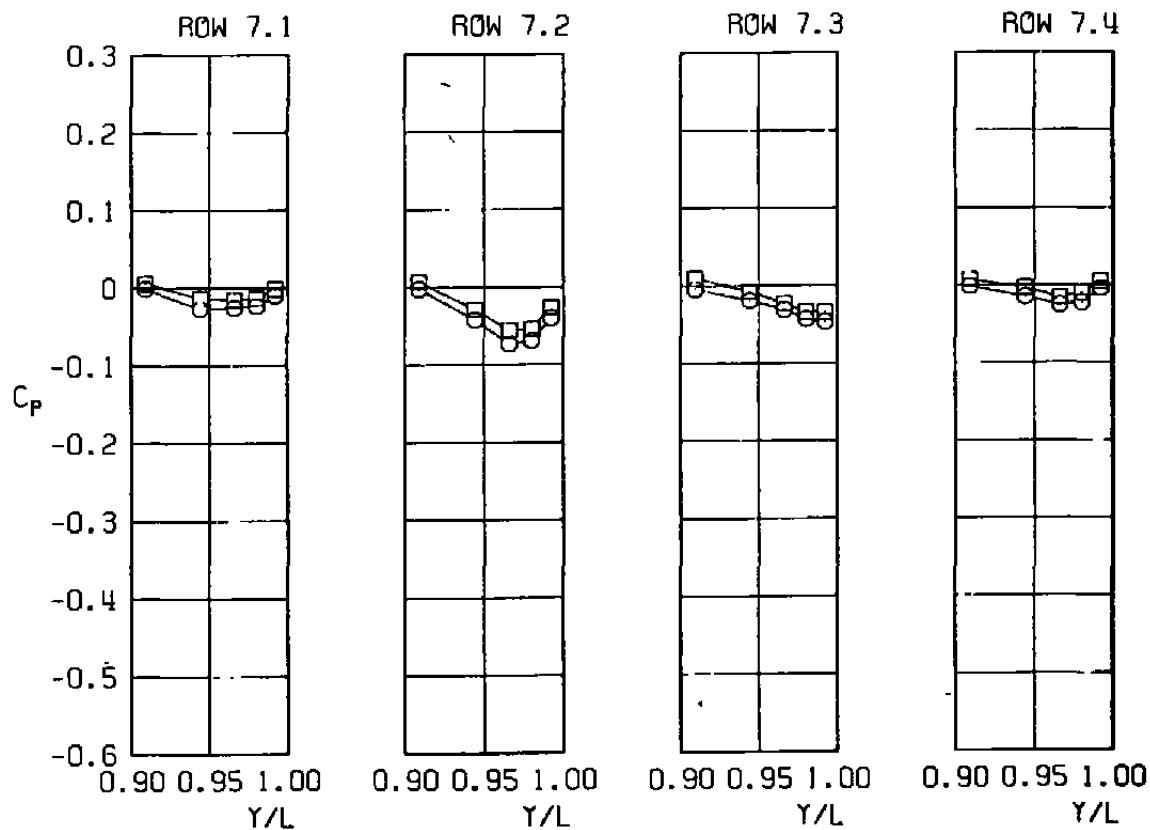
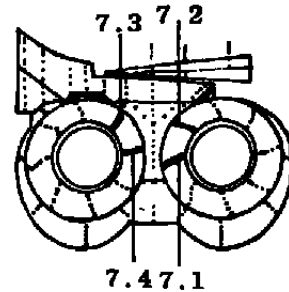
e. Row 5
Figure 35. Continued.

<u>SYM</u>	<u>M</u>	<u>ALPH</u>	<u>NPR</u>	<u>MFR</u>	<u>DELH</u>	<u>Re x 10⁻⁶</u>	<u>MODEL</u>	<u>CDNOZ</u>
□	0.85	0.04	1.96	0.396	0.16	2.53	EPES	0.0001
○	0.85	-0.01	2.00	0.397	0.08	3.61	EPES	0.0004



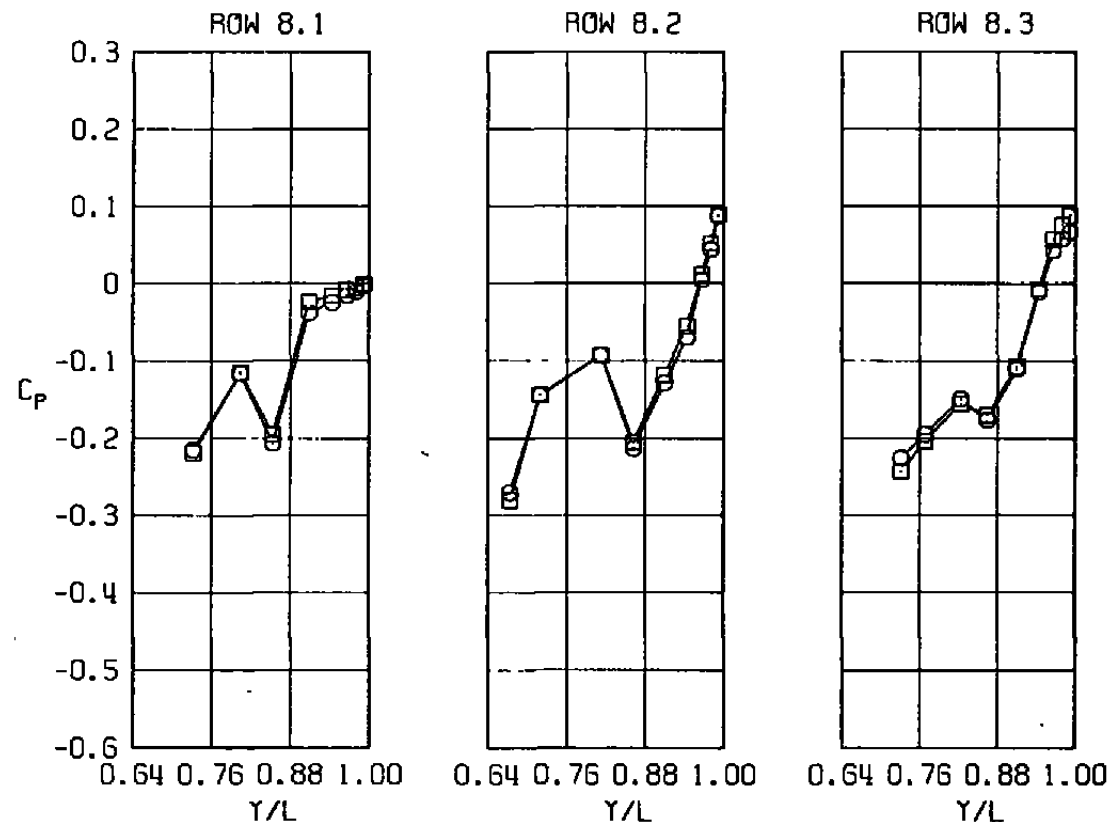
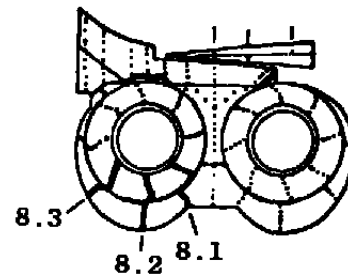
f. Row 6
Figure 35. Continued.

<u>SYM</u>	<u>M</u>	<u>ALPH</u>	<u>NPR</u>	<u>MFR</u>	<u>DELH</u>	<u>Re x 10⁻⁶</u>	<u>MODEL</u>	<u>CDNOZ</u>
□	0.85	0.04	1.96	0.396	0.16	2.53	EPES	0.0001
○	0.85	-0.01	2.00	0.397	0.08	3.61	EPES	0.0004



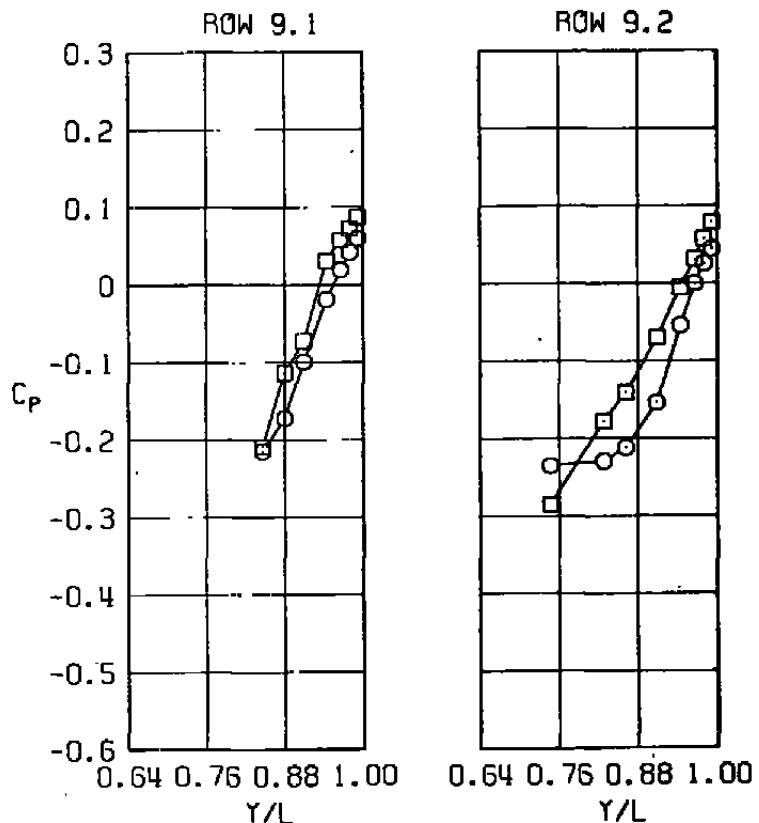
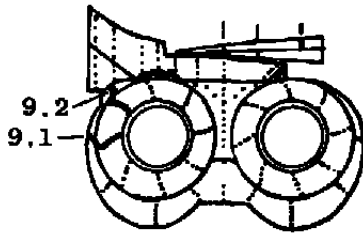
g. Row 7
Figure 35. Continued.

<u>SYM</u>	<u>M</u>	<u>ALPH</u>	<u>NPR</u>	<u>MFR</u>	<u>DELH</u>	<u>Re x 10⁻⁶</u>	<u>MODEL</u>	<u>CDNOZ</u>
□	0.85	0.04	1.96	0.396	0.16	2.53	EPES	0.0001
○	0.85	-0.01	2.00	0.397	0.08	3.61	EPES	0.0004



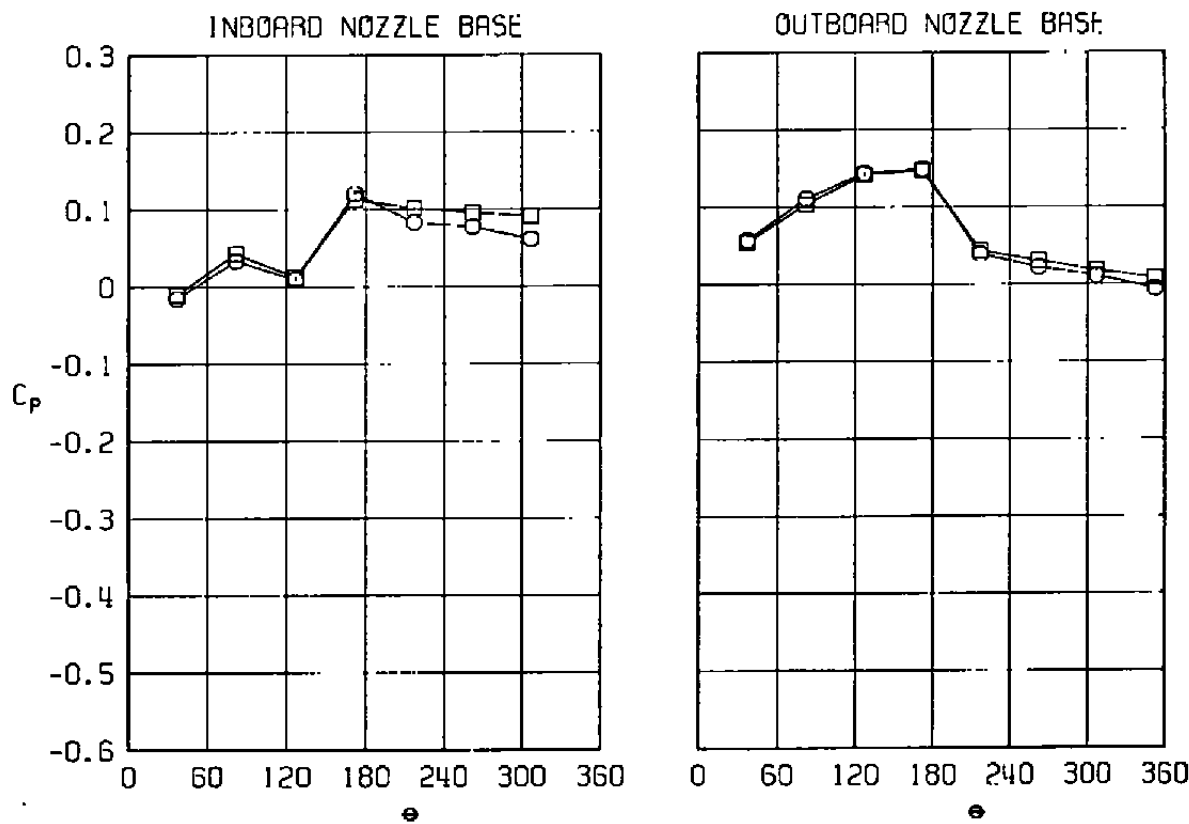
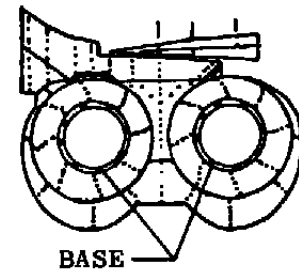
h. Row 8
Figure 35. Continued.

<u>SYM</u>	<u>M</u>	<u>ALPH</u>	<u>NPR</u>	<u>MFR</u>	<u>DELH</u>	<u>Re</u> $\times 10^{-6}$	<u>MODEL</u>	<u>CDNOZ</u>
□	0.85	0.04	1.96	0.396	0.16	2.53	EPES	0.0001
○	0.85	-0.01	2.00	0.397	0.08	3.61	EPES	0.0004



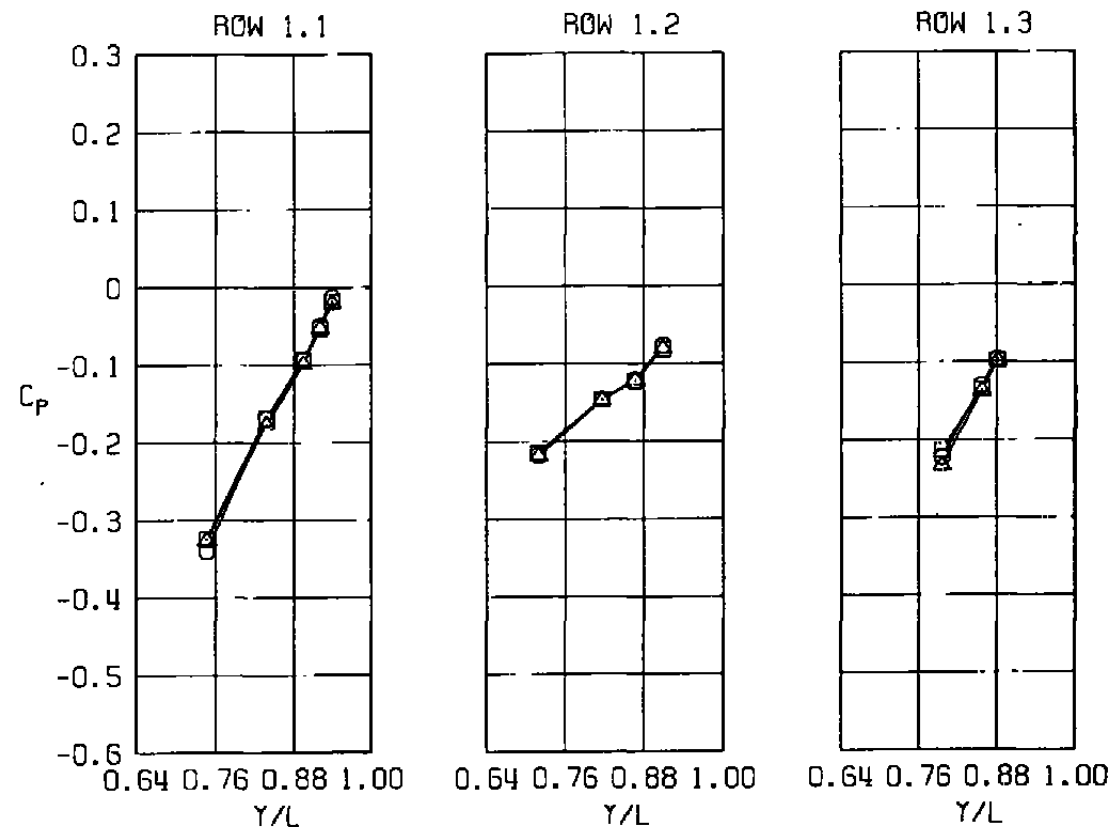
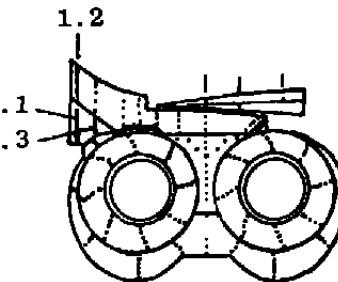
i. Row 9
Figure 35. Continued.

<u>SYM</u>	<u>M</u>	<u>ALPH</u>	<u>NPR</u>	<u>MFR</u>	<u>DELH</u>	<u>Re x 10⁻⁶</u>	<u>MODEL</u>	<u>CDNOZ</u>
□	0.85	0.04	1.96	0.396	0.16	2.53	EPES	0.0001
○	0.85	-0.01	2.00	0.397	0.08	3.61	EPES	0.0004



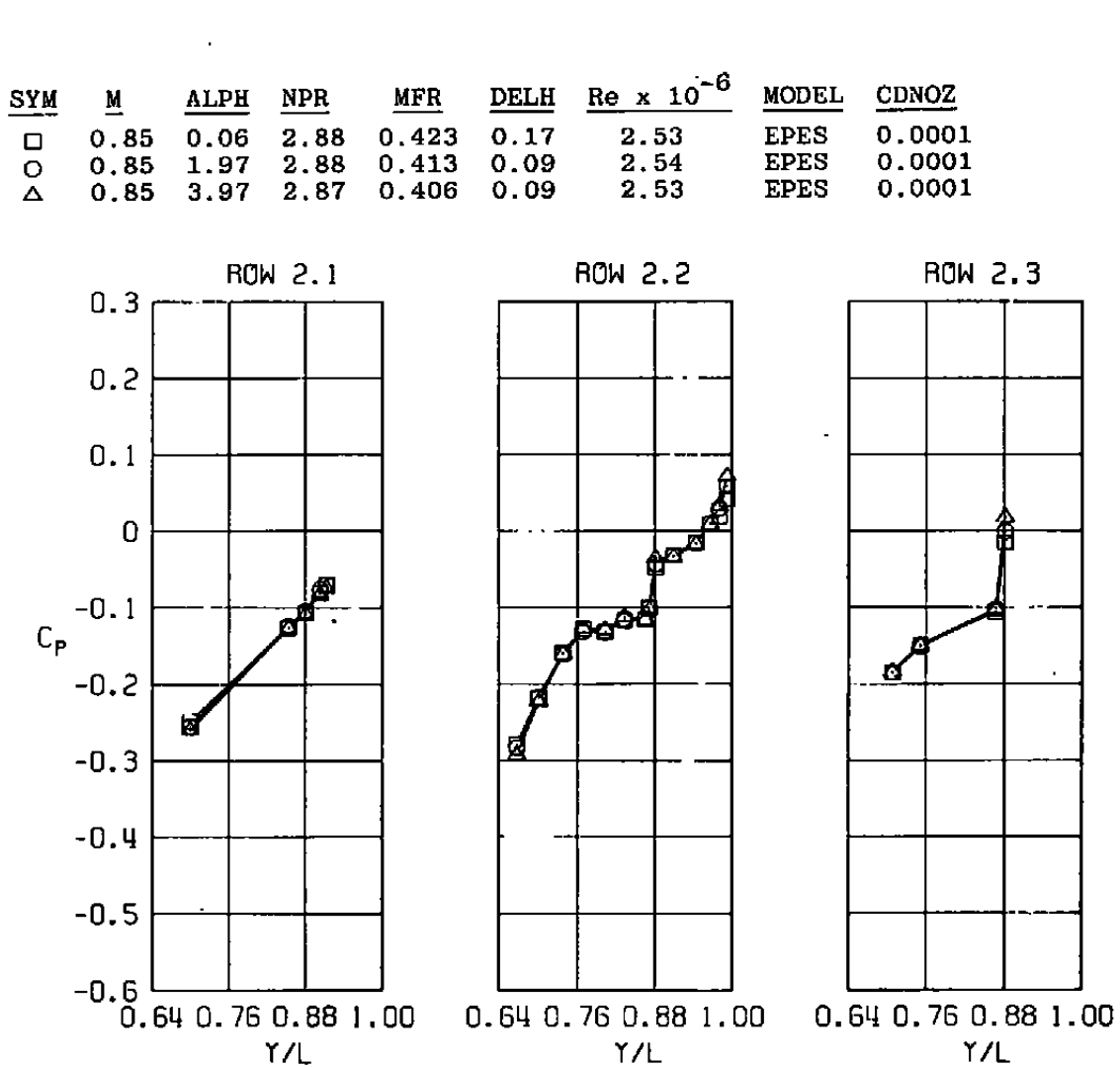
j. Nozzle base
Figure 35. Concluded.

<u>SYM</u>	<u>M</u>	<u>ALPH</u>	<u>NPR</u>	<u>MFR</u>	<u>DElh</u>	<u>Re x 10⁻⁶</u>	<u>MODEL</u>	<u>CDNOZ</u>
□	0.85	0.06	2.88	0.423	0.17	2.53	EPES	0.0001
○	0.85	1.97	2.88	0.413	0.09	2.54	EPES	0.0001
△	0.85	3.97	2.87	0.406	0.09	2.53	EPES	0.0001

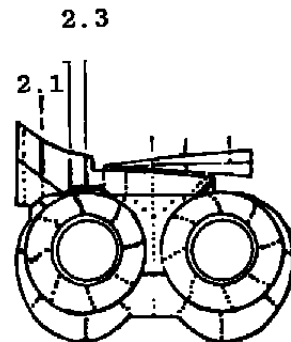


a. Row 1

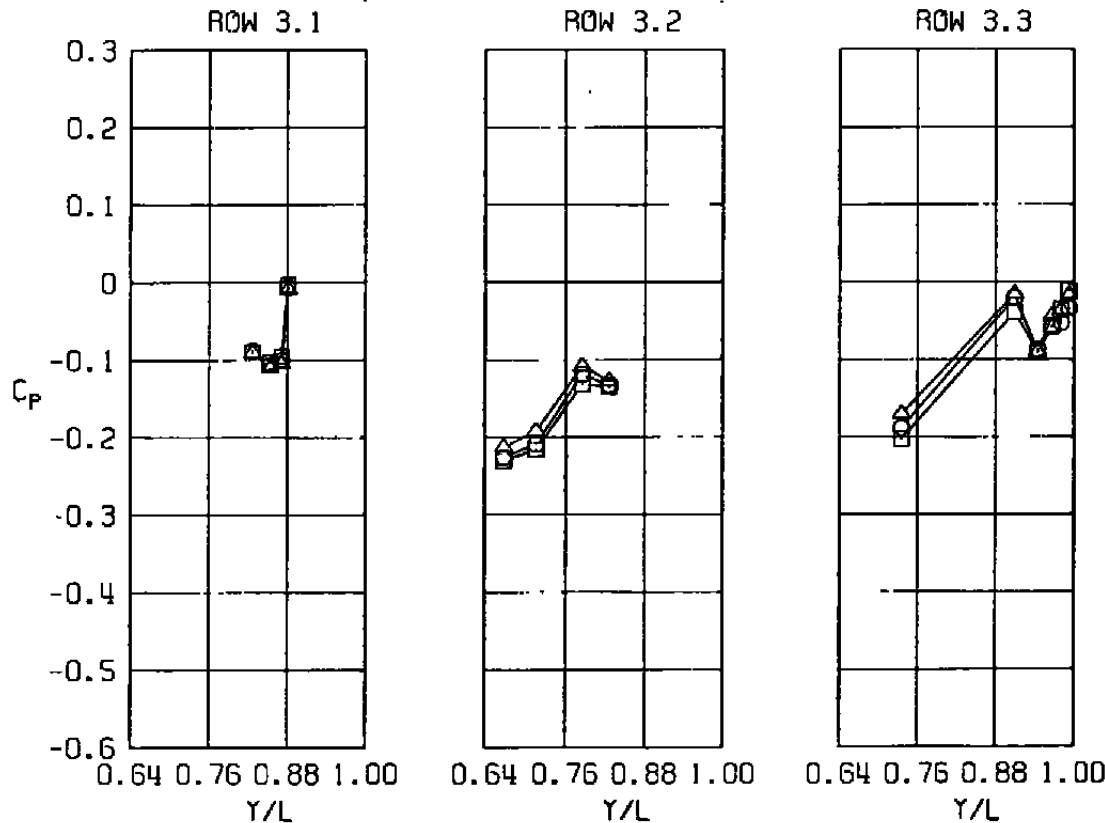
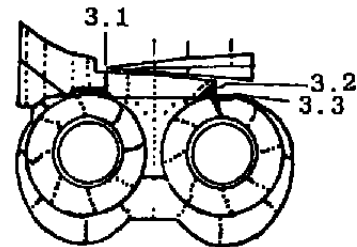
Figure 36. Effect of angle of attack on nozzle afterbody pressure distributions, $M = 0.85$.



b. Row 2
Figure 36. Continued.

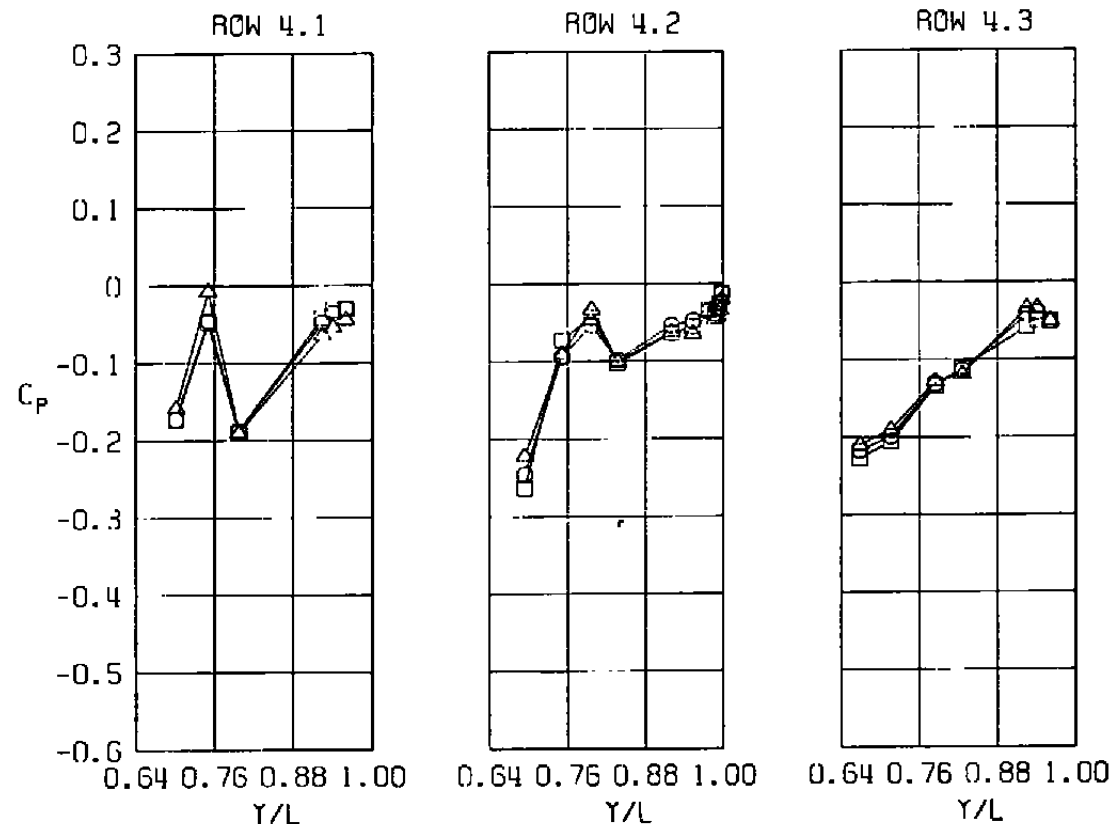
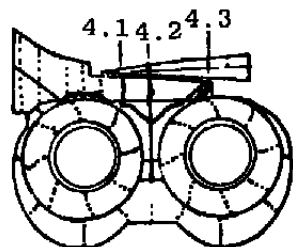


<u>SYM</u>	<u>M</u>	<u>ALPH</u>	<u>NPR</u>	<u>MFR</u>	<u>DELH</u>	<u>Re x 10⁻⁶</u>	<u>MODEL</u>	<u>CDNOZ</u>
□	0.85	0.06	2.88	0.423	0.17	2.53	EPES	0.0001
○	0.85	1.97	2.88	0.413	0.09	2.54	EPES	0.0001
△	0.85	3.97	2.87	0.406	0.09	2.53	EPES	0.0001



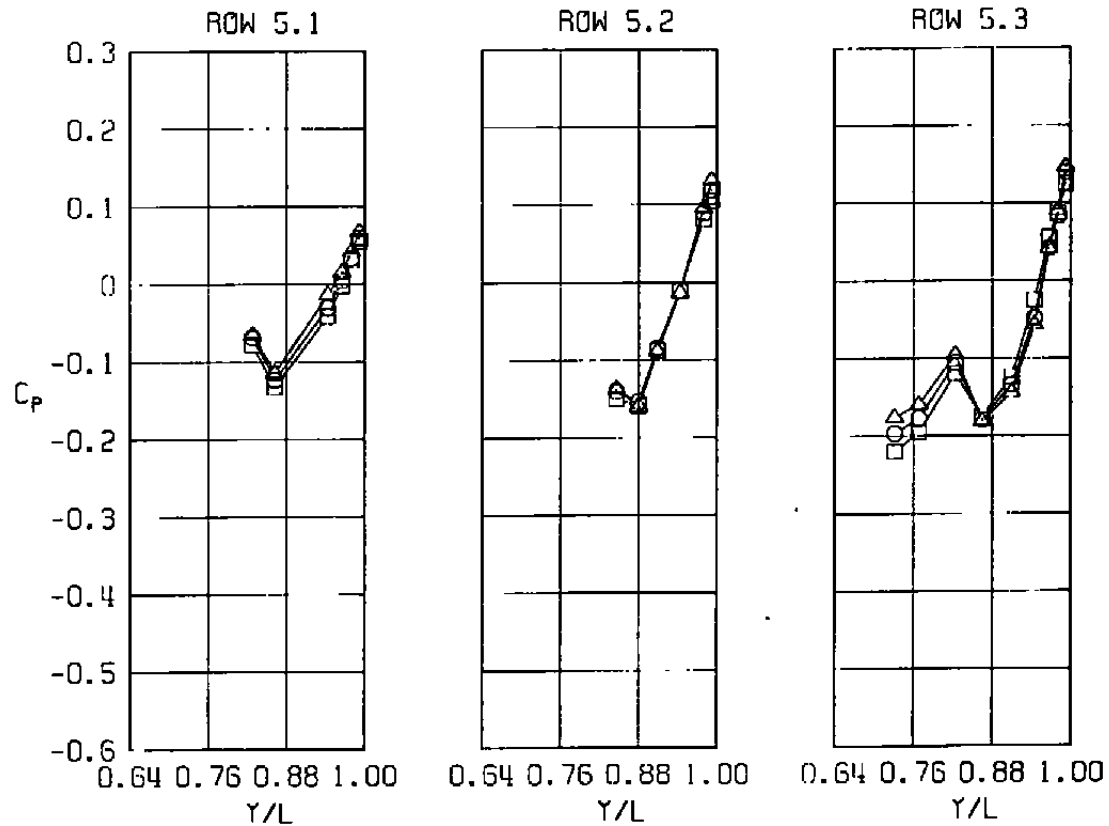
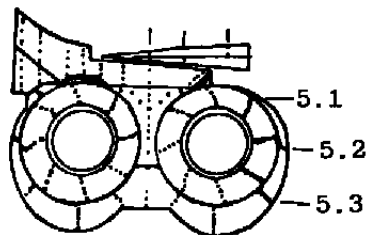
c. Row 3
Figure 36. Continued.

<u>SYM</u>	<u>M</u>	<u>ALPH</u>	<u>NPR</u>	<u>MFR</u>	<u>DElh</u>	<u>Re x 10⁻⁶</u>	<u>MODEL</u>	<u>CDNOZ</u>
□	0.85	0.06	2.88	0.423	0.17	2.53	EPES	0.0001
○	0.85	1.97	2.88	0.413	0.09	2.54	EPES	0.0001
△	0.85	3.97	2.87	0.406	0.09	2.53	EPES	0.0001



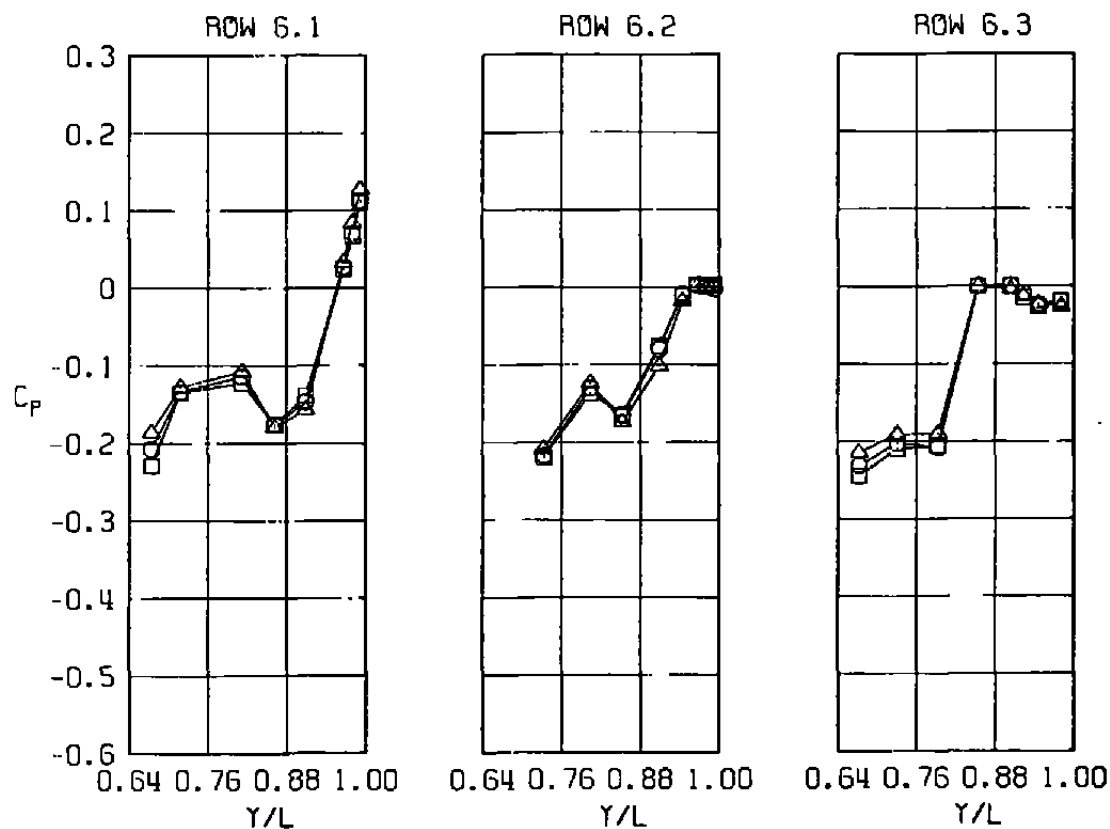
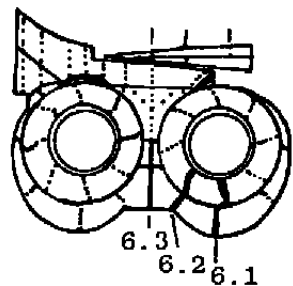
d. Row 4
Figure 36. Continued.

<u>SYM</u>	<u>M</u>	<u>ALPH</u>	<u>NPR</u>	<u>MFR</u>	<u>DElh</u>	<u>Re x 10⁻⁶</u>	<u>MODEL</u>	<u>CDNOZ</u>
□	0.85	0.06	2.88	0.423	0.17	2.53	EPES	0.0001
○	0.85	1.97	2.88	0.413	0.09	2.54	EPES	0.0001
△	0.85	3.97	2.87	0.406	0.09	2.53	EPES	0.0001

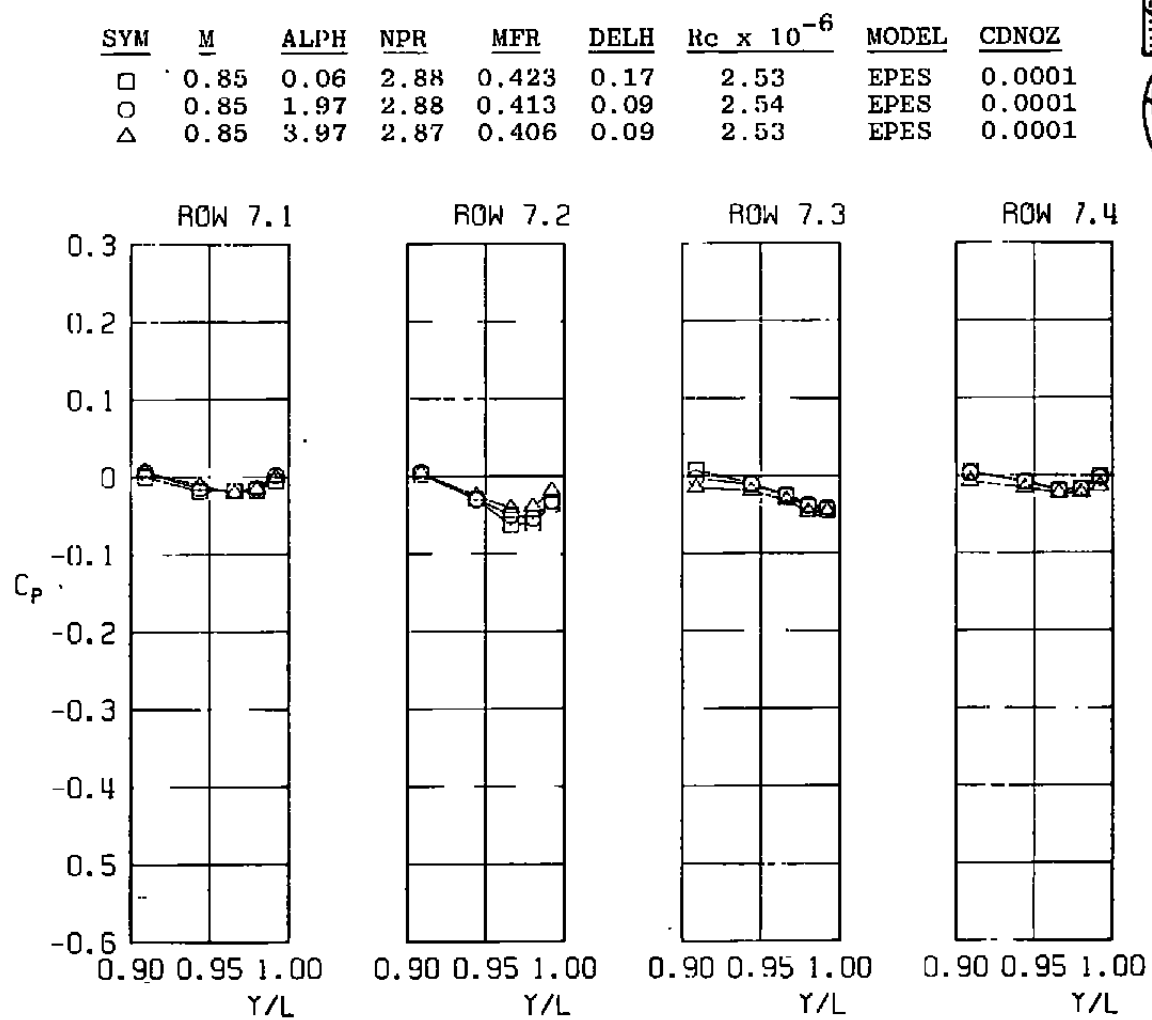


e. Row 5
Figure 36. Continued.

<u>SYM</u>	<u>M</u>	<u>ALPH</u>	<u>NPR</u>	<u>MFR</u>	<u>DELI</u>	<u>Re x 10⁻⁶</u>	<u>MODEL</u>	<u>CDNOZ</u>
□	0.85	0.06	2.88	0.423	0.17	2.53	EPES	0.0001
○	0.85	1.97	2.88	0.413	0.09	2.54	EPES	0.0001
△	0.85	3.97	2.87	0.406	0.09	2.53	EPES	0.0001

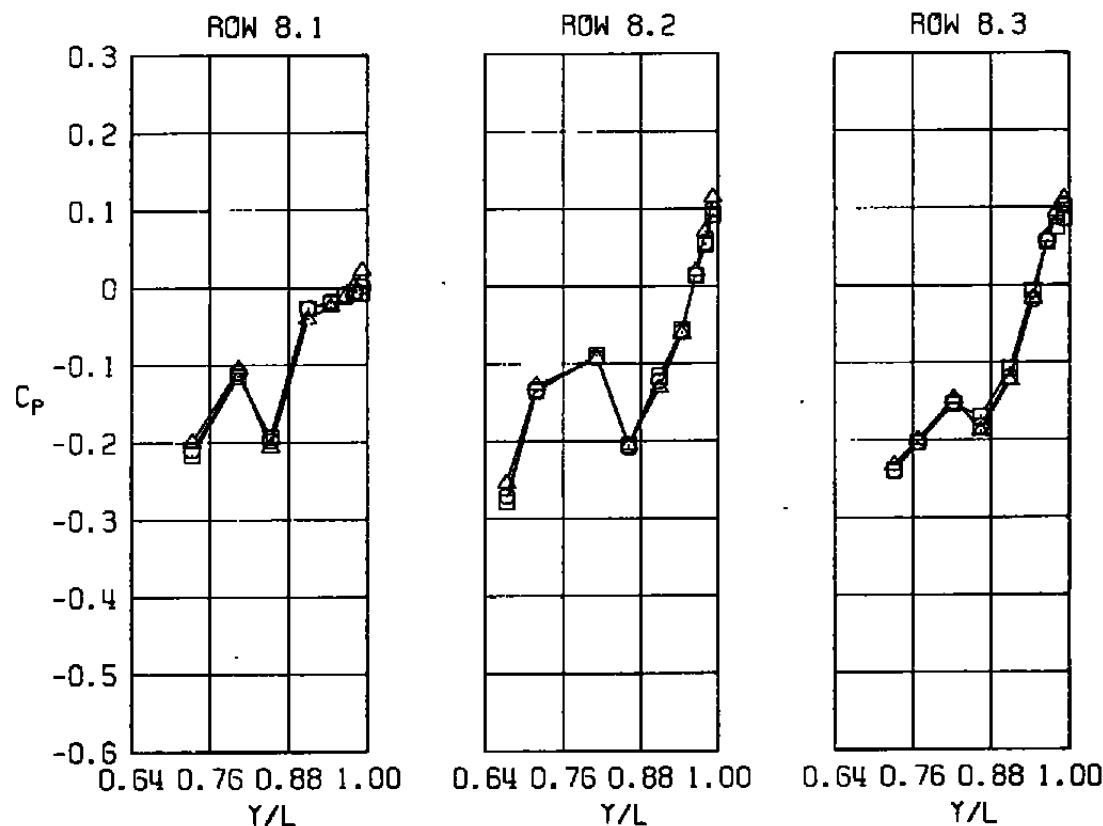
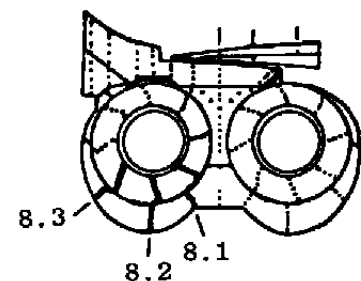


f. Row 6
Figure 36. Continued.



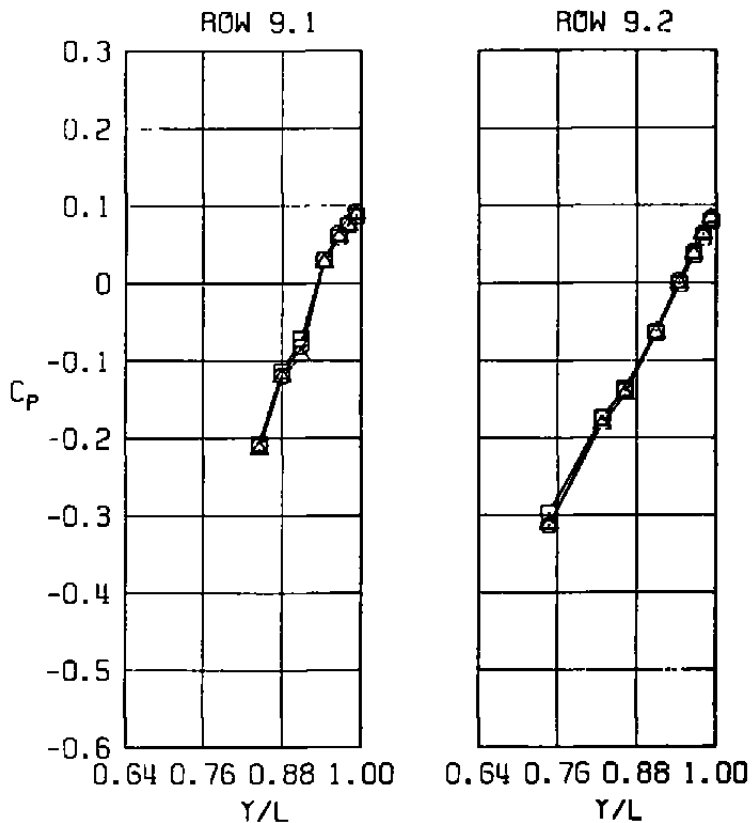
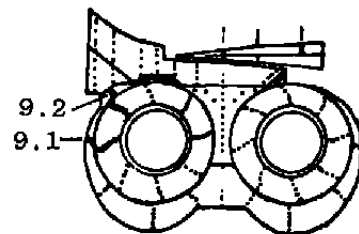
g. Row 7
Figure 36. Continued.

<u>SYM</u>	<u>M</u>	<u>ALPH</u>	<u>NPR</u>	<u>MFR</u>	<u>DELI</u>	<u>Re x 10⁻⁶</u>	<u>MODEL</u>	<u>CDNOZ</u>
□	0.85	0.06	2.88	0.423	0.17	2.53	EPES	0.0001
○	0.85	1.97	2.88	0.413	0.09	2.54	EPES	0.0001
△	0.85	3.97	2.87	0.406	0.09	2.53	EPES	0.0001



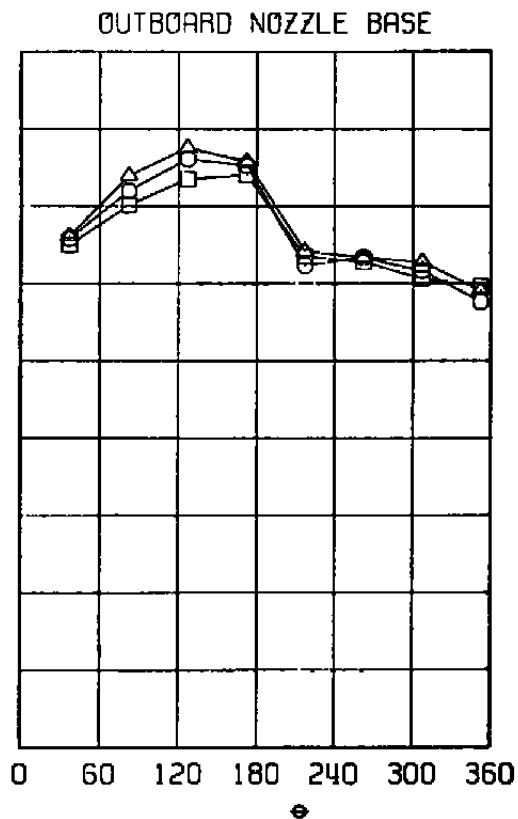
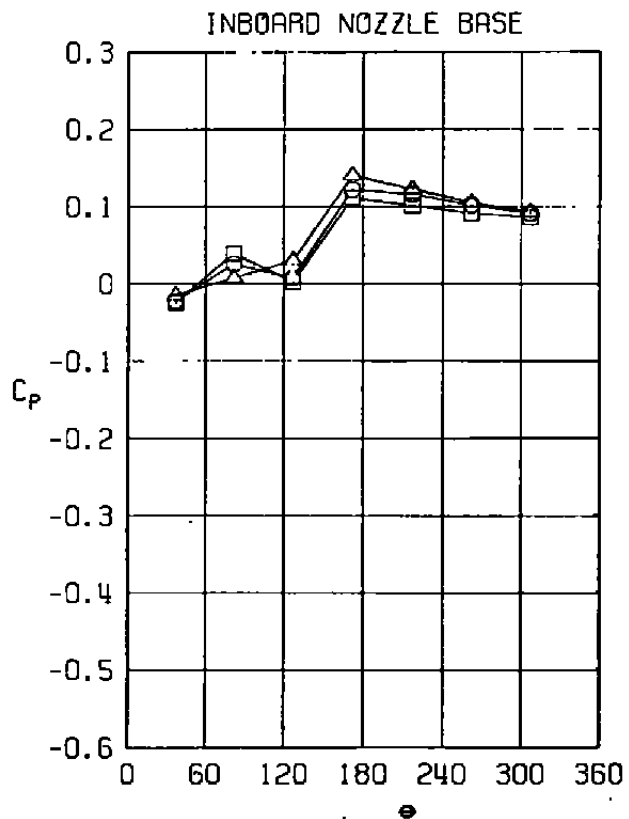
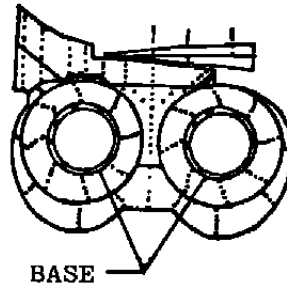
h. Row 8
Figure 36. Continued.

<u>SYM</u>	<u>M</u>	<u>AT.PH</u>	<u>NPR</u>	<u>MFR</u>	<u>DELH</u>	<u>Re x 10⁻⁶</u>	<u>MODEL</u>	<u>CDNOZ</u>
□	0.85	0.06	2.88	0.423	0.17	2.53	EPES	0.0001
○	0.85	1.97	2.88	0.413	0.09	2.54	EPES	0.0001
△	0.85	3.97	2.87	0.406	0.09	2.53	EPES	0.0001



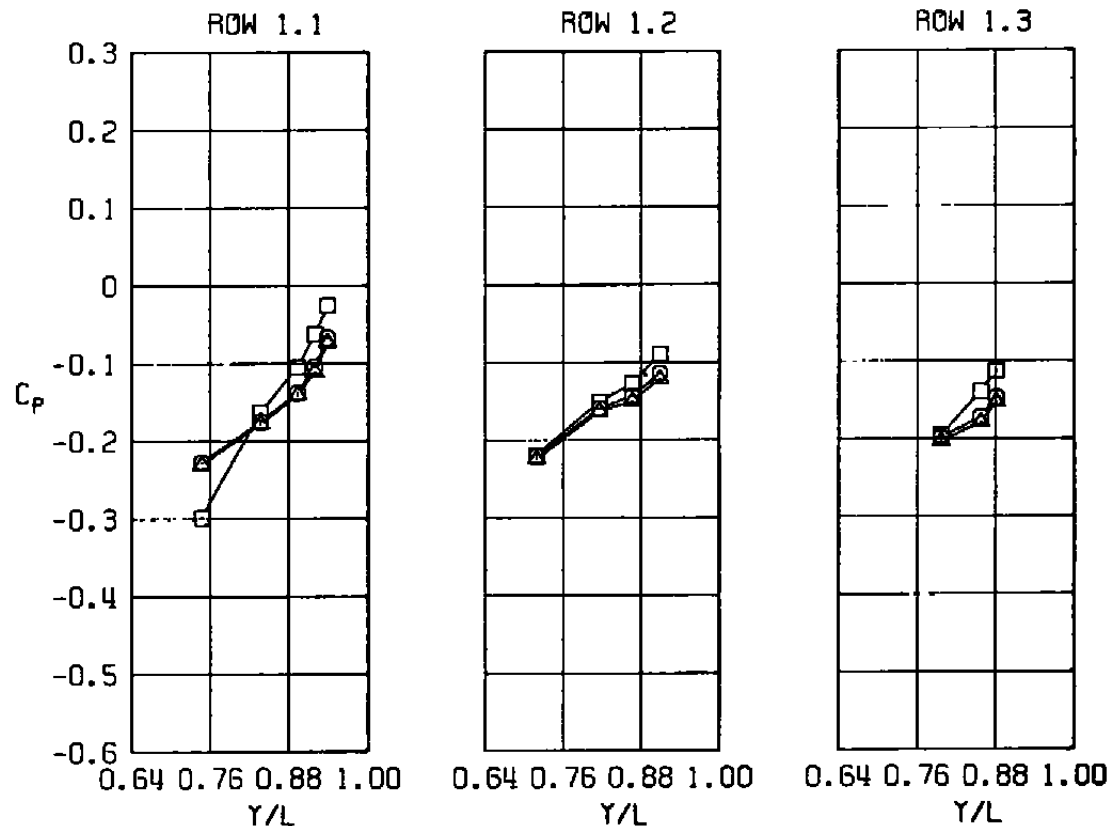
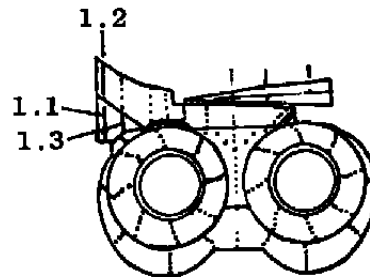
i. Row 9
Figure 36. Continued.

SYM	M	AJ.PH	NPR	MFR	DELI	$Re \times 10^{-6}$	MODEL	CDNOZ
□	0.85	0.06	2.88	0.423	0.17	2.53	EPES	0.0001
○	0.85	1.97	2.88	0.413	0.09	2.54	EPES	0.0001
△	0.85	3.97	2.87	0.406	0.09	2.53	EPES	0.0001



j. Nozzle base
Figure 36. Concluded.

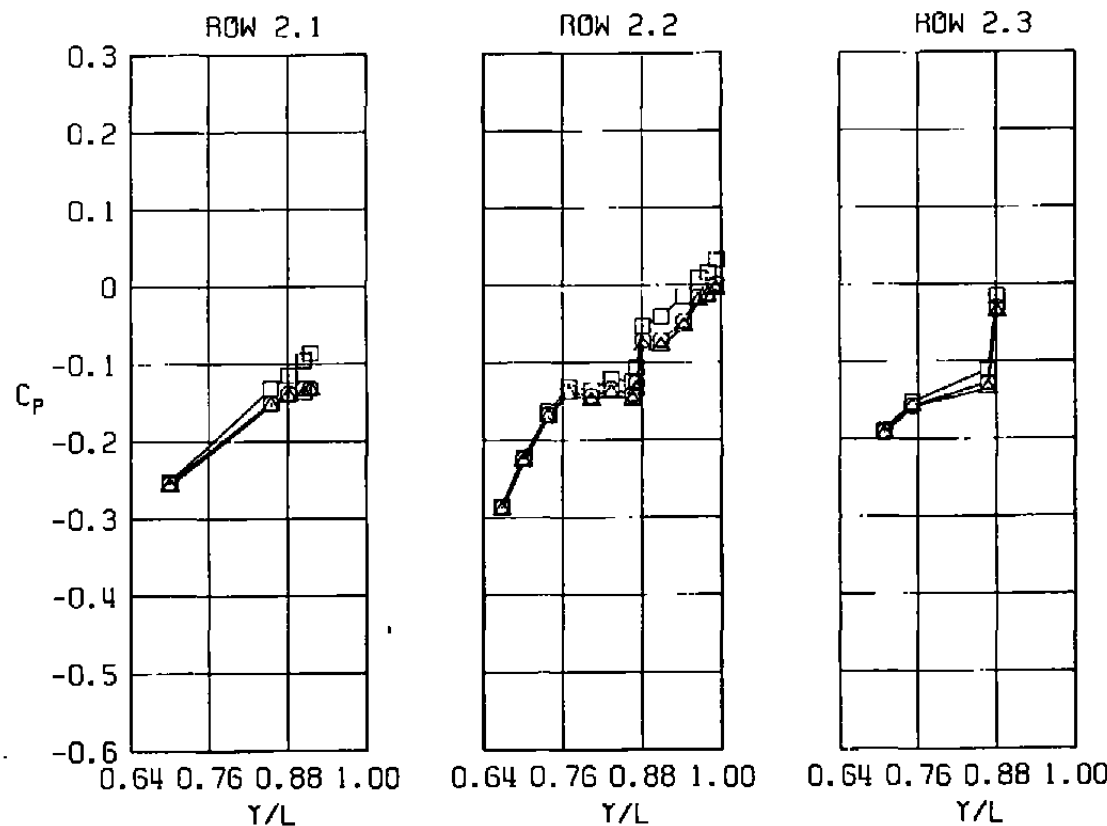
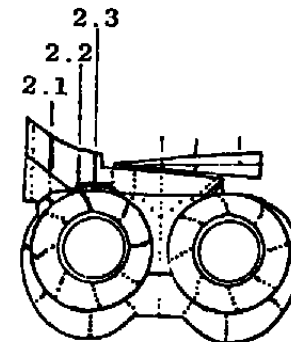
<u>SYM</u>	<u>M</u>	<u>ALPH</u>	<u>NPR</u>	<u>MFR</u>	<u>DElh</u>	<u>Re x 10⁻⁶</u>	<u>MODEL</u>	<u>CDNOZ</u>
□	0.85	0.01	1.55	0.396	0.09	2.50	EPES	0
○	0.85	0.02	2.70	0.449	0.17	2.50	EPES	0.0005
△	0.85	0.02	4.22	0.452	0.16	2.50	EPES	0.0007



a. Row 1

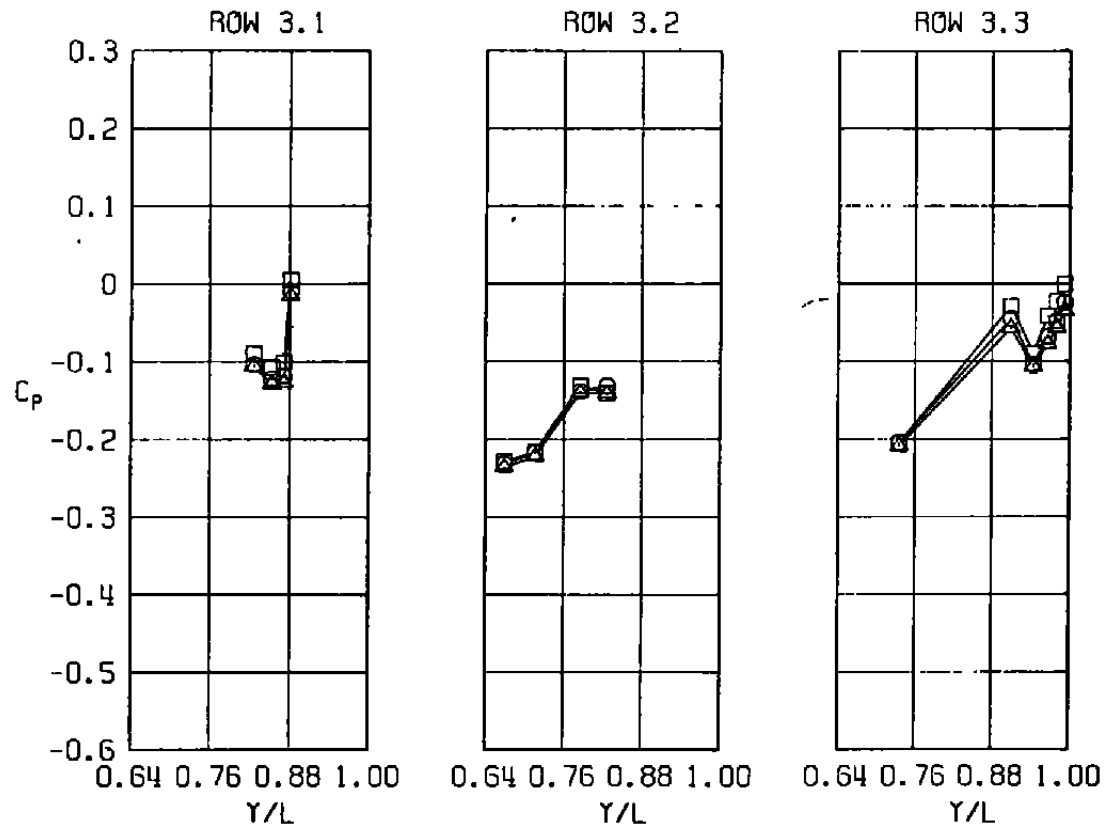
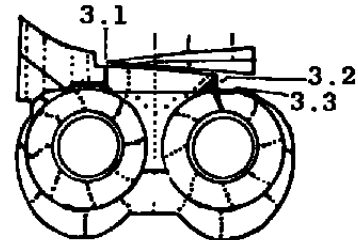
Figure 37. Effect of nozzle pressure ratio on nozzle afterbody pressure distribution, $M = 0.85, \alpha = 0$.

<u>SYM</u>	<u>M</u>	<u>ALPH</u>	<u>NPR</u>	<u>MFR</u>	<u>DELT</u>	<u>Re x 10⁻⁶</u>	<u>MODEL</u>	<u>CDNOZ</u>
□	0.85	0.01	1.55	0.396	0.09	2.50	EPES	0
○	0.85	0.02	2.70	0.449	0.17	2.50	EPES	0.0005
△	0.85	0.02	4.22	0.452	0.16	2.50	EPES	0.0007



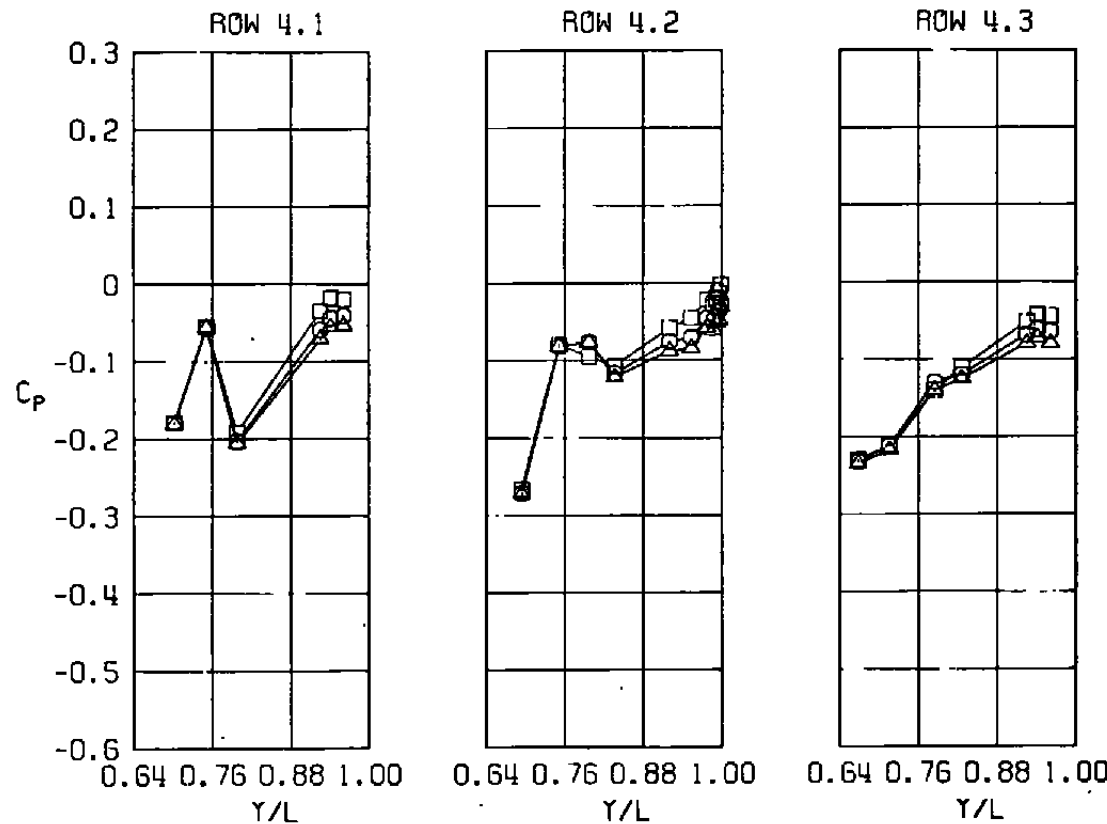
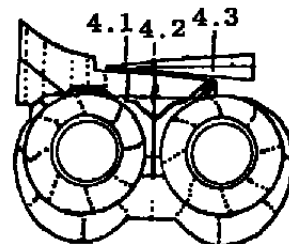
b. Row 2
Figure 37. Continued.

<u>SYM</u>	<u>M</u>	<u>ALPH</u>	<u>NPR</u>	<u>MFR</u>	<u>DELH</u>	<u>Re x 10⁻⁶</u>	<u>MODEL</u>	<u>CDNOZ</u>
□	0.85	0.01	1.55	0.396	0.09	2.50	EPES	0
○	0.85	0.02	2.70	0.449	0.17	2.50	EPES	0.0005
△	0.85	0.02	4.22	0.452	0.16	2.50	EPES	0.0007



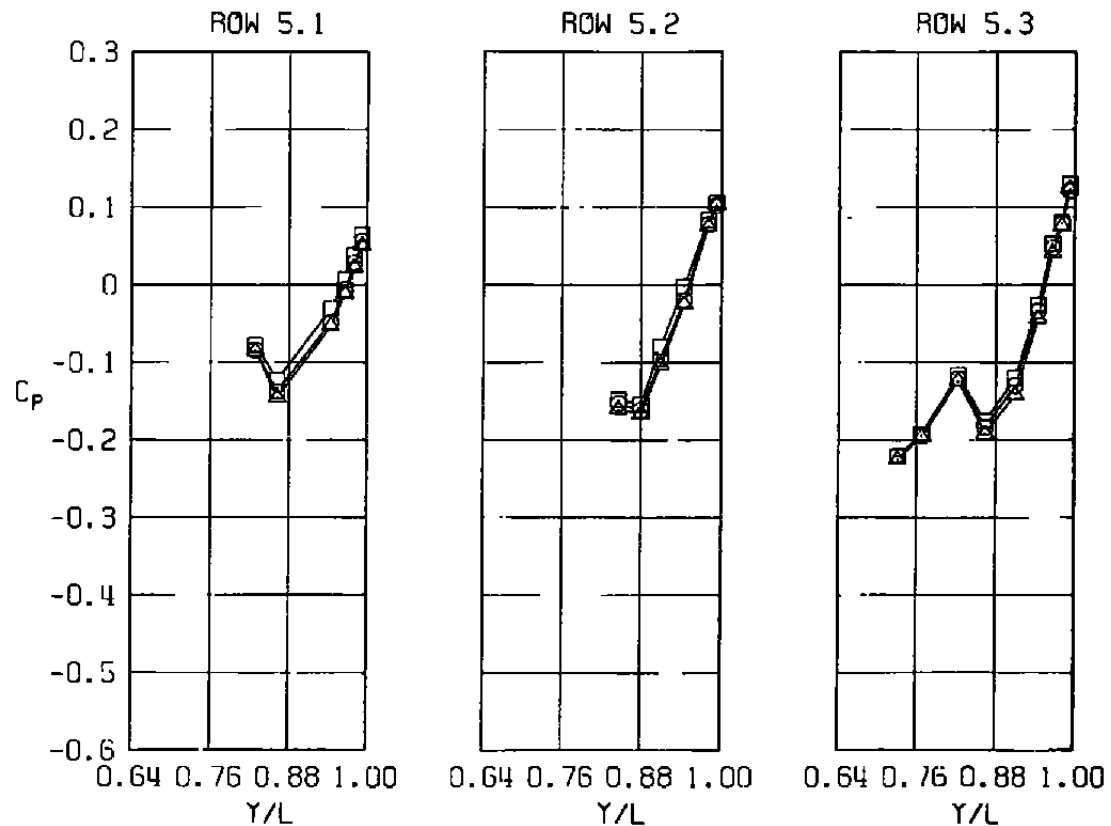
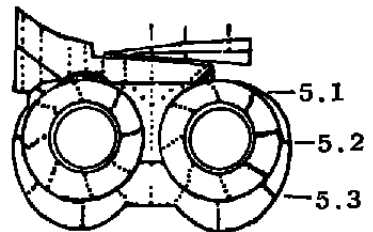
c. Row 3
Figure 37. Continued.

<u>SYM</u>	<u>M</u>	<u>ALPH</u>	<u>NPR</u>	<u>MFR</u>	<u>DELH</u>	<u>Re x 10⁻⁶</u>	<u>MODEL</u>	<u>CDNOZ</u>
□	0.85	0.01	1.55	0.396	0.09	2.50	EPES	0
○	0.85	0.02	2.70	0.449	0.17	2.50	EPES	0.0005
△	0.85	0.02	4.22	0.452	0.16	2.50	EPES	0.0007



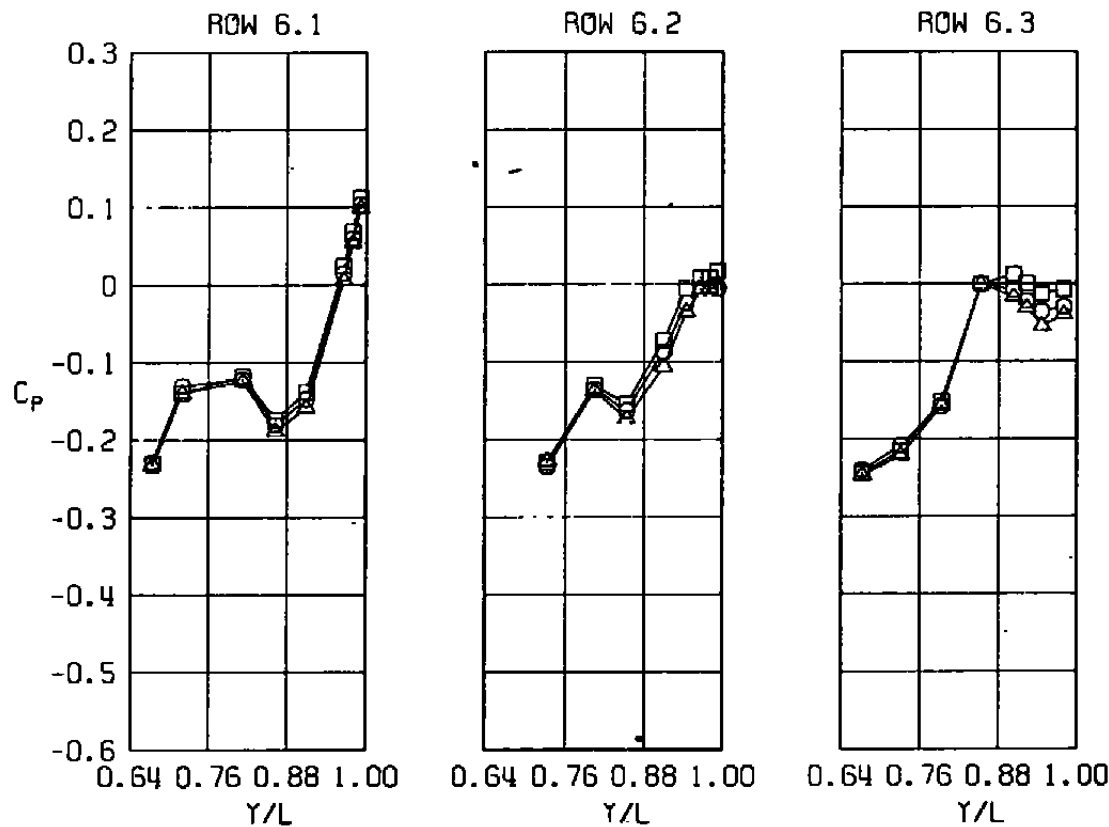
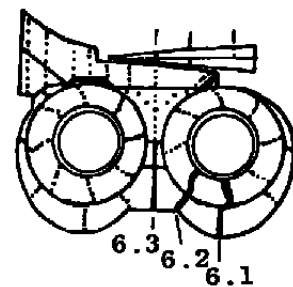
d. Row 4
Figure 37. Continued.

<u>SYM</u>	<u>M</u>	<u>ALPH</u>	<u>NPR</u>	<u>MFR</u>	<u>DELH</u>	<u>Re x 10⁻⁶</u>	<u>MODEL</u>	<u>CDNOZ</u>
□	0.85	0.01	1.55	0.396	0.09	2.50	EPES	0
○	0.85	0.02	2.70	0.449	0.17	2.50	EPES	0.0005
△	0.85	0.02	4.22	0.452	0.16	2.50	EPES	0.0007

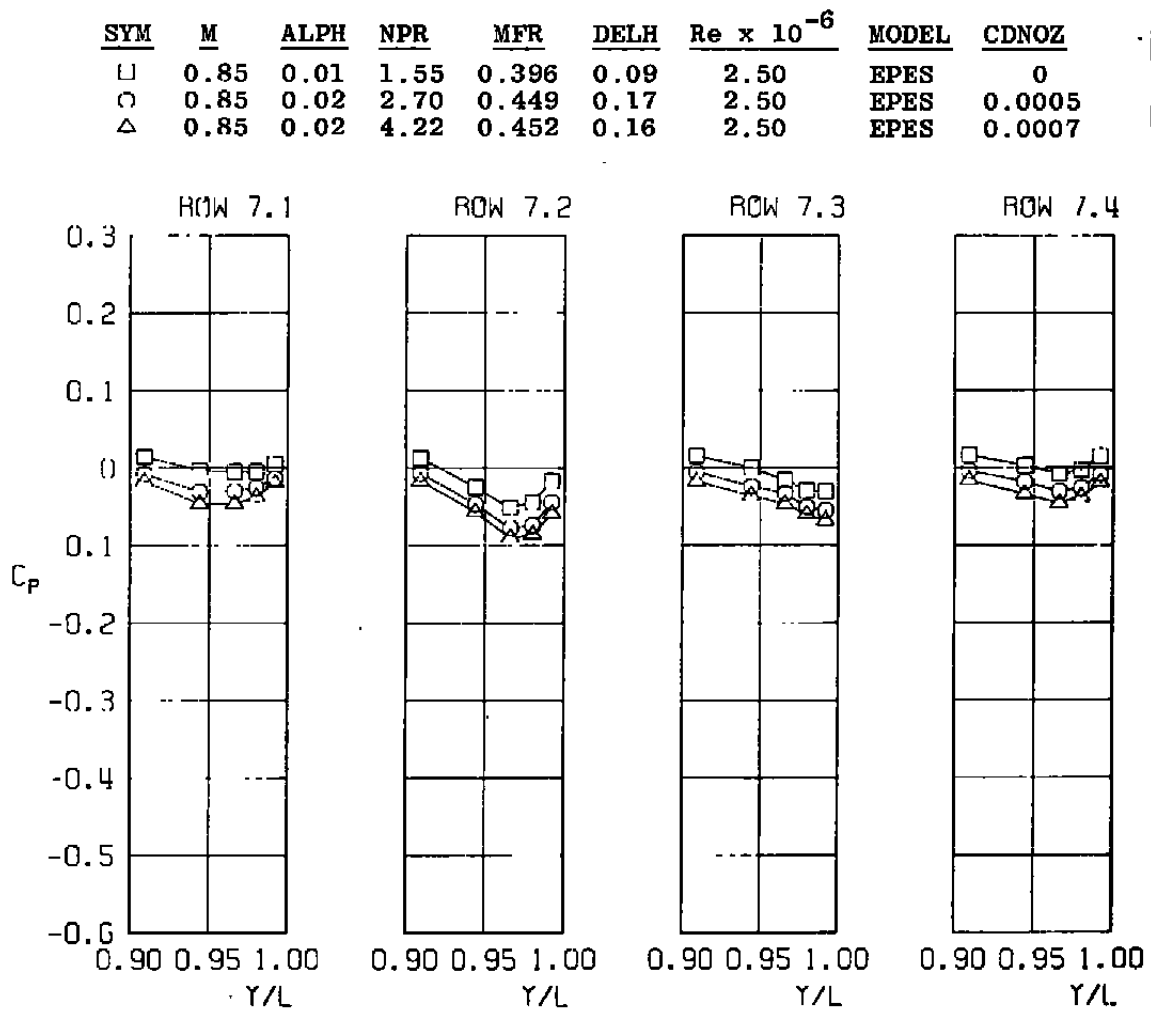


e. Row 5
Figure 37. Continued.

<u>SYM</u>	<u>M</u>	<u>ALPH</u>	<u>NPR</u>	<u>MFR</u>	<u>DElh</u>	<u>Re x 10⁻⁶</u>	<u>MODEL</u>	<u>CDNOZ</u>
□	0.85	0.01	1.55	0.396	0.09	2.50	EPES	0
○	0.85	0.02	2.70	0.449	0.17	2.50	EPES	0.0005
△	0.85	0.02	4.22	0.452	0.16	2.50	EPES	0.0007

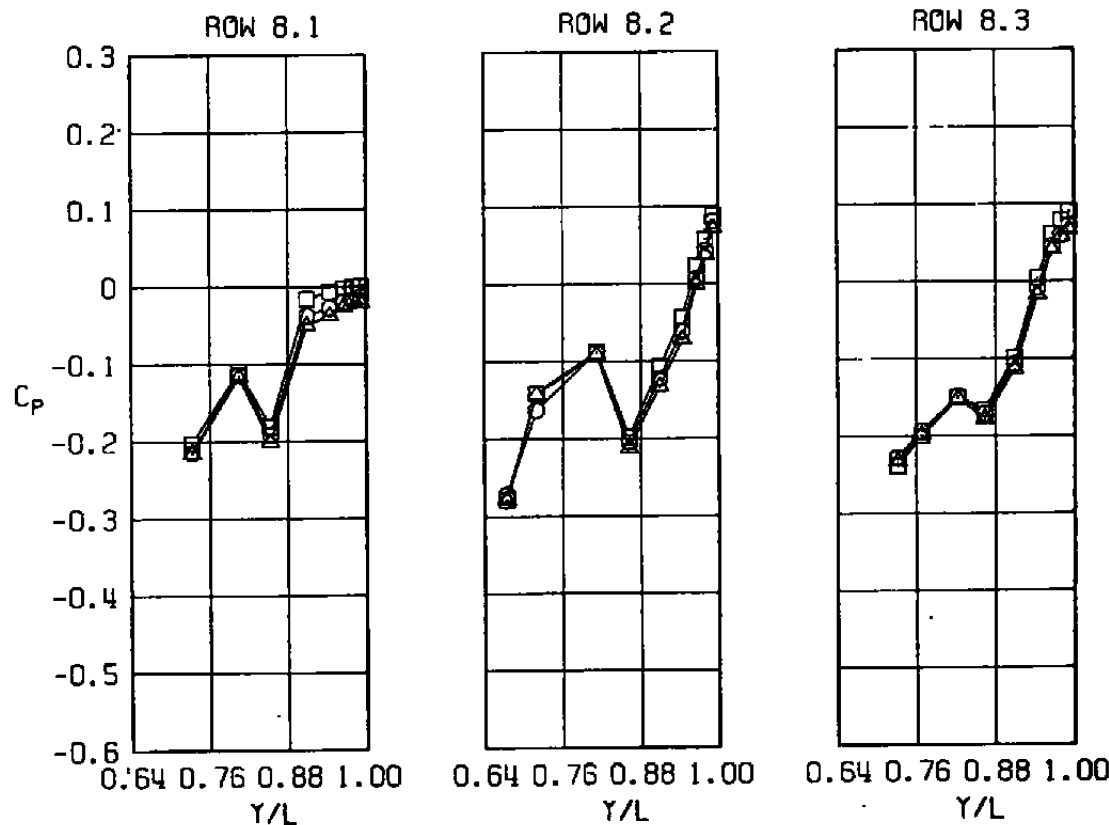
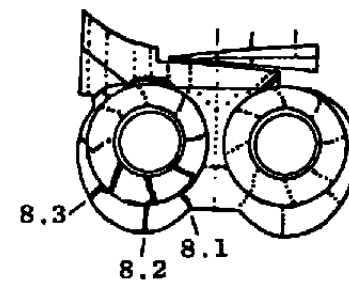


f. Row 6
Figure 37. Continued.



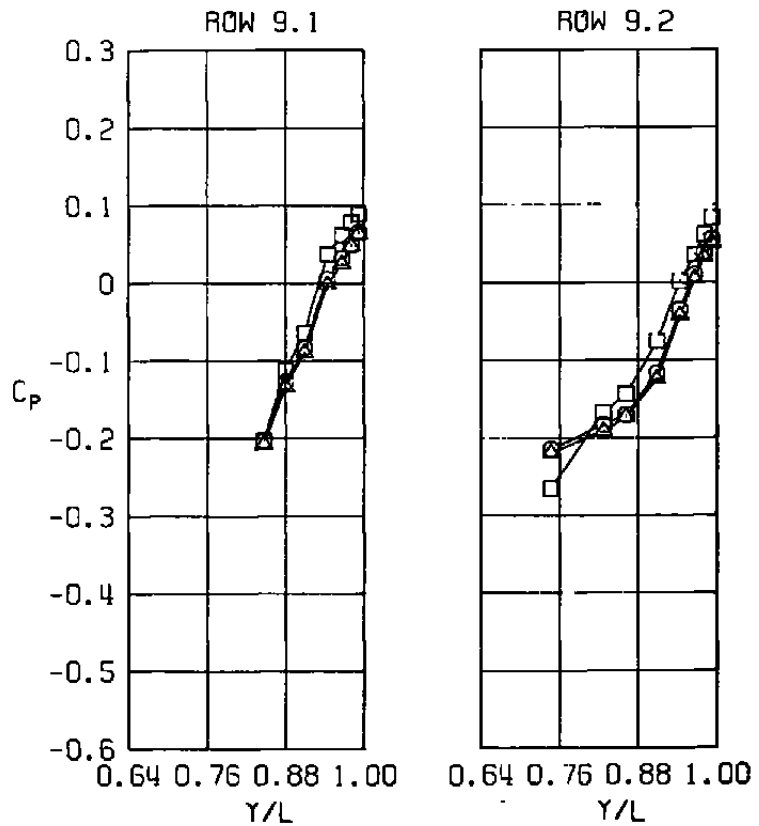
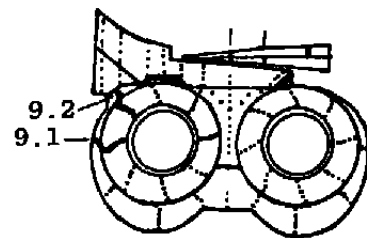
g. Row 7
Figure 37. Continued.

<u>SYM</u>	<u>M</u>	<u>ALPH</u>	<u>NPR</u>	<u>MFR</u>	<u>DELH</u>	<u>Re</u> $\times 10^{-6}$	<u>MODEL</u>	<u>CDNOZ</u>
□	0.85	0.01	1.55	0.396	0.09	2.50	EPES	0
○	0.85	0.02	2.70	0.449	0.17	2.50	EPES	0.0005
△	0.85	0.02	4.22	0.452	0.16	2.50	EPES	0.0007



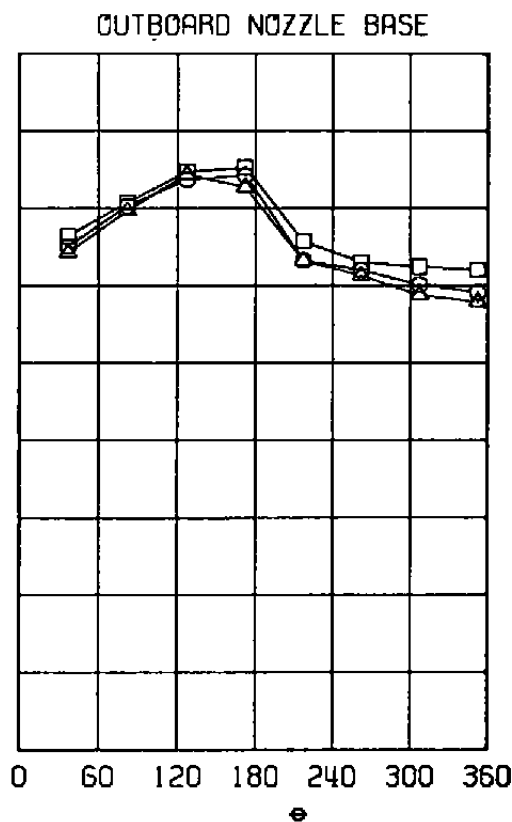
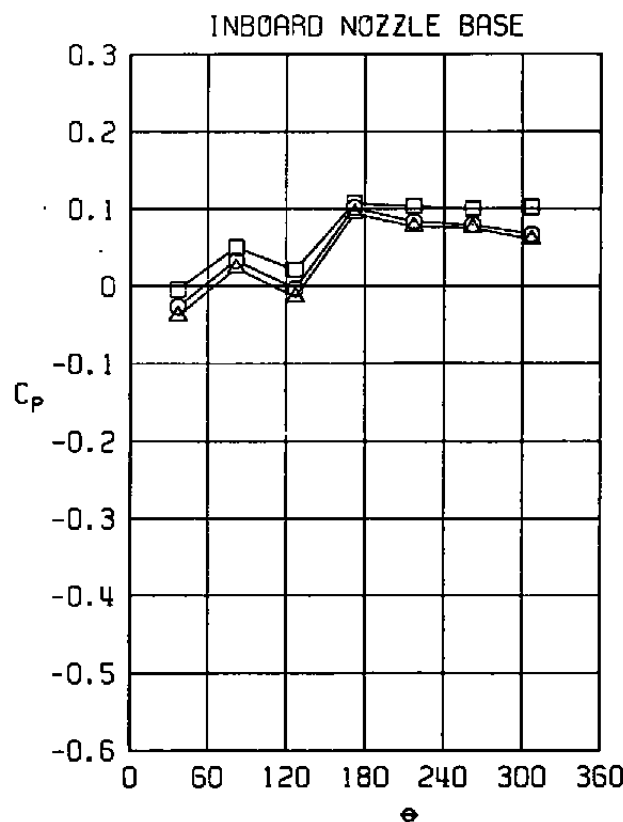
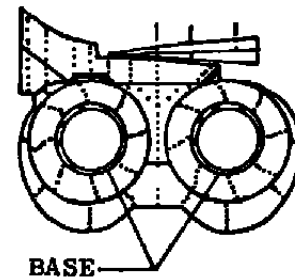
h. Row 8
Figure 37. Continued.

<u>SYM</u>	<u>M</u>	<u>ALPH</u>	<u>NPR</u>	<u>MFR</u>	<u>DELH</u>	<u>Re</u> $\times 10^{-6}$	<u>MODEL</u>	<u>CDNOZ</u>
□	0.85	0.01	1.55	0.396	0.09	2.50	EPES	0
○	0.85	0.02	2.70	0.449	0.17	2.50	EPES	0.0005
△	0.85	0.02	4.22	0.452	0.16	2.50	EPES	0.0007



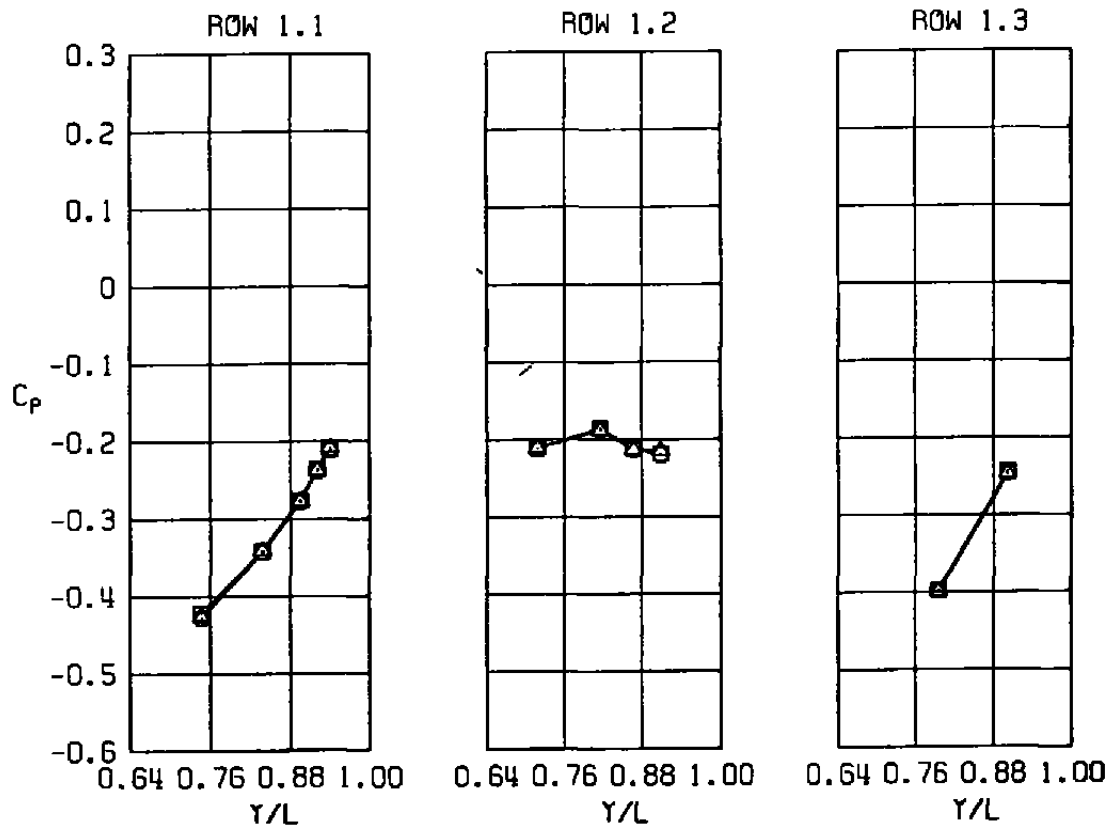
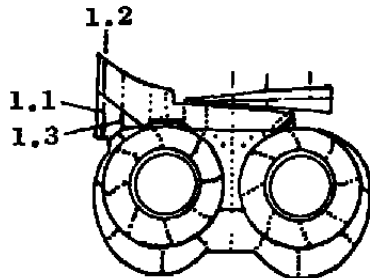
i. Row 9
Figure 37. Continued.

<u>SYM</u>	<u>M</u>	<u>ALPH</u>	<u>NPR</u>	<u>MFR</u>	<u>DELH</u>	<u>Re x 10⁻⁶</u>	<u>MODEL</u>	<u>CDNOZ</u>
□	0.85	0.01	1.55	0.396	0.09	2.50	EPES	0
○	0.85	0.02	2.70	0.449	0.17	2.50	EPES	0.0005
△	0.85	0.02	4.22	0.452	0.16	2.50	EPES	0.0007



j. Nozzle base
Figure 37. Concluded.

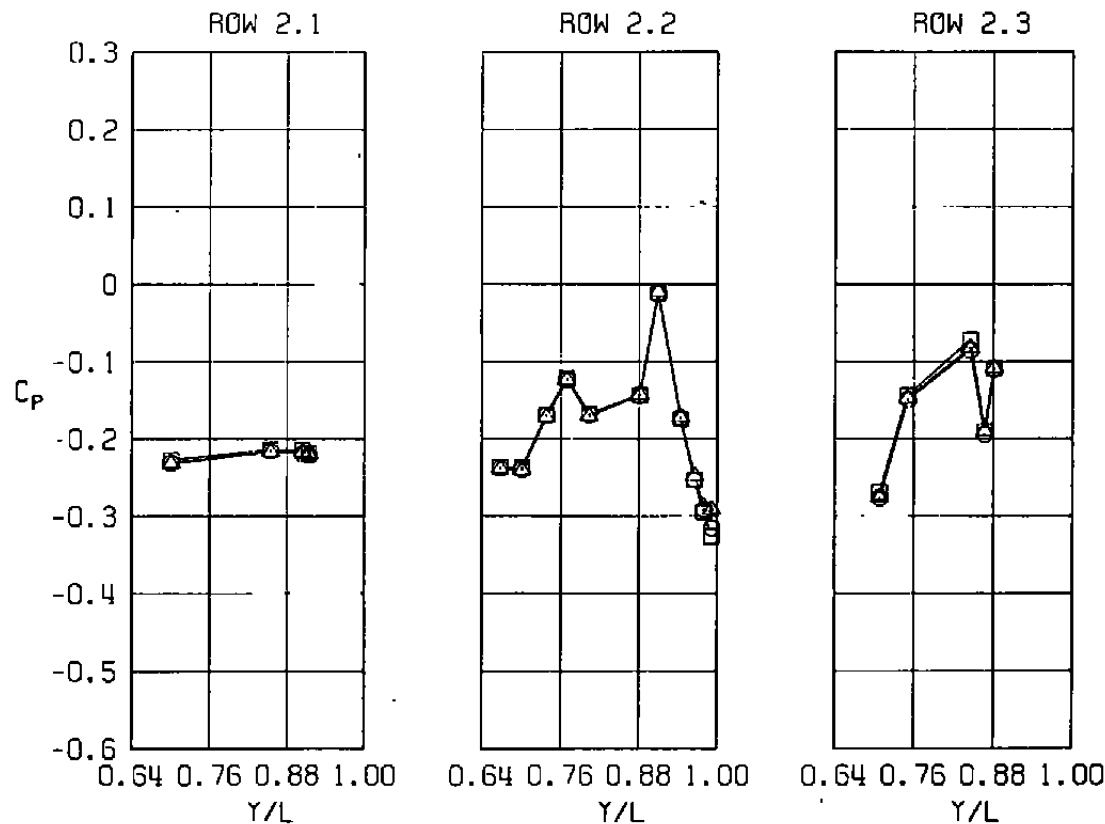
<u>SYM</u>	<u>M</u>	<u>ALPH</u>	<u>NPR</u>	<u>MFR</u>	<u>DELT</u>	<u>Re x 10⁻⁶</u>	<u>MODEL</u>	<u>CDNOZ</u>
□	1.20	-0.02	3.30	0.648	0.00	2.52	EPES	0.0020
○	1.20	-0.01	4.42	0.648	0.00	2.52	EPES	0.0018
△	1.20	-0.01	5.46	0.646	0.00	2.52	EPES	0.0016



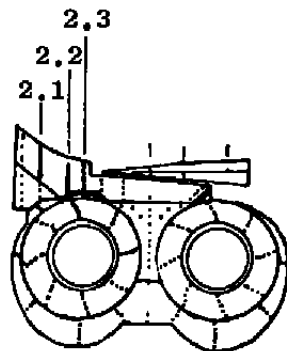
a. Row 1

Figure 38. Effect of nozzle pressure ratio on nozzle afterbody pressure distribution, $M = 1.20$, $\alpha = 0$.

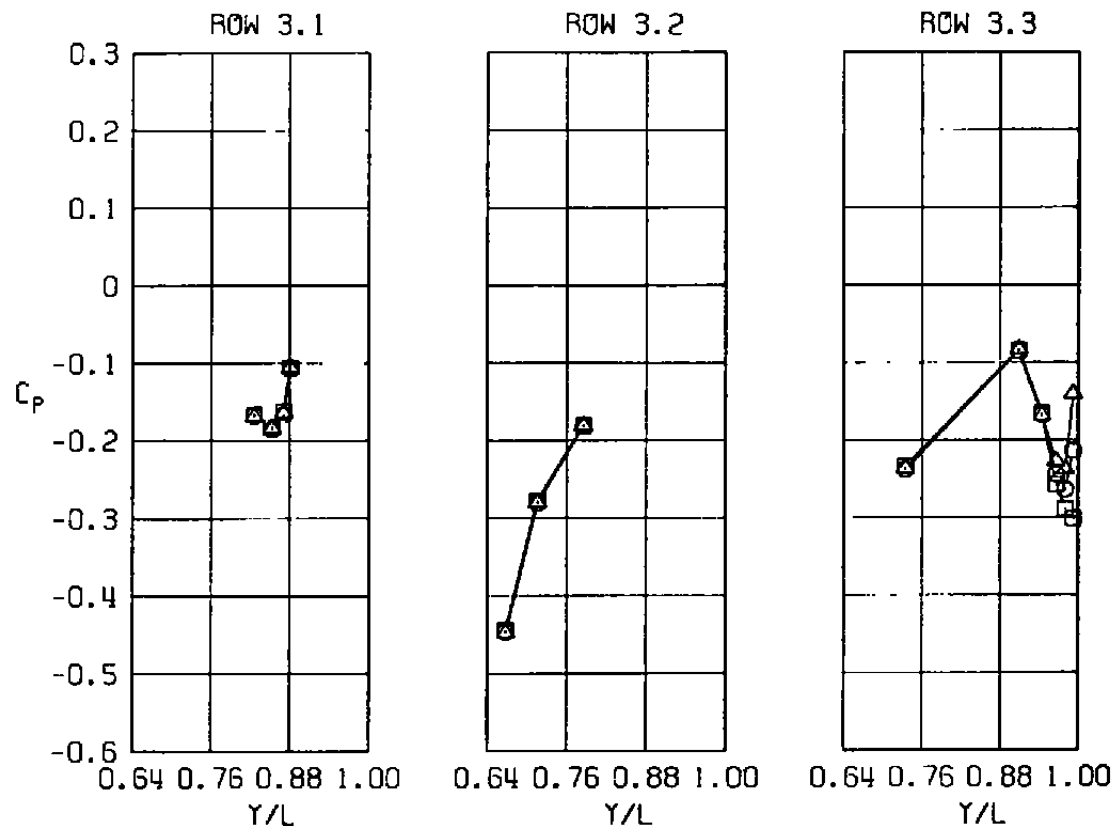
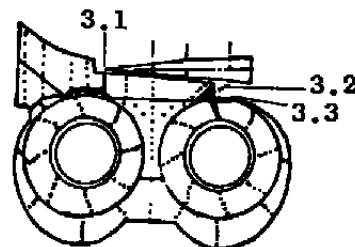
<u>SYM</u>	<u>M</u>	<u>ALPH</u>	<u>NPR</u>	<u>MFR</u>	<u>DELH</u>	<u>Re x 10⁻⁶</u>	<u>MODEL</u>	<u>CDNOZ</u>
□	1.20	-0.02	3.30	0.648	0.00	2.52	EPES	0.0020
○	1.20	-0.01	4.42	0.648	0.00	2.52	EPES	0.0018
△	1.20	-0.01	5.46	0.646	0.00	2.52	EPES	0.0016



b. Row 2
Figure 38. Continued.

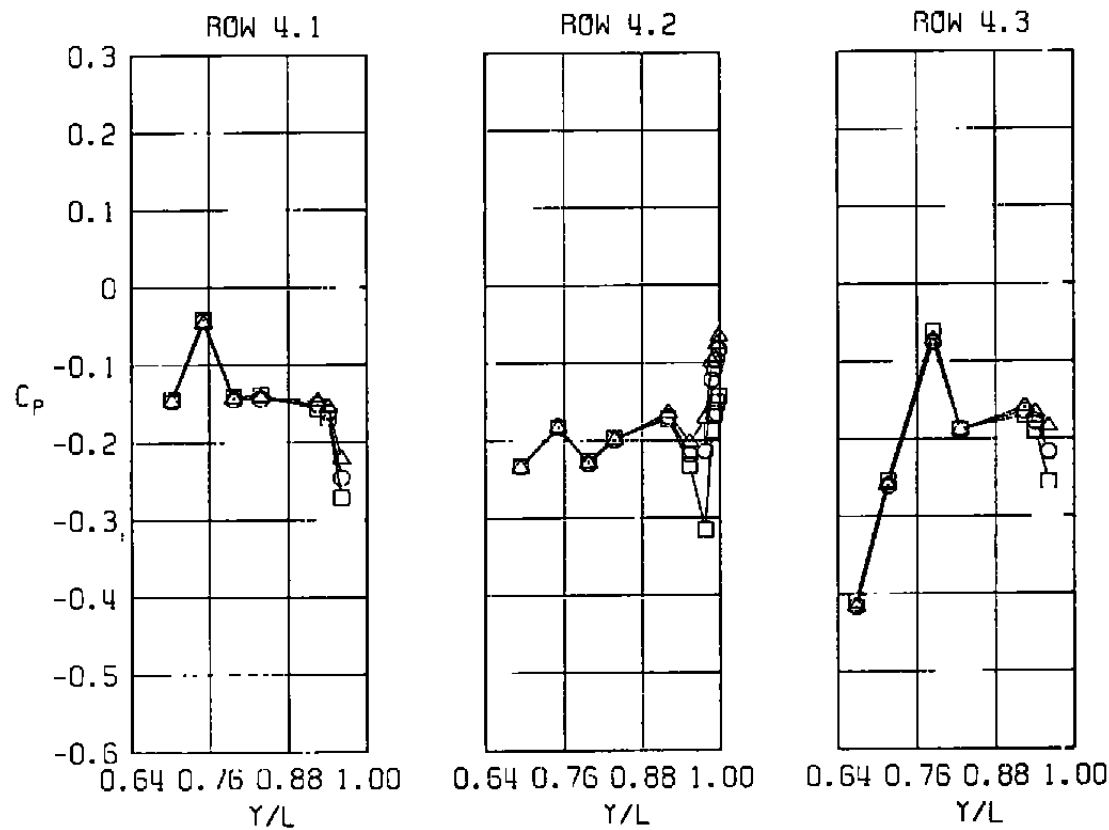
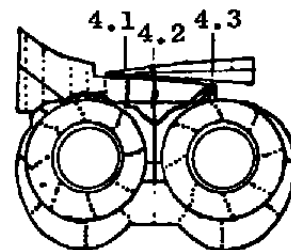


<u>SYM</u>	<u>M</u>	<u>ALPH</u>	<u>NPR</u>	<u>MFR</u>	<u>DElh</u>	<u>Re</u> $\times 10^{-6}$	<u>MODEL</u>	<u>CDNOZ</u>
□	1.20	-0.02	3.30	0.648	0.00	2.52	EPES	0.0020
○	1.20	-0.01	4.42	0.648	0.00	2.52	EPES	0.0018
^	1.20	-0.01	5.46	0.646	0.00	2.52	EPES	0.0016



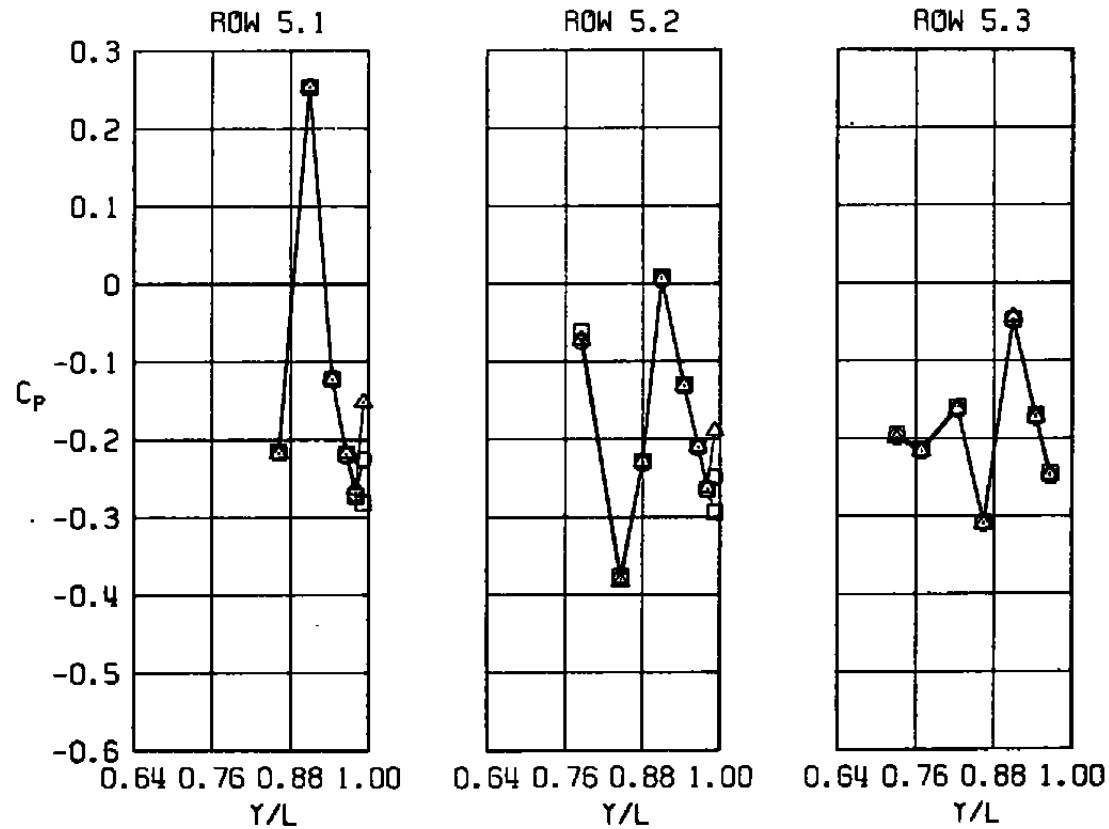
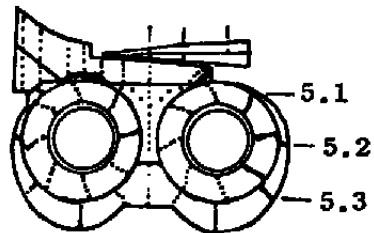
c. Row 3
Figure 38. Continued.

<u>SYM</u>	<u>M</u>	<u>ALPH</u>	<u>NPR</u>	<u>MFR</u>	<u>DELH</u>	<u>Re x 10⁻⁶</u>	<u>MODEL</u>	<u>CDNOZ</u>
□	1.20	-0.02	3.30	0.648	0.00	2.52	EPES	0.0020
○	1.20	-0.01	4.42	0.648	0.00	2.52	EPES	0.0018
△	1.20	-0.01	5.46	0.646	0.00	2.52	EPES	0.0016



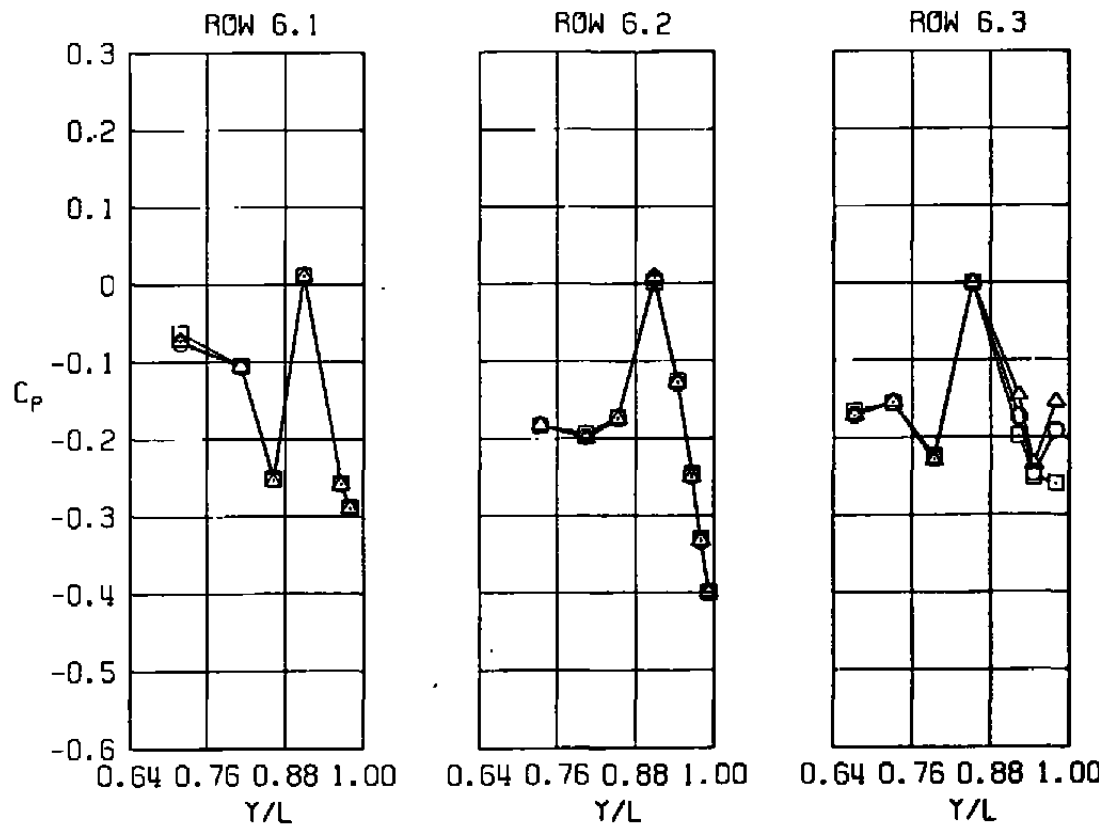
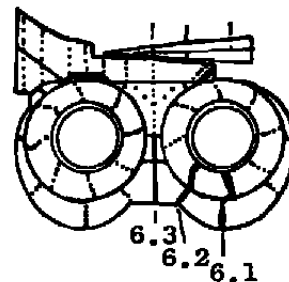
d. Row 4
Figure 38. Continued.

<u>SYM</u>	<u>M</u>	<u>ALPH</u>	<u>NPR</u>	<u>MFR</u>	<u>DELT</u>	<u>Re x 10⁻⁶</u>	<u>MODEL</u>	<u>CDNOZ</u>
□	1.20	-0.02	3.30	0.648	0.00	2.52	EPES	0.0020
○	1.20	-0.01	4.42	0.648	0.00	2.52	EPES	0.0018
△	1.20	-0.01	5.46	0.646	0.00	2.52	EPES	0.0016



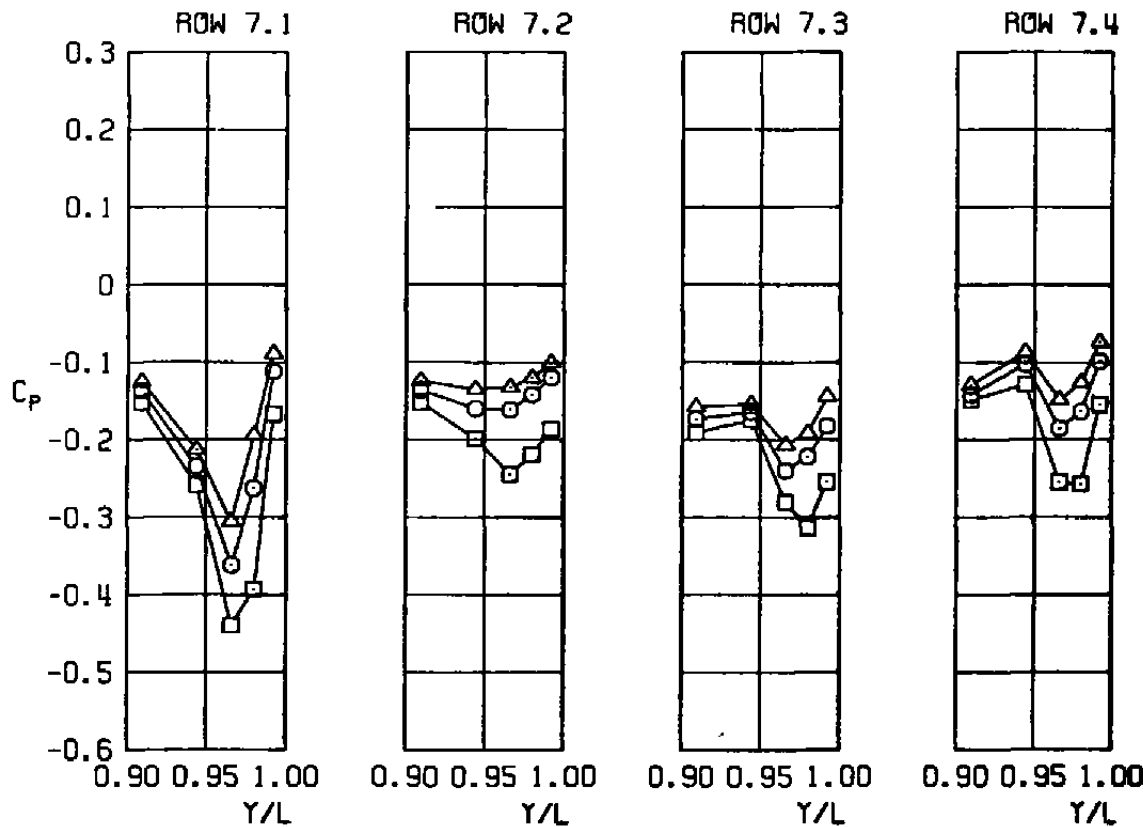
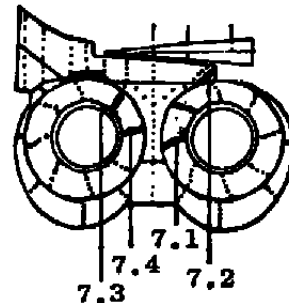
e. Row 5
Figure 38. Continued.

<u>SYM</u>	<u>M</u>	<u>ALPH</u>	<u>NPR</u>	<u>MFR</u>	<u>DELH</u>	<u>Re x 10⁻⁶</u>	<u>MODEL</u>	<u>CDNOZ</u>
□	1.20	-0.02	3.30	0.648	0.00	2.52	EPES	0.0020
○	1.20	-0.01	4.42	0.648	0.00	2.52	EPES	0.0018
△	1.20	-0.01	5.46	0.646	0.00	2.52	EPES	0.0016



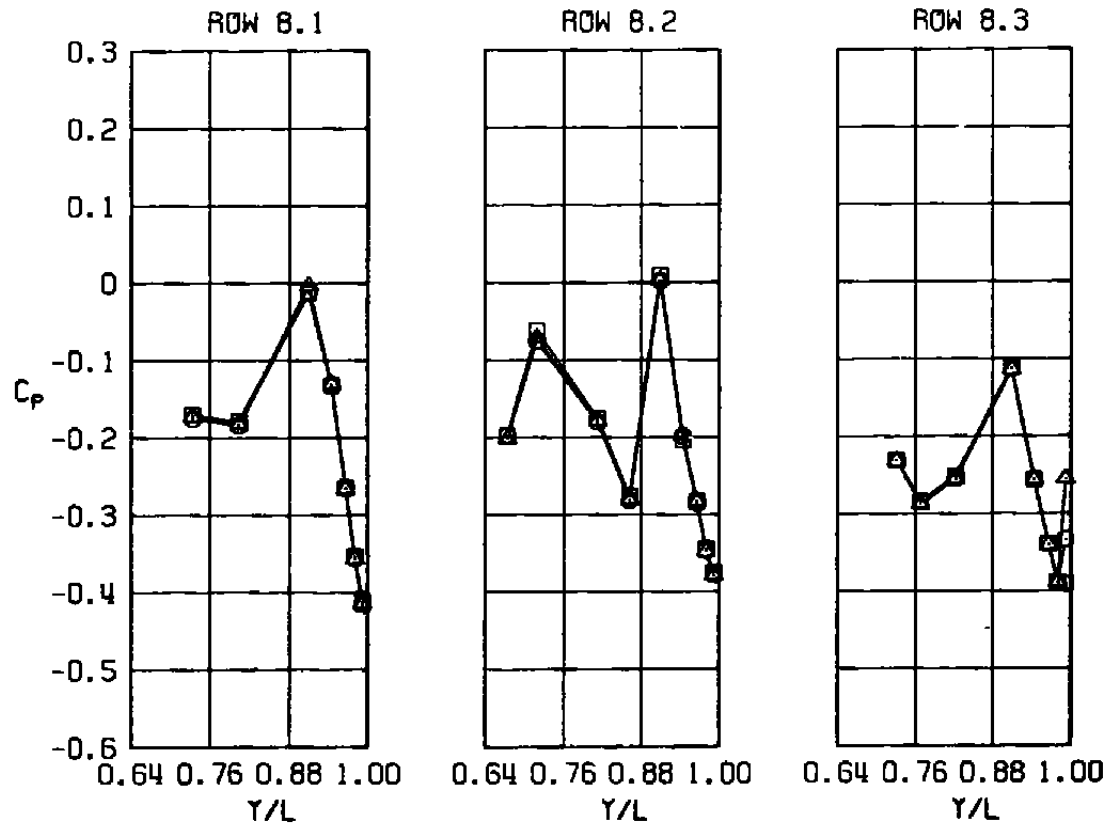
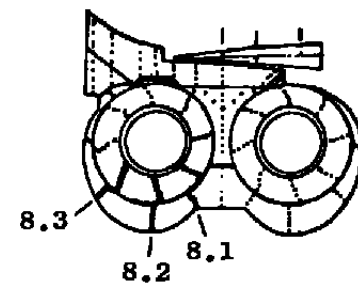
f. Row 6
Figure 38. Continued.

<u>SYM</u>	<u>M</u>	<u>ALPH</u>	<u>NPR</u>	<u>MFR</u>	<u>DELH</u>	<u>Re</u> $\times 10^{-6}$	<u>MODEL</u>	<u>CDNOZ</u>
□	1.20	-0.02	3.30	0.648	0.00	2.52	EPES	0.0020
○	1.20	-0.01	4.42	0.648	0.00	2.52	EPES	0.0018
△	1.20	-0.01	5.46	0.646	0.00	2.52	EPES	0.0016



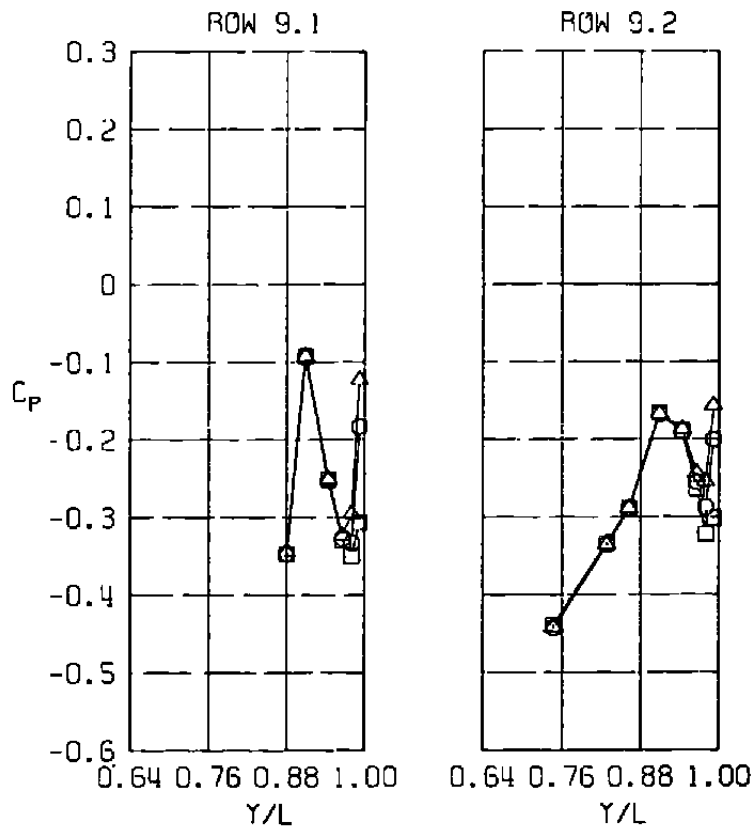
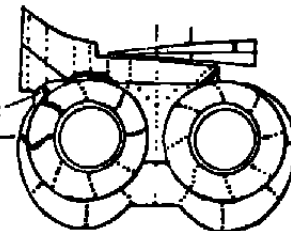
g. Row 7
Figure 38. Continued.

<u>SYM</u>	<u>M</u>	<u>ALPH</u>	<u>NPR</u>	<u>MFR</u>	<u>DELH</u>	<u>Rc x 10⁻⁶</u>	<u>MODEL</u>	<u>CDNOZ</u>
□	1.20	-0.02	3.30	0.648	0.00	2.52	EPES	0.0020
○	1.20	-0.01	4.42	0.648	0.00	2.52	EPES	0.0018
△	1.20	-0.01	5.46	0.646	0.00	2.52	EPES	0.0016



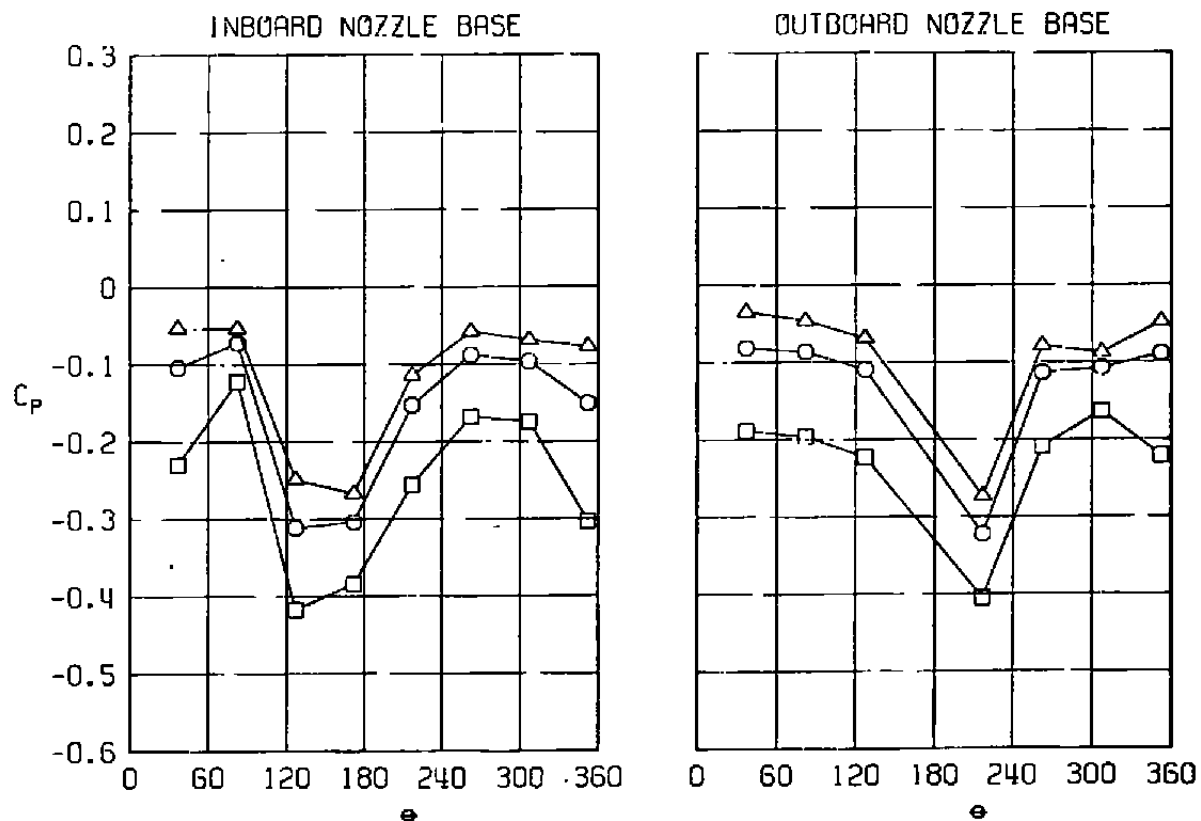
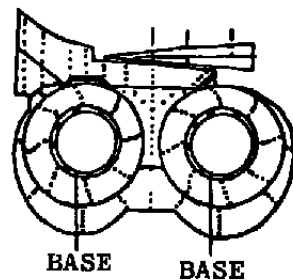
h. Row 8
Figure 38. Continued.

<u>SYM</u>	<u>M</u>	<u>ALPH</u>	<u>NPR</u>	<u>MFR</u>	<u>DELH</u>	<u>Re</u> $\times 10^{-6}$	<u>MODEL</u>	<u>CDNOZ</u>
□	1.20	-0.02	3.30	0.648	0.00	2.52	EPES	0.0020
○	1.20	-0.01	4.42	0.648	0.00	2.52	EPES	0.0018
△	1.20	-0.01	5.46	0.646	0.00	2.52	EPES	0.0016



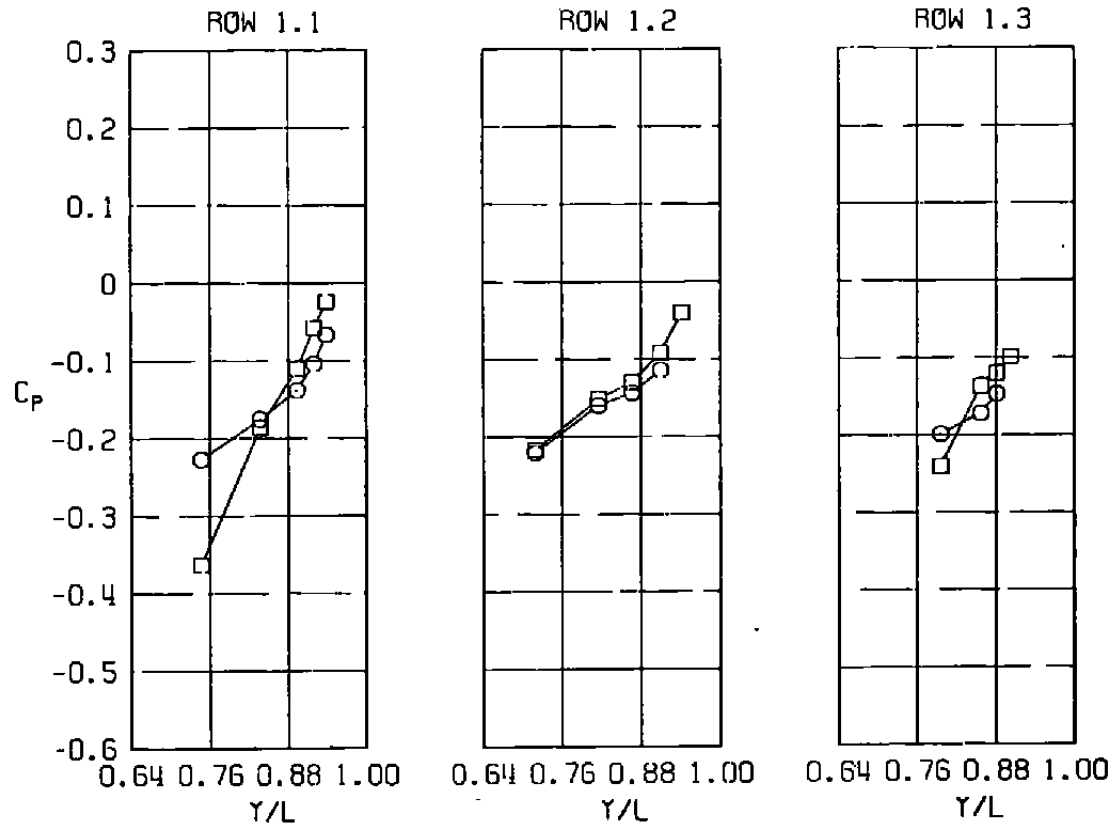
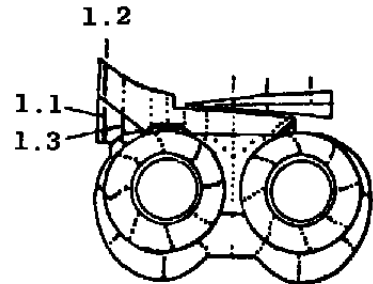
i. Row 9
Figure 38. Continued.

<u>SYM</u>	<u>M</u>	<u>ALPH</u>	<u>NPR</u>	<u>MFR</u>	<u>DELH</u>	<u>Re x 10⁻⁶</u>	<u>MODEL</u>	<u>CDNOZ</u>
□	1.20	-0.02	3.30	0.648	0.00	2.52	EPES	0.0020
○	1.20	-0.01	4.42	0.648	0.00	2.52	EPES	0.0018
△	1.20	-0.01	5.46	0.646	0.00	2.52	EPES	0.0016



j. Nozzle base
Figure 38. Concluded.

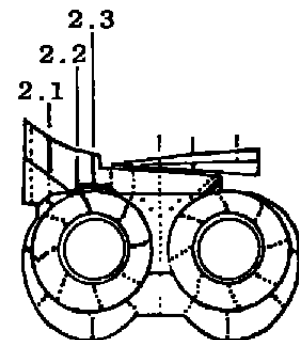
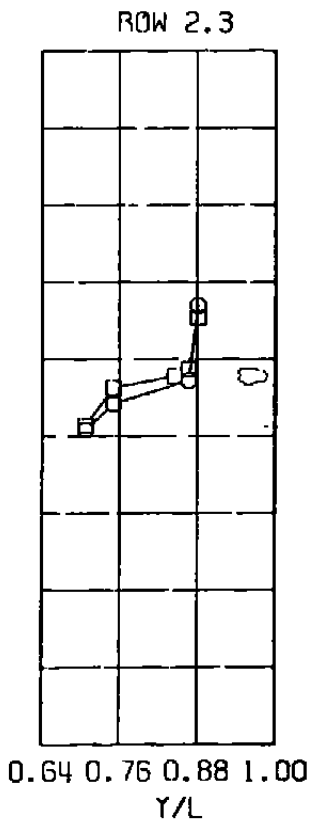
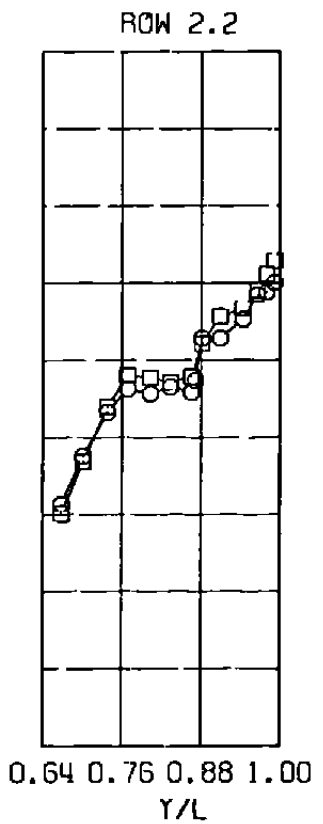
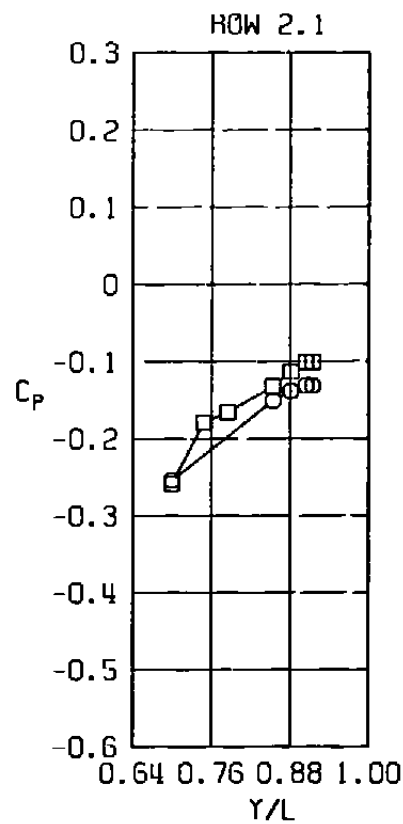
SYM	M	ALPH	NPR	MFR	DELH	$Re \times 10^{-6}$	MODEL	CDNOZ
□	0.85	0.01	2.73	0	0.03	2.50	NAB	0.0003
○	0.85	0.02	2.70	0.449	0.17	2.50	EPES	0.0005



a. Row 1

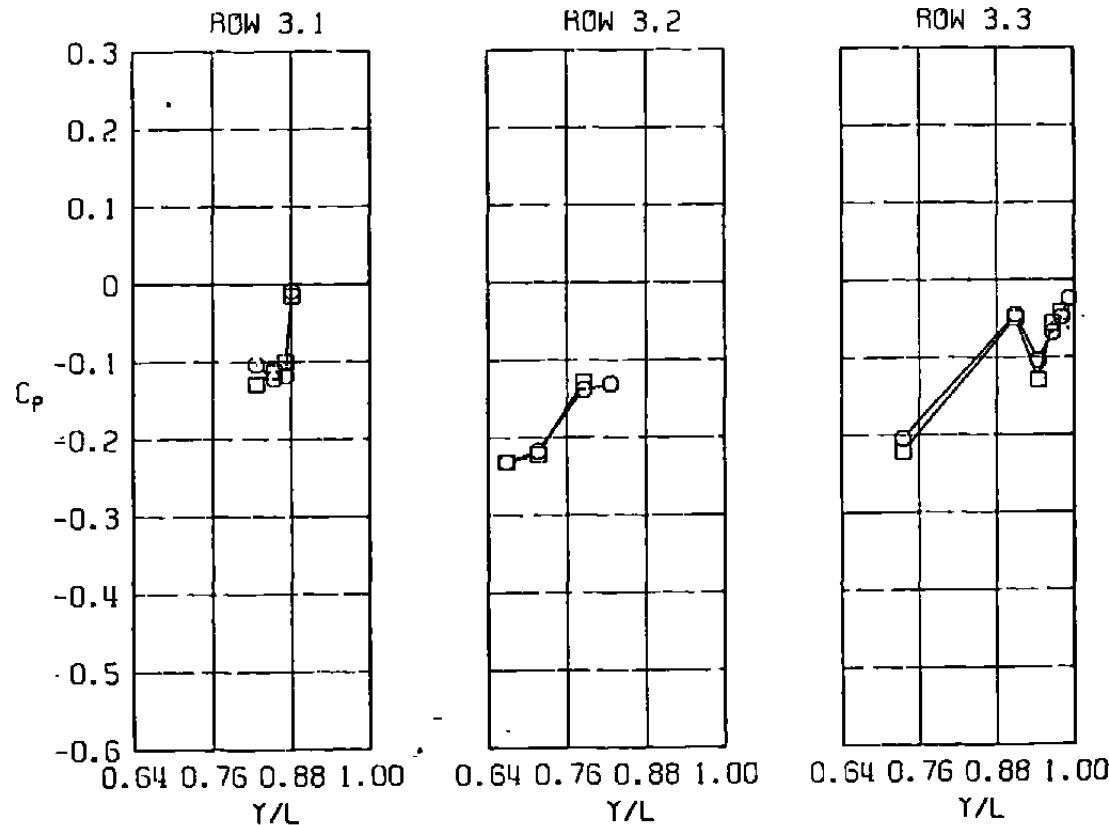
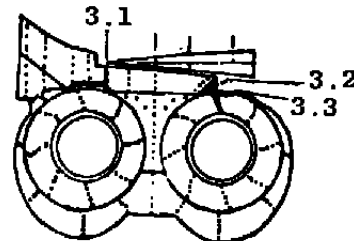
Figure 39. Comparison of nozzle afterbody pressure distribution for the EPES and NAB models, $M = 0.85$, $\alpha = 0$.

<u>SYM</u>	<u>M</u>	<u>ALPH</u>	<u>NPR</u>	<u>MFR</u>	<u>DElh</u>	<u>Re x 10⁻⁶</u>	<u>MODEL</u>	<u>CDNOZ</u>
□	0.85	0.01	2.73	0	0.03	2.50	NAB	0.0003
○	0.85	0.02	2.70	0.449	0.17	2.50	EPES	0.0005



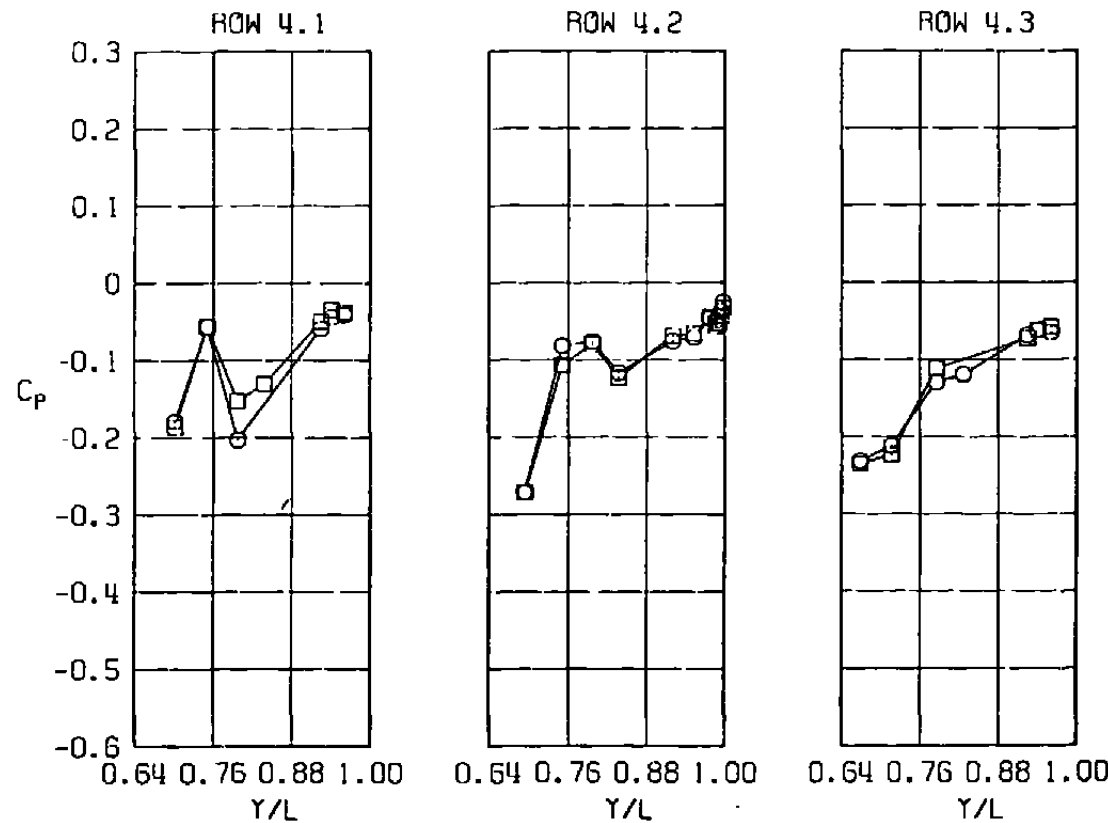
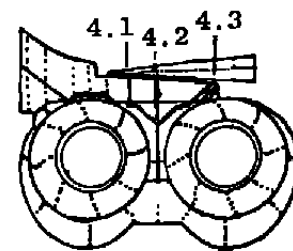
b. Row 2
Figure 39. Continued.

<u>SYM</u>	<u>M</u>	<u>ALPH</u>	<u>NPR</u>	<u>MFR</u>	<u>DElh</u>	<u>Re x 10⁻⁶</u>	<u>MODEL</u>	<u>CDNOZ</u>
□	0.85	0.01	2.73	0	0.03	2.50	NAB	0.0003
○	0.85	0.02	2.70	0.449	0.17	2.50	EPES	0.0005



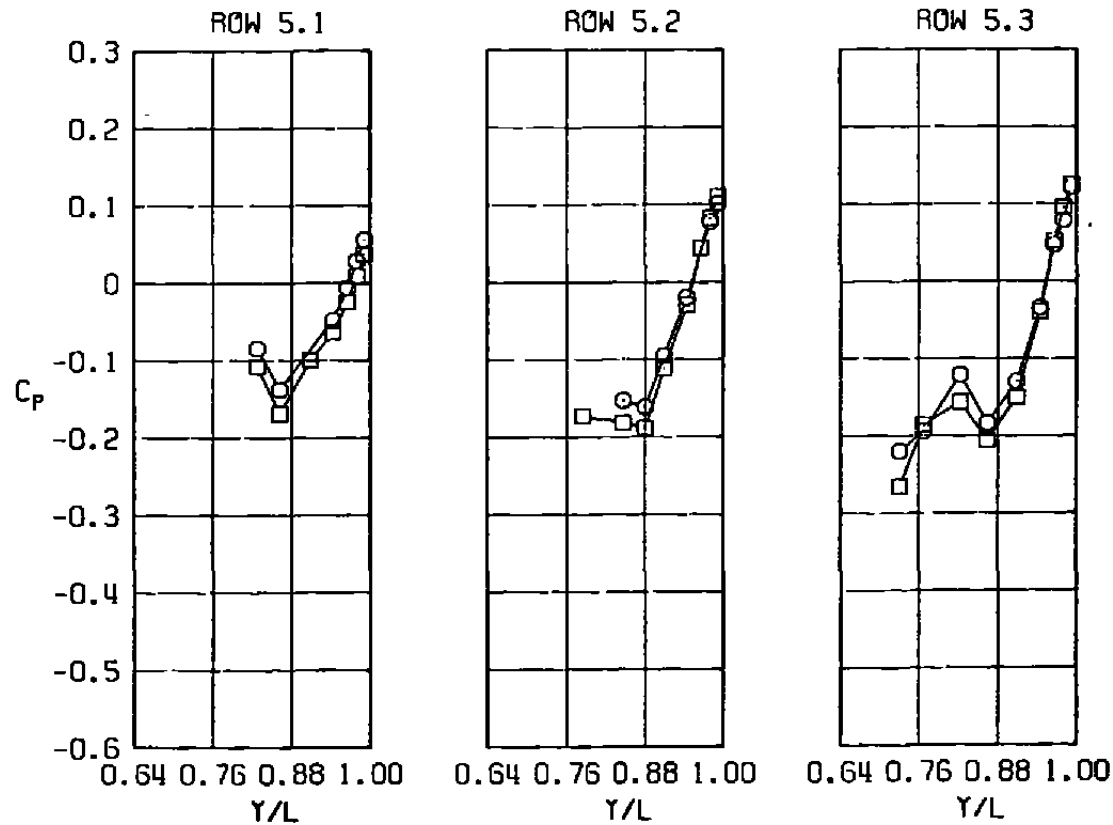
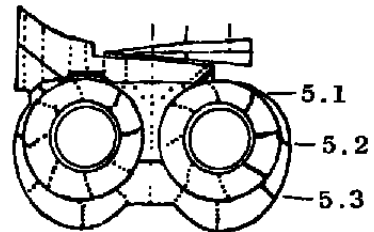
c. Row 3
Figure 39. Continued.

<u>SYM</u>	<u>M</u>	<u>ALPH</u>	<u>NPR</u>	<u>MFR</u>	<u>DELH</u>	<u>Re x 10⁻⁶</u>	<u>MODEL</u>	<u>CDNOZ</u>
□	0.85	0.01	2.73	0	0.03	2.50	NAB	0.0003
○	0.85	0.02	2.70	0.449	0.17	2.50	EPES	0.0005



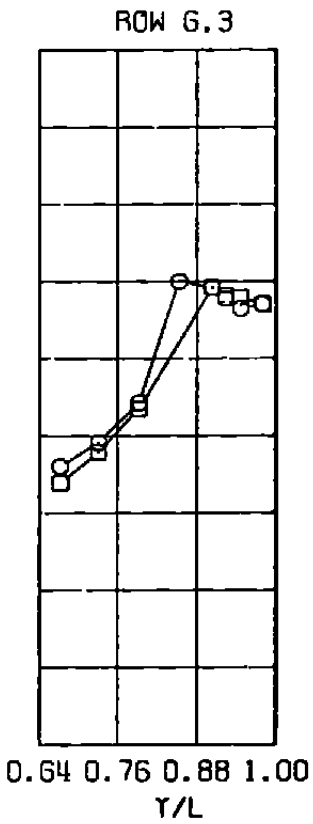
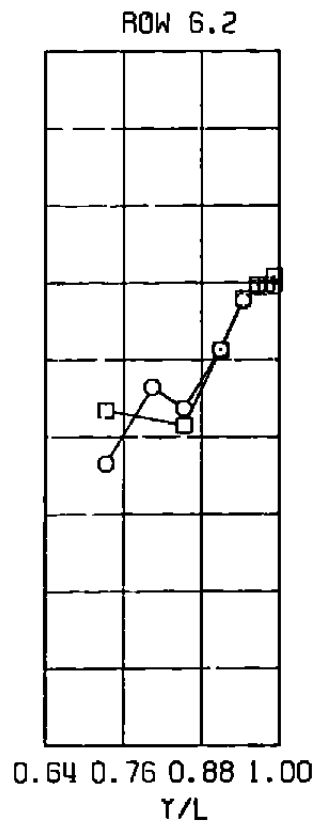
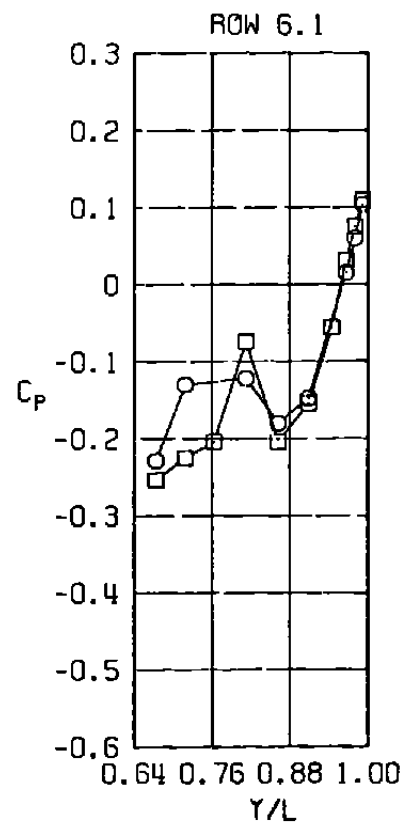
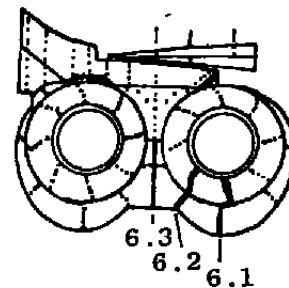
d. Row 4
Figure 39. Continued.

<u>SYM</u>	<u>M</u>	<u>ALPH</u>	<u>NPR</u>	<u>MFR</u>	<u>DELH</u>	<u>Re x 10⁻⁶</u>	<u>MODEL</u>	<u>CDNOZ</u>
□	0.85	0.01	2.73	0	0.03	2.50	NAB	0.0003
○	0.85	0.02	2.70	0.449	0.17	2.50	EPES	0.0005



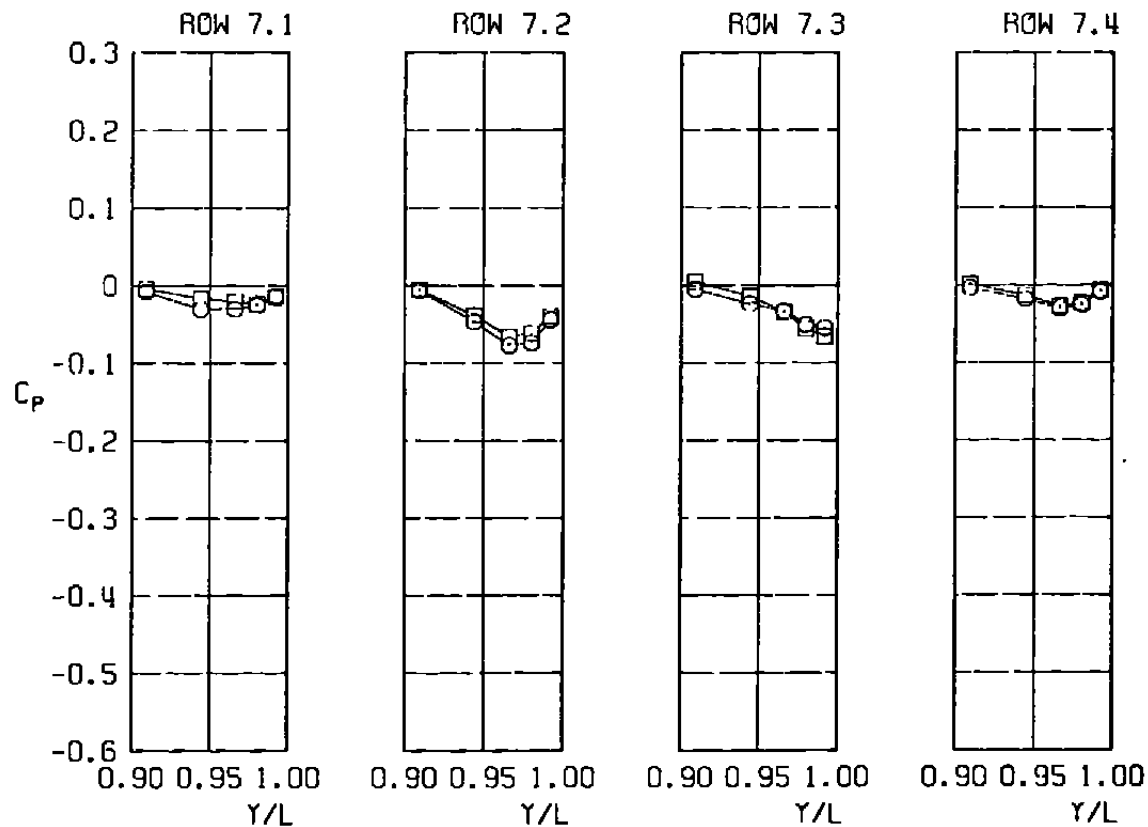
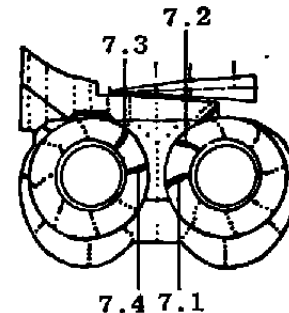
e. Row 5
Figure 39. Continued.

<u>SYM</u>	<u>M</u>	<u>ALPH</u>	<u>NPR</u>	<u>MFR</u>	<u>DELH</u>	<u>Re</u> $\times 10^{-6}$	<u>MODEL</u>	<u>CDNOZ</u>
□	0.85	0.01	2.73	0	0.03	2.50	NAB	0.0003
○	0.85	0.02	2.70	0.449	0.17	2.50	EPES	0.0005



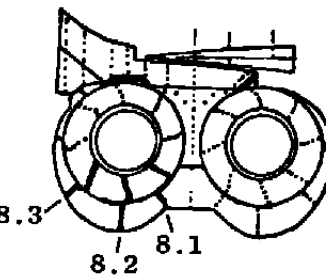
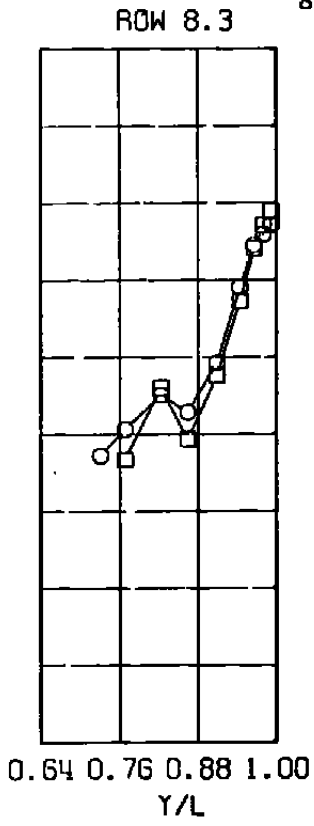
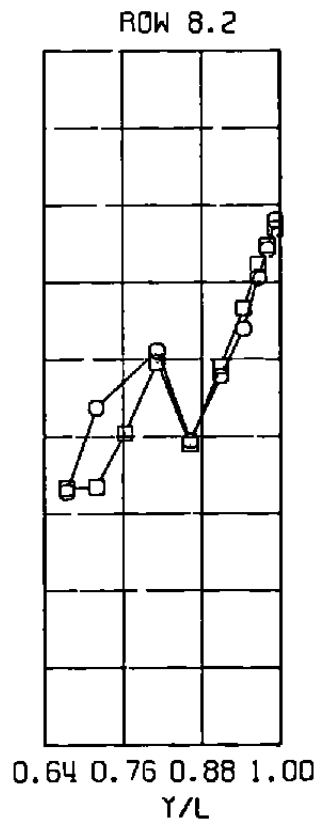
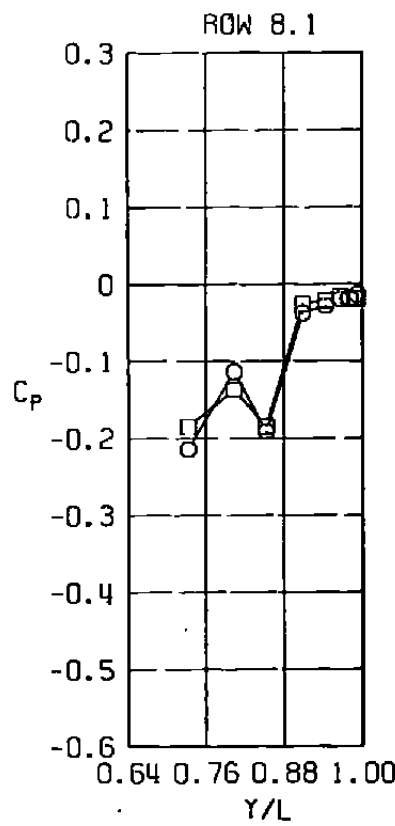
f. Row 6
Figure 39. Continued.

SYM	M	ALPH	NPR	MFR	DELH	$Re \times 10^{-6}$	MODEL	CDNOZ
□	0.85	0.01	2.73	0	0.03	2.50	NAB	0.0003
○	0.85	0.02	2.70	0.449	0.17	2.50	EPES	0.0005



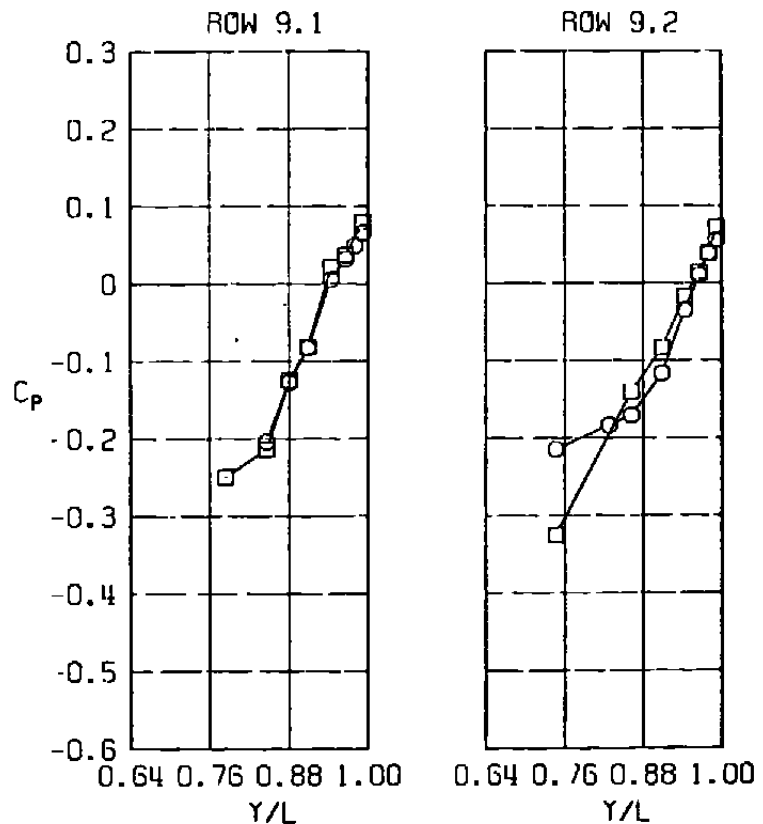
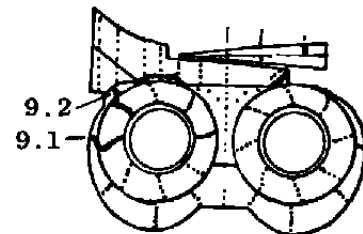
g. Row 7
Figure 39. Continued.

<u>SYM</u>	<u>M</u>	<u>ALPH</u>	<u>NPR</u>	<u>MFR</u>	<u>DELH</u>	<u>Re x 10⁻⁶</u>	<u>MODEL</u>	<u>CDNOZ</u>
□	0.85	0.01	2.73	0	0.03	2.50	NAB	0.0003
○	0.85	0.02	2.70	0.449	0.17	2.50	EPES	0.0005

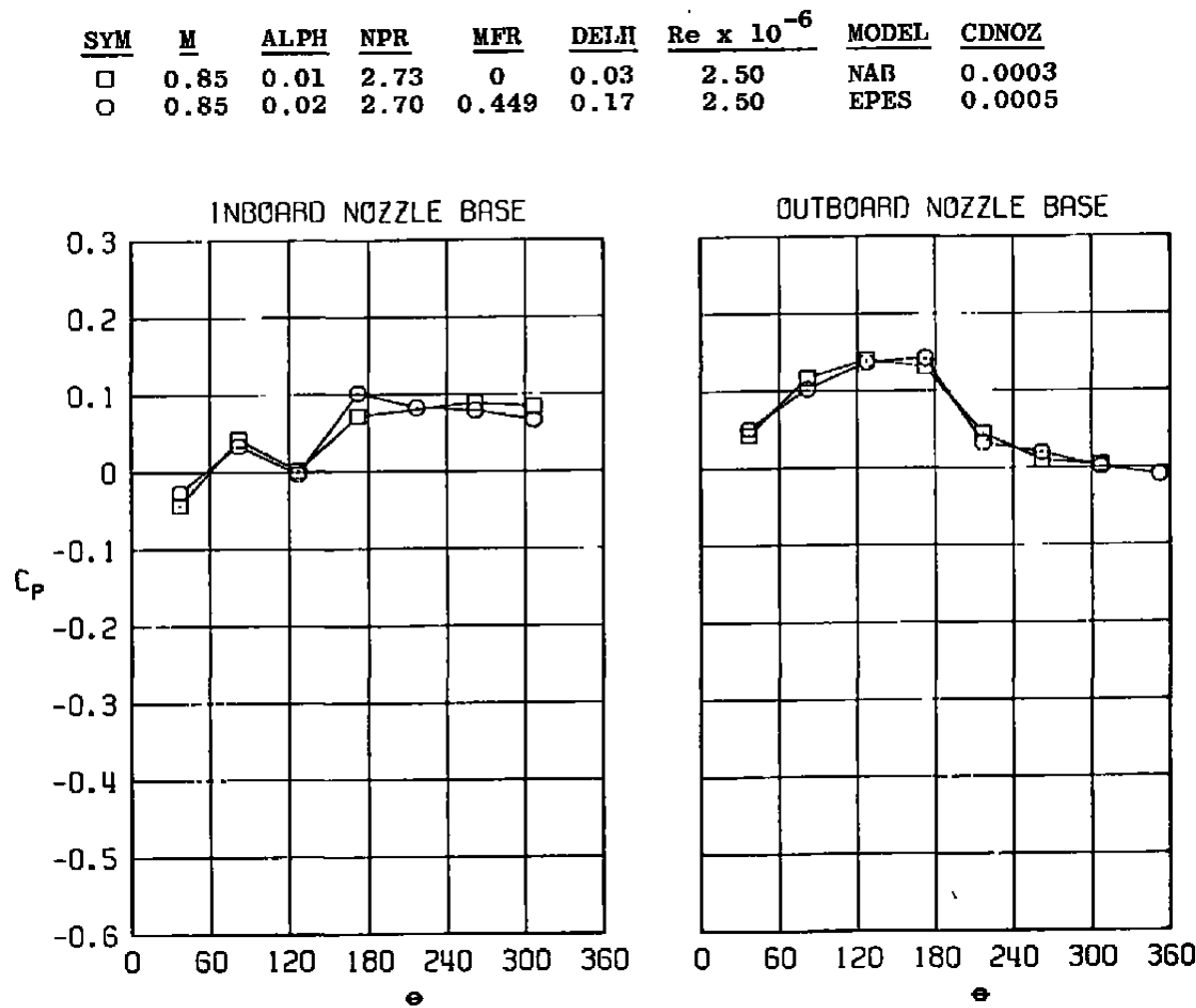


h. Row 8
Figure 39. Continued.

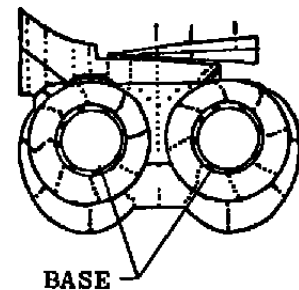
<u>SYM</u>	<u>M</u>	<u>ALPH</u>	<u>NPR</u>	<u>MFR</u>	<u>DELH</u>	<u>Re</u> $\times 10^{-6}$	<u>MODEL</u>	<u>CDNOZ</u>
□	0.85	0.01	2.73	0	0.03	2.50	NAB	0.0003
○	0.85	0.02	2.70	0.449	0.17	2.50	EPES	0.0005



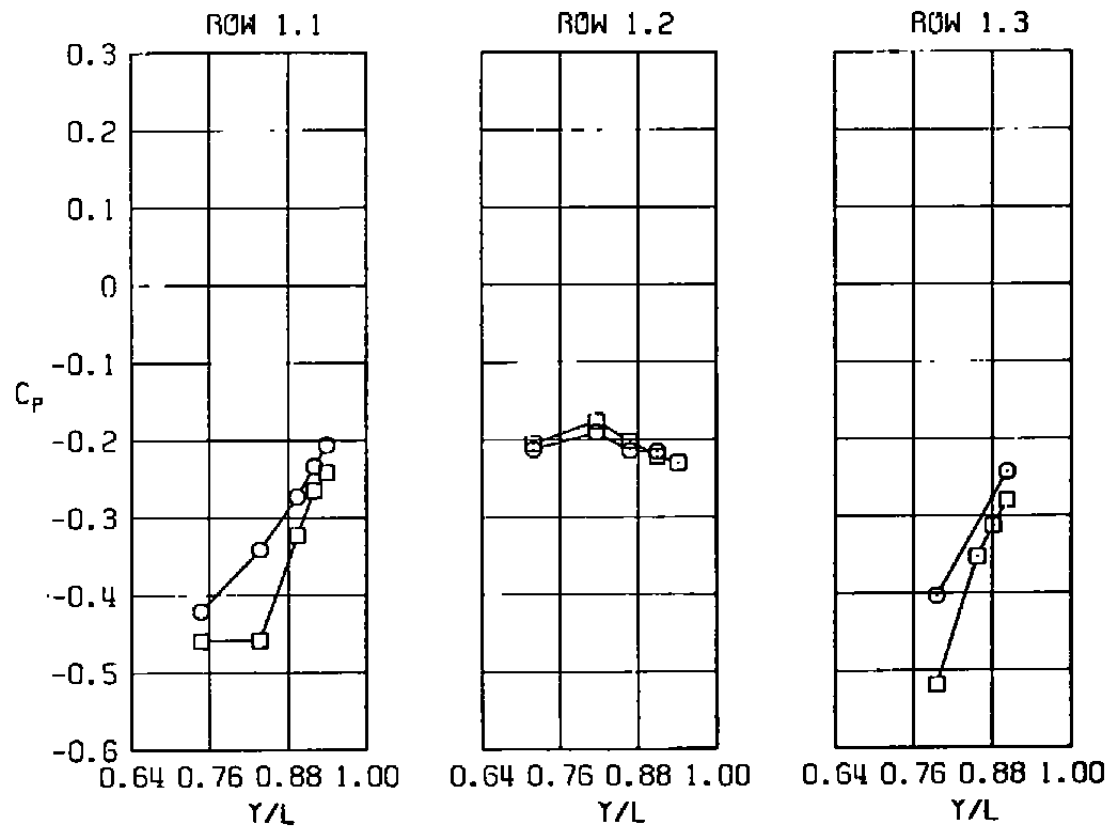
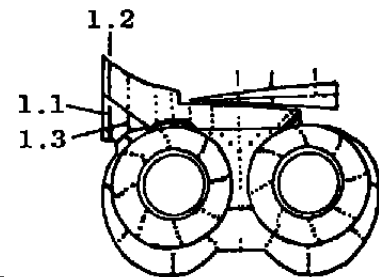
i. Row 9
Figure 39. Continued.



j. Nozzle base
Figure 39. Concluded.



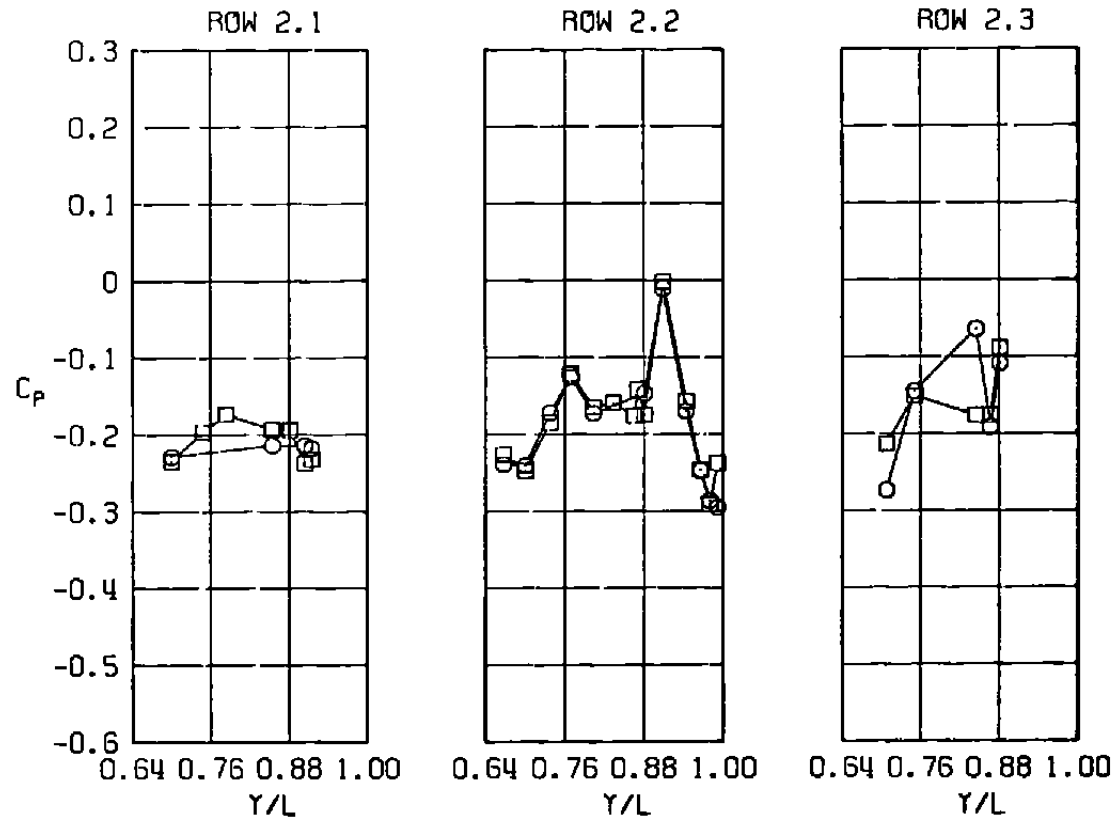
<u>SYM</u>	<u>M</u>	<u>ALPH</u>	<u>NPR</u>	<u>MFR</u>	<u>DELH</u>	<u>Re</u> $\times 10^{-6}$	<u>MODEL</u>	<u>CDNOZ</u>
□	1.20	0	5.02	0	0.02	2.50	NAB	0.0012
○	1.20	-0.01	5.13	0.627	-0.01	2.52	EPES	0.0016



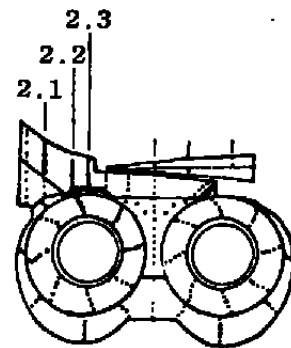
a. Row 1

Figure 40. Comparison of nozzle afterbody pressure distributions for the EPES and NAB models, $M = 1.20$, $\alpha = 0$.

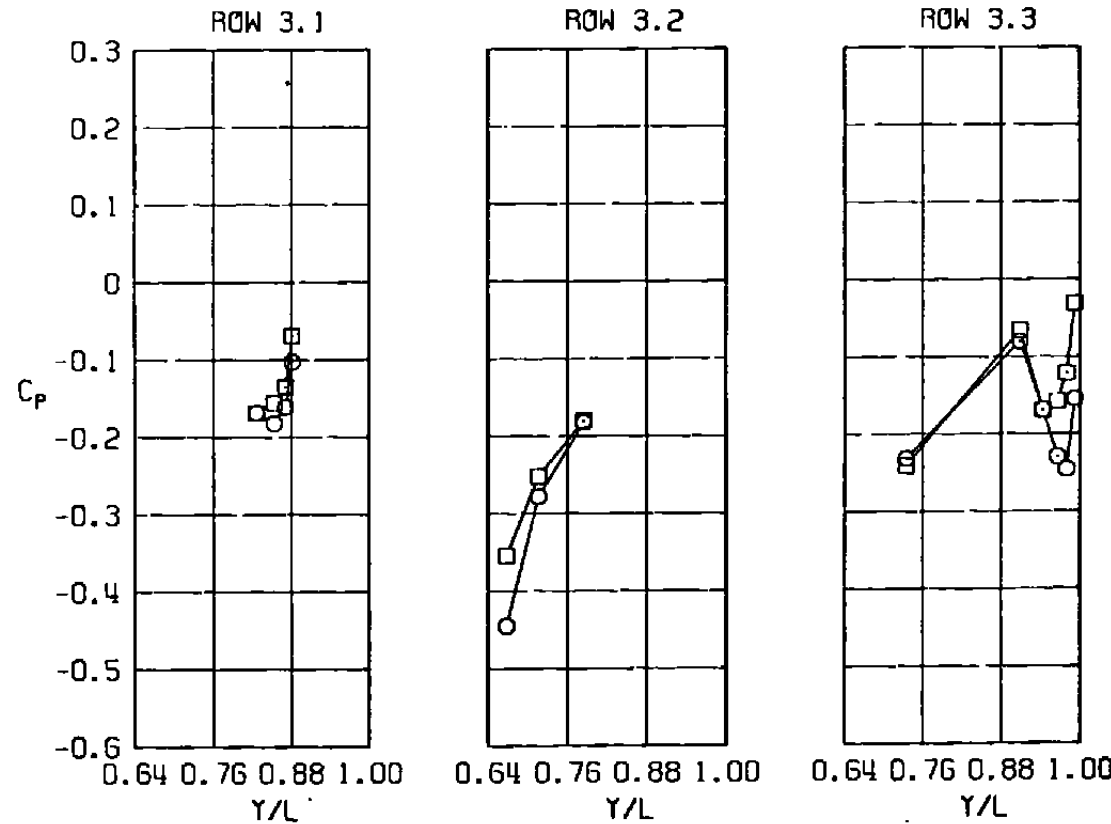
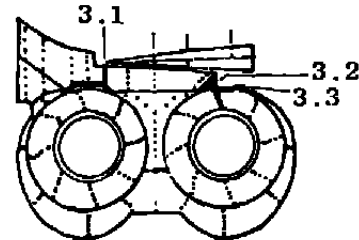
<u>SYM</u>	<u>M</u>	<u>ALPH</u>	<u>NPR</u>	<u>MFR</u>	<u>DELH</u>	<u>Re x 10⁻⁶</u>	<u>MODEL</u>	<u>CDNOZ</u>
□	1.20	0	5.02	0	0.02	2.50	NAB	0.0012
○	1.20	-0.01	5.13	0.627	-0.01	2.52	EPES	0.0016



b. Row 2
Figure 40. Continued.

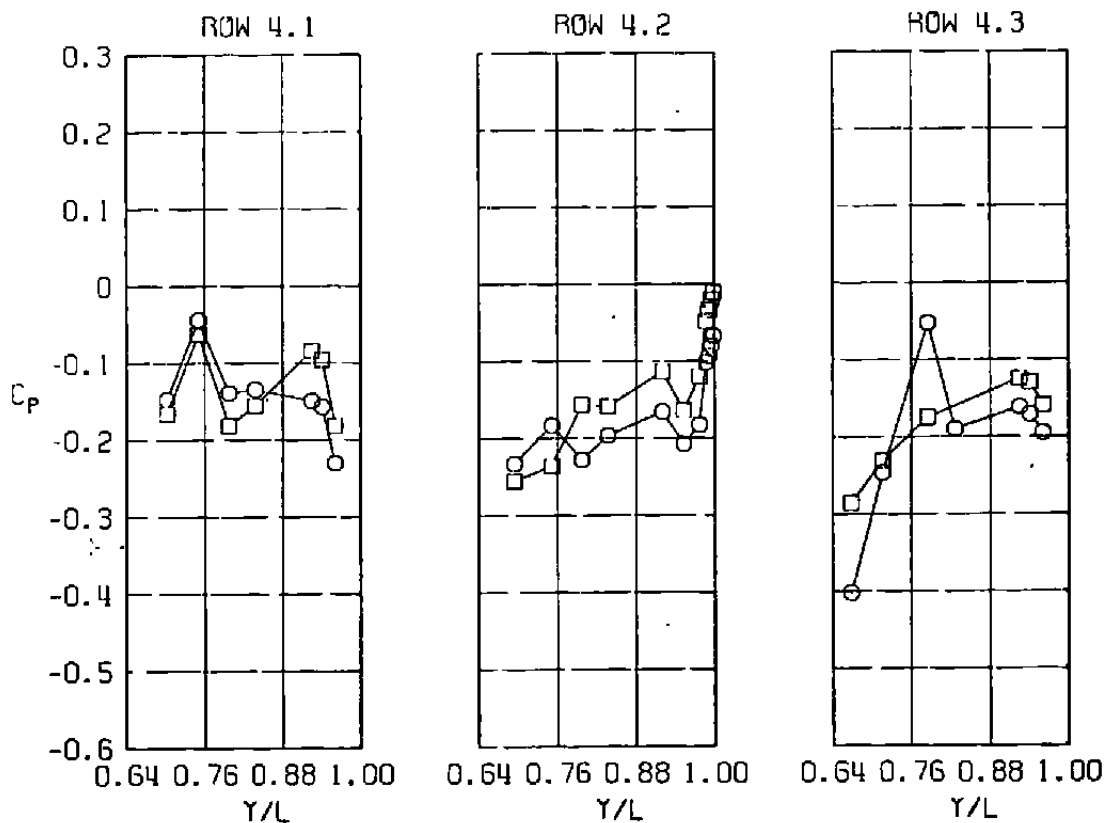
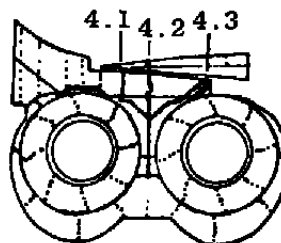


<u>SYM</u>	<u>M</u>	<u>ALPH</u>	<u>NPR</u>	<u>MFR</u>	<u>DELH</u>	<u>Re x 10⁻⁶</u>	<u>MODEL</u>	<u>CDNOZ</u>
□	1.20	0	5.02	0	0.02	2.50	NAB	0.0012
○	1.20	-0.01	5.13	0.627	-0.01	2.52	EPES	0.0016



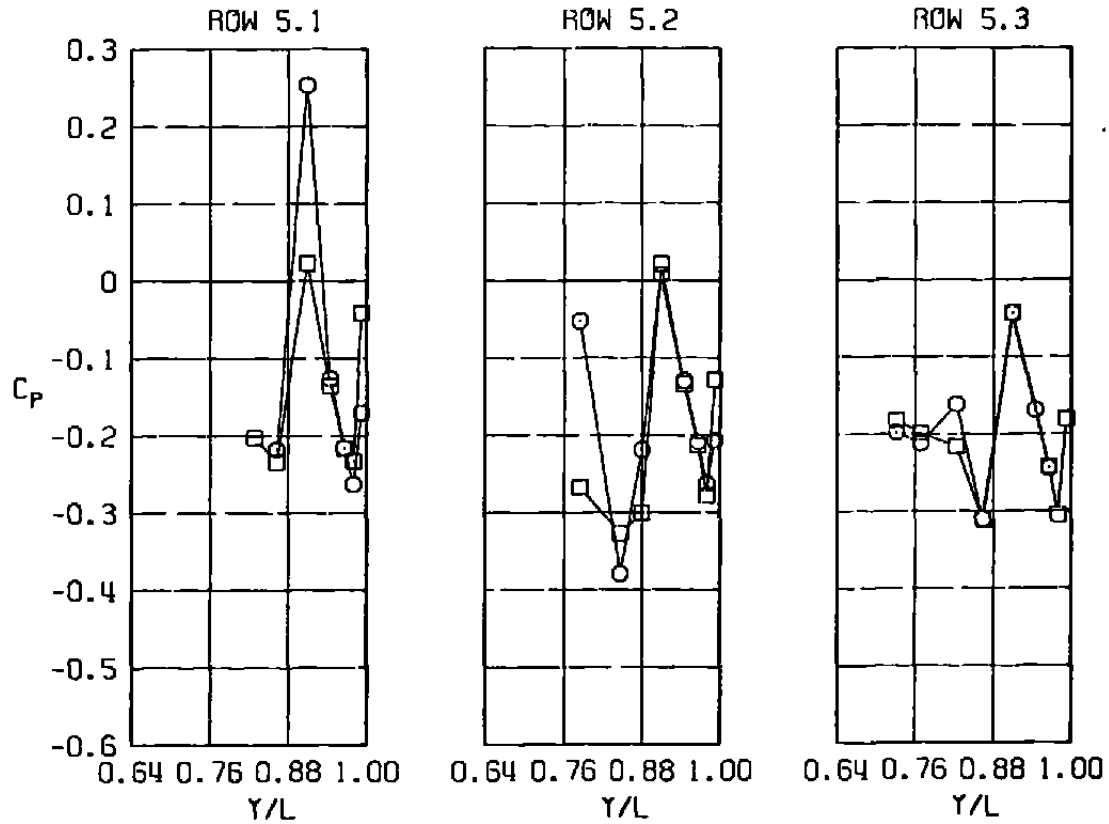
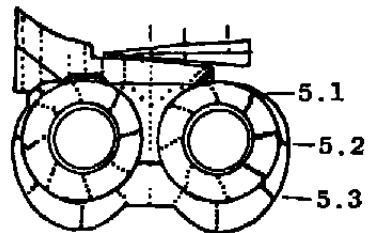
c. Row 3
Figure 40. Continued.

<u>SYM</u>	<u>M</u>	<u>ALPH</u>	<u>NPR</u>	<u>MFR</u>	<u>DELH</u>	<u>Re x 10⁻⁶</u>	<u>MODEL</u>	<u>CDNOZ</u>
□	1.20	0	5.02	0	0.02	2.50	NAB	0.0012
○	1.20	-0.01	5.13	0.627	-0.01	2.52	EPES	0.0016



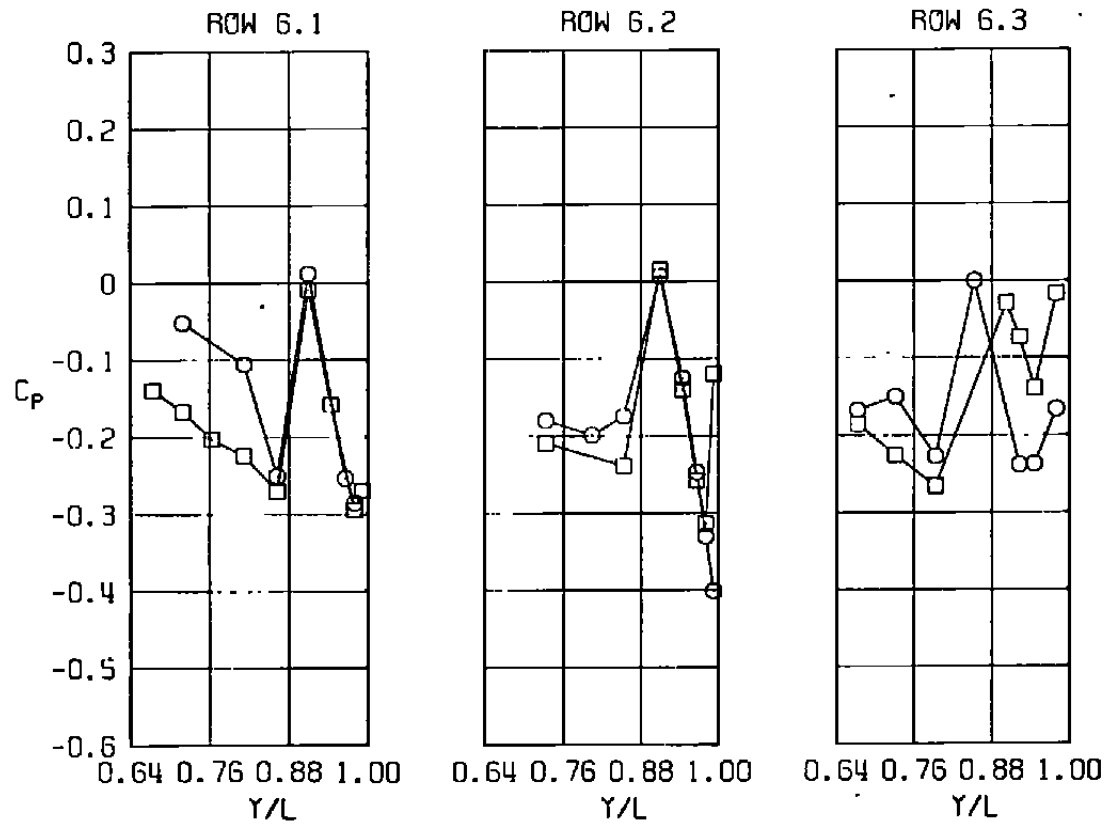
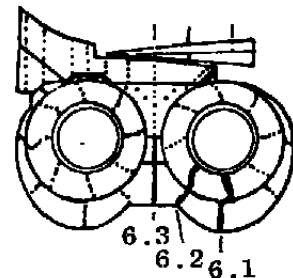
d. Row 4
Figure 40. Continued.

<u>SYM</u>	<u>M</u>	<u>ALPH</u>	<u>NPR</u>	<u>MFR</u>	<u>DELH</u>	<u>Re</u> $\times 10^{-6}$	<u>MODEL</u>	<u>CDNOZ</u>
□	1.20	0	5.02	0	0.02	2.50	NAB	0.0012
○	1.20	-0.01	5.13	0.627	-0.01	2.52	EPES	0.0016

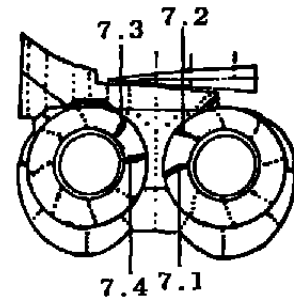
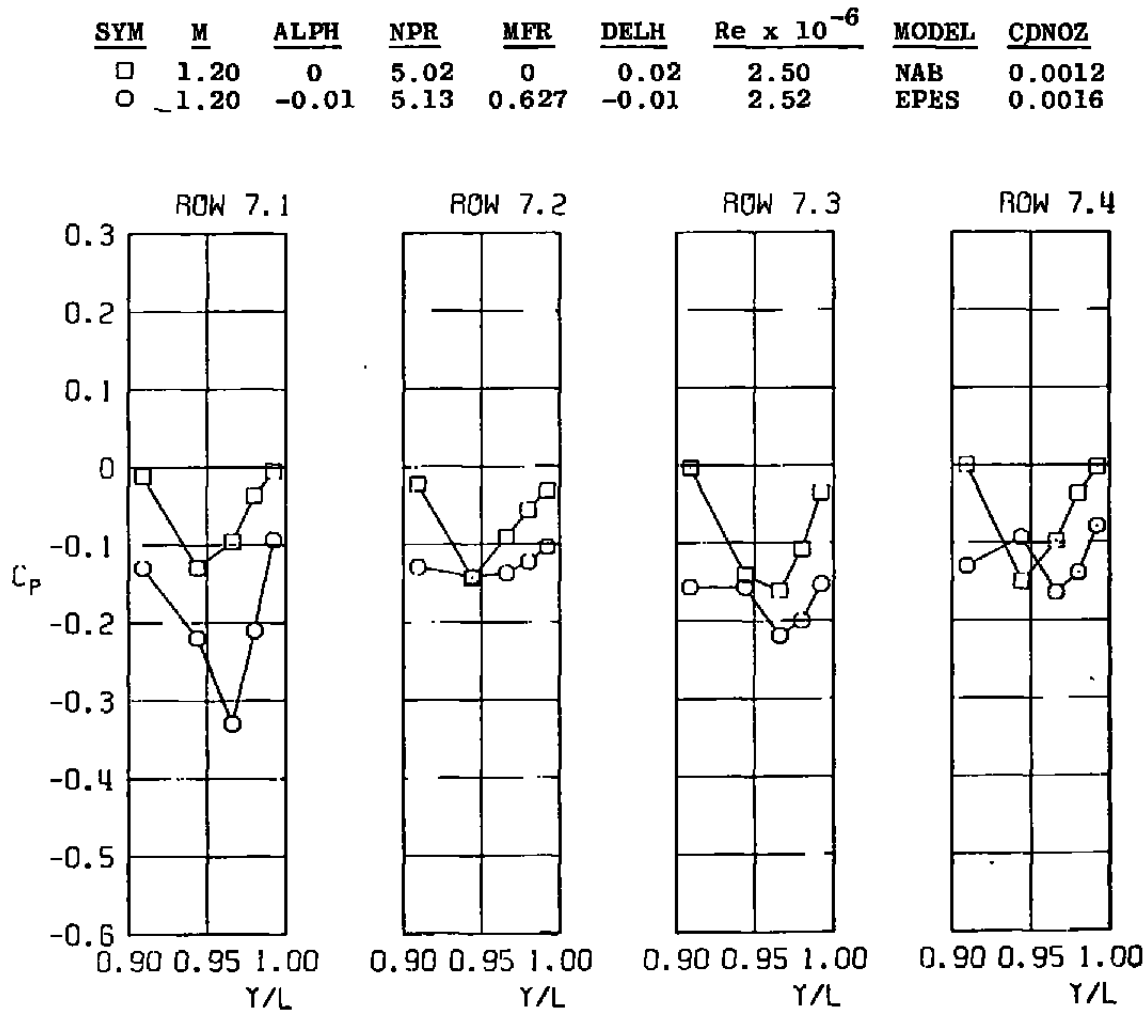


e. Row 5
Figure 40. Continued.

<u>SYM</u>	<u>M</u>	<u>ALPH</u>	<u>NPR</u>	<u>MFR</u>	<u>DELH</u>	<u>Rc x 10⁻⁶</u>	<u>MODEL</u>	<u>CDNOZ</u>
□	1.20	0	5.02	0	0.02	2.50	NAB	0.0012
O	1.20	-0.01	5.13	0.627	-0.01	2.52	EPES	0.0016

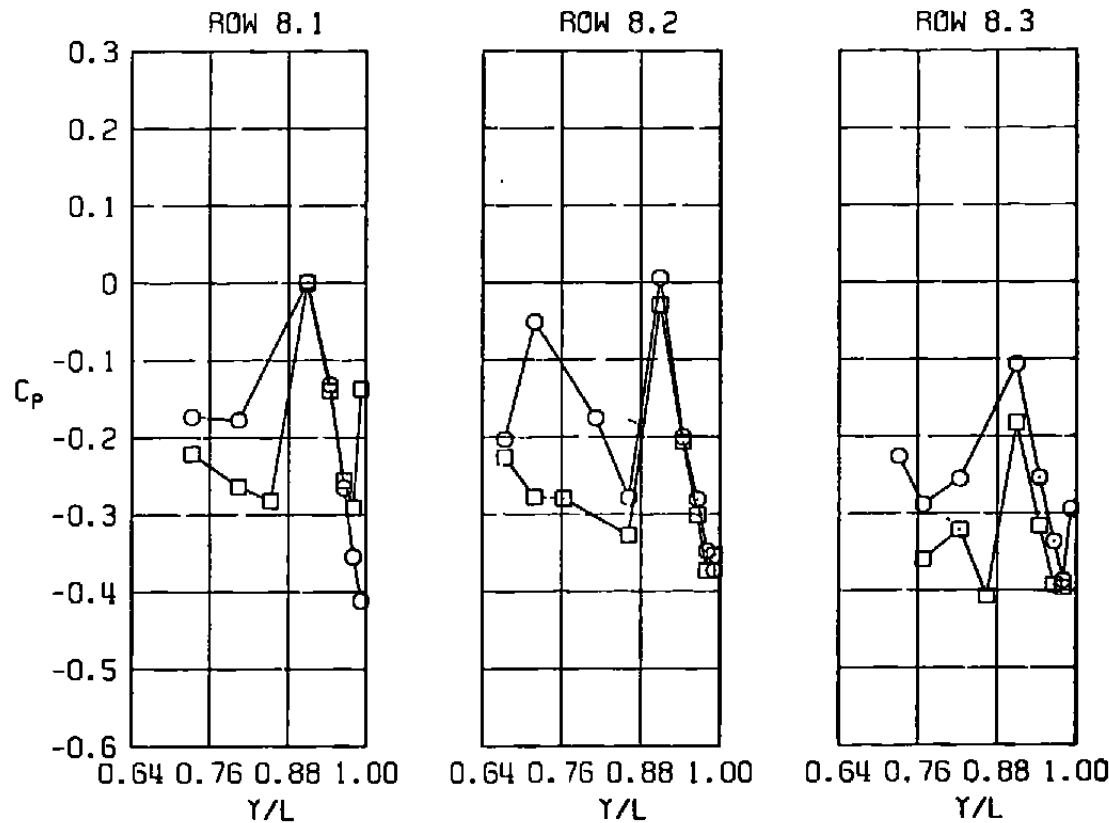
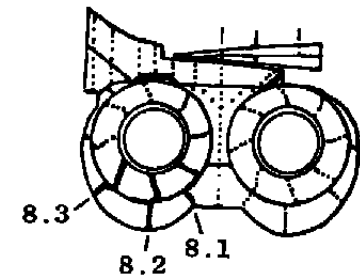


f. Row 6
Figure 40. Continued.



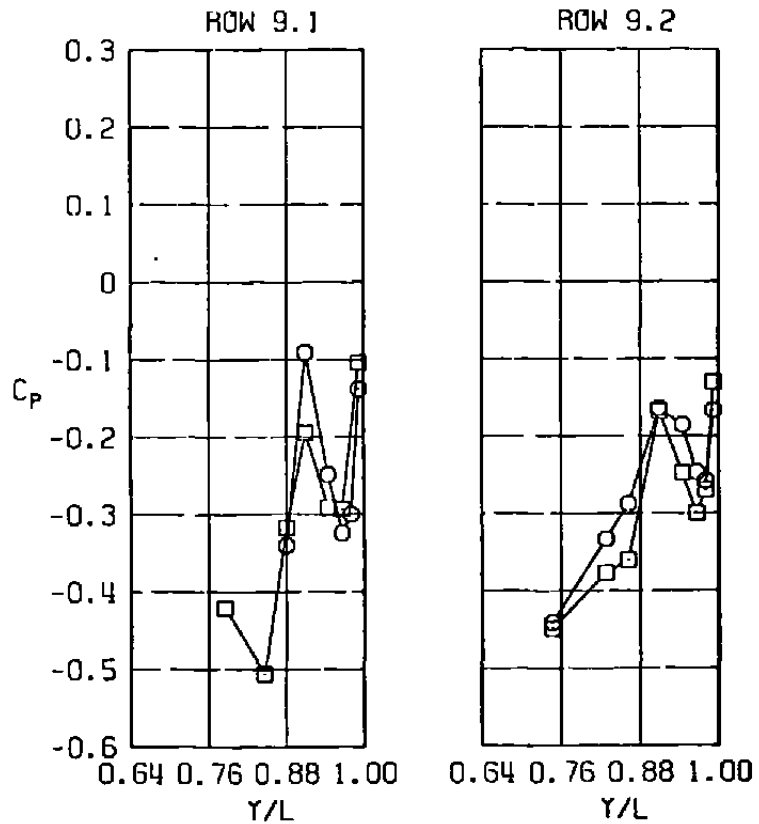
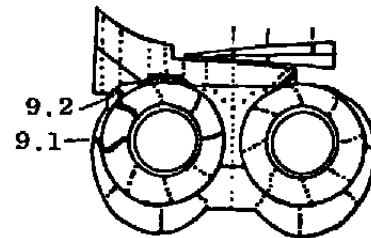
g. Row 7
Figure 40. Continued.

<u>SYM</u>	<u>M</u>	<u>ALPH</u>	<u>NPR</u>	<u>MFR</u>	<u>DELH</u>	<u>Re x 10⁻⁶</u>	<u>MODEL</u>	<u>CDNOZ</u>
□	1.20	0	5.02	0	0.02	2.50	NAB	0.0012
○	1.20	-0.01	5.13	0.627	-0.01	2.52	EPES	0.0016



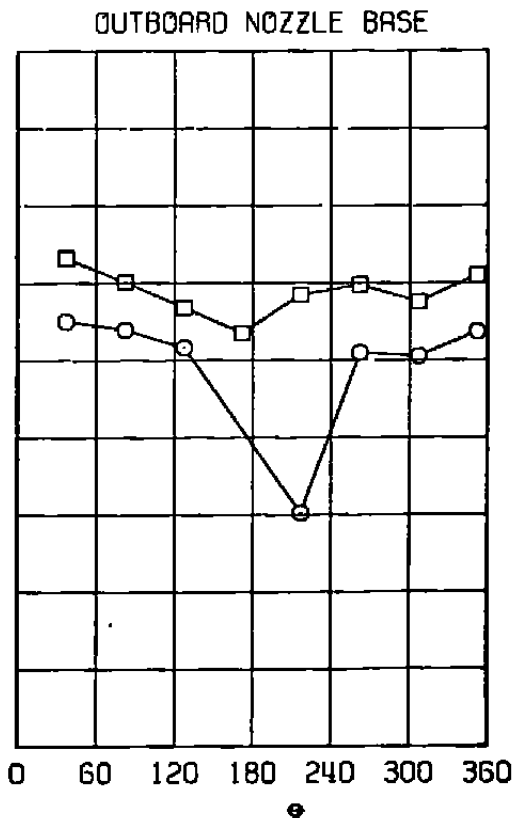
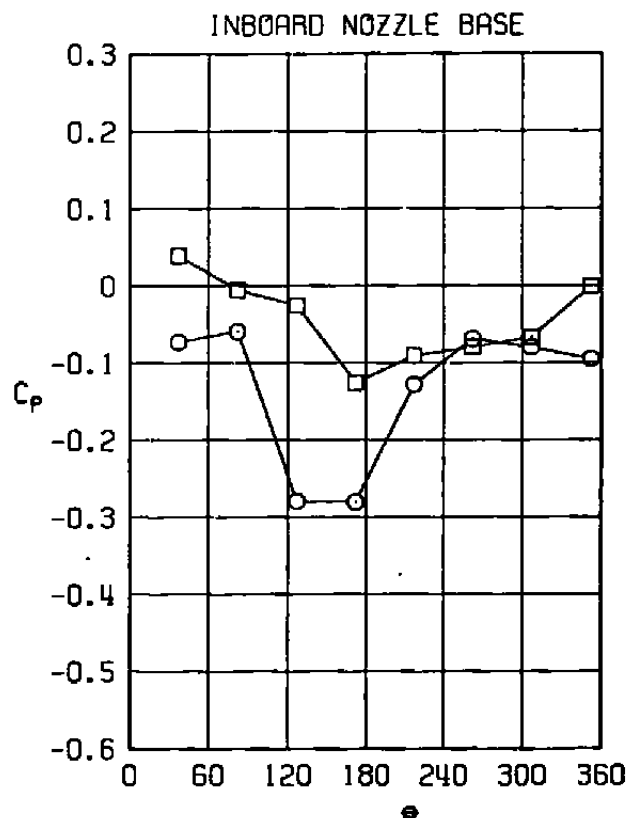
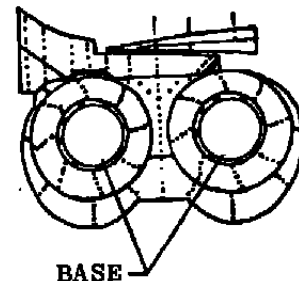
h. Row 8
Figure 40. Continued.

<u>SYM</u>	<u>M</u>	<u>ALPH</u>	<u>NPR</u>	<u>MFR</u>	<u>DELH</u>	<u>Re x 10⁻⁶</u>	<u>MODEL</u>	<u>CDNOZ</u>
□	1.20	0	5.02	0	0.02	2.50	NAB	0.0012
○	1.20	-0.01	5.13	0.627	-0.01	2.52	EPES	0.0016



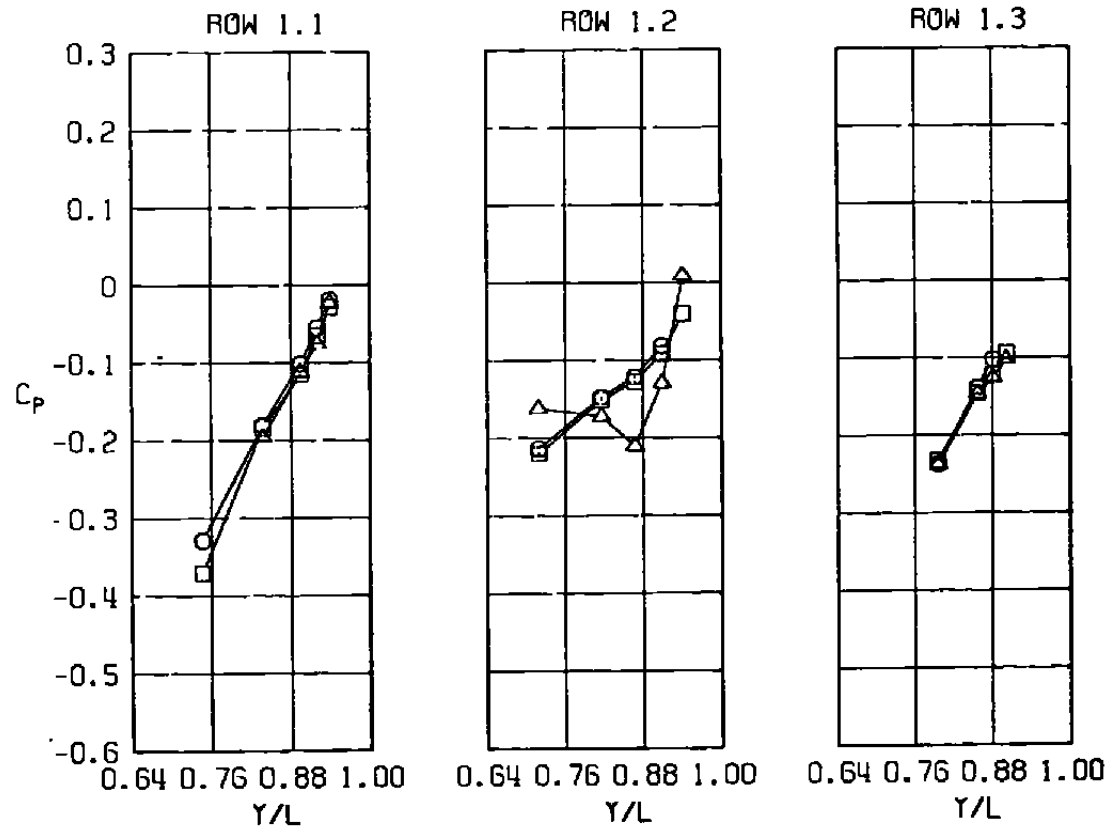
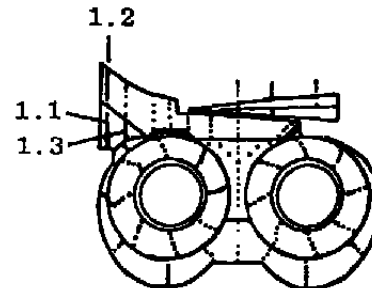
i. Row 9
Figure 40. Continued.

<u>SYM</u>	<u>M</u>	<u>ALPH</u>	<u>NPR</u>	<u>MFR</u>	<u>DElh</u>	<u>Re</u> $\times 10^{-6}$	<u>MODEL</u>	<u>CDNOZ</u>
□	1.20	0	5.02	0	0.02	2.50	NAB	0.0012
○	1.20	-0.01	5.13	0.627	-0.01	2.52	EPES	0.0016



j. Nozzle base
Figure 40. Concluded.

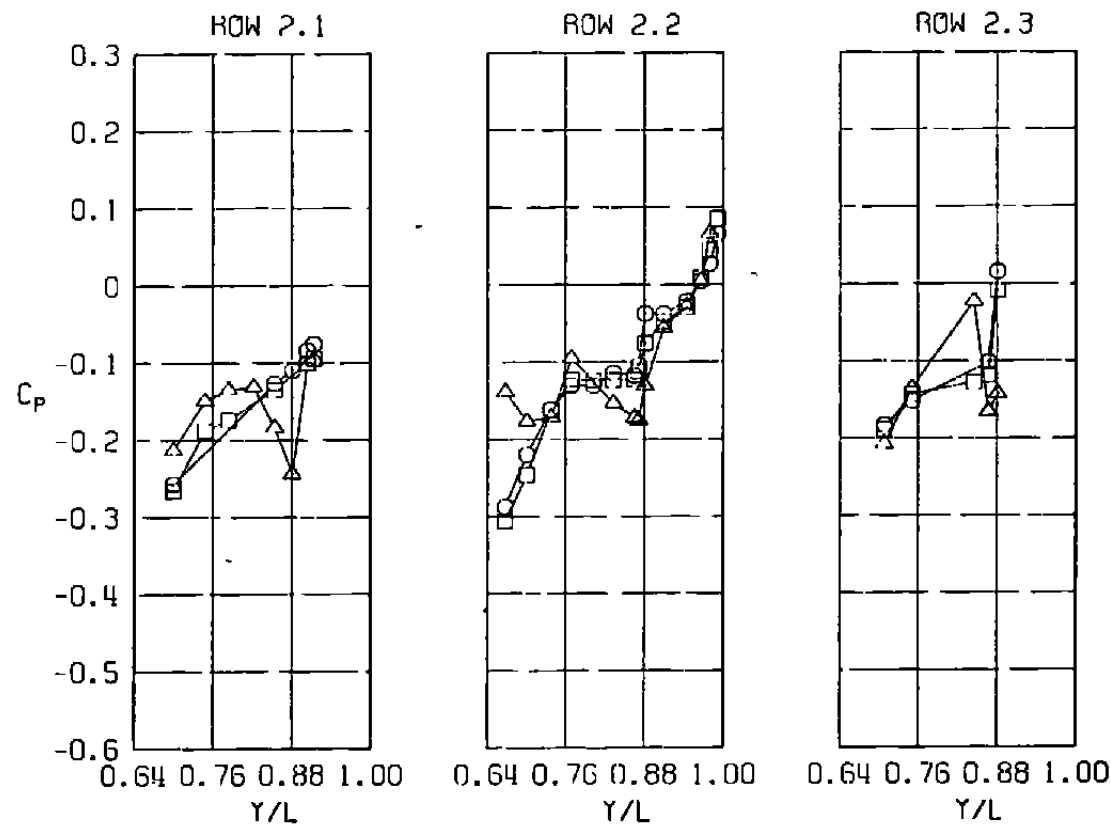
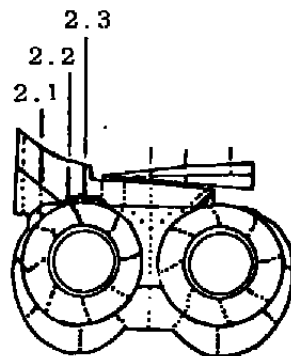
<u>SYM</u>	<u>M</u>	<u>ALPH</u>	<u>NPR</u>	<u>MFR</u>	<u>DELH</u>	<u>Re</u> $\times 10^{-6}$	<u>MODEL</u>	<u>CDNOZ</u>
□	0.85	3.45	2.73	0.0	0.74	2.50	NAB	-0.0002
○	0.85	3.43	2.87	0.474	0.74	2.53	EPES	0.0001
△	0.85	3.45	2.65	0.563	0.78	3.79	FLIGHT	0



a. Row 1

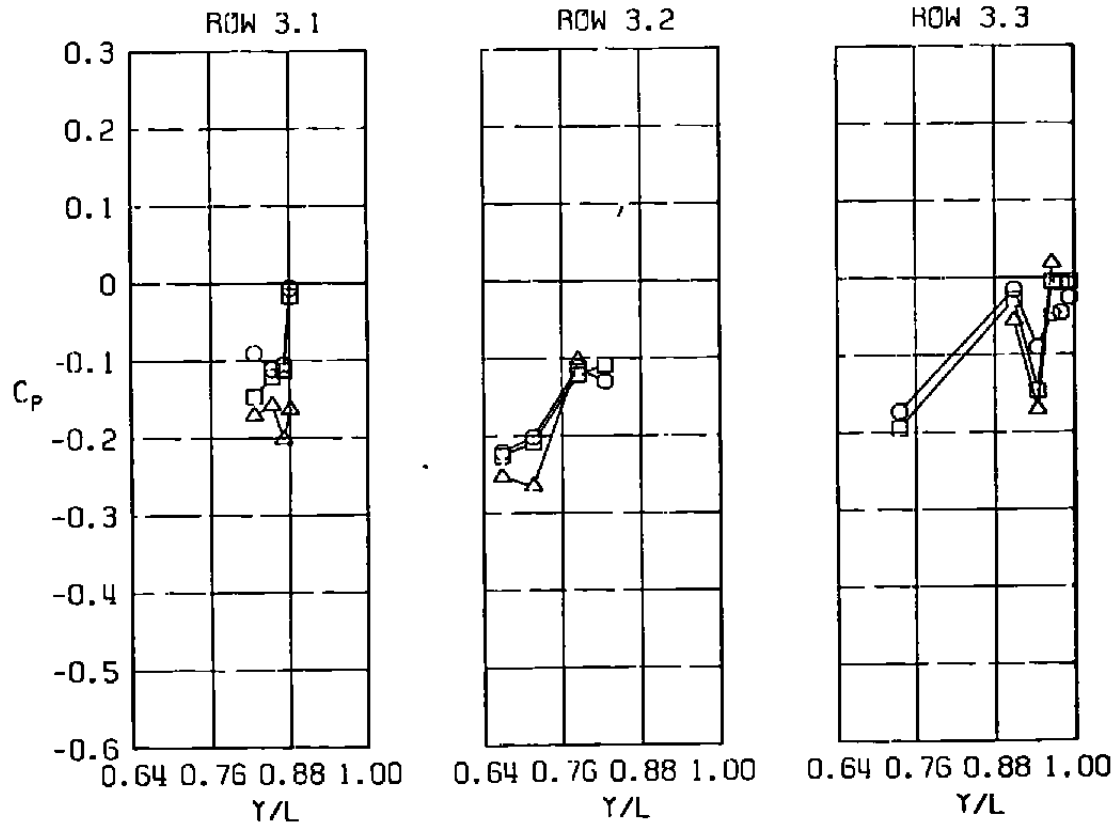
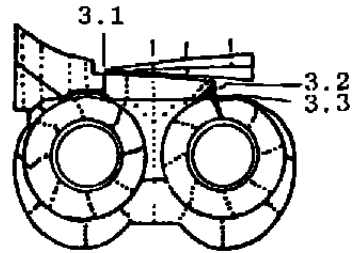
Figure 41. Comparison of nozzle afterbody pressure distributions for the EPES and NAB models and the flight vehicle, $M = 0.85$, $\alpha = 3.45$ deg.

<u>SYM</u>	<u>M</u>	<u>ALPH</u>	<u>NPR</u>	<u>MFR</u>	<u>DELH</u>	<u>Re</u> $\times 10^{-6}$	<u>MODEL</u>	<u>CDNOZ</u>
□	0.85	3.45	2.73	0.0	0.74	2.50	NAB	-0.0002
○	0.85	3.43	2.87	0.474	0.74	2.53	FPES	0.0001
△	0.85	3.45	2.65	0.563	0.78	3.79	FLIGHT	0



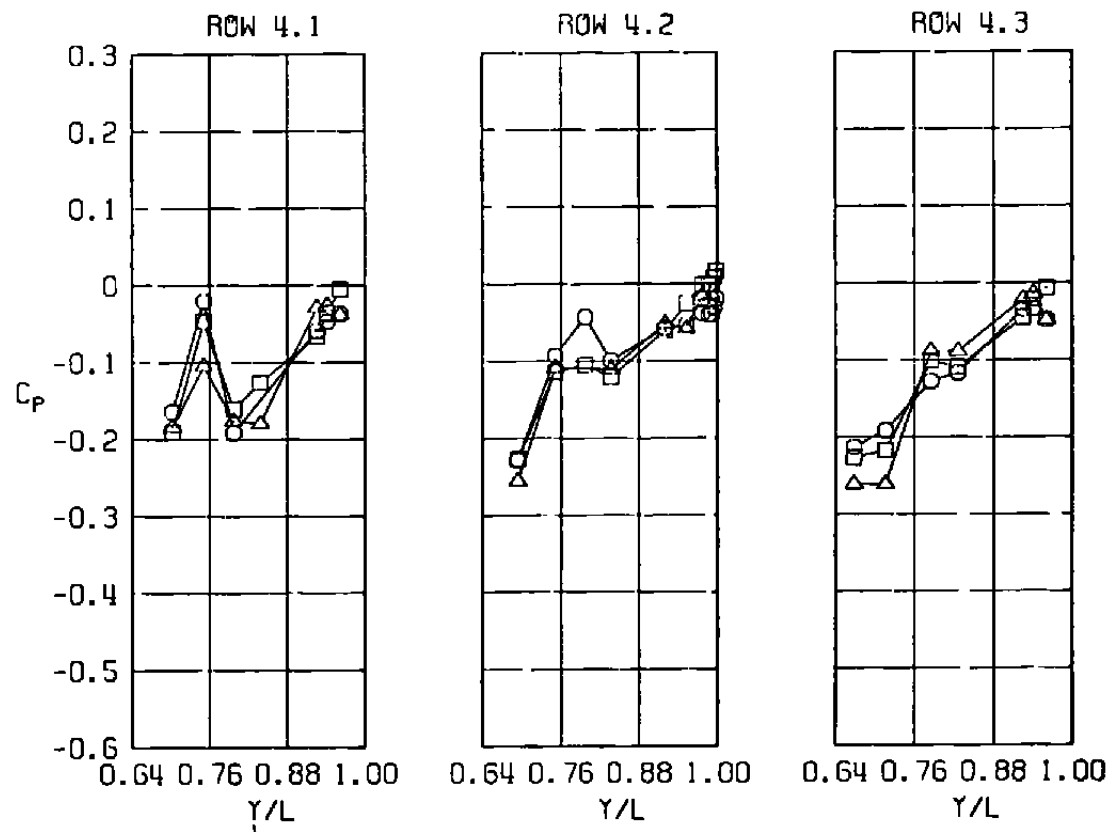
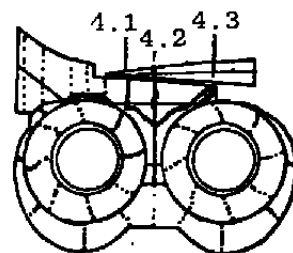
b. Row 2
Figure 41. Continued.

<u>SYM</u>	<u>M</u>	<u>ALPH</u>	<u>NPR</u>	<u>MFR</u>	<u>DELH</u>	<u>Re</u> $\times 10^{-6}$	<u>MODEL</u>	<u>CDNOZ</u>
□	0.85	3.45	2.73	0.0	0.74	2.50	NAB	-0.0002
○	0.85	3.43	2.87	0.474	0.74	2.53	EPES	0.0001
△	0.85	3.45	2.65	0.563	0.78	3.79	FLIGHT	0



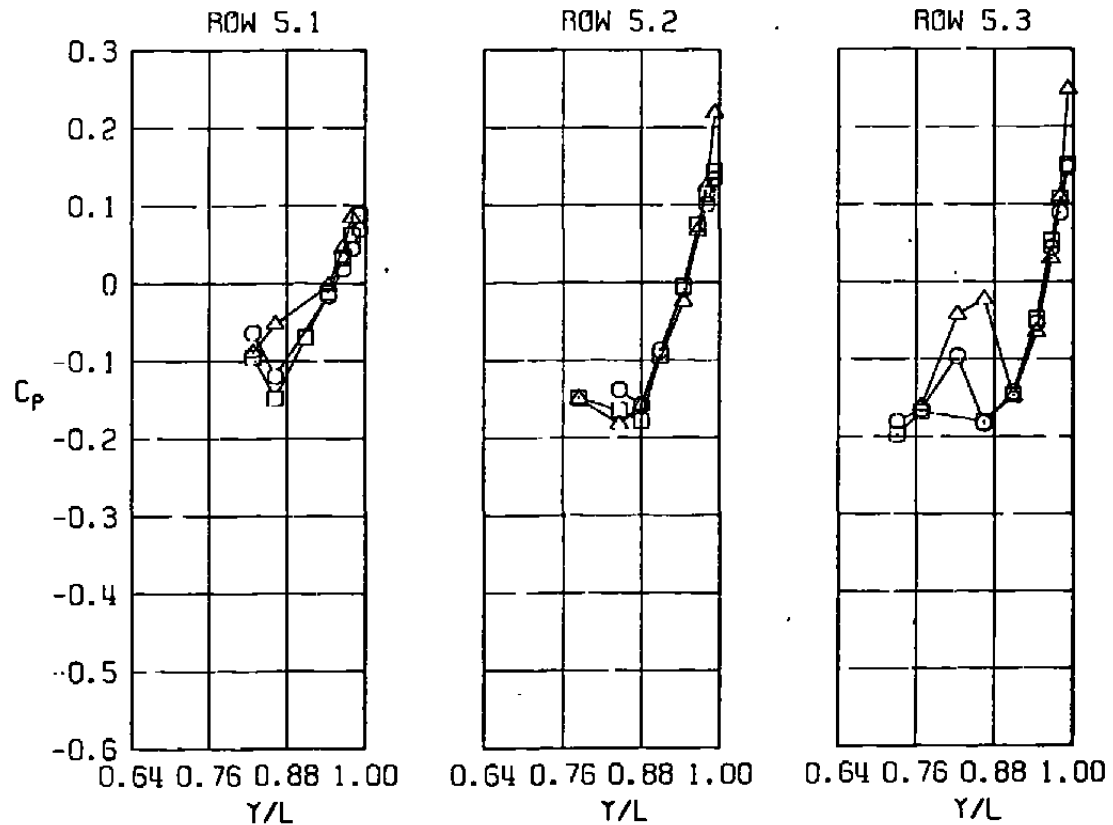
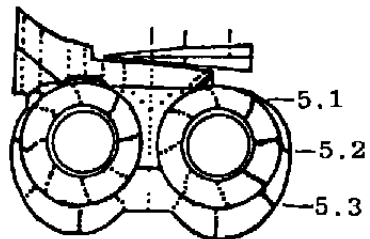
c. Row 3
Figure 41. Continued.

<u>SYM</u>	<u>M</u>	<u>ALPH</u>	<u>NPR</u>	<u>MFR</u>	<u>DELH</u>	<u>Re x 10⁻⁶</u>	<u>MODEL</u>	<u>CDNOZ</u>
□	0.85	3.45	2.73	0.0	0.74	2.50	NAB	-0.0002
○	0.85	3.43	2.87	0.474	0.74	2.53	EPES	0.0001
△	0.85	3.45	2.65	0.563	0.78	3.79	FLIGHT	0



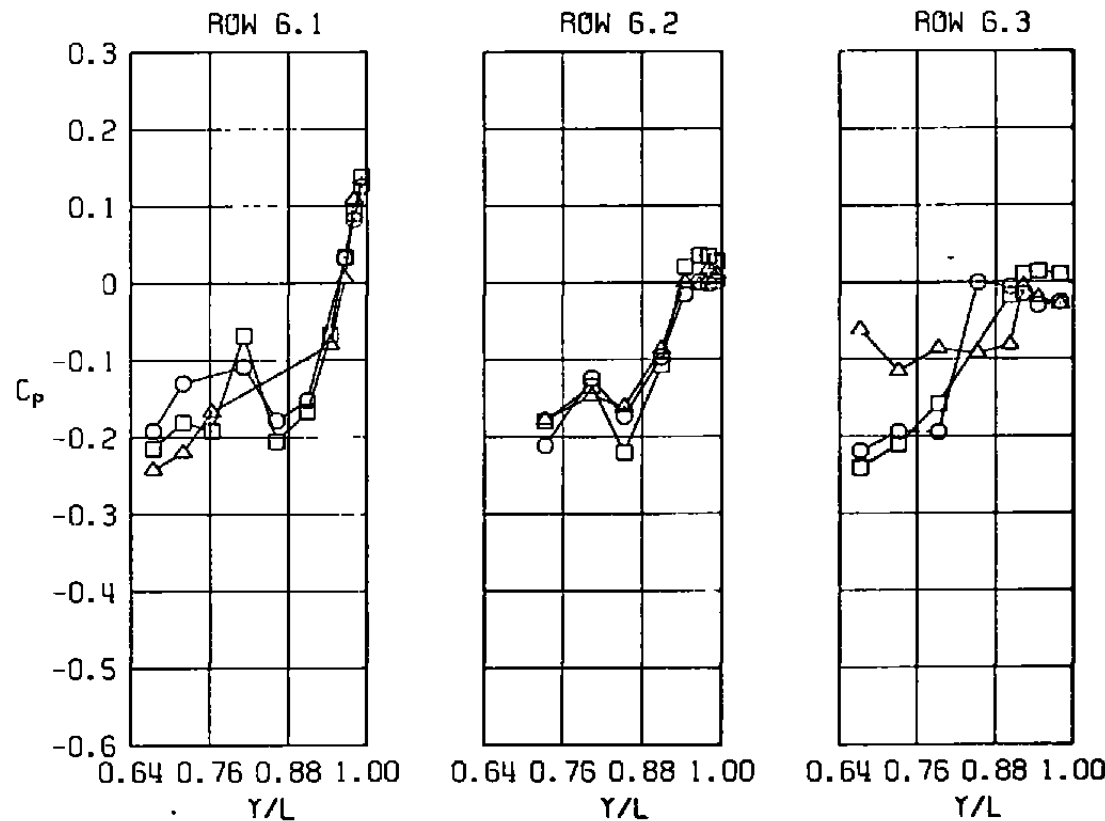
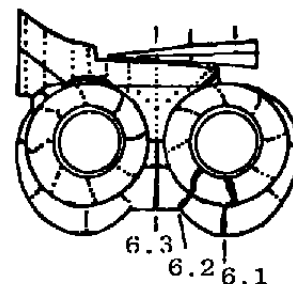
d. Row 4
Figure 41. Continued.

<u>SYM</u>	<u>M</u>	<u>ALPH</u>	<u>NPR</u>	<u>MFR</u>	<u>DELH</u>	<u>Re</u> $\times 10^{-6}$	<u>MODEL</u>	<u>CDNOZ</u>
□	0.85	3.45	2.73	0.0	0.74	2.50	NAB	-0.0002
○	0.85	3.43	2.87	0.474	0.74	2.53	EPES	0.0001
△	0.85	3.45	2.65	0.563	0.78	3.79	FLIGHT	0

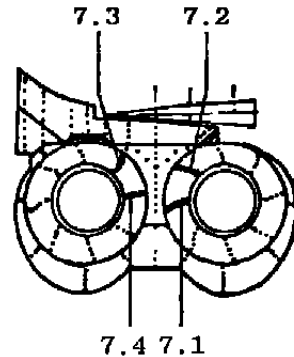
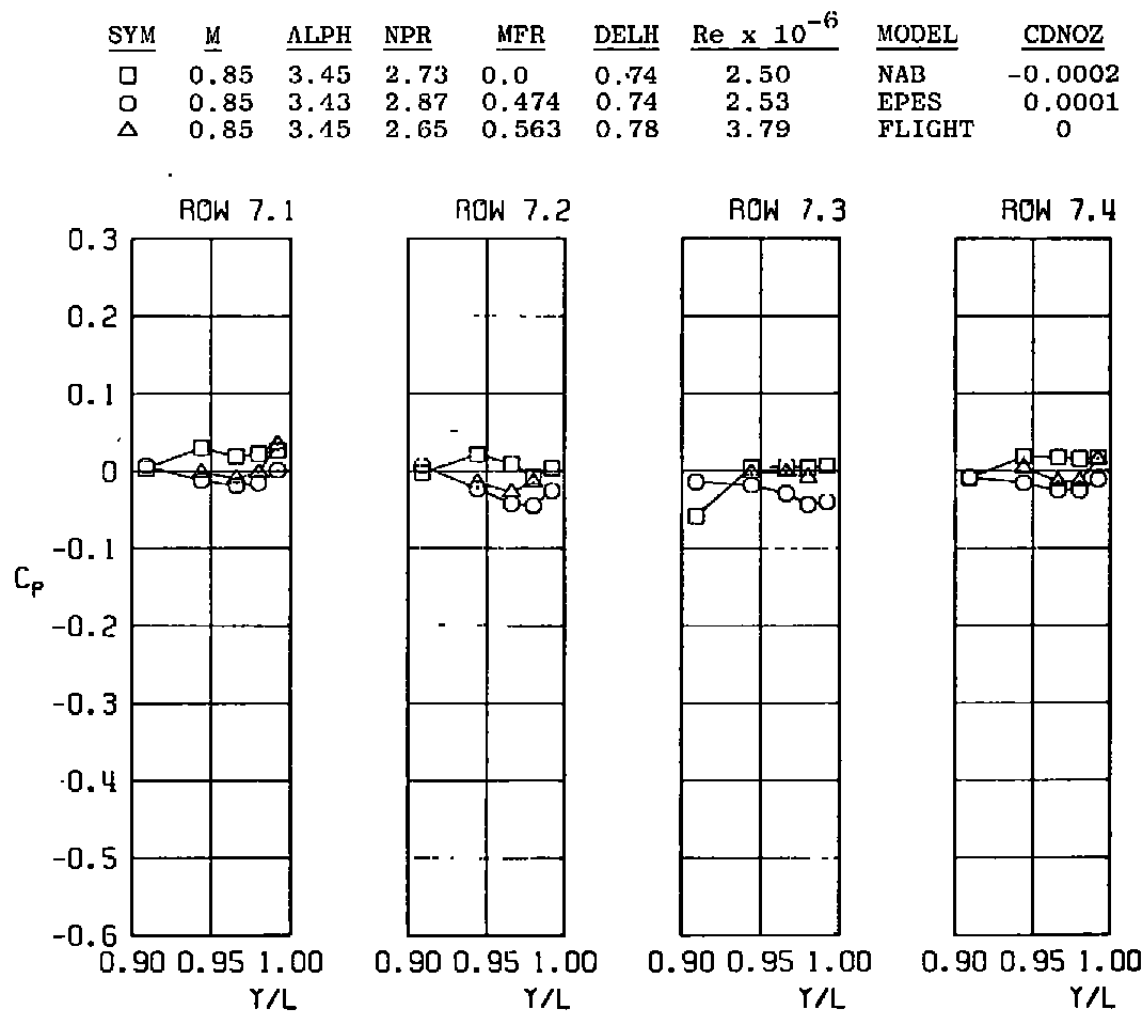


e. Row 5
Figure 41. Continued.

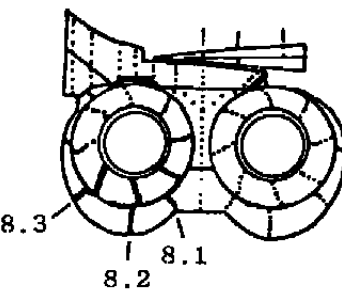
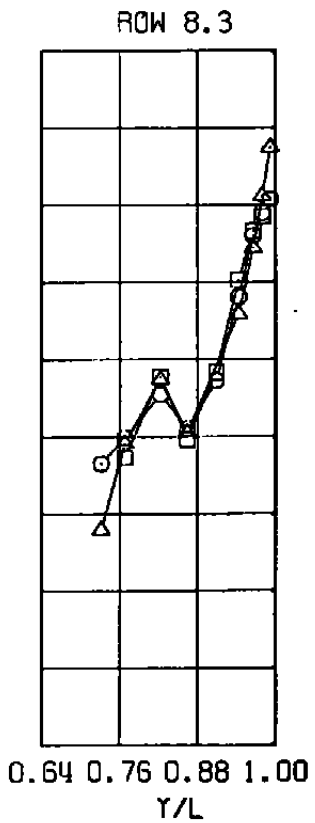
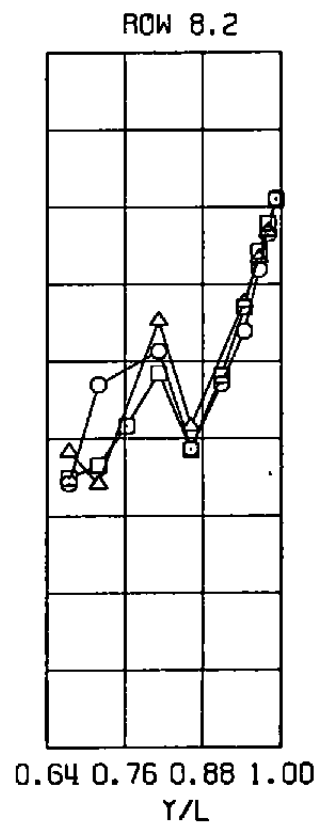
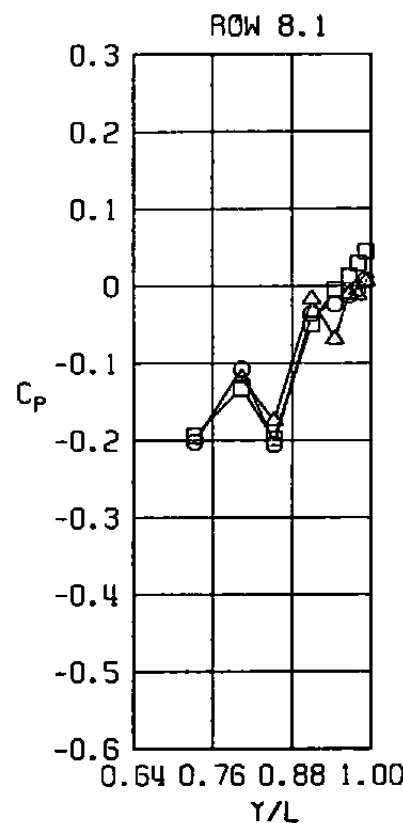
<u>SYM</u>	<u>M</u>	<u>ALPH</u>	<u>NPR</u>	<u>MFR</u>	<u>DELH</u>	<u>Re x 10⁻⁶</u>	<u>MODEL</u>	<u>CDNOZ</u>
□	0.85	3.45	2.73	0.0	0.74	2.50	NAB	-0.0002
○	0.85	3.43	2.87	0.474	0.74	2.53	EPES	0.0001
△	0.85	3.45	2.65	0.563	0.78	3.79	FLIGHT	0



f. Row 6
Figure 41. Continued.

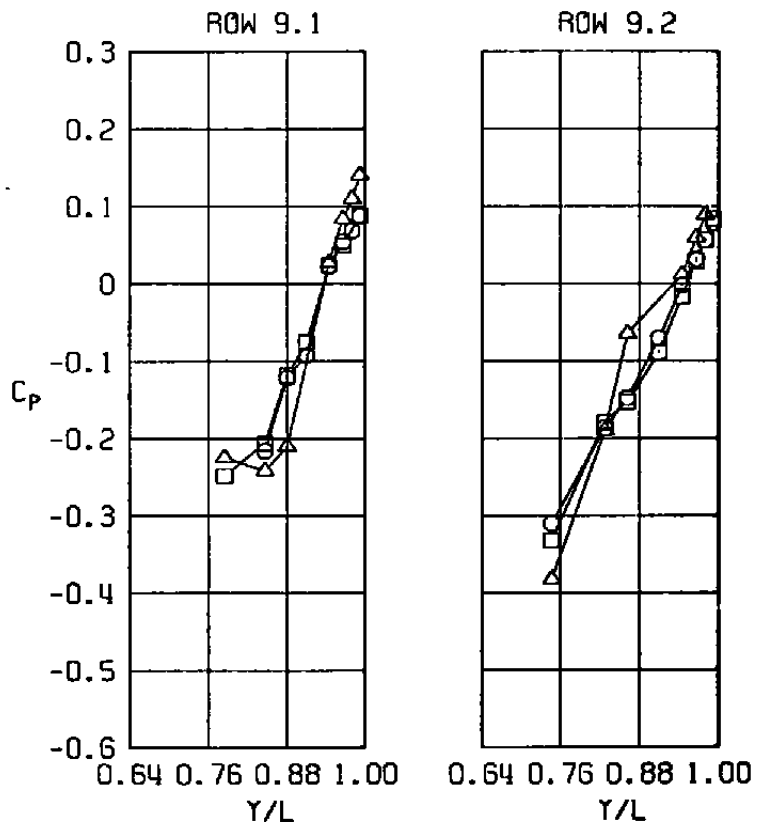
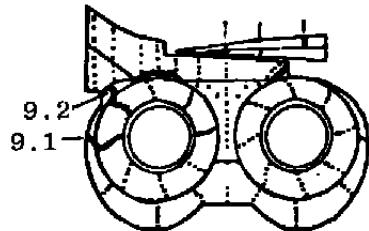


<u>SYM</u>	<u>M</u>	<u>ALPH</u>	<u>NPR</u>	<u>MFR</u>	<u>DELH</u>	<u>Re x 10⁻⁶</u>	<u>MODEL</u>	<u>CDNOZ</u>
□	0.85	3.45	2.73	0.0	0.74	2.50	NAB	-0.0002
○	0.85	3.43	2.87	0.474	0.74	2.53	EPES	0.0001
△	0.85	3.45	2.65	0.563	0.78	3.79	FLIGHT	0



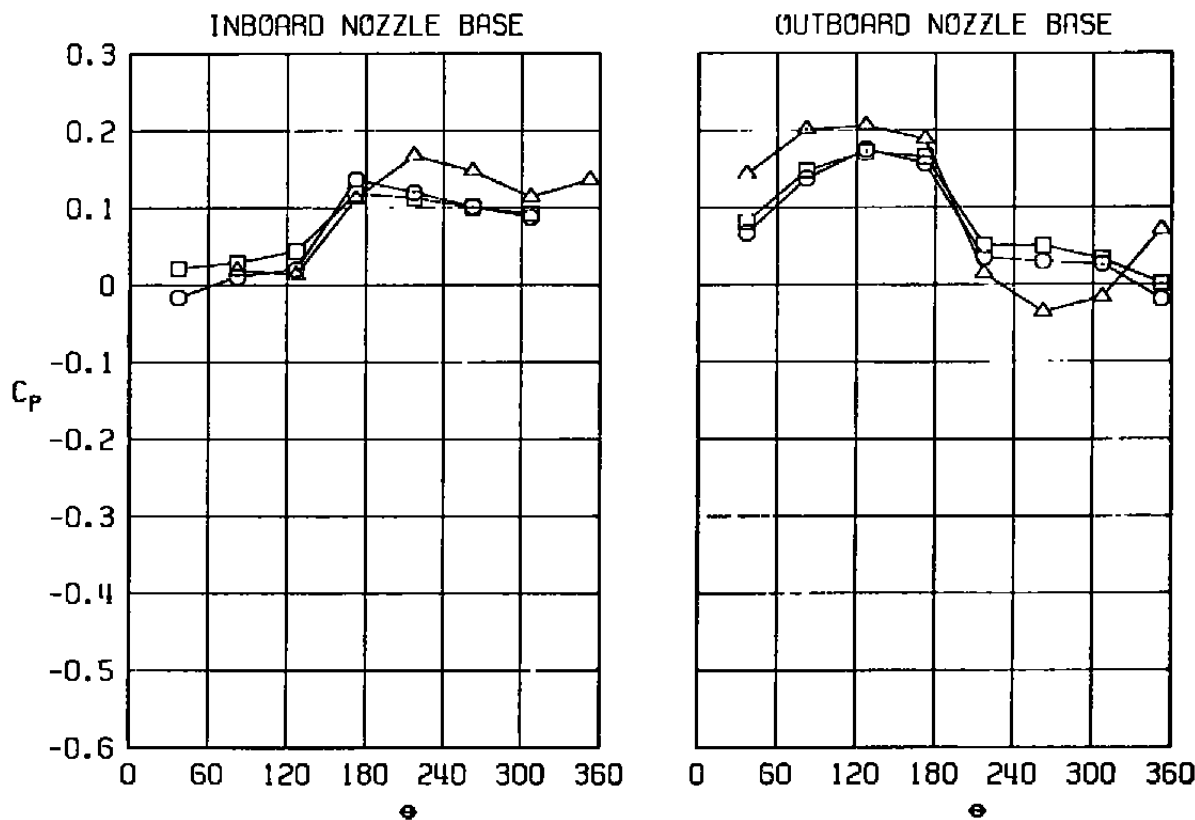
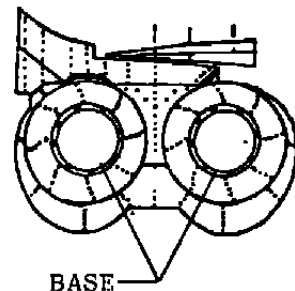
h. Row 8
Figure 41. Continued.

SYM	M	ALPH	NPR	MFR	DELH	$Re \times 10^{-6}$	MODEL	CDNOZ
□	0.85	3.45	2.73	0.0	0.74	2.50	NAB	-0.0002
○	0.85	3.43	2.87	0.474	0.74	2.53	EPES	0.0001
△	0.85	3.45	2.65	0.563	0.78	3.79	FLIGHT	0



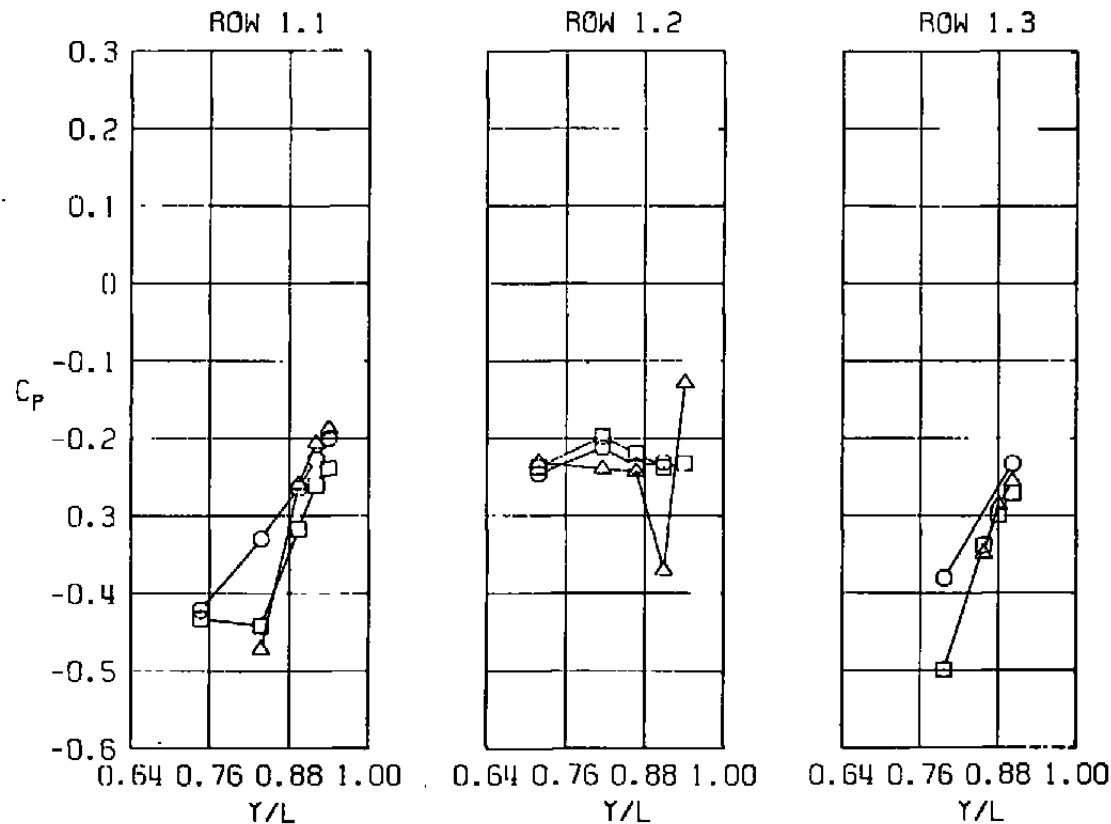
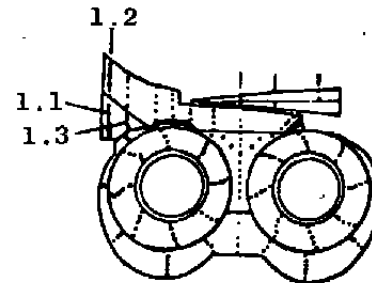
i. Row 9
Figure 41. Continued.

<u>SYM</u>	<u>M</u>	<u>ALPH</u>	<u>NPR</u>	<u>MFR</u>	<u>DELH</u>	<u>Re</u> $\times 10^{-6}$	<u>MODEL</u>	<u>CDNOZ</u>
□	0.85	3.45	2.73	0.0	0.74	2.50	NAB	-0.0002
○	0.85	3.43	2.87	0.474	0.74	2.53	EPES	0.0001
△	0.85	3.45	2.65	0.563	0.78	3.79	FLIGHT	0



j. Nozzle base
Figure 41. Concluded.

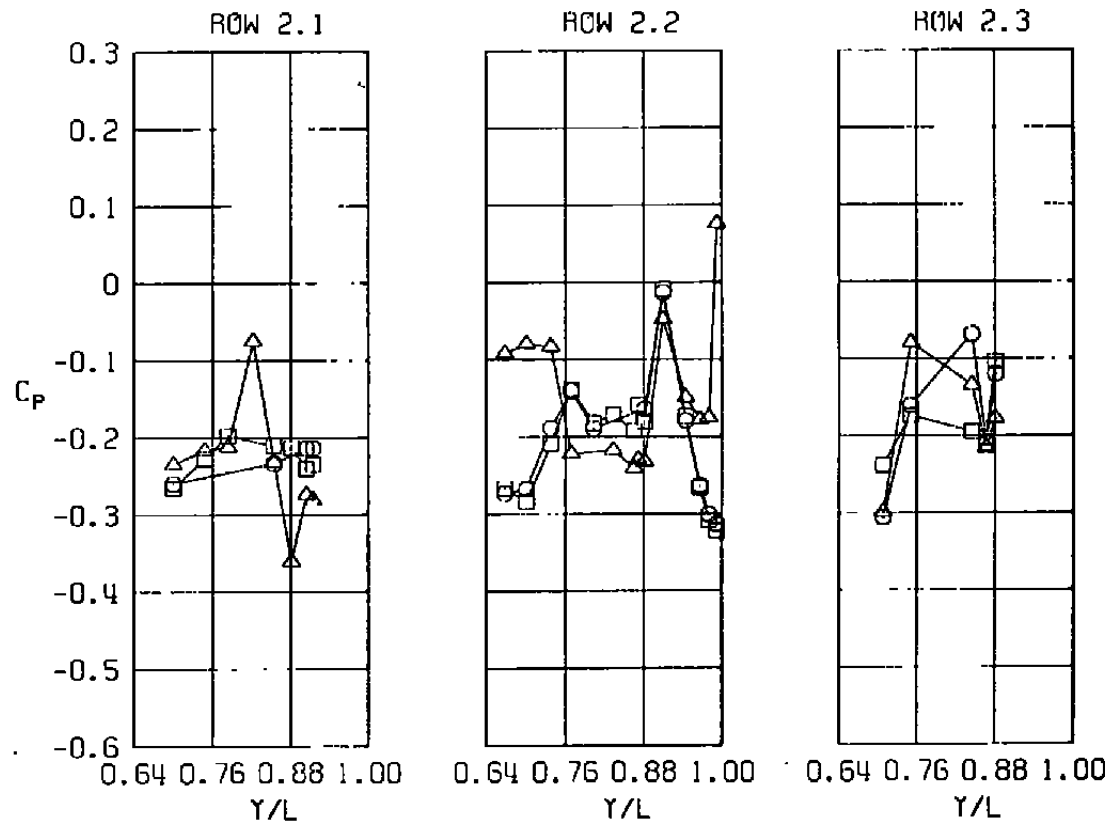
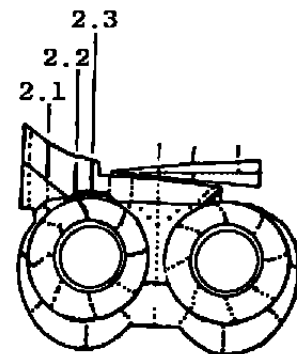
SYM	M	ALPH	NPR	MFR	DELH	$Re \times 10^{-6}$	MODEL	CDNOZ
□	1.20	2.80	4.40	0	0.22	2.48	NAB	0.0015
○	1.20	2.79	4.55	0.641	0.29	2.52	EPES	0.0017
△	1.20	2.82	4.28	0.645	0.23	3.22	FLIGHT	0.0008



a. Row 1

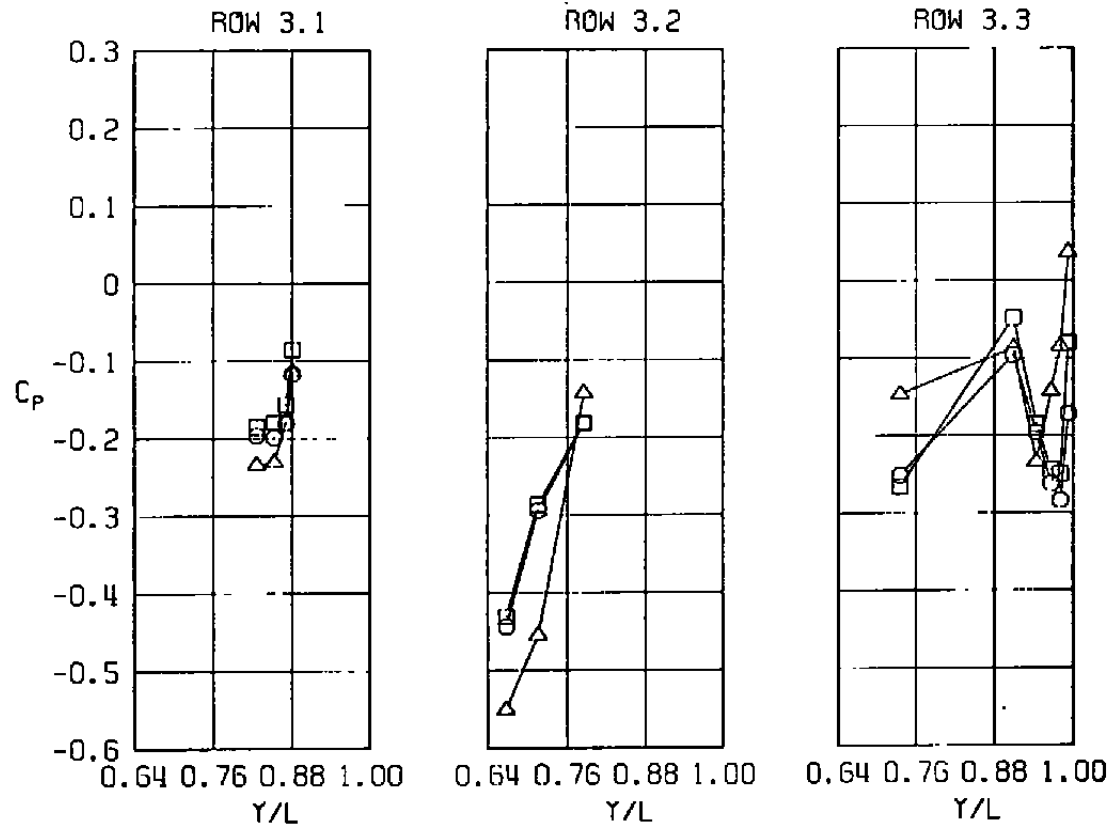
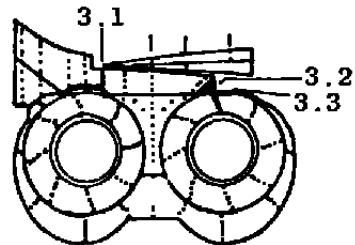
Figure 42. Comparison of nozzle afterbody pressure distributions for the EPES and NAB models and the flight vehicle, $M = 1.20$, $\alpha = 2.8$ deg.

<u>SYM</u>	<u>M</u>	<u>ALPH</u>	<u>NPR</u>	<u>MFR</u>	<u>DELH</u>	<u>Re x 10⁻⁶</u>	<u>MODEL</u>	<u>CDNOZ</u>
□	1.20	2.80	4.40	0	0.22	2.48	NAB	0.0015
○	1.20	2.79	4.55	0.641	0.29	2.52	EPES	0.0017
△	1.20	2.82	4.28	0.645	0.23	3.22	FLIGHT	0.0008



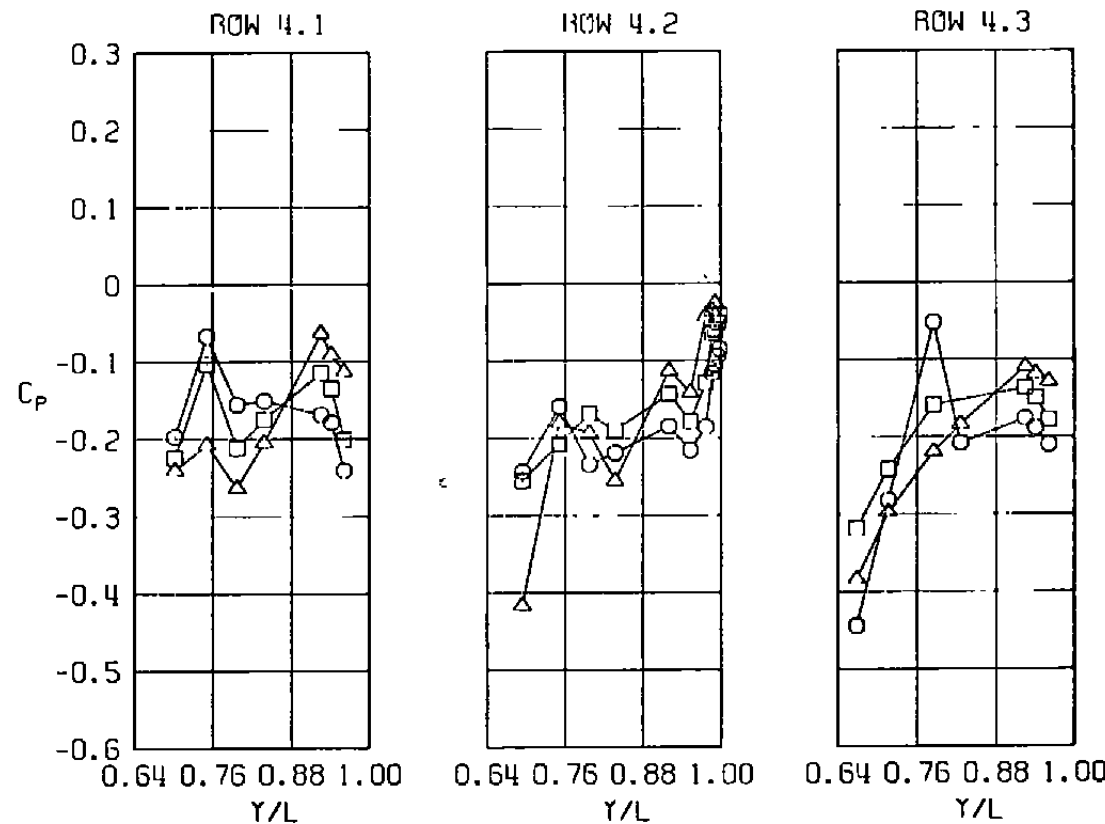
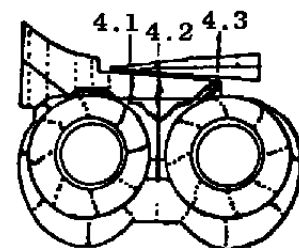
b. Row 2
Figure 42. Continued.

<u>SYM</u>	<u>M</u>	<u>ALPH</u>	<u>NPR</u>	<u>MFR</u>	<u>DELH</u>	<u>Re x 10⁻⁶</u>	<u>MODEL</u>	<u>CDNOZ</u>
□	1.20	2.80	4.40	0	0.22	2.48	NAB	0.0015
○	1.20	2.79	4.55	0.641	0.29	2.52	EPES	0.0017
△	1.20	2.82	4.28	0.645	0.23	3.22	FLIGHT	0.0008



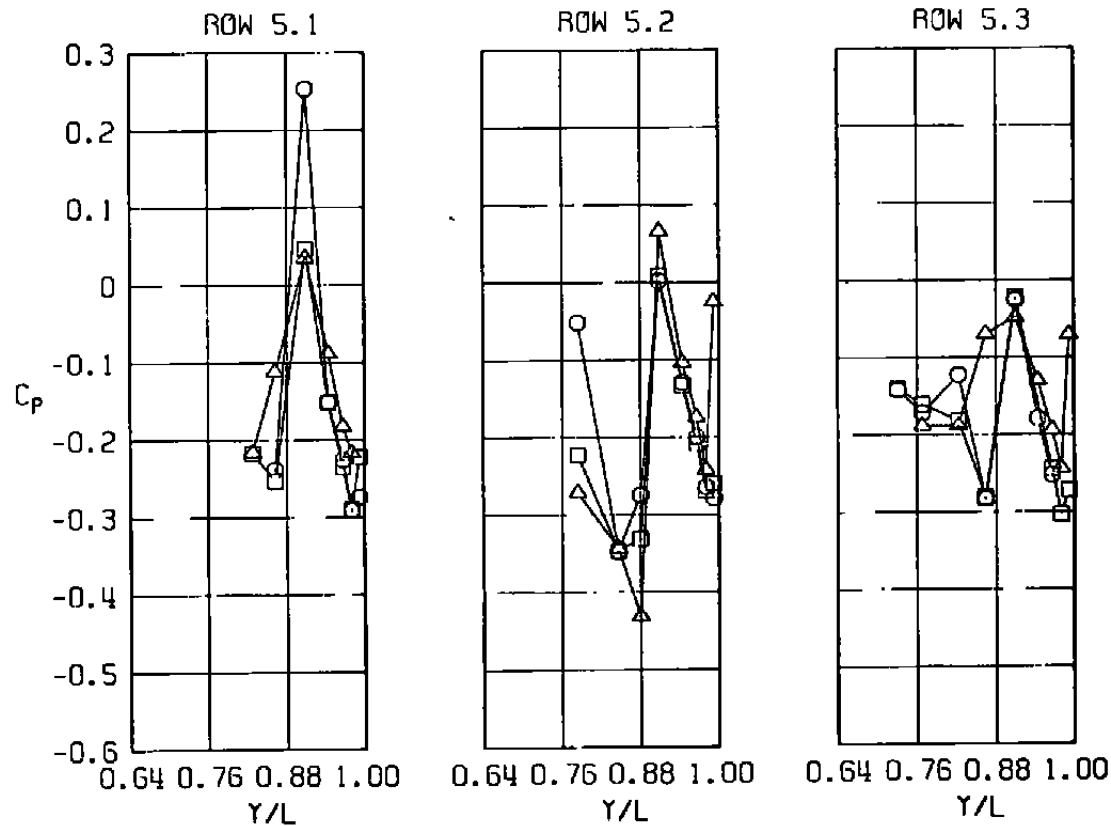
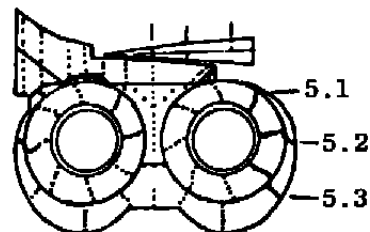
c. Row 3
Figure 42. Continued.

<u>SYM</u>	<u>M</u>	<u>ALPH</u>	<u>NPR</u>	<u>MFR</u>	<u>DELH</u>	<u>Re x 10⁻⁶</u>	<u>MODEL</u>	<u>CDNOZ</u>
□	1.20	2.80	4.40	0	0.22	2.48	NAB	0.0015
○	1.20	2.79	4.55	0.641	0.29	2.52	EPES	0.0017
△	1.20	2.82	4.28	0.645	0.23	3.22	FLIGHT	0.0008



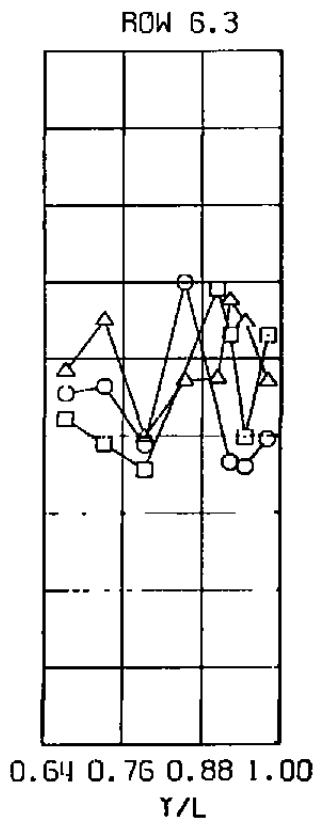
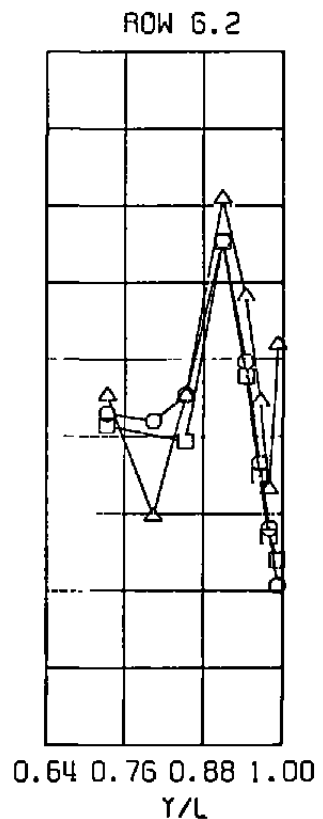
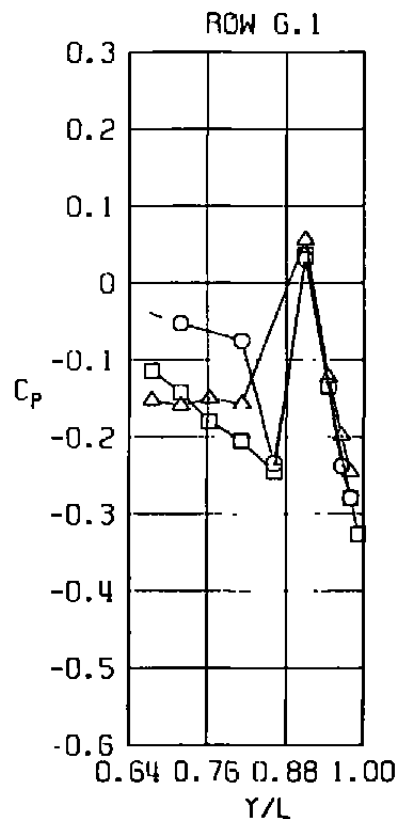
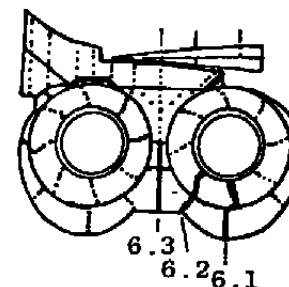
d. Row 4
Figure 42. Continued.

<u>SYM</u>	<u>M</u>	<u>ALPH</u>	<u>NRP</u>	<u>MFR</u>	<u>DELH</u>	<u>Re</u> $\times 10^{-6}$	<u>MODEL</u>	<u>CDNOZ</u>
□	1.20	2.80	4.40	0	0.22	2.48	NAB	0.0015
○	1.20	2.79	4.55	0.641	0.29	2.52	EPES	0.0017
△	1.20	2.82	4.28	0.645	0.23	3.22	FLIGHT	0.0008

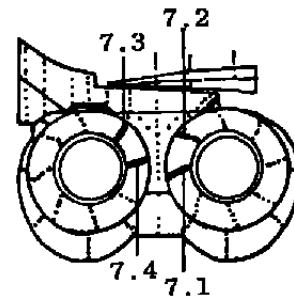
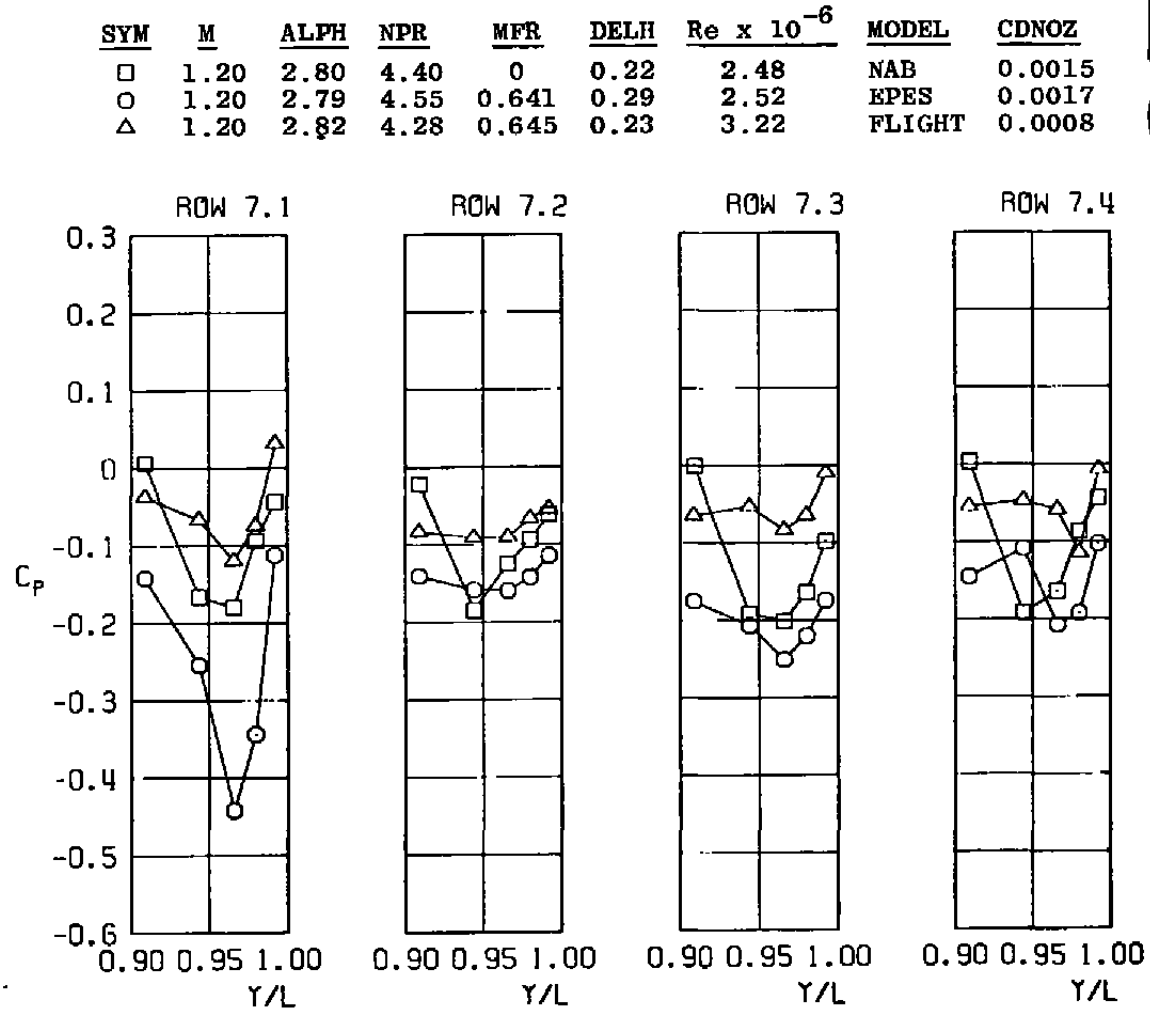


e. Row 5
Figure 42. Continued.

<u>SYM</u>	<u>M</u>	<u>ALPH</u>	<u>NPR</u>	<u>MFR</u>	<u>DELH</u>	<u>Re x 10⁻⁶</u>	<u>MODEL</u>	<u>CDNOZ</u>
□	1.20	2.80	4.40	0	0.22	2.48	NAB	0.0015
○	1.20	2.79	4.55	0.641	0.29	2.52	EPES	0.0017
△	1.20	2.82	4.28	0.645	0.23	3.22	FLIGHT	0.0008

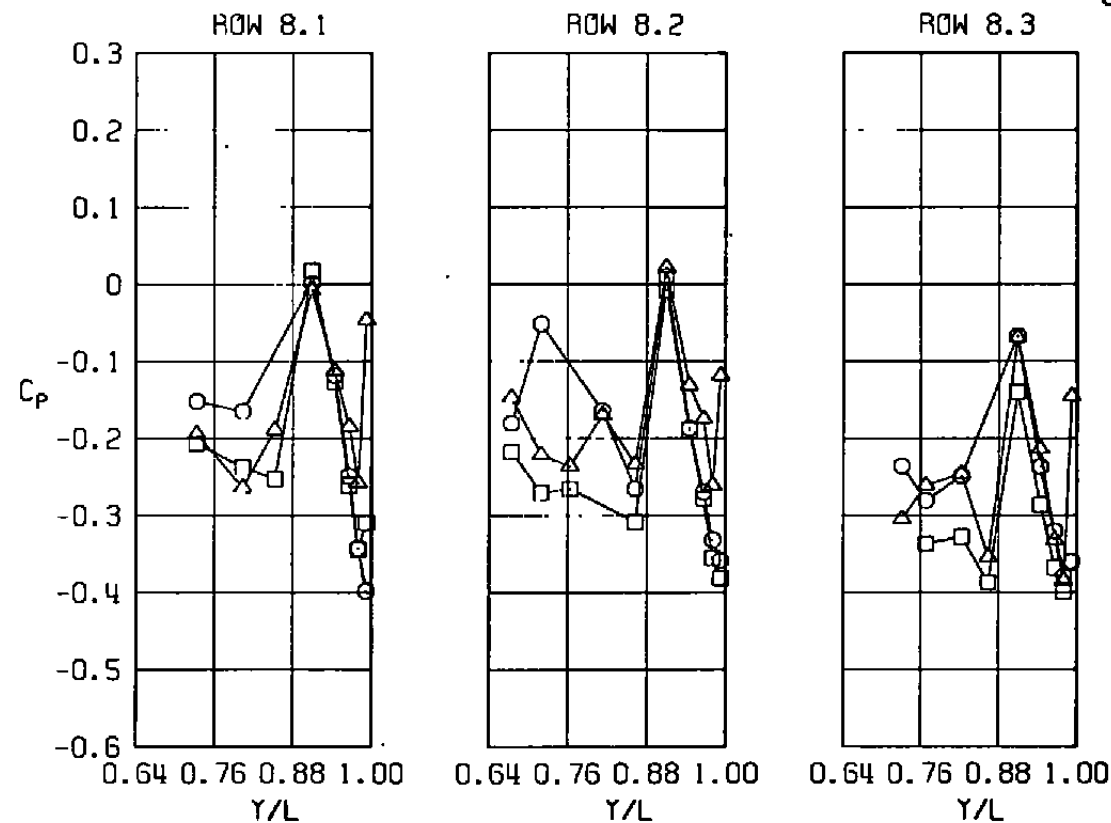
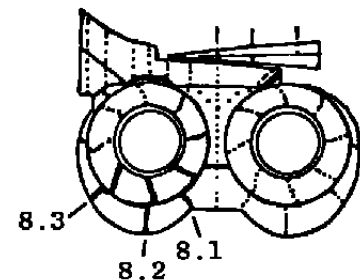


f. Row 6
Figure 42. Continued.



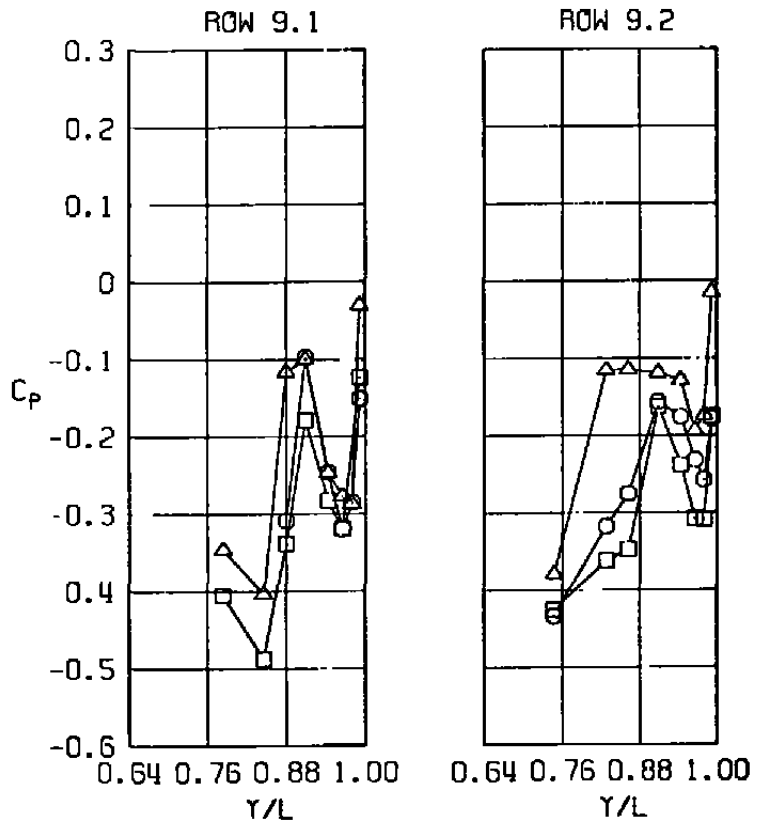
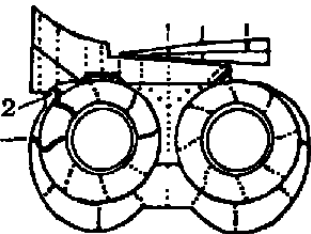
g. Row 7
Figure 42. Continued.

<u>SYM</u>	<u>M</u>	<u>ALPH</u>	<u>NPR</u>	<u>MFR</u>	<u>DELR</u>	<u>Re x 10⁻⁶</u>	<u>MODEL</u>	<u>CDNOZ</u>
□	1.20	2.80	4.40	0	0.22	2.48	NAB	0.0015
○	1.20	2.79	4.55	0.641	0.29	2.52	EPES	0.0017
△	1.20	2.82	4.28	0.645	0.23	3.22	FLIGHT	0.0008

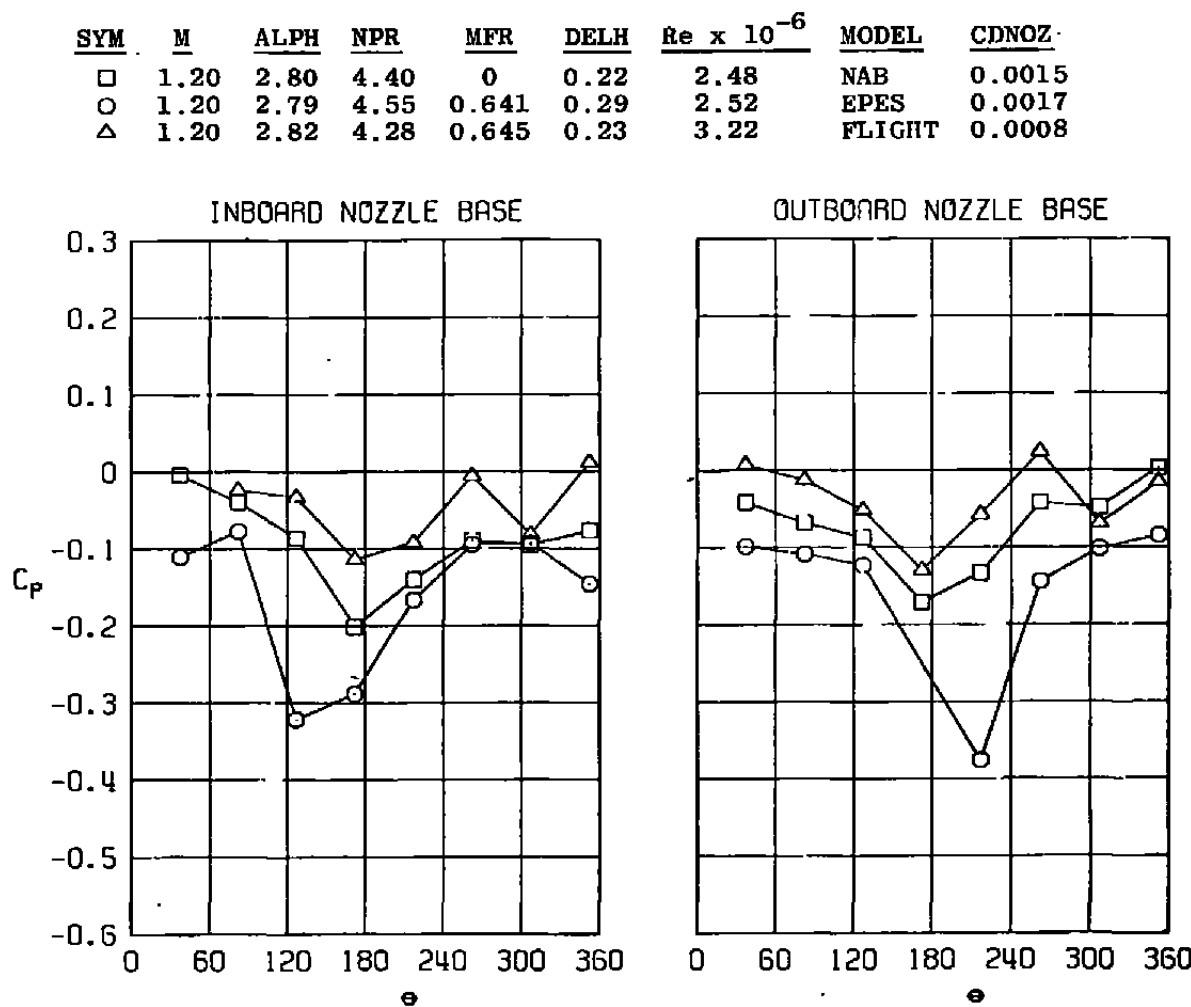


h. Row 8
Figure 42. Continued.

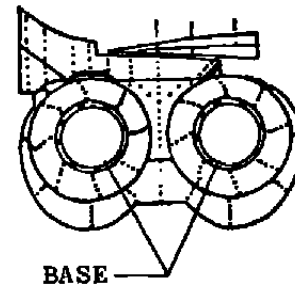
<u>SYM</u>	<u>M</u>	<u>ALPH</u>	<u>NPR</u>	<u>MFR</u>	<u>DELH</u>	<u>Re</u> $\times 10^{-6}$	<u>MODEL</u>	<u>CDNOZ</u>
□	1.20	2.80	4.40	0	0.22	2.48	NAB	0.0015
○	1.20	2.79	4.55	0.641	0.29	2.52	EPES	0.0017
△	1.20	2.82	4.28	0.645	0.23	3.22	FLIGHT	0.0008



i. Row 9
Figure 42. Continued.



j. Nozzle base
Figure 42. Concluded.



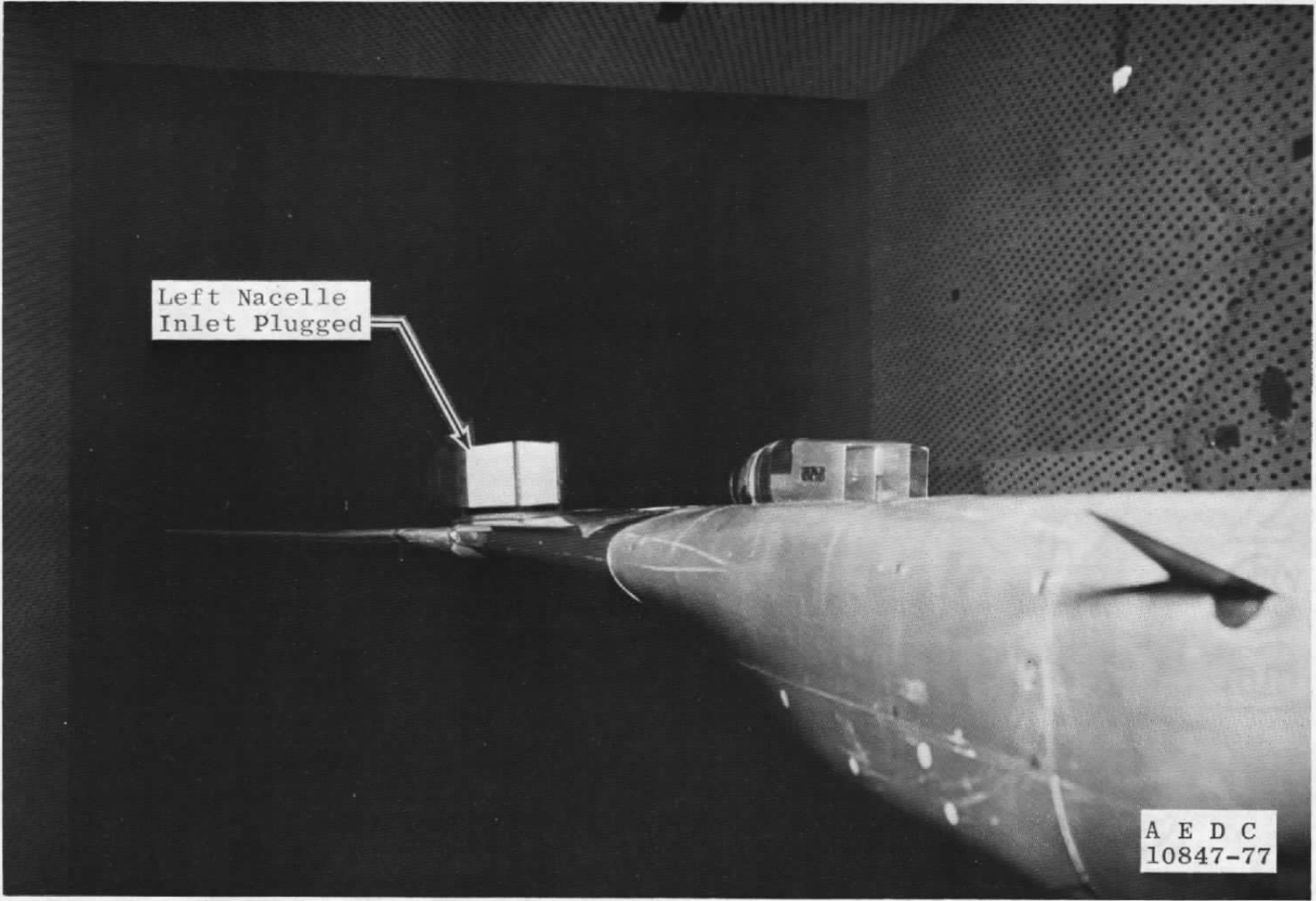
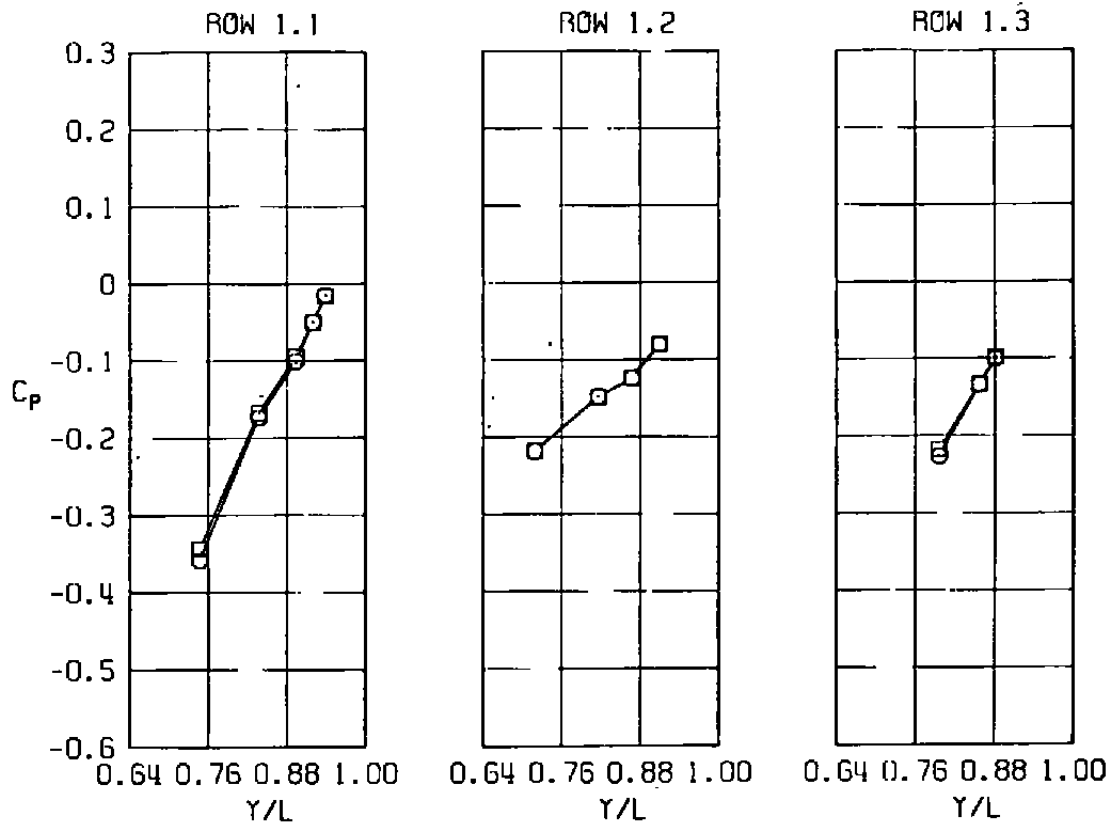
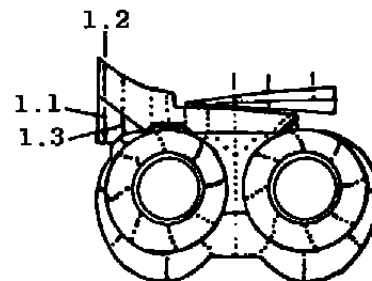


Figure 43. Left-hand nacelle inlets plugged with wood inserts.

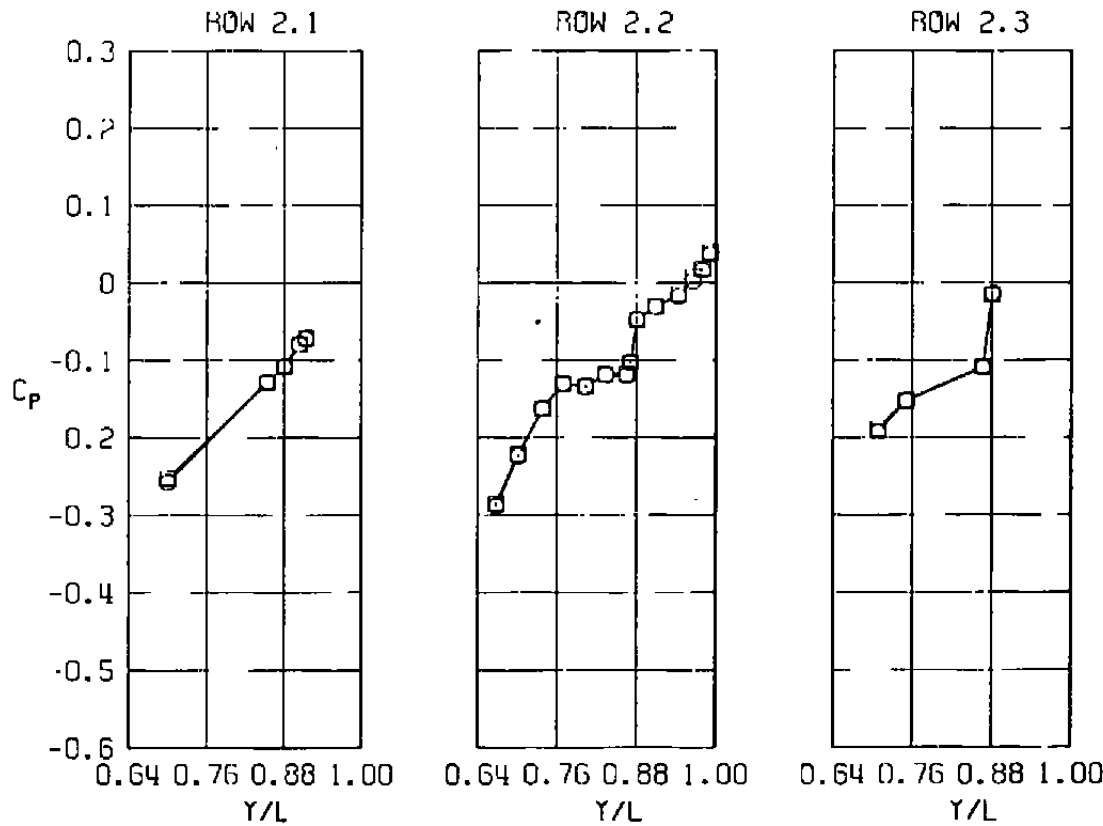
<u>SYM</u>	<u>M</u>	<u>ALPHI</u>	<u>NPR</u>	<u>MFR</u>	<u>DELH</u>	<u>Re x 10⁻⁶</u>	<u>MODEL</u>	<u>CDNOZ</u>	<u>PLUGGED</u>
□	0.85	0.06	2.88	0.480	0.17	2.53	EPES	0.0002	NO
○	0.85	0	2.89	0.475	0	2.53	EPES	0.0002	YES



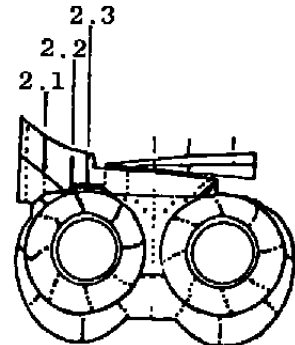
a. Row 1

Figure 44. Effect of spillage from the opposite nacelle on the nozzle afterbody flow field, $M = 0.85$.

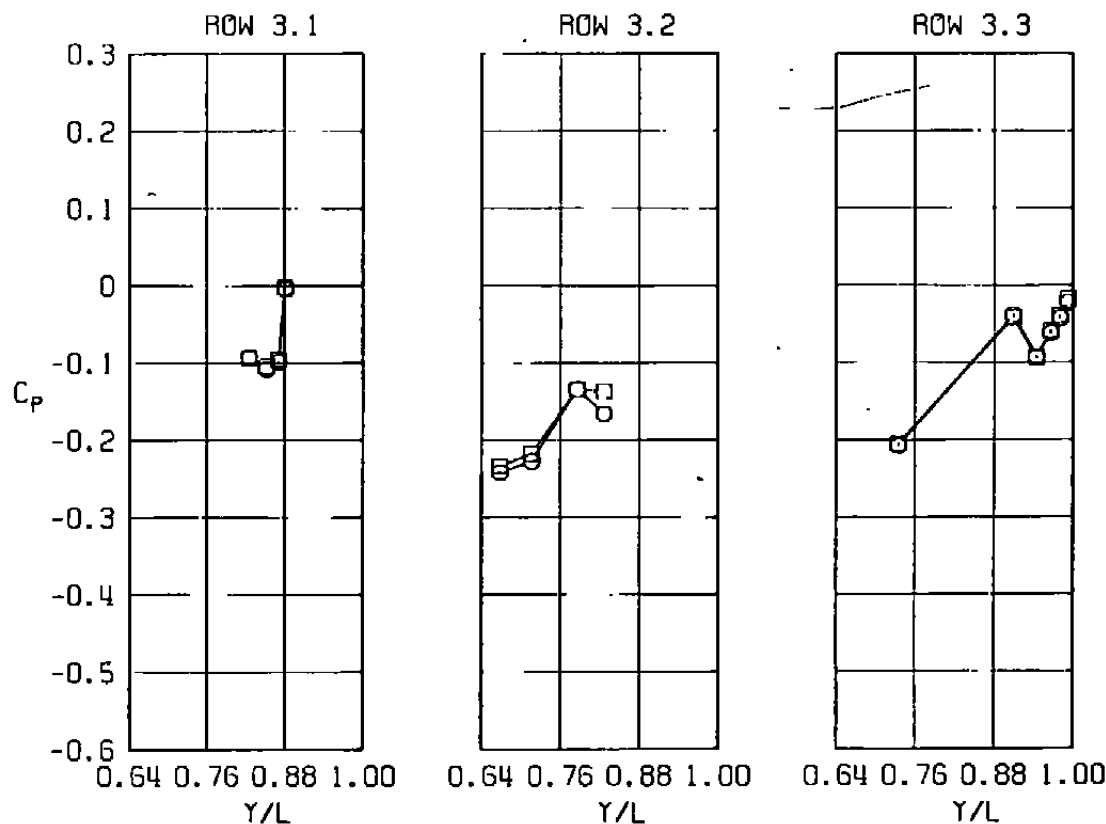
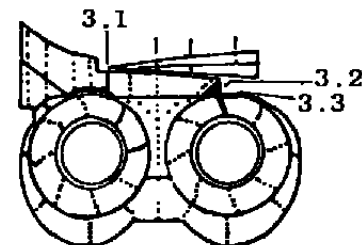
<u>SYM</u>	<u>M</u>	<u>ALPH</u>	<u>NPR</u>	<u>MFR</u>	<u>DELH</u>	<u>Rc x 10⁻⁶</u>	<u>MODEL</u>	<u>CDNOZ</u>	<u>PLUGGED</u>
□	0.85	0.06	2.88	0.480	0.17	2.53	EPES	0.0002	NO
○	0.85	0	2.89	0.475	0	2.53	EPES	0.0002	YES



b. Row 2
Figure 44. Continued.

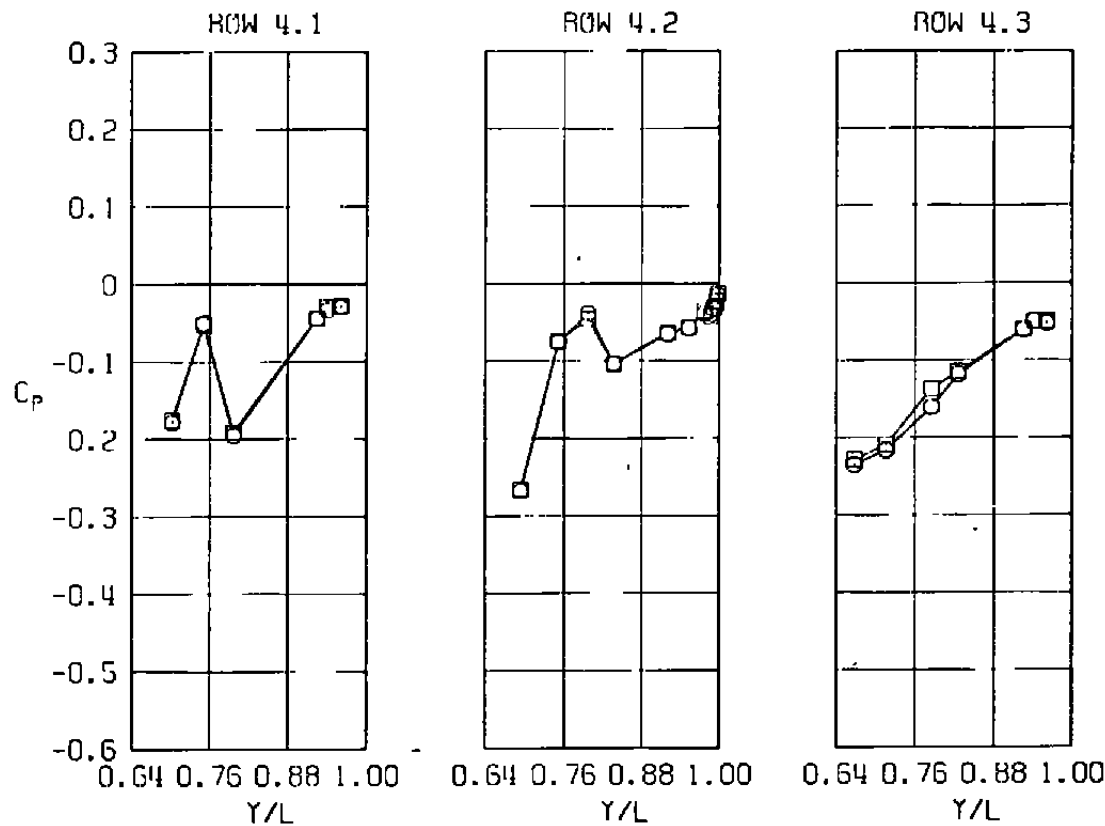
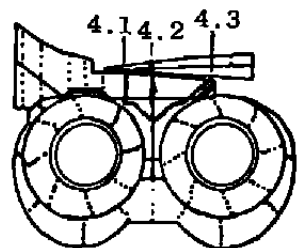


<u>SYM</u>	<u>M</u>	<u>ALPH</u>	<u>NPR</u>	<u>MFR</u>	<u>DElh</u>	<u>Re x 10⁻⁶</u>	<u>MODEL</u>	<u>CDNOZ</u>	<u>PLUGGED</u>
□	0.85	0.06	2.88	0.480	0.17	2.53	EPES	0.0002	NO
○	0.85	0	2.89	0.475	0	2.53	EPES	0.0002	YES



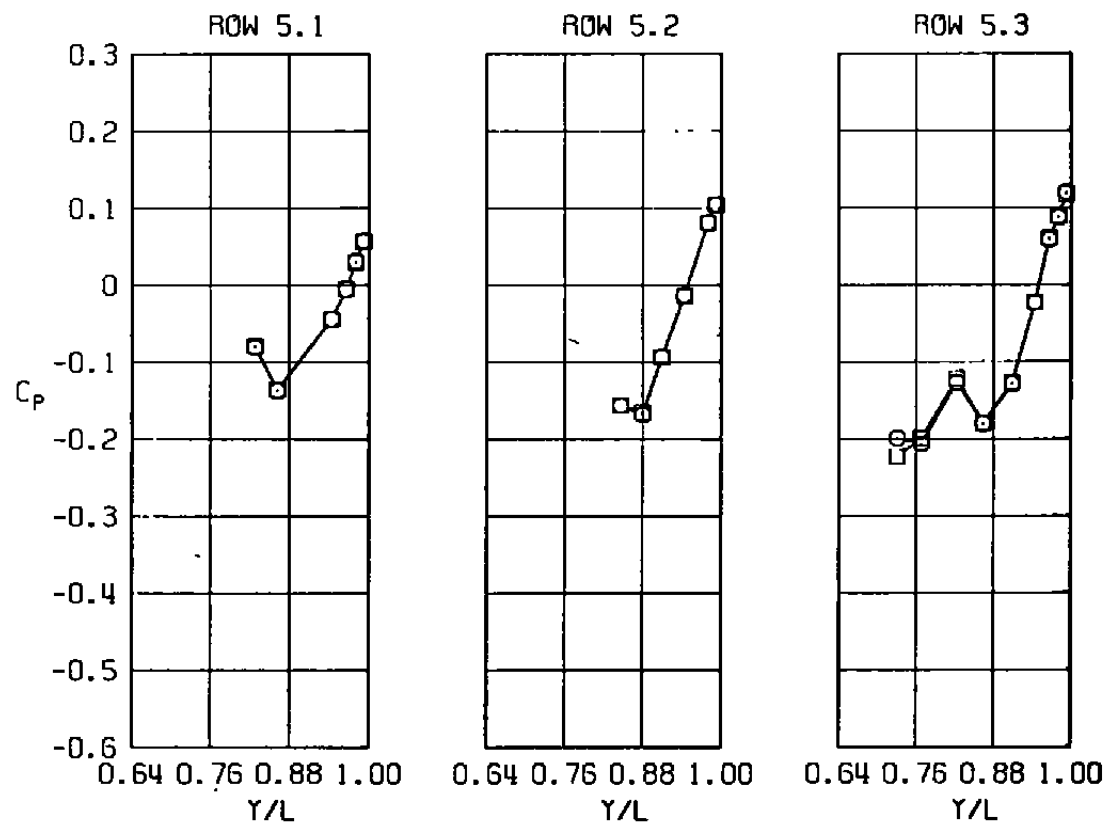
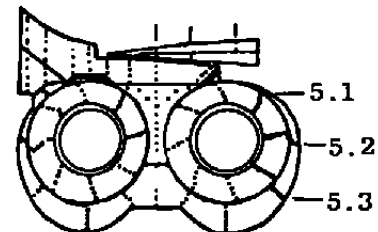
c. Row 3
Figure 44. Continued.

<u>SYM</u>	<u>M</u>	<u>ALPH</u>	<u>NPR</u>	<u>MFR</u>	<u>DELH</u>	<u>Re</u> $\times 10^{-6}$	<u>MODEL</u>	<u>CDNOZ</u>	<u>PLUGGED</u>
□	0.85	0.06	2.88	0.480	0.17	2.53	EPES	0.0002	NO
○	0.85	0	2.89	0.475	0	2.53	EPES	0.0002	YES



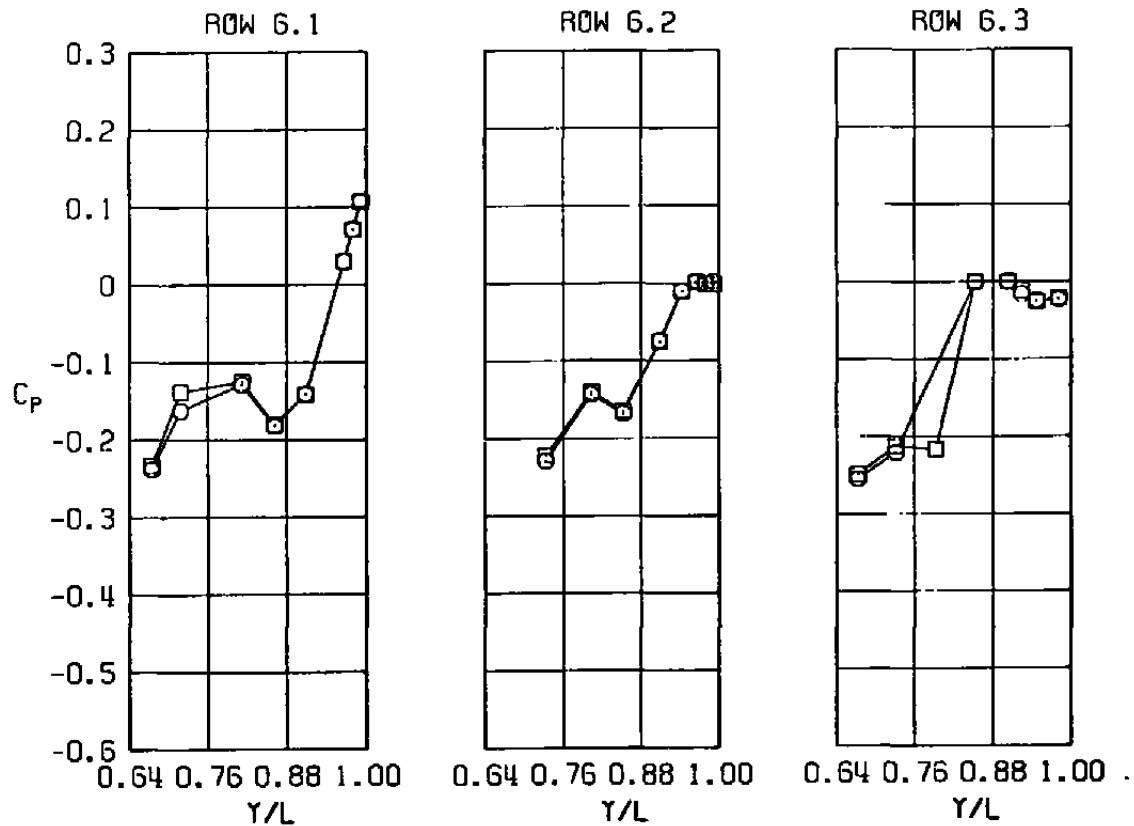
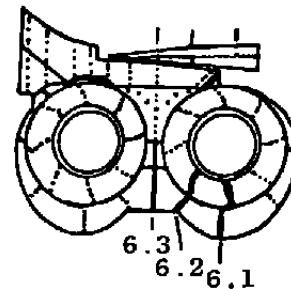
d. Row 4
Figure 44. Continued.

<u>SYM</u>	<u>M</u>	<u>ALPH</u>	<u>NPR</u>	<u>MFR</u>	<u>DELH</u>	<u>Re x 10⁻⁶</u>	<u>MODEL</u>	<u>CDNOZ</u>	<u>PLUGGED</u>
□	0.85	0.06	2.88	0.480	0.17	2.53	EPES	0.0002	NO
○	0.85	0	2.89	0.475	0	2.53	EPES	0.0002	YES



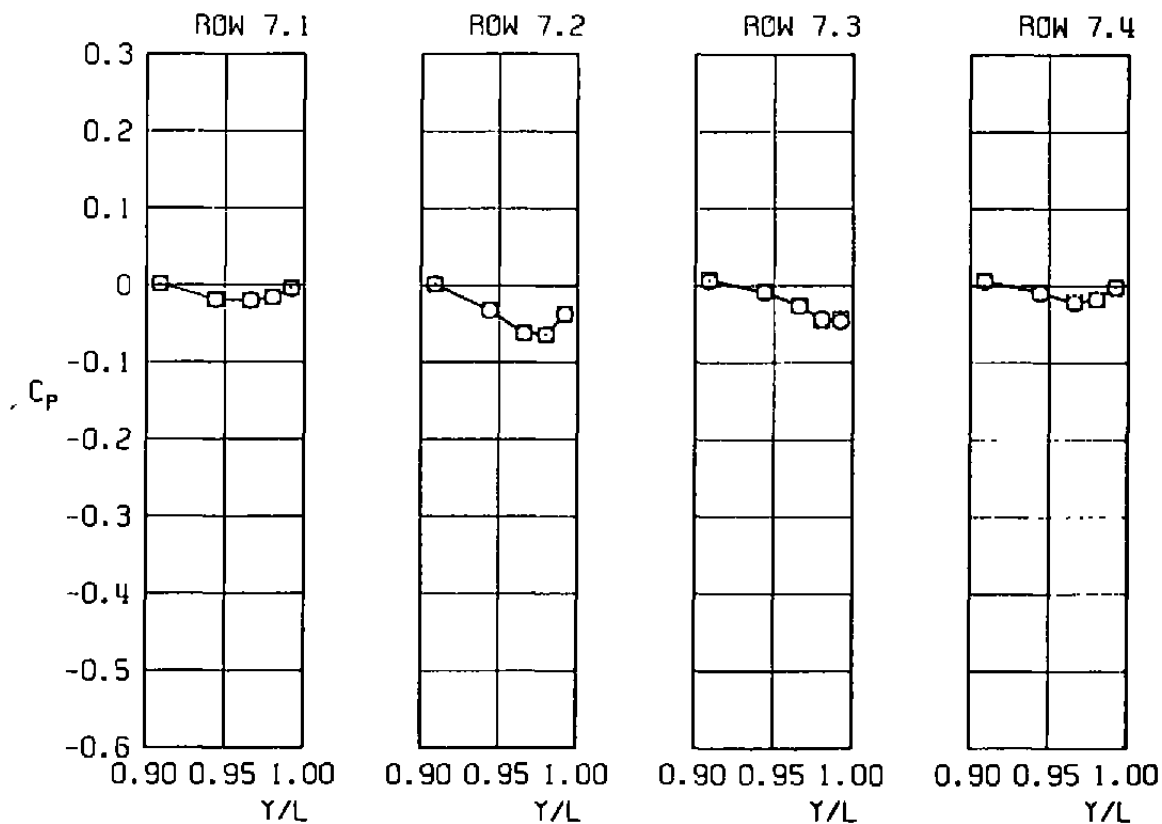
e. Row 5
Figure 44. Continued.

<u>SYM</u>	<u>M</u>	<u>ALPH</u>	<u>NPR</u>	<u>MFR</u>	<u>DELH</u>	<u>Re</u> $\times 10^{-6}$	<u>MODEL</u>	<u>CDNOZ</u>	<u>PLUGGED</u>
□	0.85	0.06	2.88	0.480	0.17	2.53	EPES	0.0002	NO
○	0.85	0	2.89	0.475	0	2.53	EPES	0.0002	YES

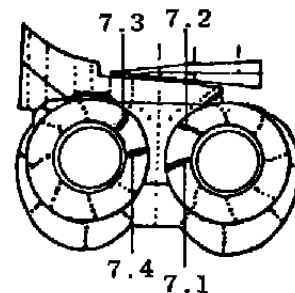


f. Row 6
Figure 44. Continued.

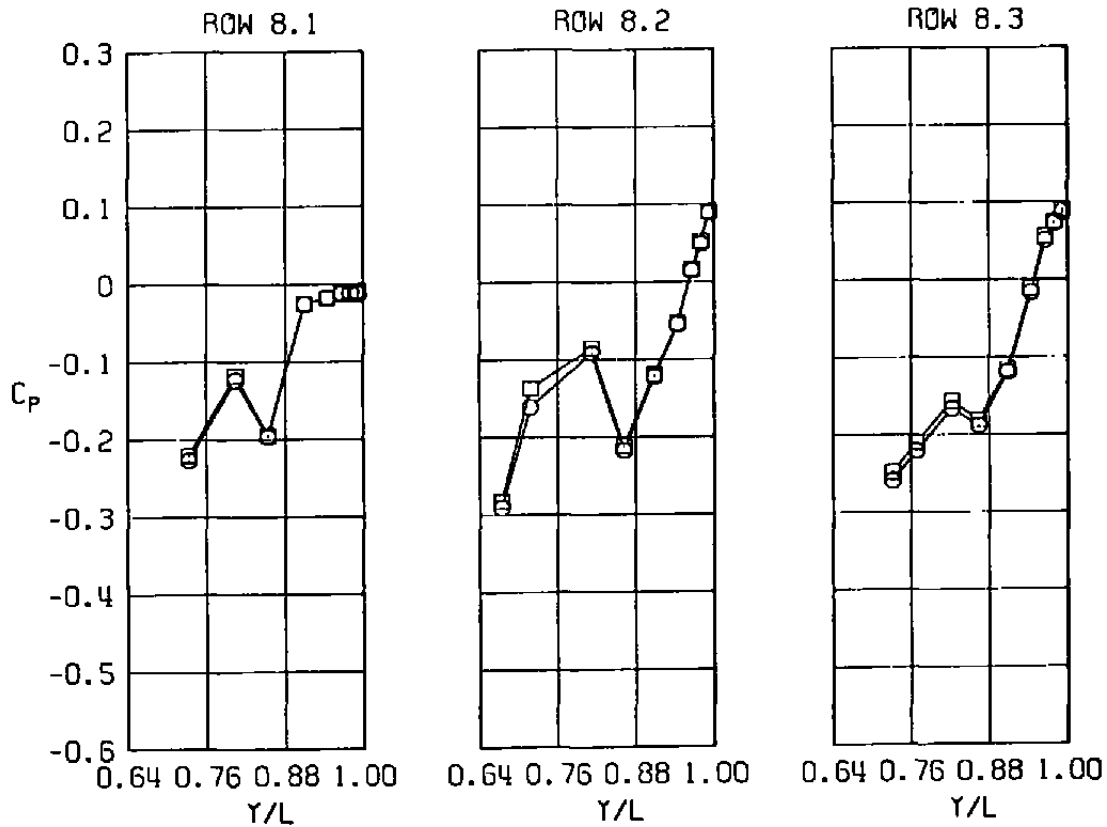
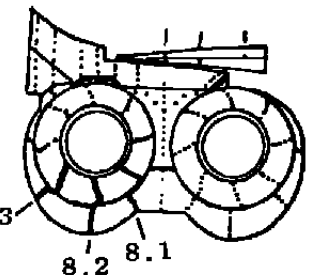
<u>SYM</u>	<u>M</u>	<u>ALPH</u>	<u>NPR</u>	<u>MFR</u>	<u>DELH</u>	<u>Re</u> $\times 10^{-6}$	<u>MODEL</u>	<u>CDNOZ</u>	<u>PLUGGED</u>
□	0.85	0.06	2.88	0.480	0.17	2.53	EPES	0.0002	NO
○	0.85	0	2.89	0.475	0	2.53	EPES	0.0002	YES



g. Row 7
Figure 44. Continued.

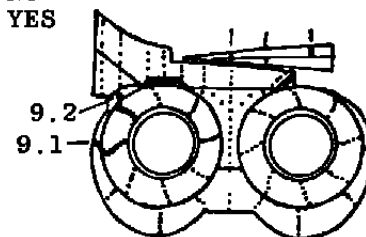
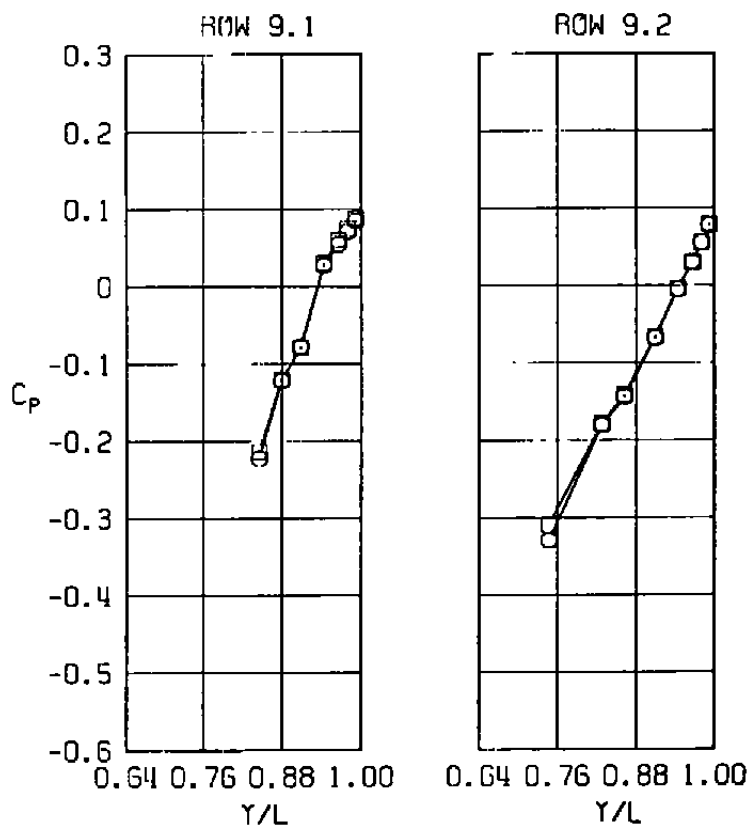


SYM	M	ALPH	NPR	MFR	DELH	$Re \times 10^{-6}$	MODEL	CDNOZ	PLUGGED
□	0.85	0.06	2.88	0.480	0.17	2.53	EPES	0.0002	NO
○	0.85	0	2.89	0.475	0	2.53	EPES	0.0002	YES



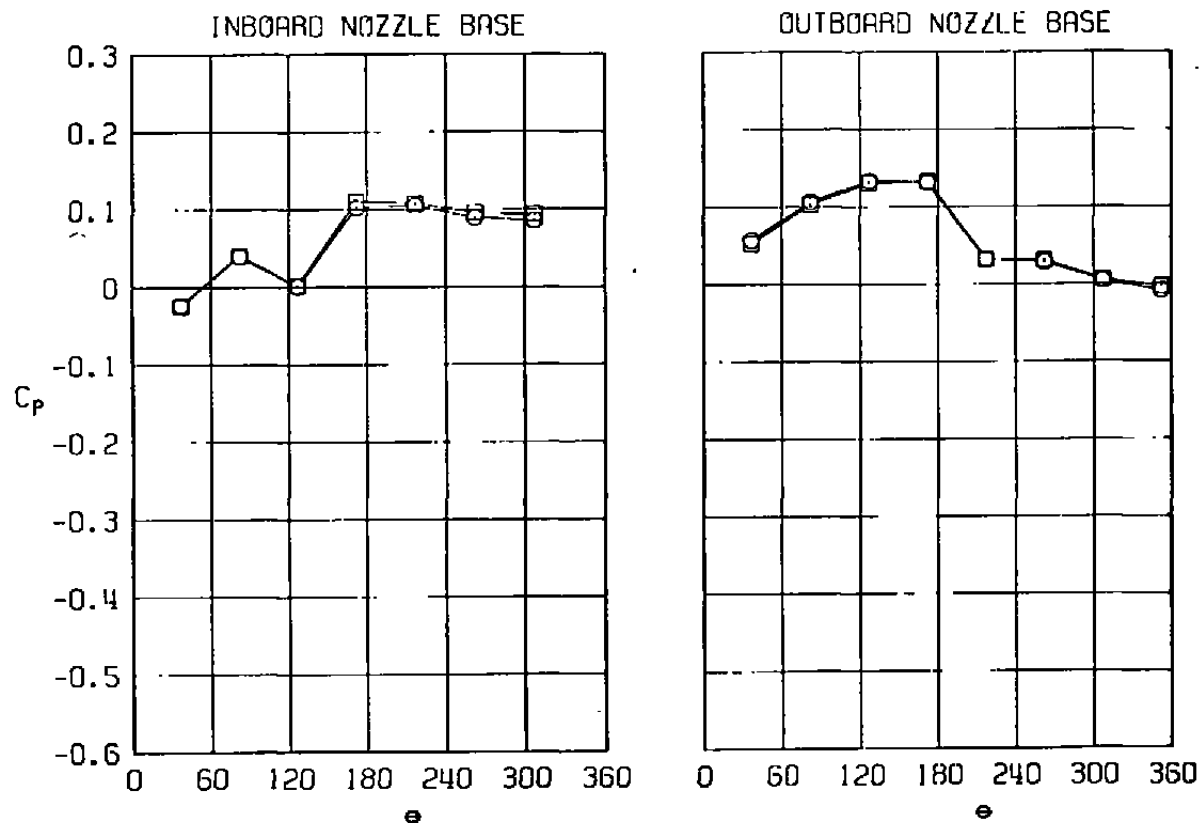
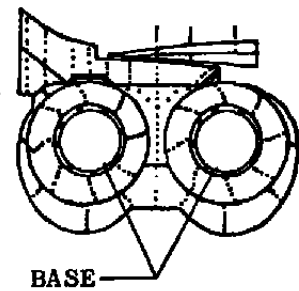
h. Row 8
Figure 44. Continued.

<u>SYM</u>	<u>M</u>	<u>ALPH</u>	<u>NPR</u>	<u>MFR</u>	<u>DELH</u>	<u>Re x 10⁻⁶</u>	<u>MODEL</u>	<u>CDNOZ</u>	<u>PLUGGED</u>
□	0.85	0.06	2.88	0.480	0.17	2.53	EPES	0.0002	NO
○	0.85	0	2.89	0.475	0	2.53	EPES	0.0002	YES

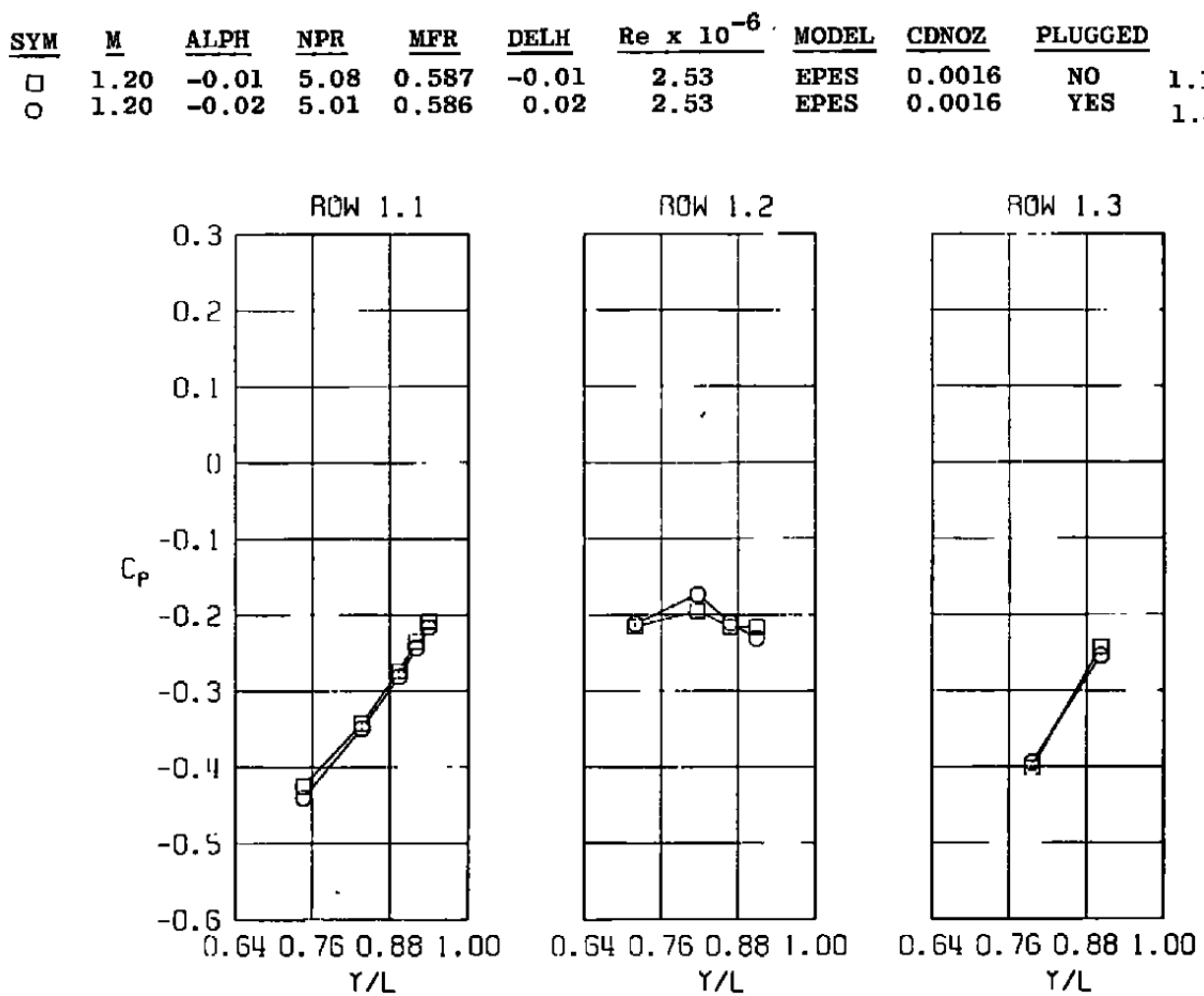


i. Row 9
Figure 44. Continued.

<u>SYM</u>	<u>M</u>	<u>ALPH</u>	<u>NPR</u>	<u>MFR</u>	<u>DELH</u>	<u>Re</u> $\times 10^{-6}$	<u>MODEL</u>	<u>CDNOZ</u>	<u>PLUGGED</u>
□	0.85	0.06	2.88	0.480	0.17	2.53	EPES	0.0002	NO
○	0.85	0	2.89	0.475	0	2.53	EPES	0.0002	YES

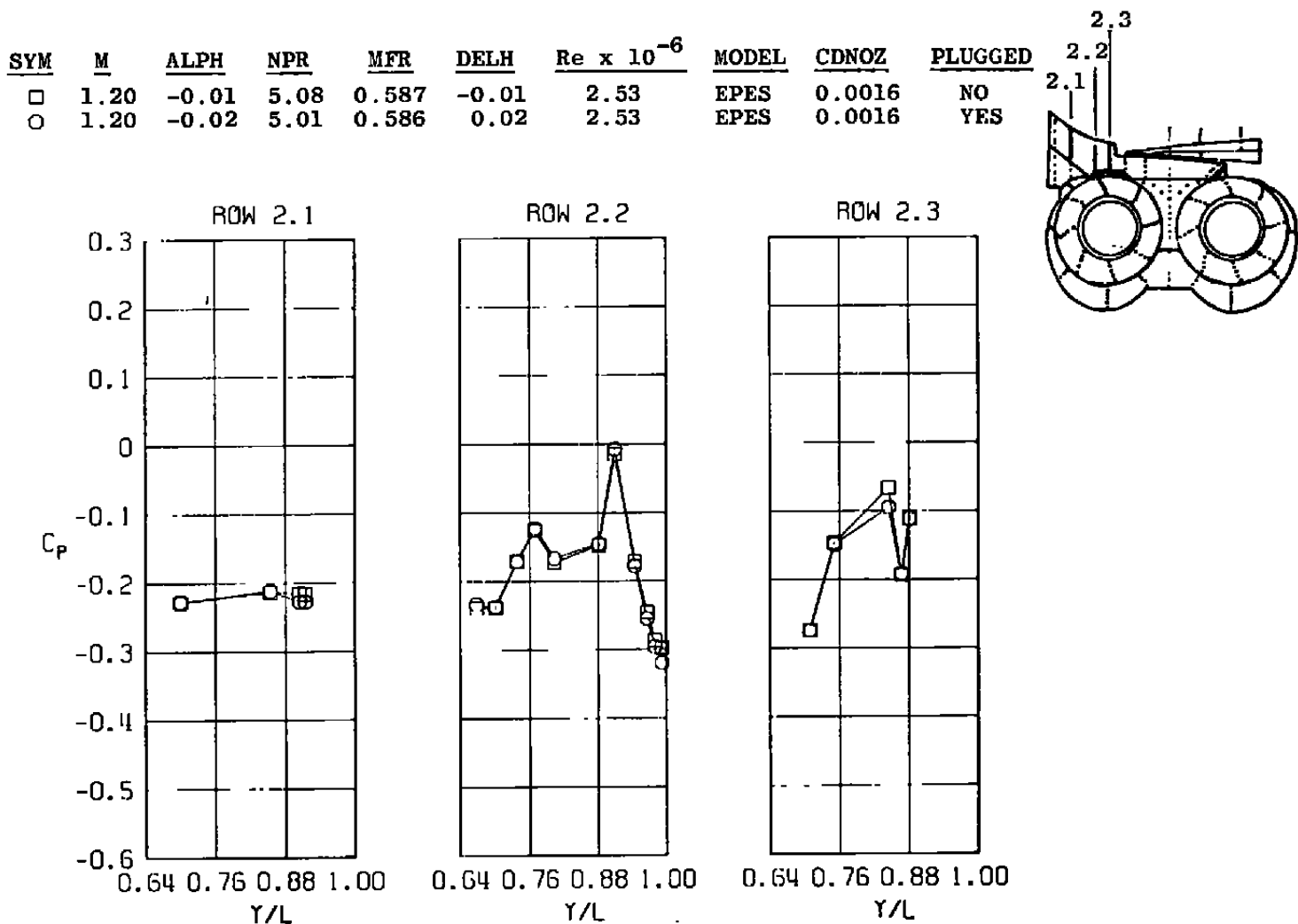


j. Nozzle base
Figure 44. Concluded.



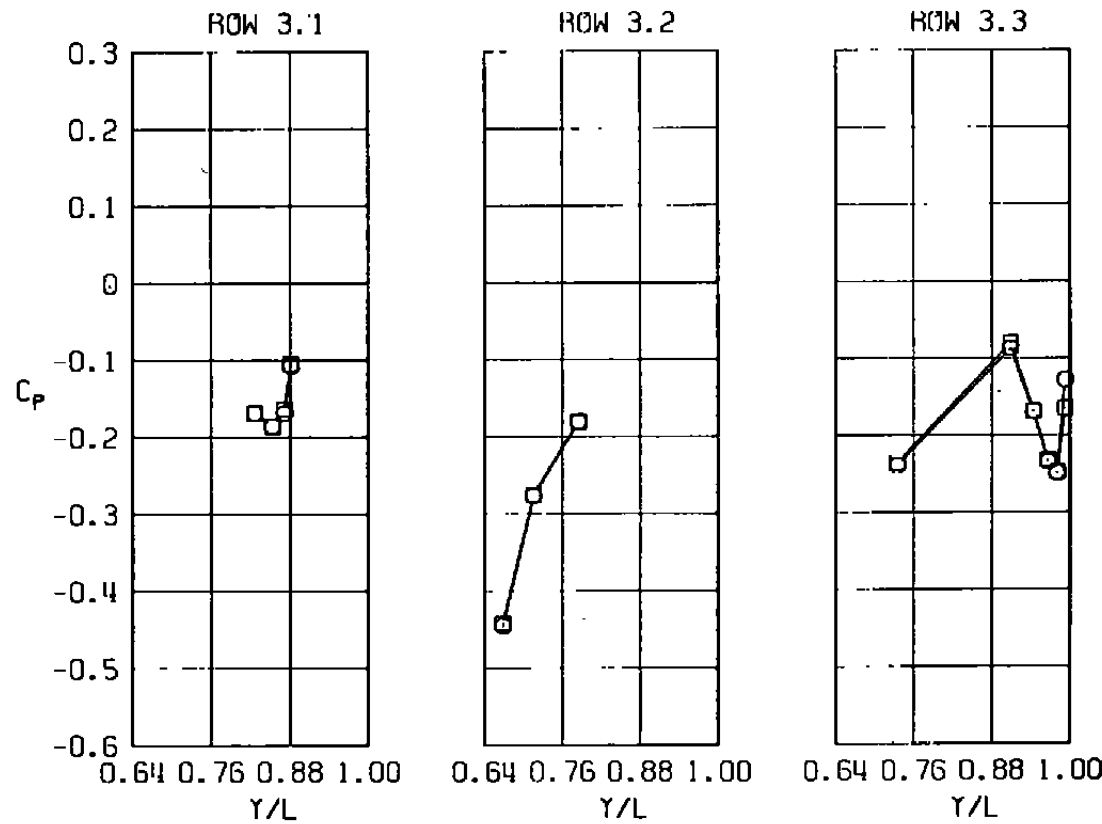
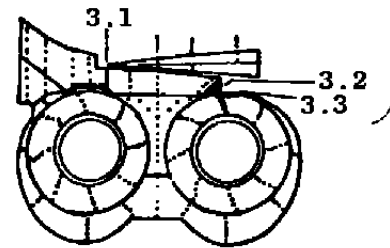
a. Row 1 :

Figure 45. Effect of spillage from the opposite nacelle on the nozzle afterbody flow field, $M = 1.20$.



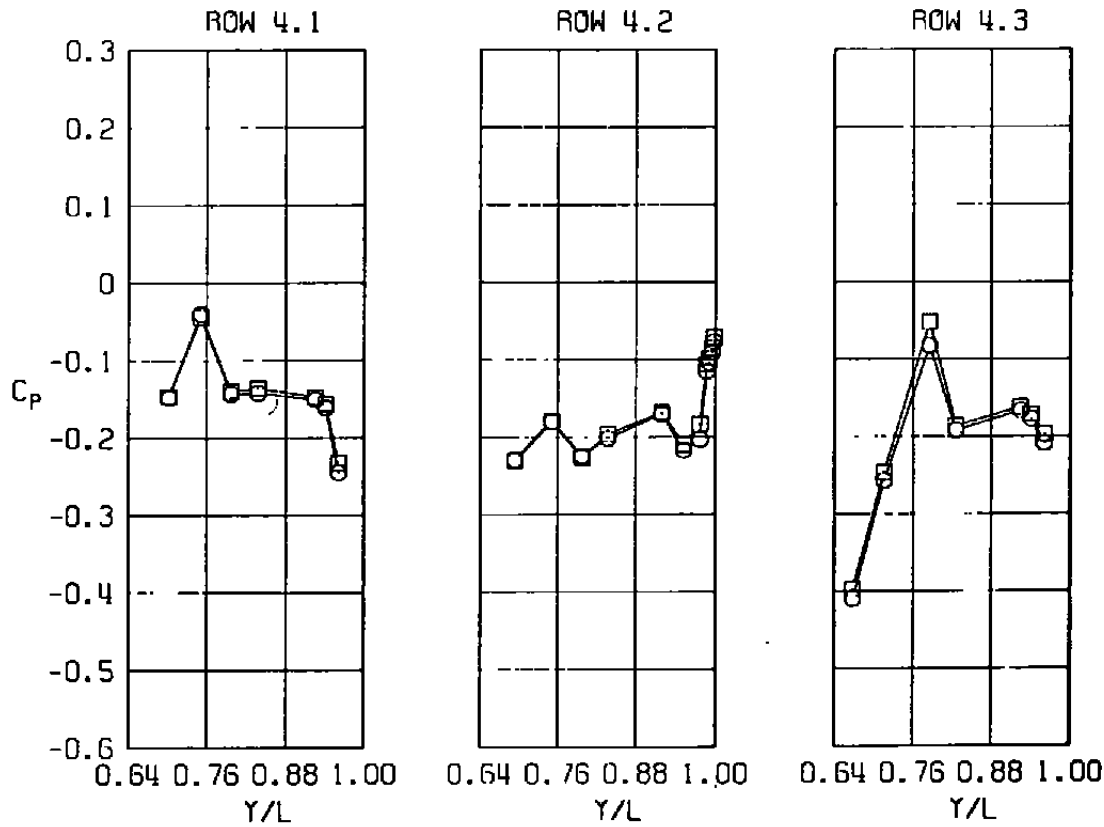
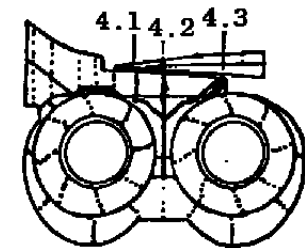
b. Row 2
Figure 45. Continued.

<u>SYM</u>	<u>M</u>	<u>ALPH</u>	<u>NPR</u>	<u>MFR</u>	<u>DELH</u>	<u>Re x 10⁻⁶</u>	<u>MODEL</u>	<u>CDNOZ</u>	<u>PLUGGED</u>
□	1.20	-0.01	5.08	0.587	-0.01	2.53	EPES	0.0016	NO
○	1.20	-0.02	5.01	0.586	0.02	2.53	EPES	0.0016	YES

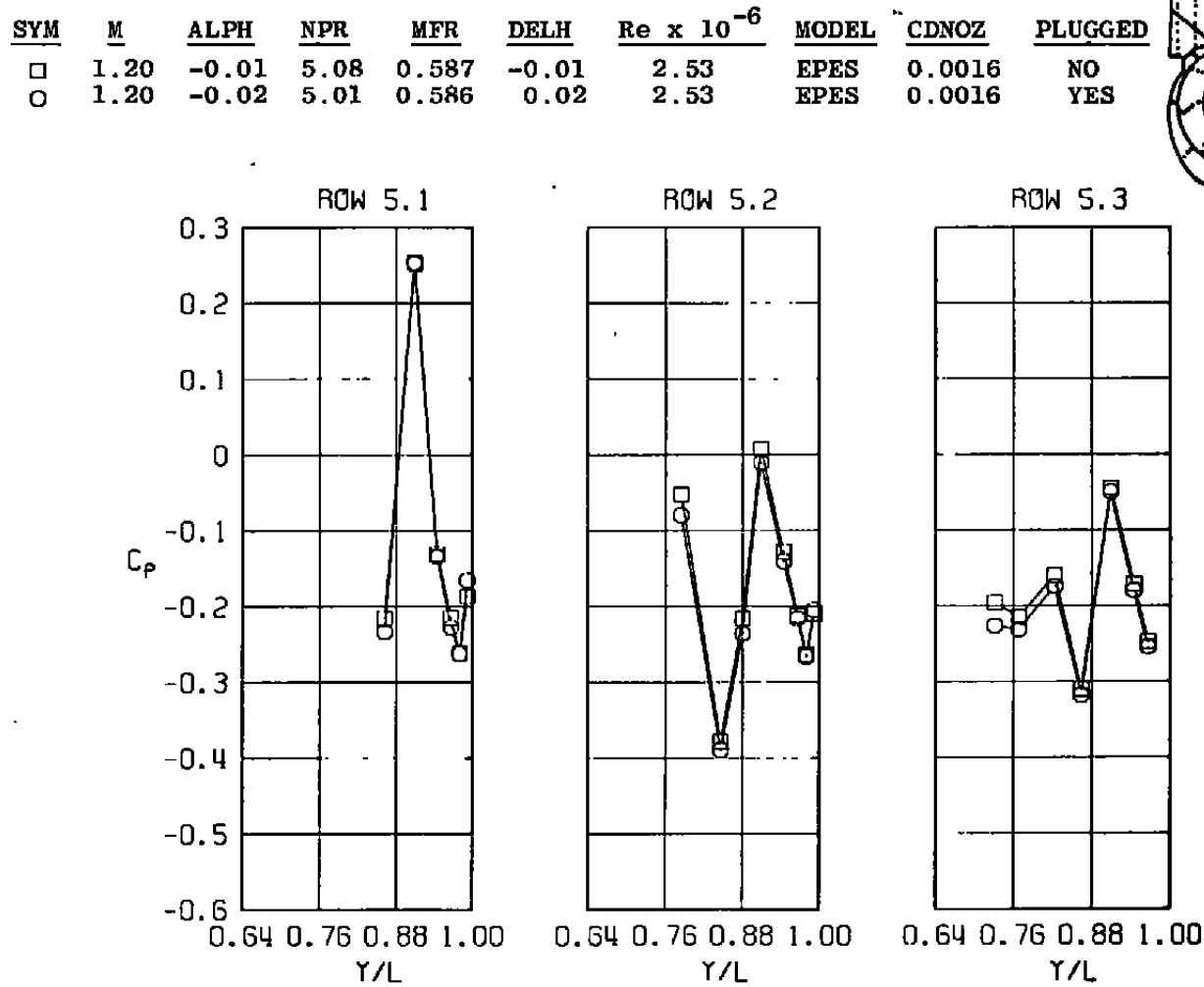


c. Row 3
Figure 45. Continued.

<u>SYM</u>	<u>M</u>	<u>ALPH</u>	<u>NPR</u>	<u>MFR</u>	<u>DELH</u>	<u>Re x 10⁻⁶</u>	<u>MODEL</u>	<u>CDNOZ</u>	<u>PLUGGED</u>
□	1.20	-0.01	5.08	0.587	-0.01	2.53	EPES	0.0016	NO
○	1.20	-0.02	5.01	0.586	0.02	2.53	EPES	0.0016	YES

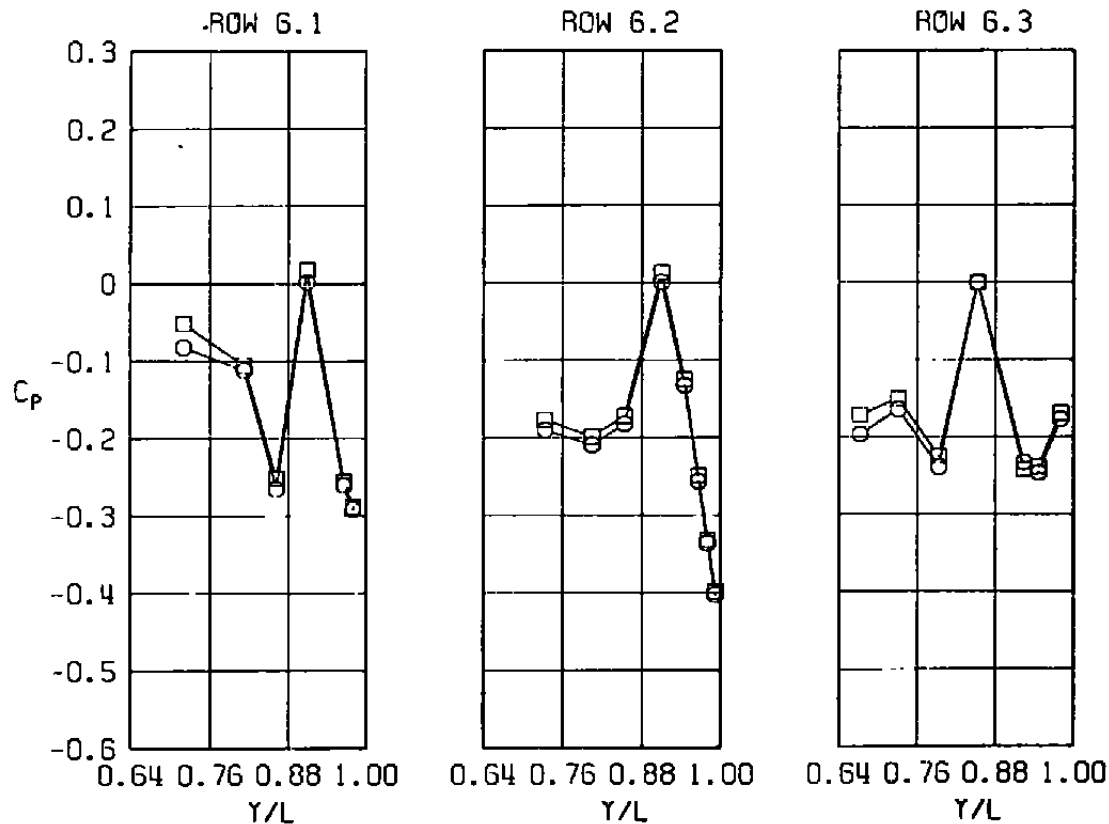
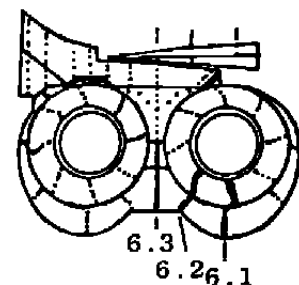


d. Row 4
Figure 45. Continued.



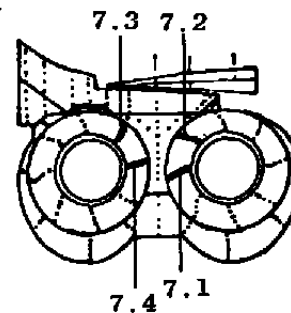
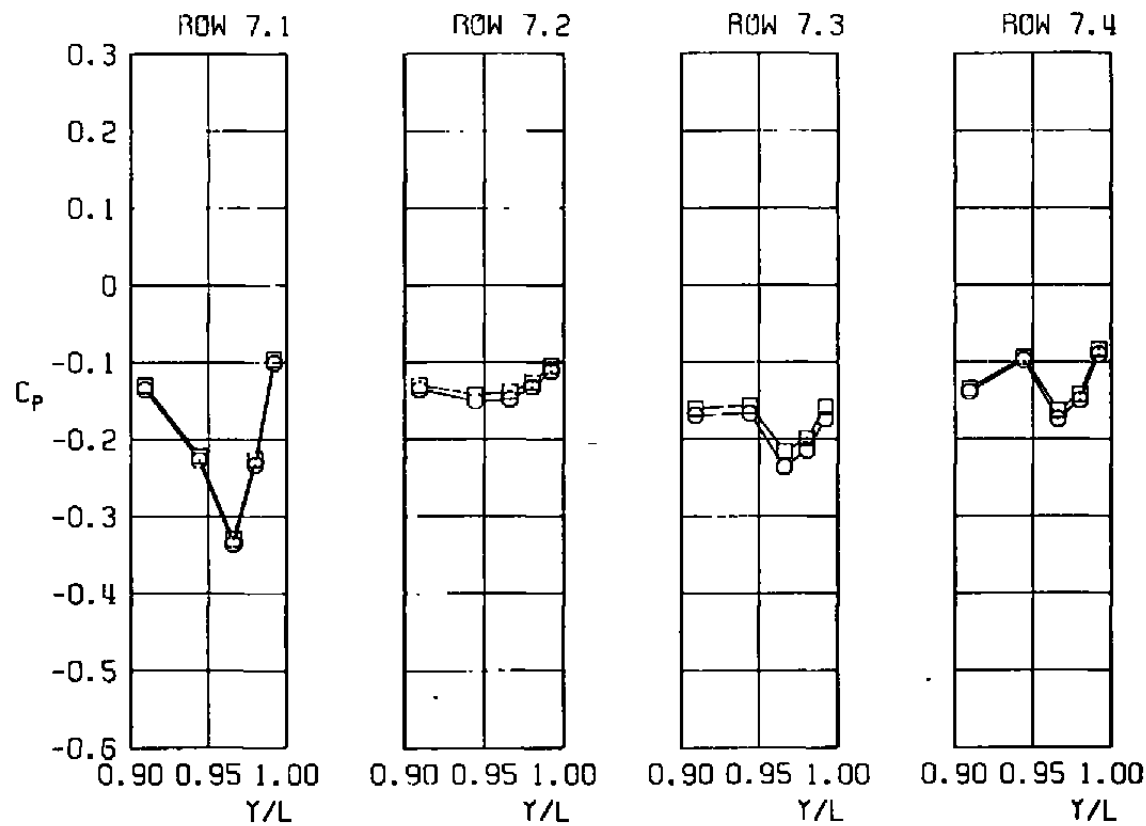
e. Row 5
Figure 45. Continued.

<u>SYM</u>	<u>M</u>	<u>ALPH</u>	<u>NPR</u>	<u>MFR</u>	<u>DELH</u>	<u>Re x 10⁻⁶</u>	<u>MODEL</u>	<u>CDNOZ</u>	<u>PLUGGED</u>
□	1.20	-0.01	5.08	0.587	-0.01	2.53	EPES	0.0016	NO
○	1.20	-0.02	5.01	0.586	0.02	2.53	EPES	0.0016	YES



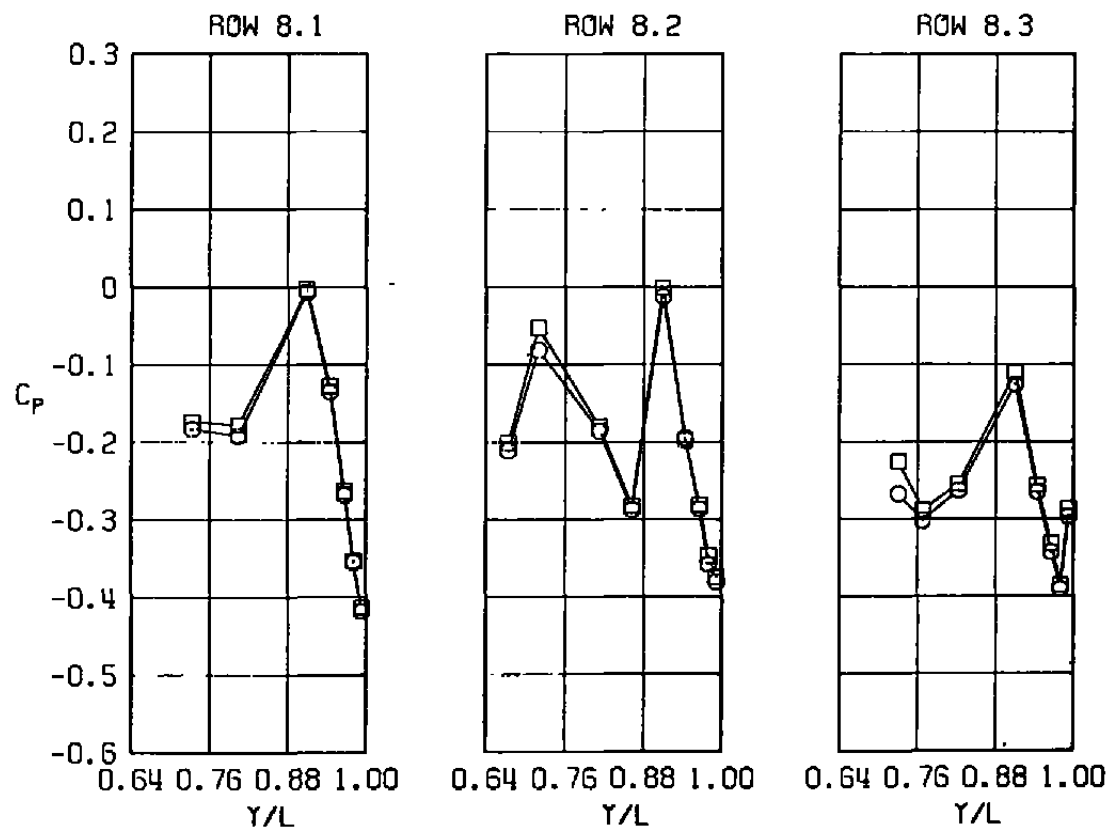
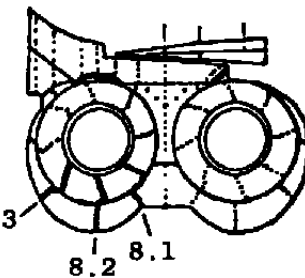
f. Row 6
Figure 45. Continued.

<u>SYM</u>	<u>M</u>	<u>ALPH</u>	<u>NPR</u>	<u>MFR</u>	<u>DELH</u>	<u>Re</u> $\times 10^{-6}$	<u>MODEL</u>	<u>CDNOZ</u>	<u>PLUGGED</u>
□	1.20	-0.01	5.08	0.587	-0.01	2.53	EPES	0.0016	NO
○	1.20	-0.02	5.01	0.586	0.02	2.53	EPES	0.0016	YES



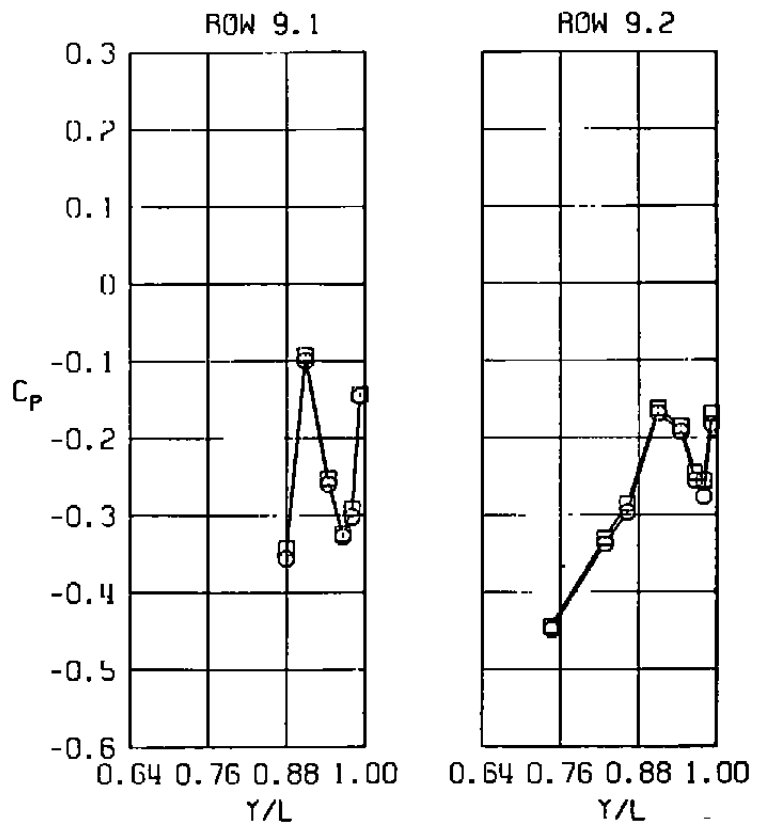
g. Row 7
Figure 45. Continued.

<u>SYM</u>	<u>M</u>	<u>ALPH</u>	<u>NPR</u>	<u>MFR</u>	<u>DELH</u>	<u>Re x 10⁻⁶</u>	<u>MODEL</u>	<u>CDNOZ</u>	<u>PLUGGED</u>
□	1.20	-0.01	5.08	0.587	-0.01	2.53	EPES	0.0016	NO
○	1.20	-0.02	5.01	0.586	0.02	2.53	EPES	0.0016	YES

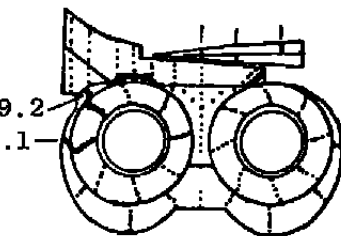


h. Row 8
Figure 45. Continued.

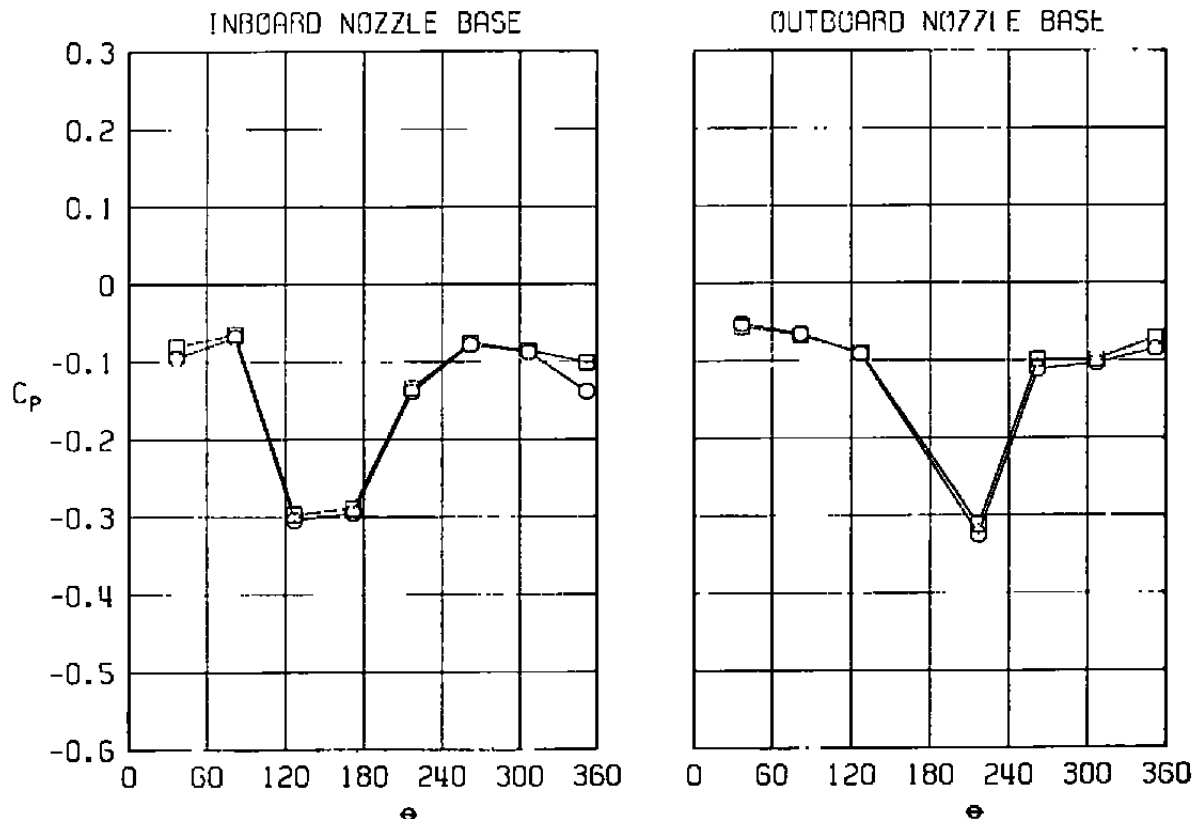
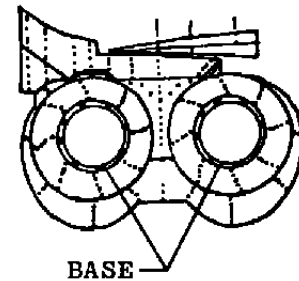
<u>SYM</u>	<u>M</u>	<u>ALPH</u>	<u>NPR</u>	<u>MFR</u>	<u>DELH</u>	<u>Re x 10⁻⁶</u>	<u>MODEL</u>	<u>CDNOZ</u>	<u>PLUGGED</u>
□	1.20	-0.01	5.08	0.587	-0.01	2.53	EPES	0.0016	NO
○	1.20	-0.02	5.01	0.586	0.02	2.53	EPES	0.0016	YES



i. Row 9
Figure 45. Continued.



<u>SYM</u>	<u>M</u>	<u>ALPH.</u>	<u>NPR</u>	<u>MFR</u>	<u>DELH</u>	<u>Re x 10⁻⁶</u>	<u>MODEL</u>	<u>CDNOZ</u>	<u>PLUGGED</u>
□	1.20	-0.01	5.08	0.587	-0.01	2.53	EPES	0.0016	NO
○	1.20	-0.02	5.01	0.586	0.02	2.53	EPES	0.0016	YES



j. Nozzle base
Figure 45. Concluded.

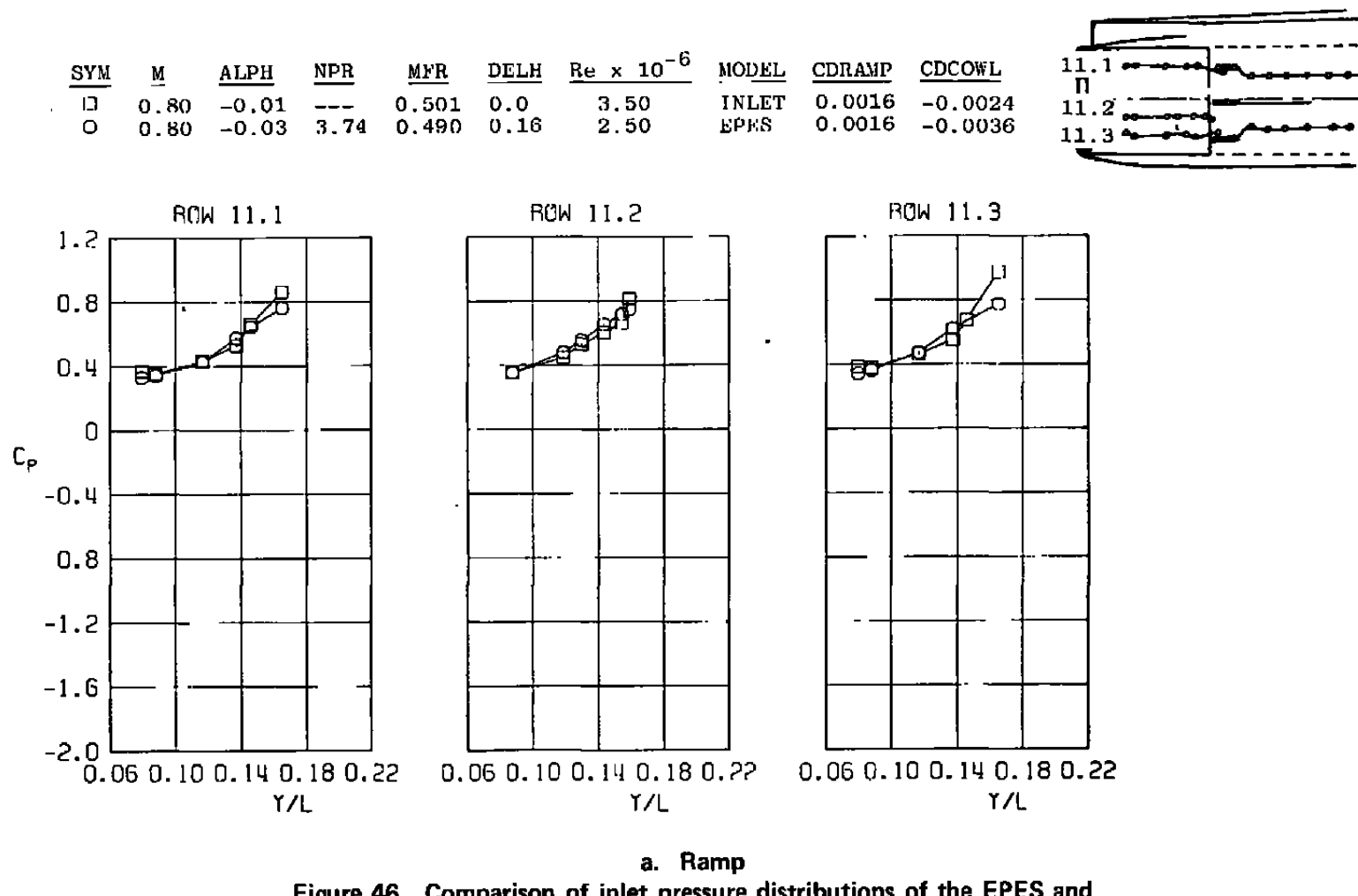
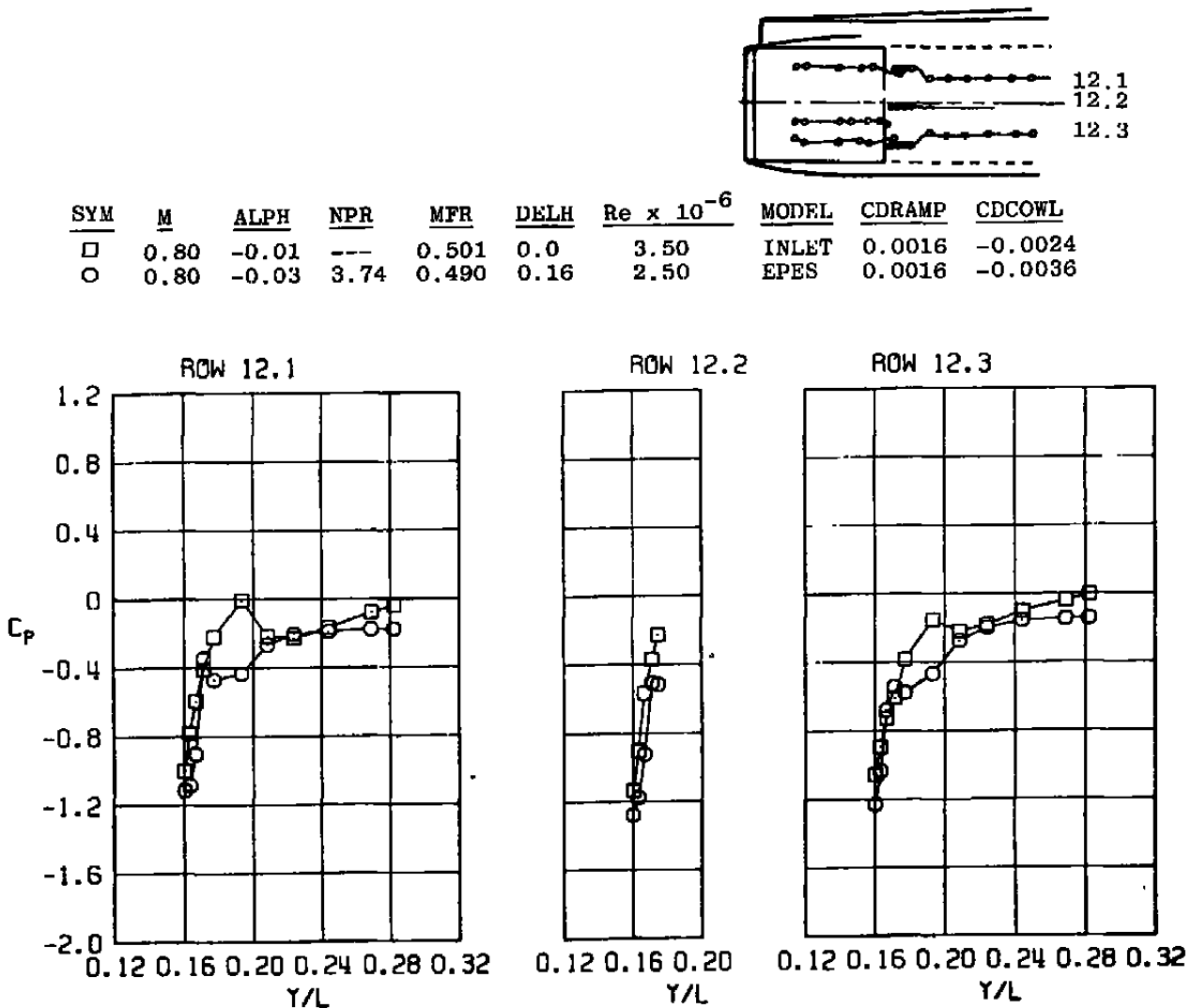


Figure 46. Comparison of inlet pressure distributions of the EPES and 0.07-scale models, $M = 0.80$.



b. Cowl
Figure 46. Concluded.

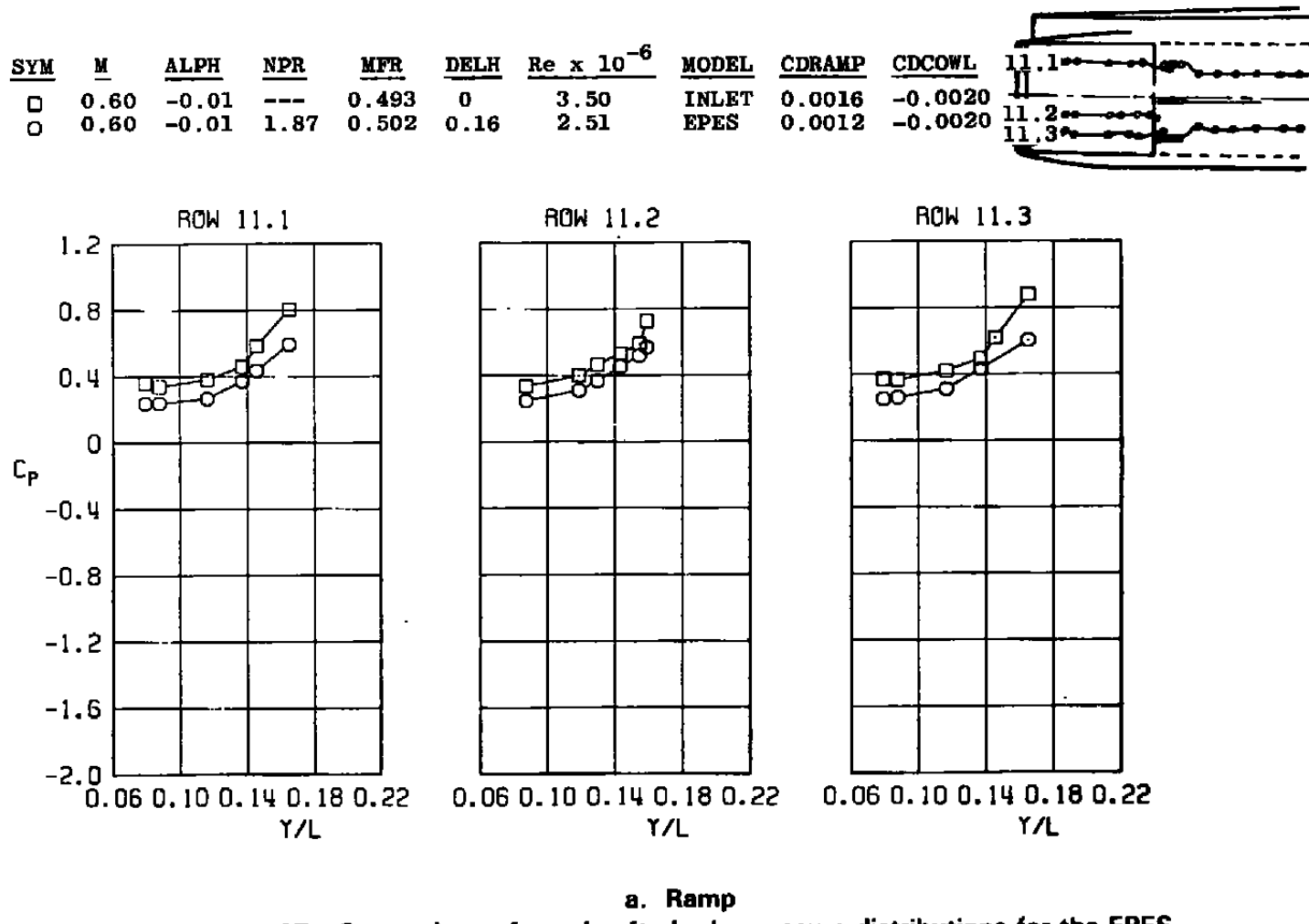
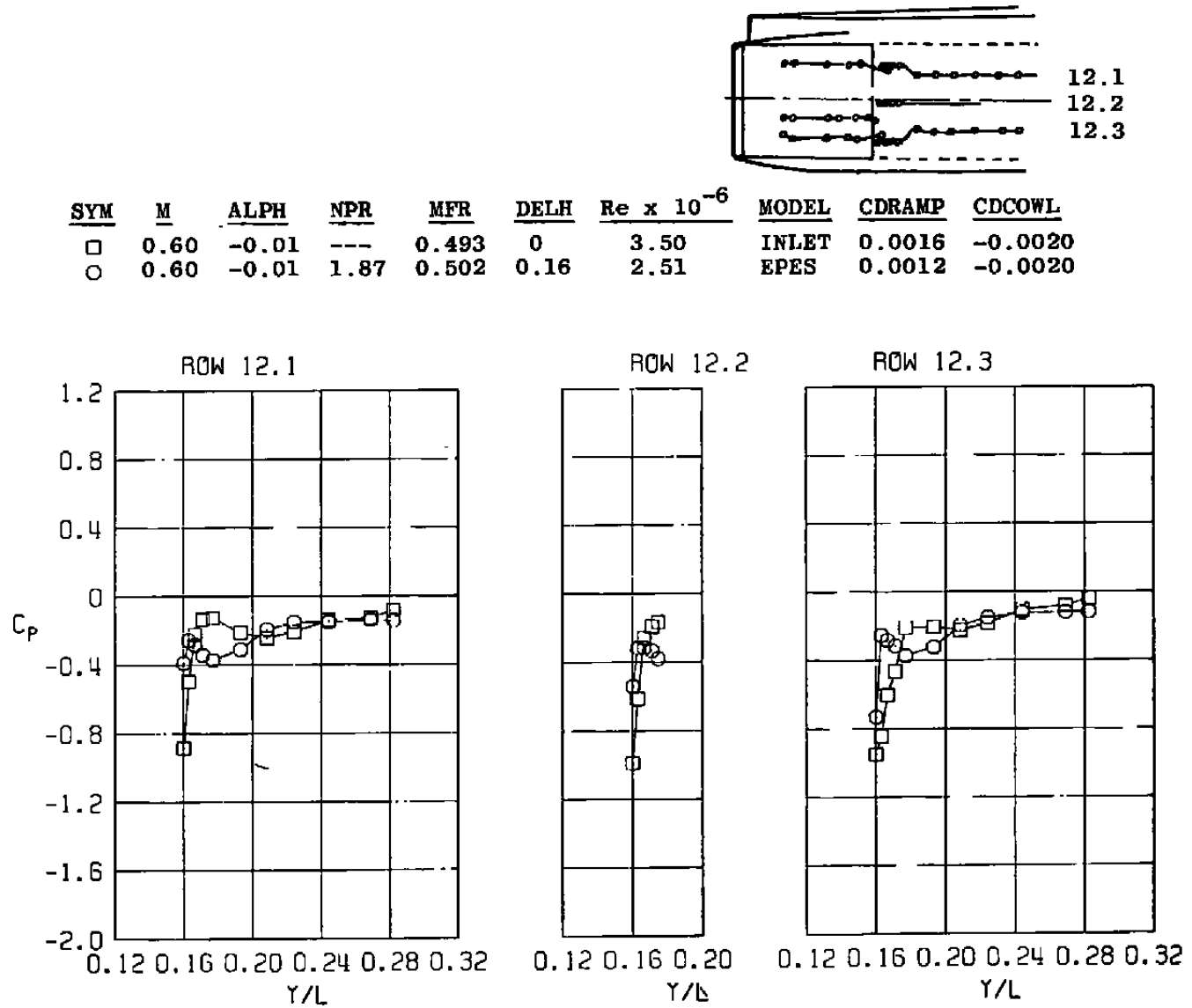
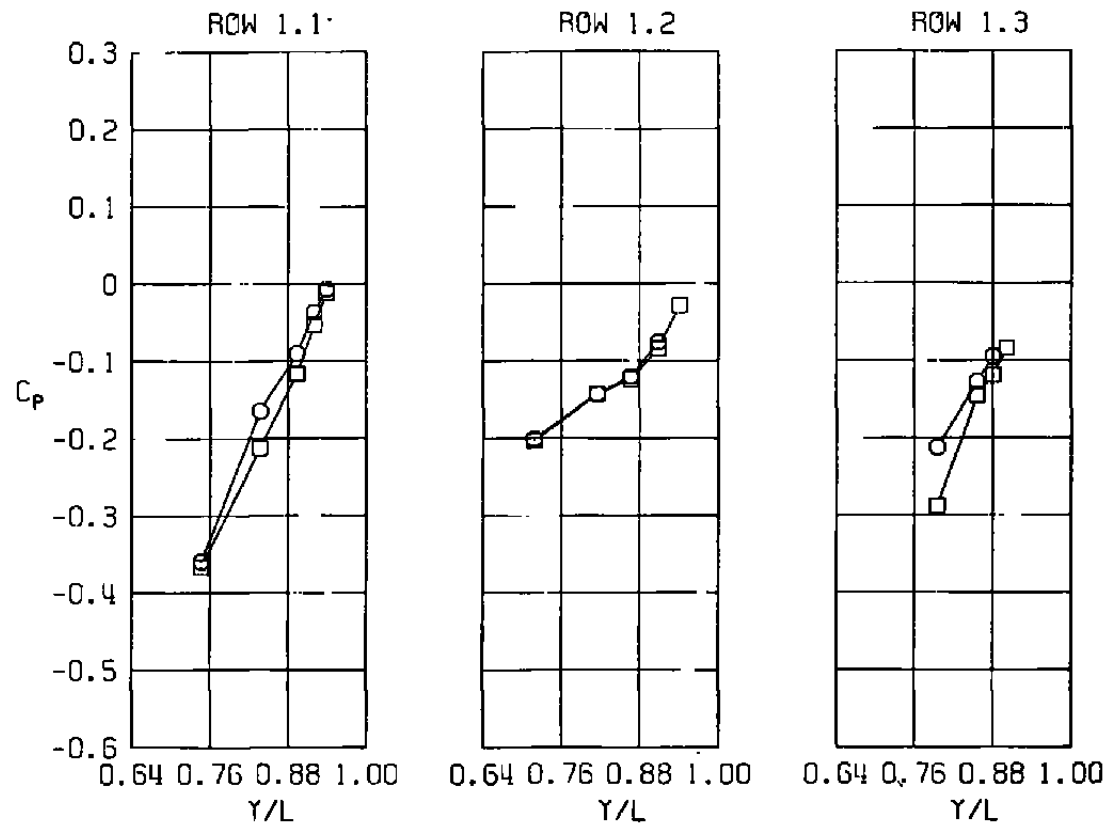
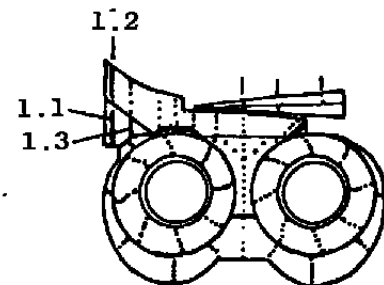


Figure 47. Comparison of nozzle afterbody pressure distributions for the EPES 0.07-scale models, $M = 0.60$.



b. Cowl
Figure 47. Concluded.

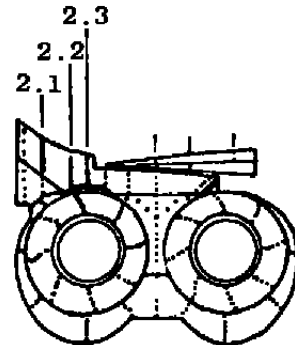
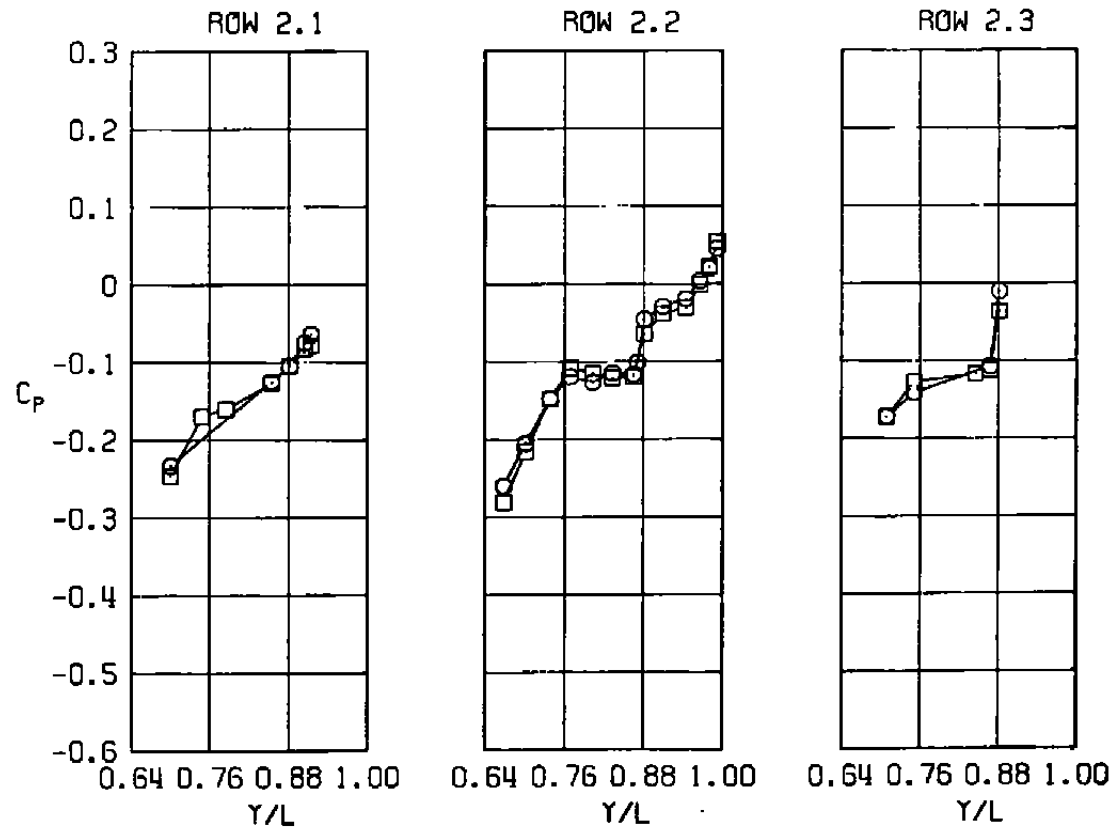
<u>SYM</u>	<u>M</u>	<u>ALPH</u>	<u>NPR</u>	<u>MFR</u>	<u>DELH</u>	<u>Re x 10⁻⁶</u>	<u>MODEL</u>	<u>CDNOZ</u>
□	0.80	0.98	2.59	0	0.02	2.50	NAB	0.0004
○	0.80	-0.03	2.59	0.457	0.16	2.50	EPES	0.0003



a. Row 1

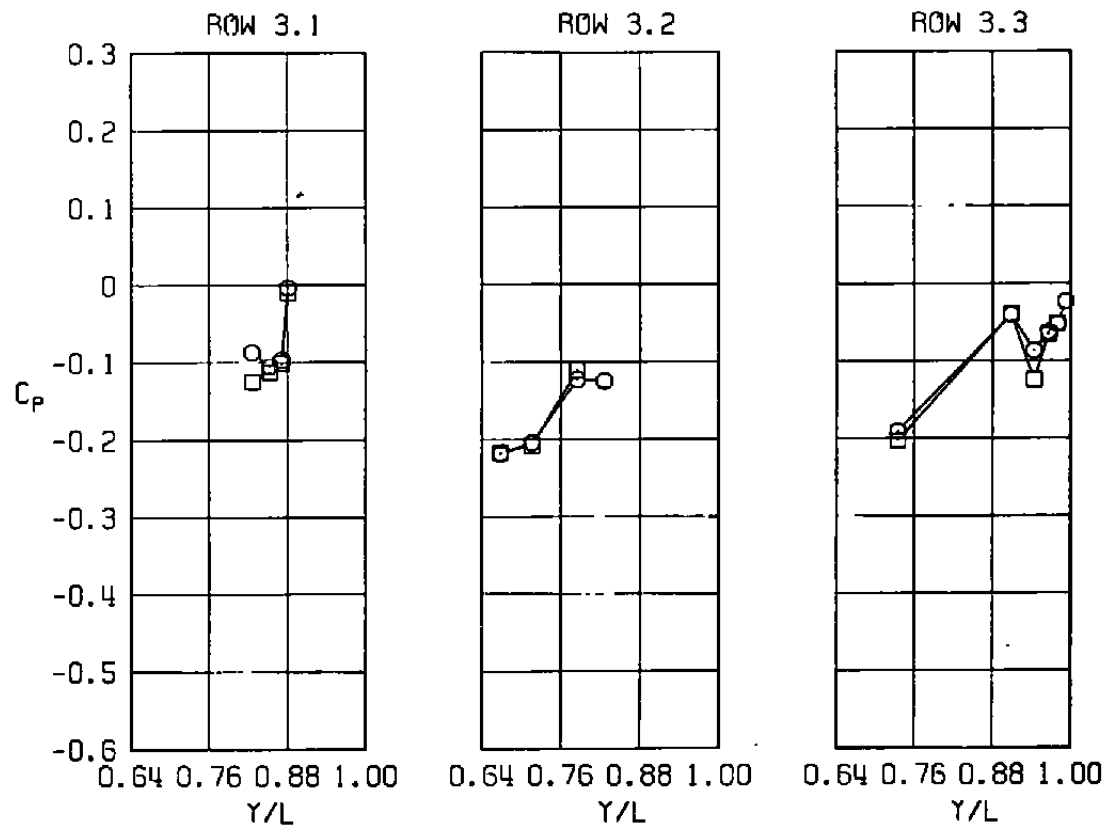
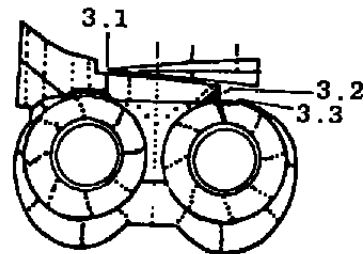
Figure 48. Comparison of nozzle afterbody pressure distributions for the EPES and NAB models, $M = 0.80$.

<u>SYM</u>	<u>M</u>	<u>ALPH</u>	<u>NPR</u>	<u>MFR</u>	<u>DELH</u>	<u>Re x 10⁻⁶</u>	<u>MODEL</u>	<u>CDNOZ</u>
□	0.80	0.98	2.59	0	0.02	2.50	NAB	0.0004
○	0.80	-0.03	2.59	0.457	0.16	2.50	EPES	0.0003



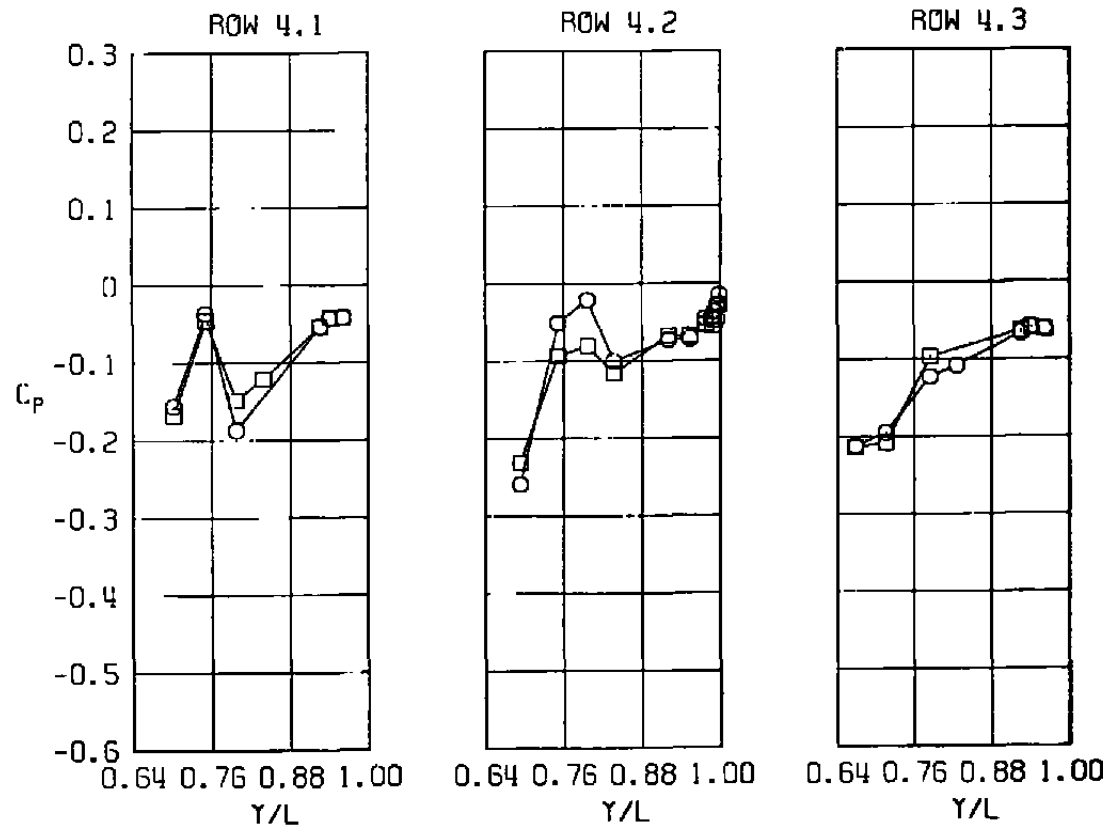
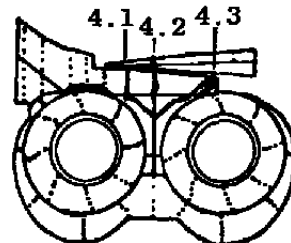
b. Row 2
Figure 48. Continued.

<u>SYM</u>	<u>M</u>	<u>ALPH</u>	<u>NPR</u>	<u>MFR</u>	<u>DELH</u>	<u>Re x 10⁻⁶</u>	<u>MODEL</u>	<u>CDNOZ</u>
□	0.80	0.98	2.59	0	0.02	2.50	NAB	0.0004
○	0.80	-0.03	2.59	0.457	0.16	2.50	EPES	0.0003



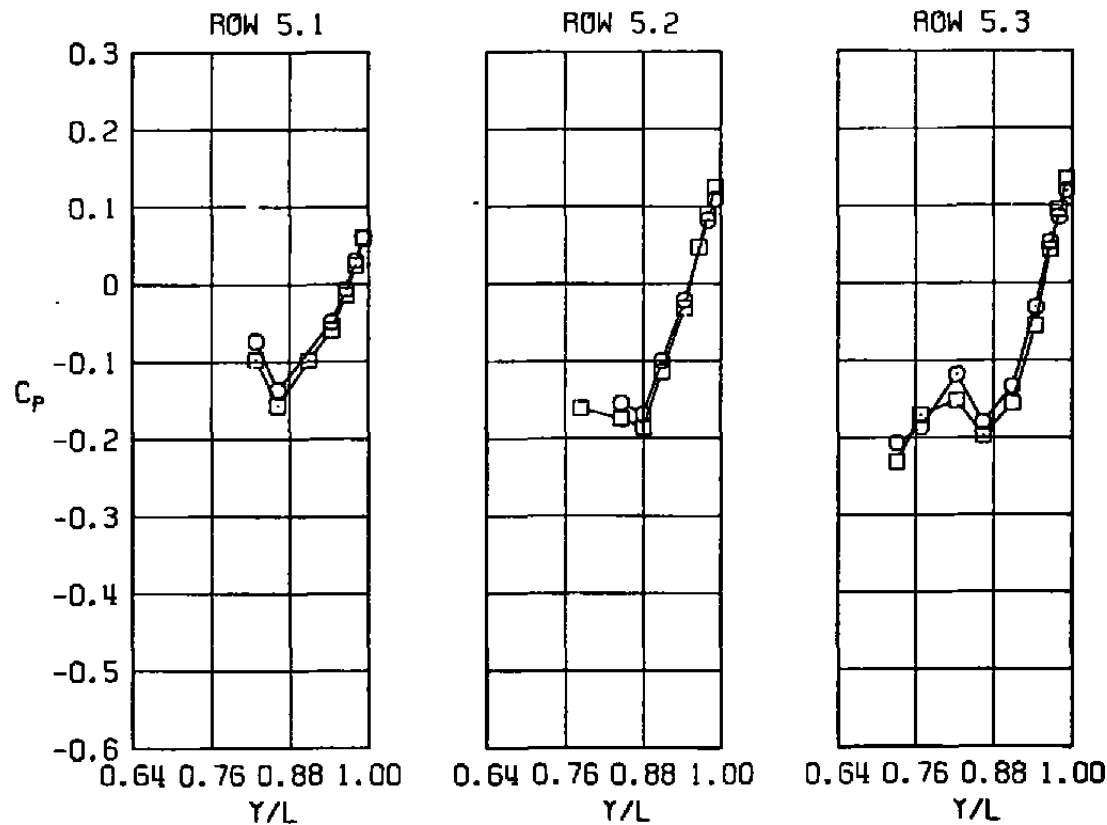
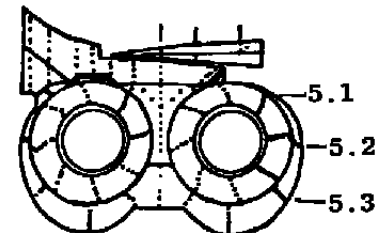
c. Row 3
Figure 48. Continued.

<u>SYM</u>	<u>M</u>	<u>ALPH</u>	<u>NPR</u>	<u>MFR</u>	<u>DELH</u>	<u>Re x 10⁻⁶</u>	<u>MODEL</u>	<u>CDNOZ</u>
□	0.80	0.98	2.59	0	0.02	2.50	NAB	0.0004
○	0.80	-0.03	2.59	0.457	0.16	2.50	EPES	0.0003



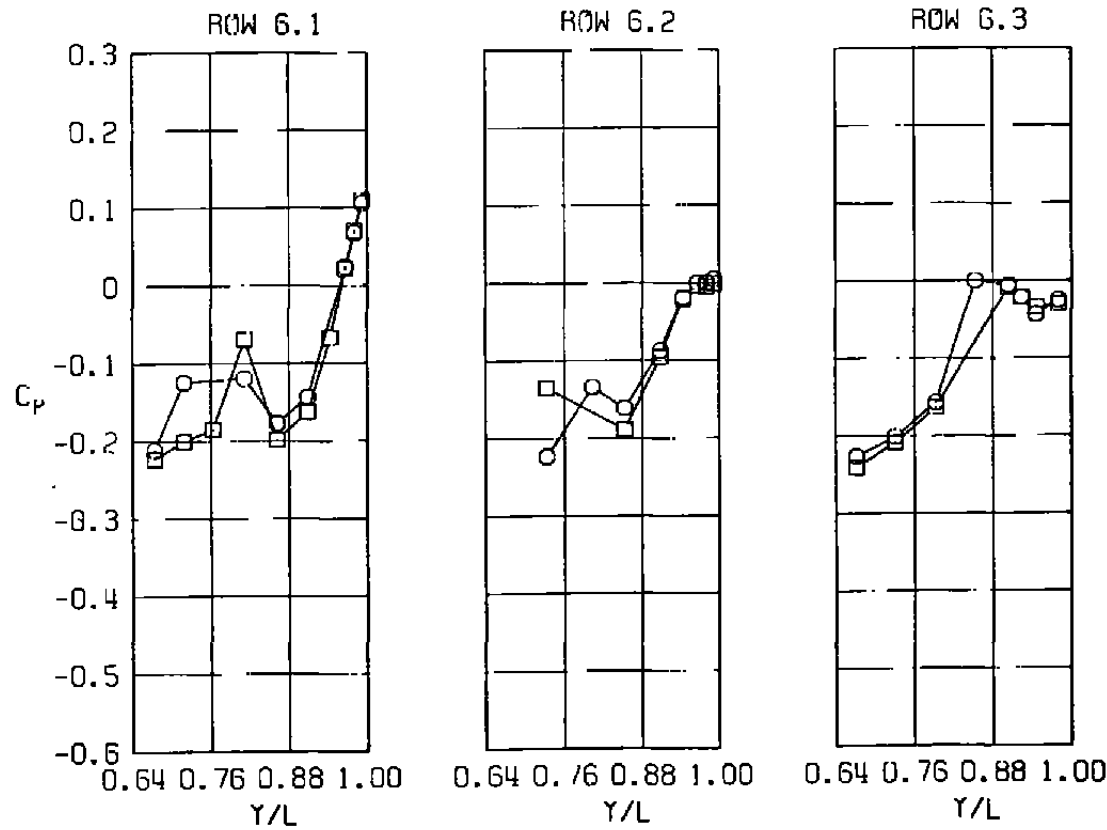
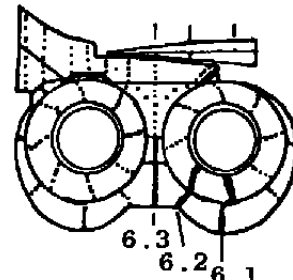
d. Row 4
Figure 48. Continued.

<u>SYM</u>	<u>M</u>	<u>ALPH</u>	<u>NPR</u>	<u>MFR</u>	<u>DELH</u>	<u>Re</u> $\times 10^{-6}$	<u>MODEL</u>	<u>CDNOZ</u>
□	0.80	0.98	2.59	0	0.02	2.50	NAB	0.0004
○	0.80	-0.03	2.59	0.457	0.16	2.50	EPES	0.0003

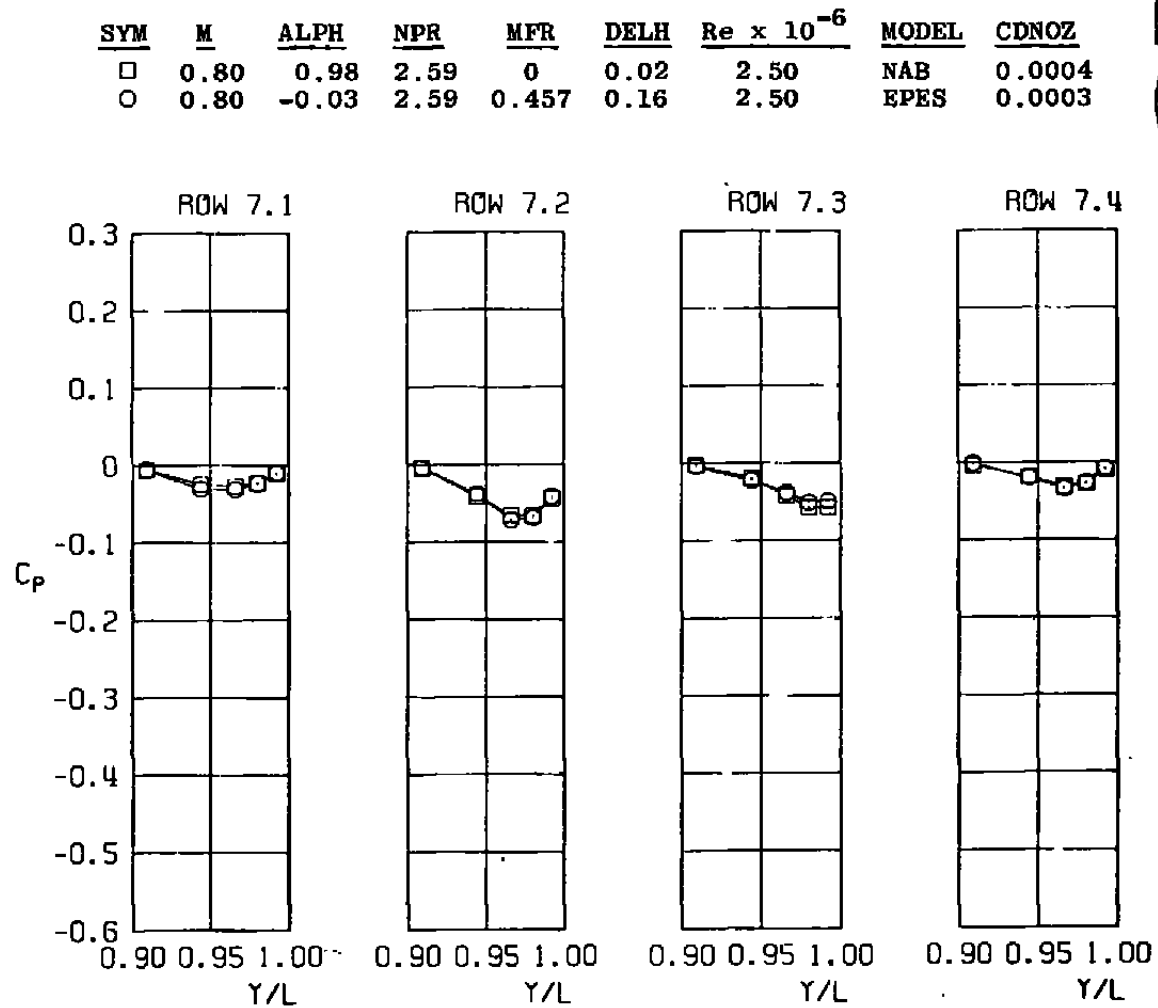


e. Row 5
Figure 48. Continued.

<u>SYM</u>	<u>M</u>	<u>ALPH</u>	<u>NPR</u>	<u>MFR</u>	<u>DELL</u>	<u>Re x 10⁻⁶</u>	<u>MODEL</u>	<u>CDNOZ</u>
□	0.80	0.98	2.59	0	0.02	2.50	NAB	0.0004
○	0.80	-0.03	2.59	0.457	0.16	2.50	EPES	0.0003

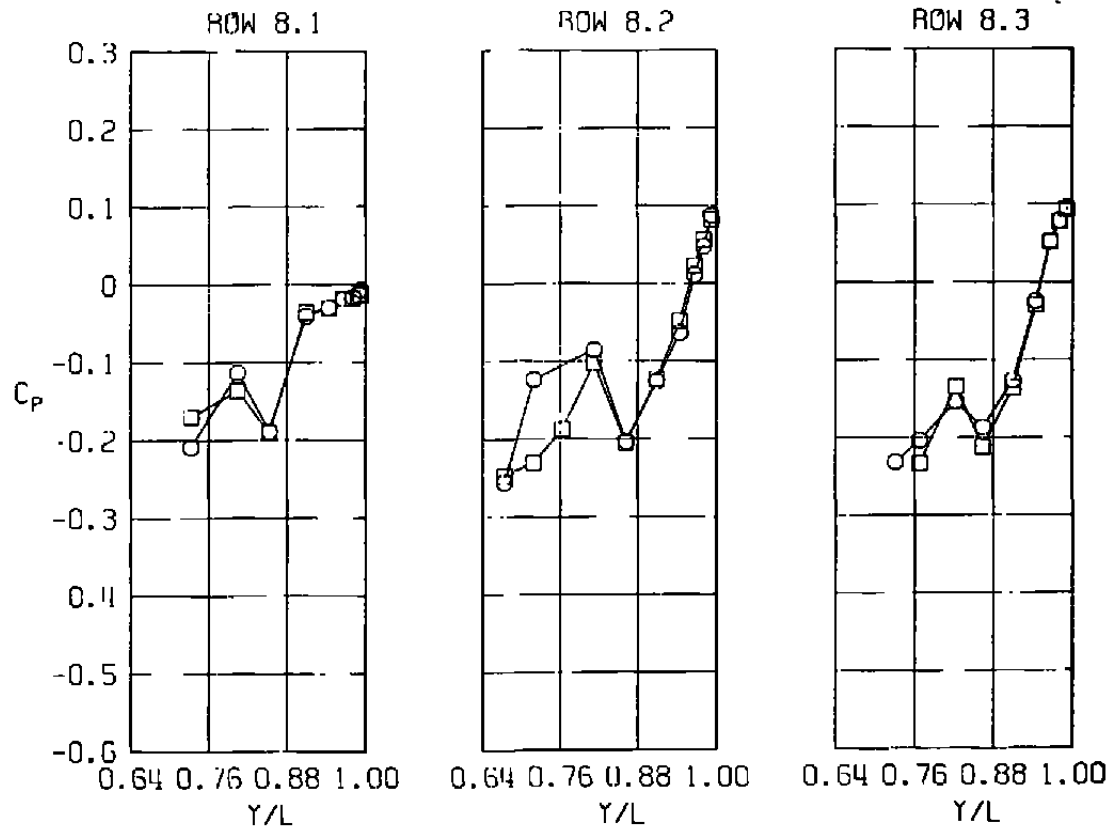
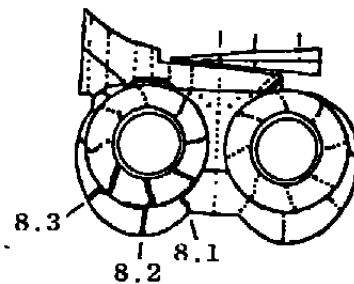


f. Row 6
Figure 48. Continued.



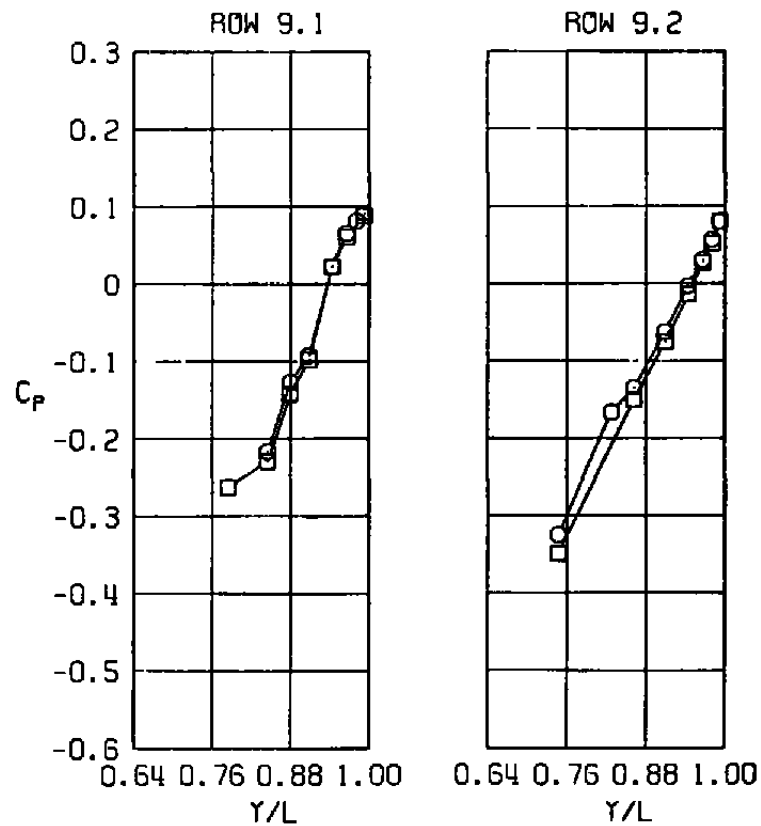
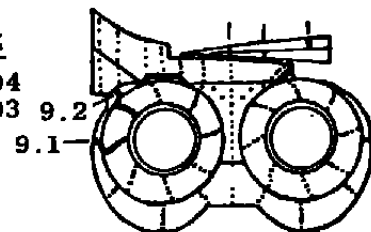
g. Row 7
Figure 48. Continued.

<u>SYM</u>	<u>M</u>	<u>ALPH</u>	<u>NPR</u>	<u>MFR</u>	<u>DELH</u>	<u>Re</u> $\times 10^{-6}$	<u>MODEL</u>	<u>CDNOZ</u>
□	0.80	0.98	2.59	0	0.02	2.50	NAB	0.0004
○	0.80	-0.03	2.59	0.457	0.16	2.50	EPES	0.0003



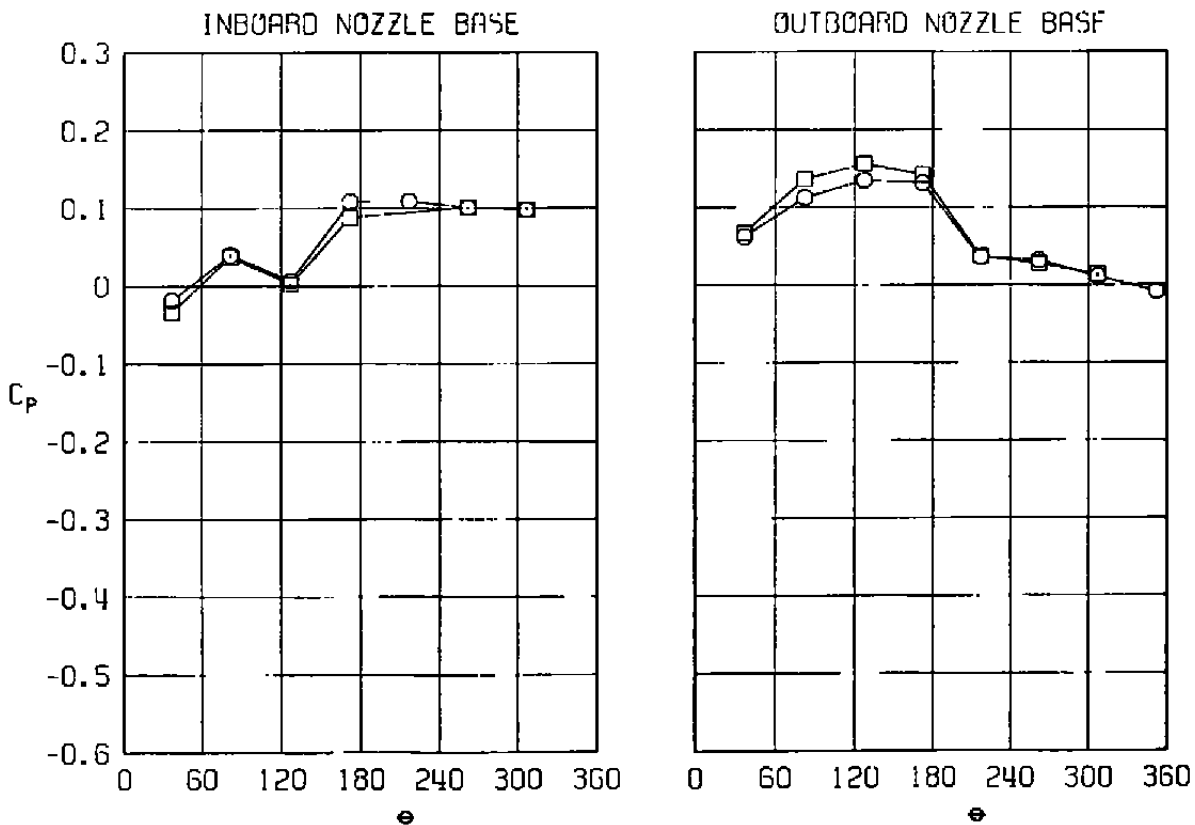
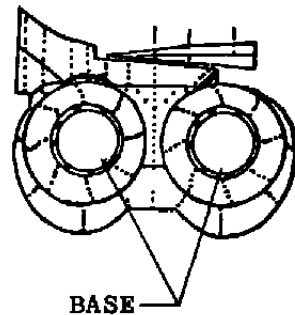
h. Row 8
Figure 48. Continued.

<u>SYM</u>	<u>M</u>	<u>ALPH</u>	<u>NPR</u>	<u>MFR</u>	<u>DELH</u>	<u>Re x 10⁻⁶</u>	<u>MODEL</u>	<u>CDNOZ</u>
□	0.80	0.98	2.59	0	0.02	2.50	NAB	0.0004
O	0.80	-0.03	2.59	0.457	0.16	2.50	EPES	0.0003



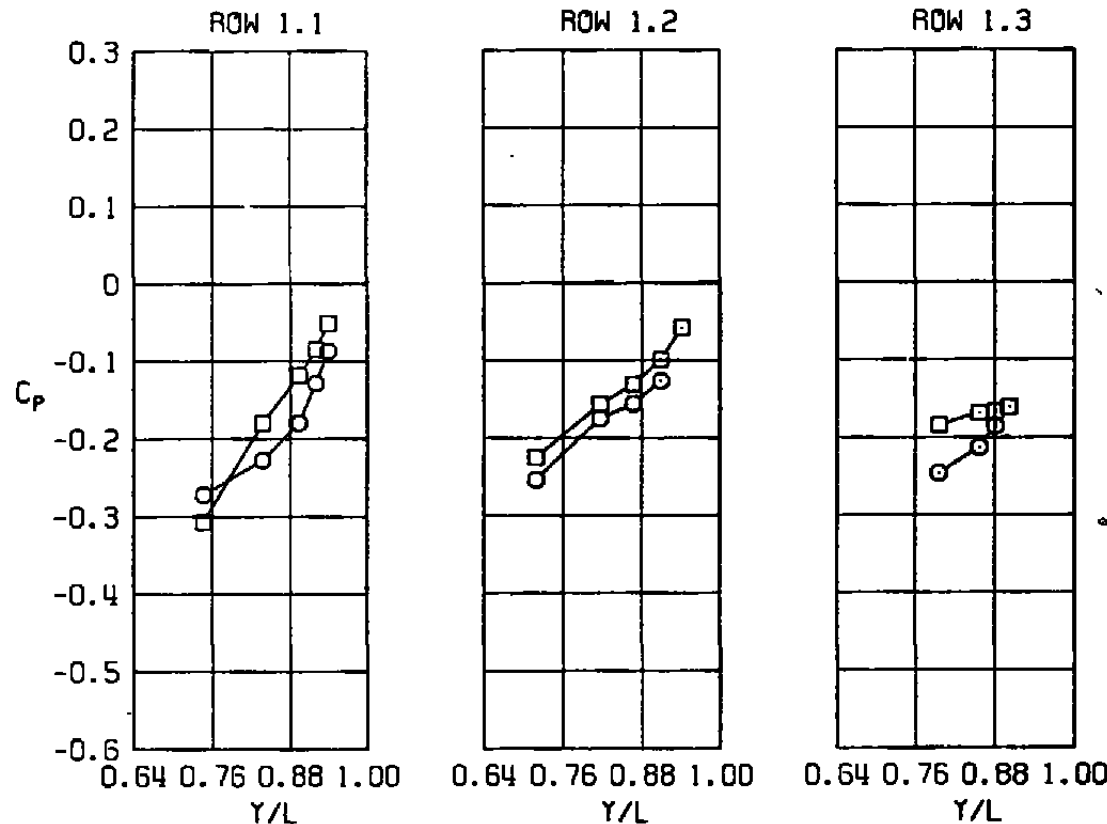
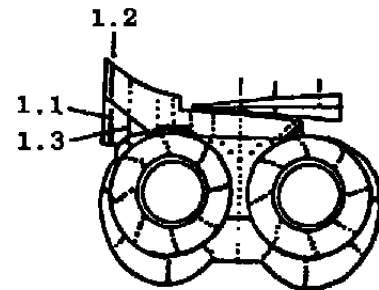
i. Row 9
Figure 48. Continued.

<u>SYM</u>	<u>M</u>	<u>ALPH</u>	<u>NPR</u>	<u>MFR</u>	<u>DELH</u>	<u>Re x 10⁻⁶</u>	<u>MODEL</u>	<u>CDNOZ</u>
□	0.80	0.98	2.59	0	0.02	2.50	NAB	0.0004
○	0.80	-0.03	2.59	0.457	0.16	2.50	EPES	0.0003



j. Nozzle base
Figure 48. Concluded.

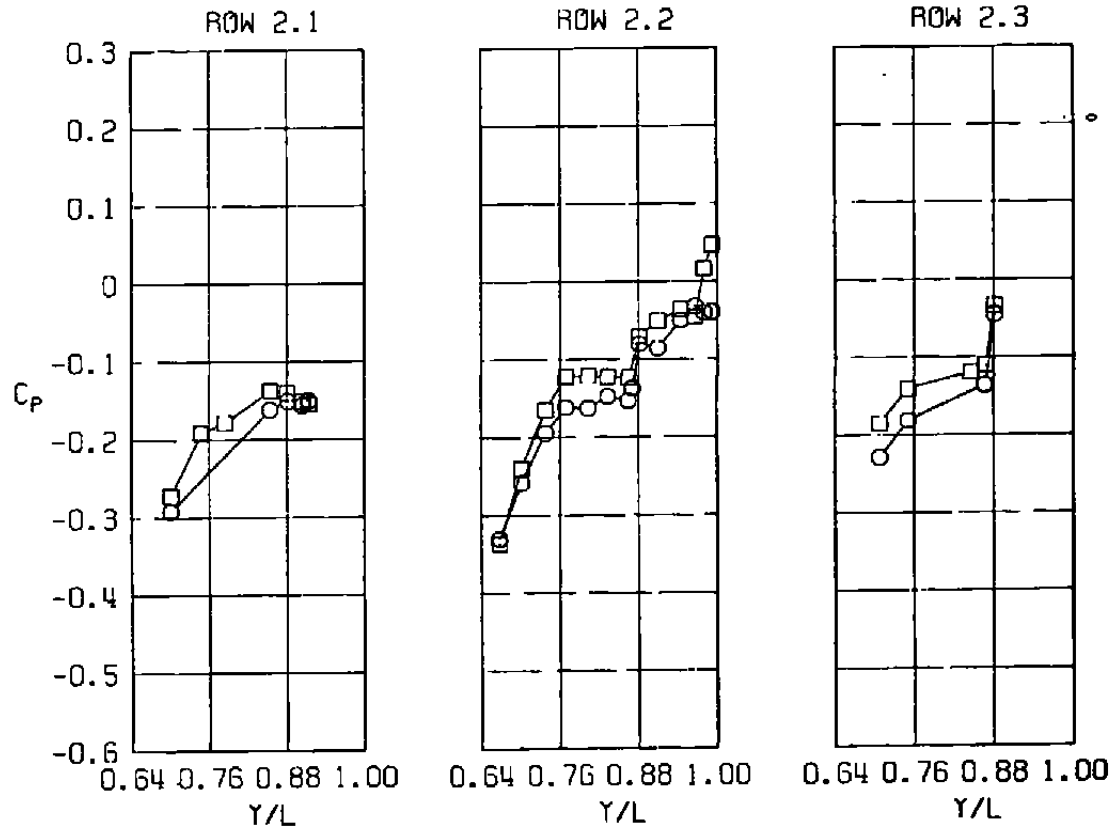
<u>SYM</u>	<u>M</u>	<u>ALPH</u>	<u>NPR</u>	<u>MFR</u>	<u>DELH</u>	<u>Re x 10⁻⁶</u>	<u>MODEL</u>	<u>CDNOZ</u>
□	0.90	0.01	2.90	0.0	0.10	2.50	NAB	0.0003
○	0.90	-0.02	3.15	0.472	0.08	2.53	EPES	0.0005



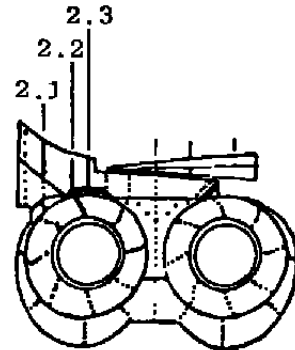
a. Row 1

Figure 49. Comparison of nozzle afterbody pressure distributions for the EPES and the NAB models, $M = 0.90$.

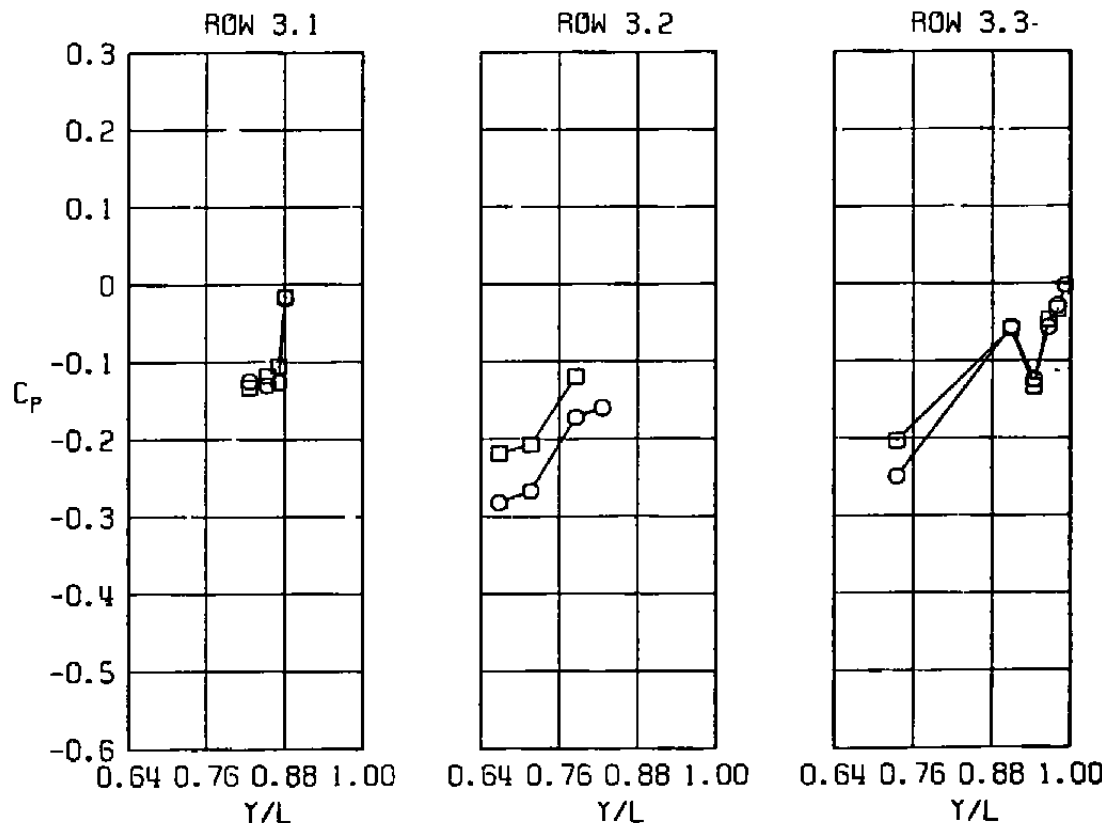
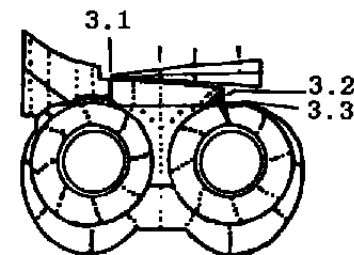
<u>SYM</u>	<u>M</u>	<u>ALPH</u>	<u>NPR</u>	<u>MFR</u>	<u>DElh</u>	<u>Re x 10⁻⁶</u>	<u>MODEL</u>	<u>CDNOZ</u>
□	0.90	0.01	2.90	0.0	0.10	2.50	NAB	0.0003
○	0.90	-0.02	3.15	0.472	0.08	2.53	EPES	0.0005



b. Row 2
Figure 49. Continued.

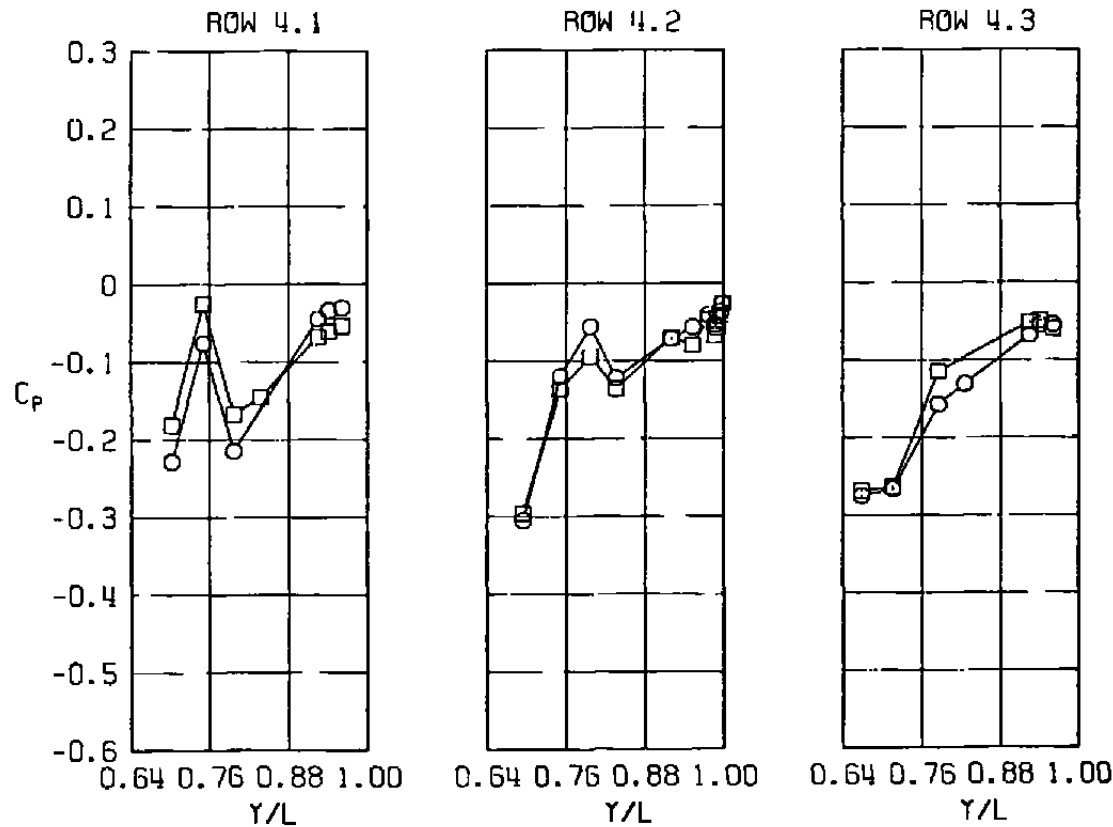
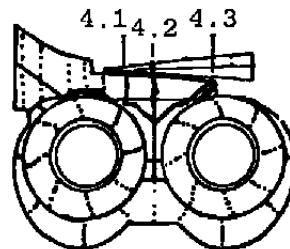


<u>SYM</u>	<u>M</u>	<u>ALPH</u>	<u>NPR</u>	<u>MFR</u>	<u>DELH</u>	<u>Re</u> $\times 10^{-6}$	<u>MODEL</u>	<u>CDNOZ</u>
□	0.90	0.01	2.90	0.0	0.10	2.50	NAB	0.0003
○	0.90	-0.02	3.15	0.472	0.08	2.53	EPES	0.0005



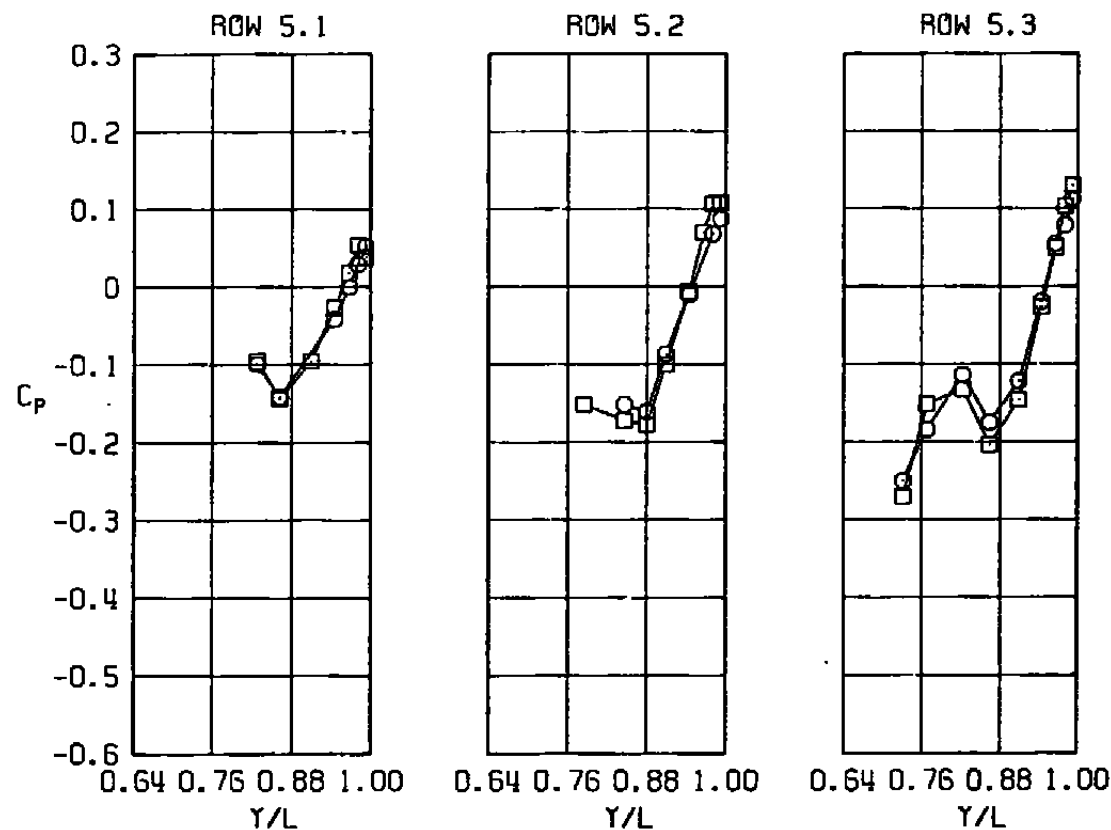
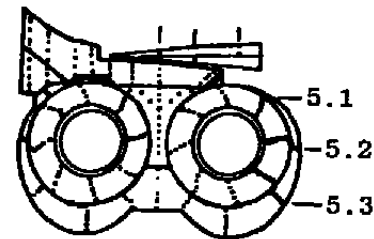
c. Row 3
Figure 49. Continued.

<u>SYM</u>	<u>M</u>	<u>ALPH</u>	<u>NPR</u>	<u>MFR</u>	<u>DELI</u>	<u>Re x 10⁻⁶</u>	<u>MODEL</u>	<u>CDNOZ</u>
□	0.90	0.01	2.90	0.0	0.10	2.50	NAB	0.0003
○	0.90	-0.02	3.15	0.472	0.08	2.53	EPES	0.0005



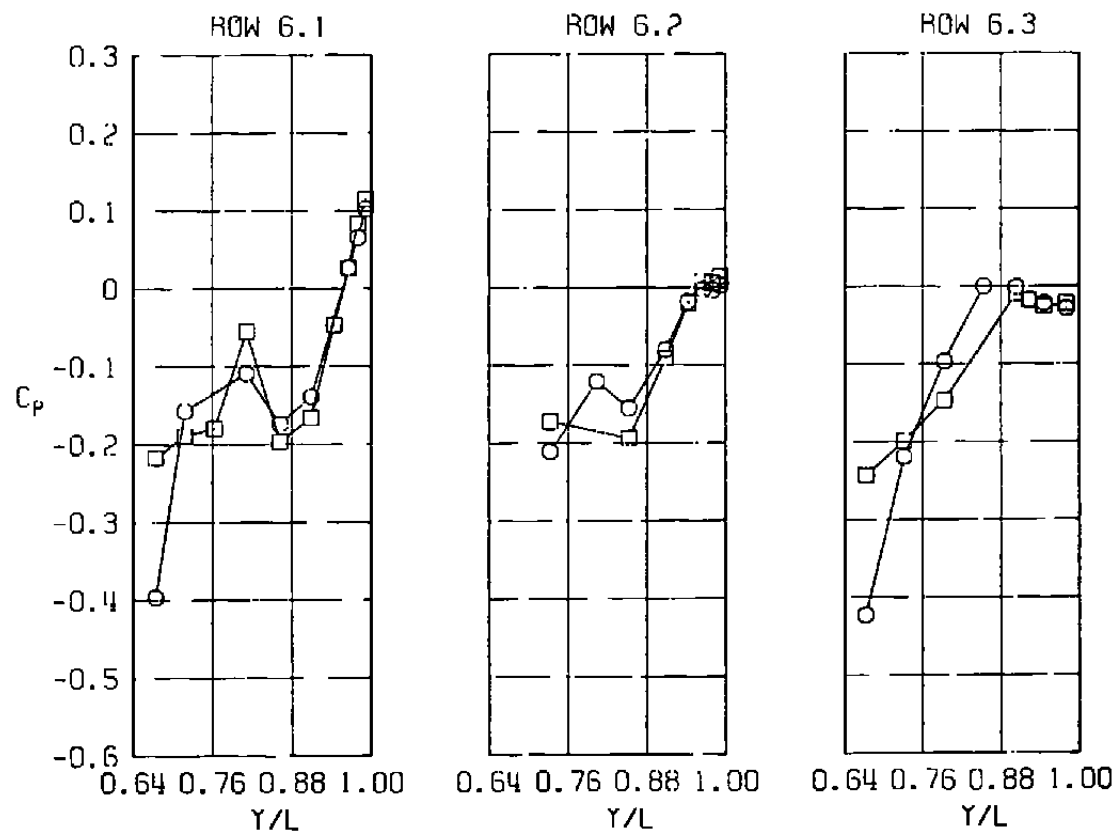
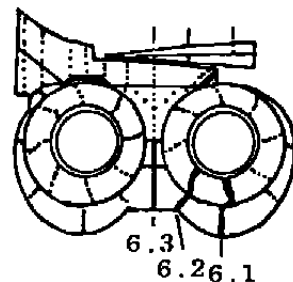
d. Row 4
Figure 49. Continued.

<u>SYM</u>	<u>M</u>	<u>ALPH</u>	<u>NPR</u>	<u>MFR</u>	<u>DELH</u>	<u>Re x 10⁻⁶</u>	<u>MODEL</u>	<u>CDNOZ</u>
□	0.90	0.01	2.90	0.0	0.10	2.50	NAB	0.0003
○	0.90	-0.02	3.15	0.472	0.08	2.53	EPES	0.0005

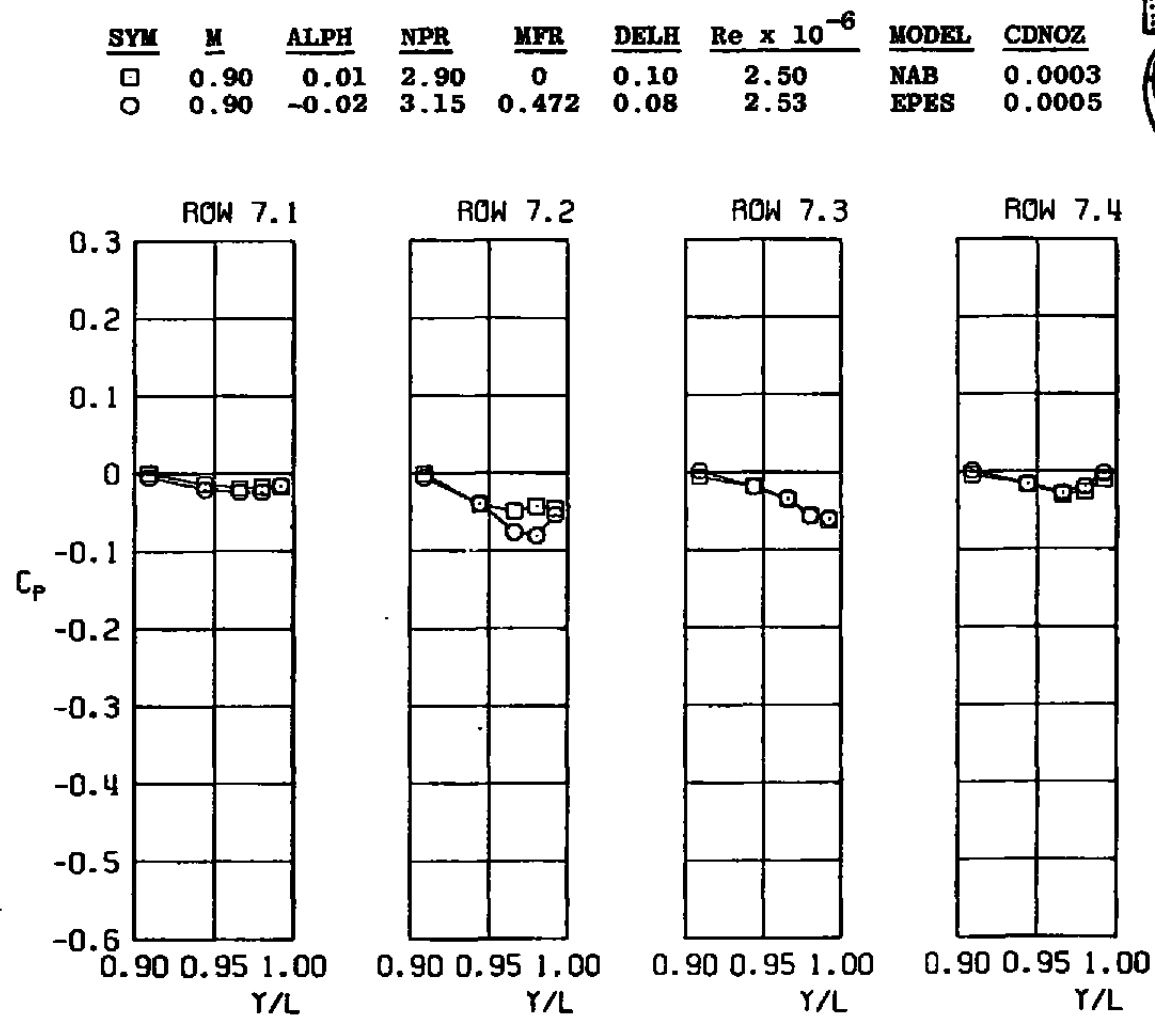


e. Row 5
Figure 49. Continued.

<u>SYM</u>	<u>M</u>	<u>ALPHI</u>	<u>NPR</u>	<u>MFR</u>	<u>DELIH</u>	<u>Re x 10⁻⁶</u>	<u>MODEL</u>	<u>CDNOZ</u>
□	0.90	0.01	2.90	0	0.10	2.50	NAB	0.0003
○	0.90	-0.02	3.15	0.472	0.08	2.53	EPES	0.0005

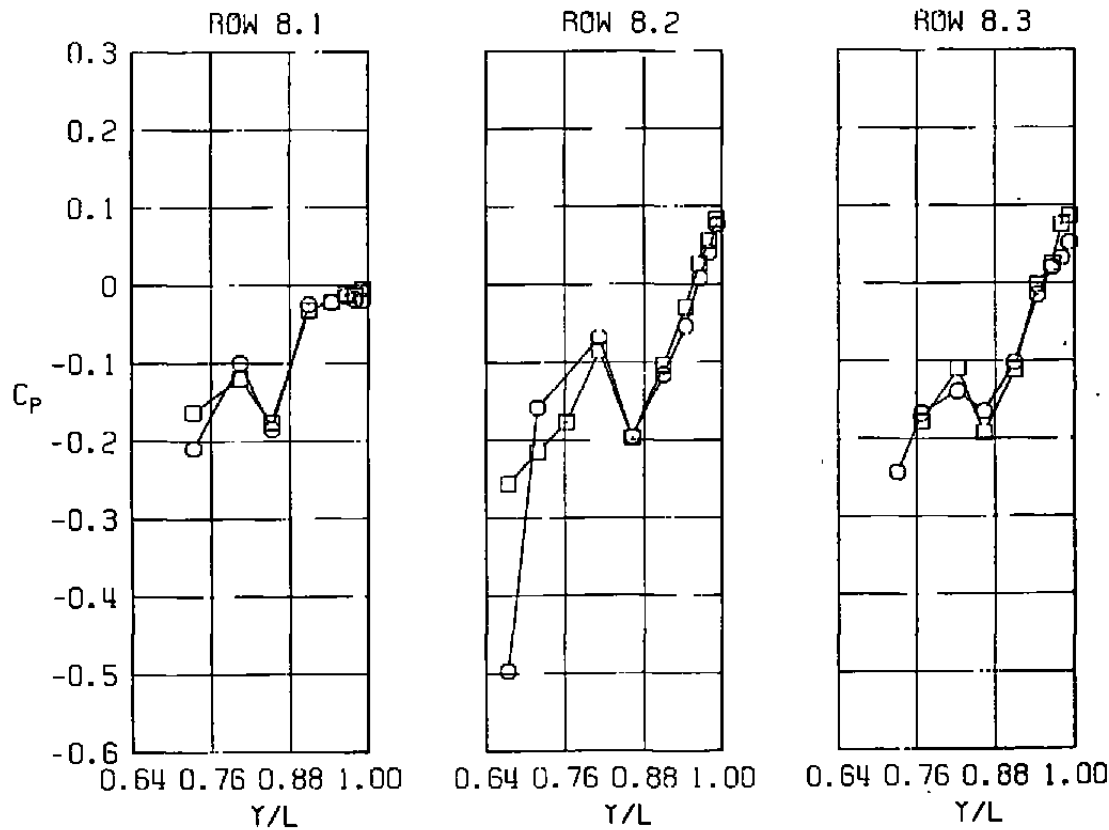
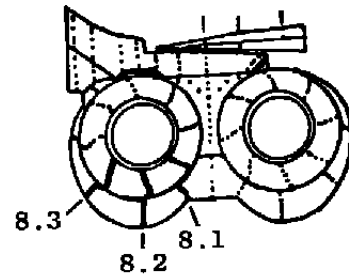


f. Row 6
Figure 49. Continued.



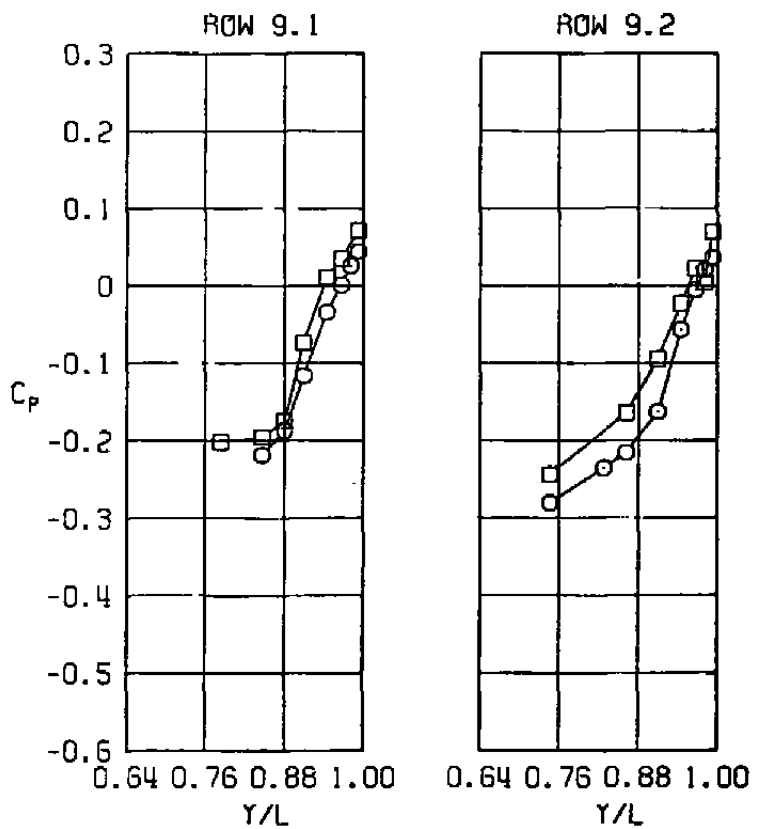
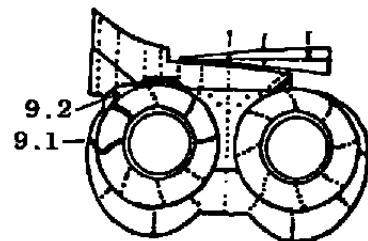
g. Row 7
Figure 49. Continued.

<u>SYM</u>	<u>M</u>	<u>ALPH</u>	<u>NPR</u>	<u>MFR</u>	<u>DELH</u>	<u>Re x 10⁻⁶</u>	<u>MODEL</u>	<u>CDNOZ</u>
□	0.90	0.01	2.90	0	0.10	2.50	NAB	0.0003
○	0.90	-0.02	3.15	0.472	0.08	2.53	EPES	0.0005

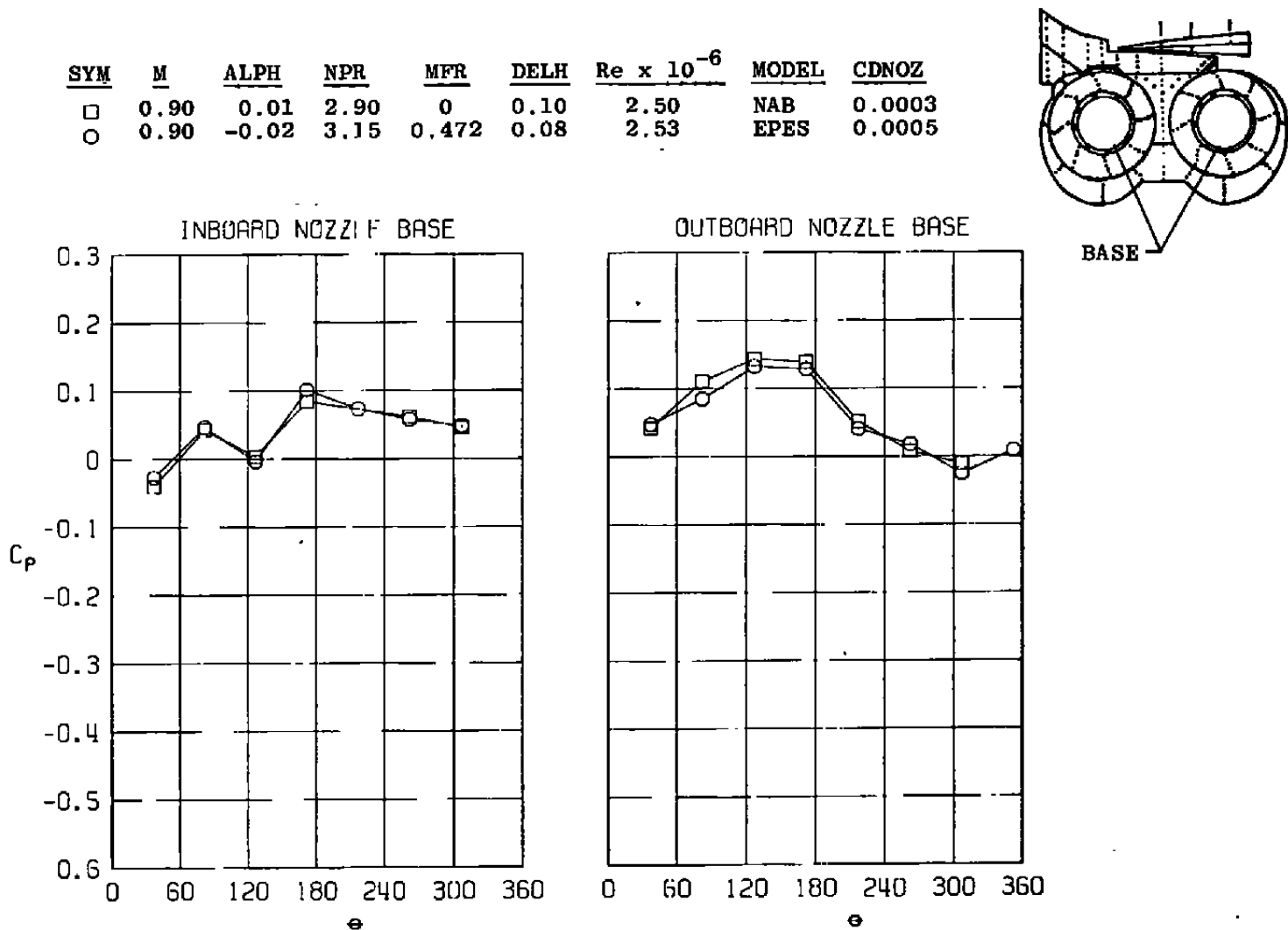


h. Row 8
Figure 49. Continued.

SYM	M	ALPH	NPR	MFR	DELH	$Re \times 10^{-6}$	MODEL	CDNOZ
□	0.90	0.01	2.90	0	0.10	2.50	NAB	0.0003
○	0.90	-0.02	3.15	0.472	0.08	2.53	EPES	0.0005



i. Row 9
Figure 49. Continued.



j. Nozzle base
Figure 49. Concluded.

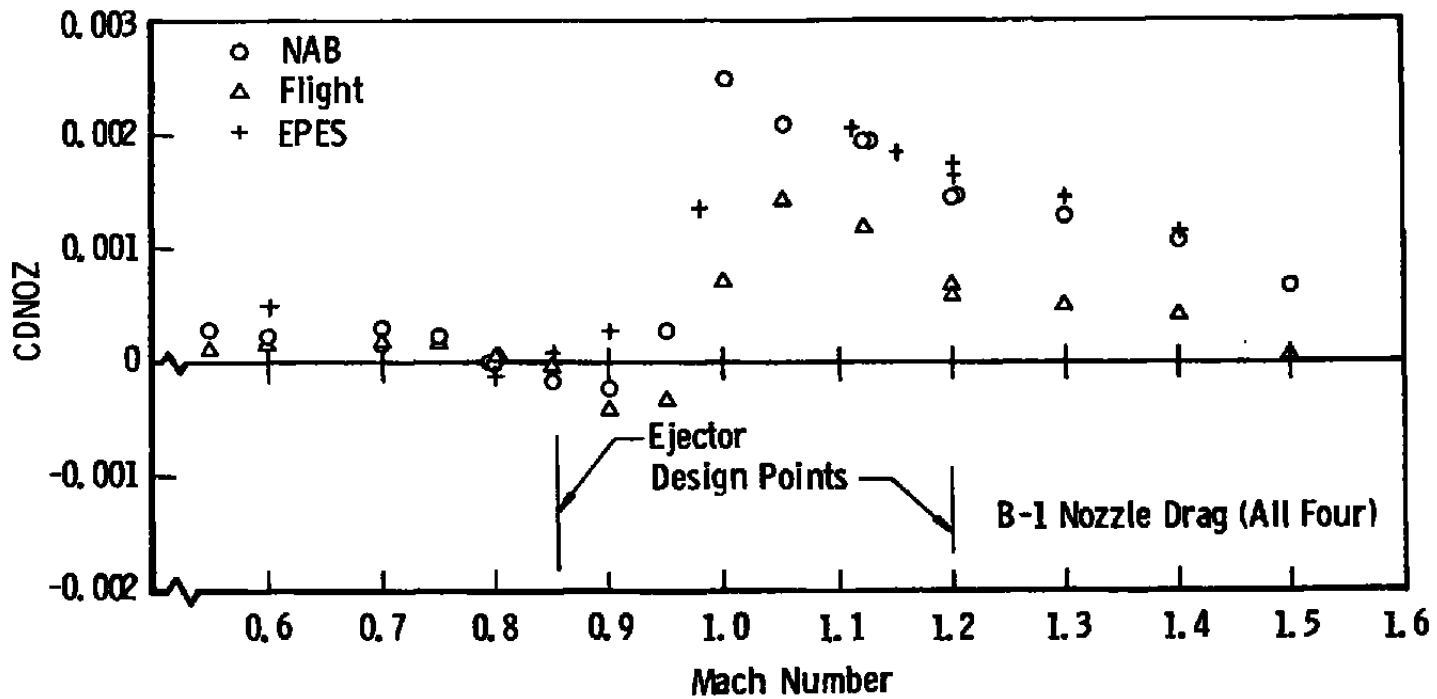


Figure 50. Comparison of axial force coefficient for EPES and NAB models and flight vehicle.

Table 1. Summary of Test Conditions

<u>M_{∞}</u>	<u>$Re/l \times 10^{-6}$</u>	<u>α, deg</u>	<u>NPR</u>	<u>MFR</u>	<u>Configuration</u>
0.85	2.5	0-4	1.5-3.8	0.40-0.48	Subsonic Cruise
0.80	2.5	0 and 4	1.5-3.8	0.40-0.48	Subsonic Cruise
0.60	2.5	0 and 4	1.2-2.6	0.29-0.52	Subsonic Cruise
0.90	2.5	0	1.6-3.6	0.38-0.47	Subsonic Cruise
0.85	3.6	0 and 4	2.0-2.9	0.38-0.48	Subsonic Cruise
0.85	2.5	0 and 4	2.0-3.8	0.38-0.48	Subsonic Cruise
					Left Nacelle Plugged
1.20	2.5	0-4	3.2-6.0	0.58-0.65	Supersonic Dash
1.30	2.5	1.92	4.80	0.64	Supersonic Dash
1.40	2.5	0	3.9-7.0	0.61-0.68	Supersonic Dash
1.15	2.5	3.5	4.4	0.63	Supersonic Dash
1.11	2.5	3.9	4.30	0.63	Supersonic Dash
0.97	2.5	0 and 3.76	2.3-3.8	0.57-0.63	Supersonic Dash
1.20	2.5	0, 2 and 4	3.5-5.0	0.58-0.65	Supersonic Dash
					Left Nacelle Plugged

Table 2. Measurement Uncertainties

<u>Parameter</u>	<u>$M_{\infty} = 0.55$</u>	<u>$M_{\infty} = 0.85$</u>	<u>$M_{\infty} = 1.60$</u>
C_p	± 0.0159	± 0.0104	± 0.0075
M_{∞}	± 0.003	± 0.003	± 0.004
NPR	± 0.005	± 0.010	± 0.040
P_{∞}	± 2.4	± 2.0	± 1.6
q_{∞}	± 3.2	± 2.2	± 0.8
α	± 0.05	± 0.05	± 0.05

APPENDIX A

DESIGN AND CALIBRATION OF EJECTOR-POWERED ENGINE SIMULATORS FOR THE B-1 MODEL

A-1.0 INTRODUCTION

The ejector-powered engine simulators (EPES) designed for the 0.06-scale B-1 model were based upon the results of preliminary investigations (Ref. 2) which demonstrated feasibility of the EPES concept. However, operational requirements and constraints imposed by the incorporation of the EPES in an existing model/strut system required consideration of components that were not evaluated in the preliminary investigations. Operational checkouts and calibration tests of the EPES were accomplished in the Arnold Engineering Development Center (AEDC) Engine Test Facility (ETF) Propulsion Research Cell (R-1A-2) to (1) verify aspects of the EPES designs and (2) determine internal performance characteristics that could not readily be obtained in the wind tunnel installation.

Design considerations and details of the EPES tests accomplished before the wind tunnel entry are summarized in this appendix.

A-2.0 EJECTOR-POWERED ENGINE SIMULATOR DESIGN

A-2.1 PRELIMINARY CONSIDERATIONS

The B-1 vehicle was selected for the EPES proof-of-concept tests because of the availability of conventional test techniques data on both the inlet and nozzle afterbody for comparison with the EPES results and the availability of flight data from a fully instrumented B-1 aircraft. The B-1 model was also chosen because the short nacelle length-to-diameter ratio represents a more difficult problem for the EPES than would a fighter with fuselage-mounted engines.

Design features of the existing B-1 model nacelles precluded incorporation of EPES without significant modifications. Since further testing of the original B-1 model was planned, no alterations to the existing model and support strut were permitted. However, the model was originally designed to accommodate different nacelle configurations so a new right-wing nacelle was designed and built specifically for the EPES investigations.

A-2.2 PERFORMANCE REQUIREMENTS

Simulators were designed for conditions representative of B-1 engine operation at subsonic cruise and supersonic dash conditions. Based upon the preliminary EPES

investigations (Ref. 2), engine performance considered in the EPES design was characterized by an inlet mass flux parameter (WEC) and the exhaust-to-inlet total-pressure ratio (SPR). Inlet mass flux parameters and total-pressure ratios, determined at flight altitudes and Mach numbers corresponding to the rating points of the General Electric F101 engine, were found to lie in two bands corresponding to augmented (i.e., supersonic dash) and unaugmented (i.e., subsonic cruise) operation (Fig. A-1). Comparison of the engine requirements with potential EPES operating capabilities deduced from the preliminary EPES investigations indicated that the supersonic dash conditions were well within the demonstrated EPES operating range. However, to achieve the subsonic cruise condition, it was evident that up to 35 percent of captured flow would need to be removed upstream of the EPES to cover the entire operating map.

Determination of the effects of changes in WEC and SPR (which are related to MFR and NPR, respectively, at a given flight condition) on nacelle pressures was a requirement of the wind tunnel test program. Although SPR variations can readily be accomplished by varying ejector (i.e., primary) driving pressure, WEC variations can only be accomplished in a constant geometry system by varying the inlet duct outbleed flow with some auxiliary system. With the imposed stipulation that no alterations were to be made in the model and support strut, maximum outbleed potential was already established by pressure loss characteristics of the existing flow passages. Fanno line calculations indicated the maximum outbleed potential to be between 10 and 15 percent. There, the practical design point selected for the subsonic cruise condition (Fig. A-1) corresponded to 20-percent outbleed.

A-2.3 DESIGN APPROACH

The EPES nacelle was designed to have the same contours as the existing 0.07-scale inlet and 0.06-scale afterbody models. Internal inlet contours were scaled from the ramp lip (model nacelle station 0.9) to a point in the duct transition section (model nacelle station 11.4). The limited internal volume of the nacelle and a conservative design on the ejector air supply manifold required some deviation from the internal inlet contour downstream of model nacelle station 11.4. As a result, the EPES inlet diameter was 2.30 in. at nacelle station 15.0 rather than 2.701 in. scaled from the engine fan inlet station diameter. Exhaust nozzle contours were scaled from the intersection of the EPES mixing duct with the nozzle contraction cone to the nozzle exit.

A-2.3.1 Subsonic Cruise Configuration

The mixing duct for the subsonic cruise configuration was selected to produce a mixing duct-to-exhaust nozzle throat area contraction of 1.188 which, according to the preliminary studies (Ref. 2), is one of the requirements for achieving maximum WEC capability.

Nineteen area ratio 25.0 conical primary nozzles were strut mounted in a uniform symmetrical pattern (Fig. A-2a) over the mixing duct cross-sectional area. The mixing duct length selected corresponded to an equivalent single jet mixing duct length-to-diameter ratio* of 20 which the preliminary studies indicated was adequate to achieve well-mixed flow into the exhaust nozzle. An annular outbleed slot was originally incorporated in the design between the ejectors and the mixing duct inlet. When initial tests indicated outbleed was limited to about six percent, the annular slot was replaced with a scoop (Fig. A-2a) which increased the outbleed capability to 20 percent.

A-2.3.2 Supersonic Dash Configuration

The mixing duct geometry that could be considered for the supersonic dash configuration was controlled by several factors. Mixing duct length was dictated by the requirement that the ejector location be identical for both the subsonic cruise and supersonic dash configurations. The mixing duct diameter was limited to values between the Mach number 1.20 exhaust nozzle throat diameter (2.678 in.) and the maximum diameter (2.808 in.) consistent with the nacelle external contour. The maximum diameter was used for the mixing duct which resulted in a mixing duct-to-exhaust nozzle contraction ratio of 1.099 which is closer to unity than desirable for several reasons. First, optimum EPES performance is achieved with contraction ratios near 1.2. Also, contraction ratios approaching unity require very uniform flow, particularly near the wall, to achieve uniform exit Mach numbers corresponding to the one-dimensional values associated with the area distribution. Finally, with exhaust nozzle contraction ratios near unity it is difficult to establish the desired subsonic conditions at the mixing duct since the exhaust nozzle will function like an overspeeded fixed-geometry supersonic inlet (Ref. 8) and produce supersonic flow throughout with relatively low exhaust total pressures (Ref. 2). Operational checks indicated incomplete mixing conditions were experienced with various modifications to the ejector assembly. Screens were finally installed near the mixing duct exit to accelerate mixing and improve exhaust flow uniformity. Even with these modifications, exhaust flow uniformity (discussed below) was not achieved. The configuration used in the wind tunnel tests represented the best combination of ejector and screen geometries as determined from the development tests.

* $(L/D)_{\text{equivalent}} = (L/D)_{\text{mixing duct}} \sqrt{\text{No. of primary nozzles}}$

A-3.0 EJECTOR-POWERED ENGINE SIMULATOR DEVELOPMENT/CALIBRATION TESTS

Before testing with the EPES units in wind tunnel models, checkout and calibration testing of the units were accomplished to determine the as-built performance characteristics, including exhaust nozzle total-pressure profiles, percent inlet outbleed obtainable, and the overall pumping characteristics.

A-3.1--SB2--TEST APPARATUS

The EPES calibration test series was conducted in the AEDC Propulsion Research Cell (R-1A-2). The test cell configuration is shown in Fig. A-2b. A bellmouth entry section was installed between the plenum chamber and the EPES inlet station. An oversize inlet bleed line was provided to ensure no line size limitation effects on the EPES calibration data. Air from a high-pressure supply system was used as the working fluid. A portion of the air was throttled to pressures from 200 to 1,200 psia to supply the EPES primary nozzles, and the remainder of the air was throttled to from 5 to 40 psia to supply the engine simulator inlet mass flow. The simulator inlet mass flow rate was metered with a circular arc metering venturi located upstream of the plenum section. The primary mass flow rate was calculated from choked conditions at the throats of the primary nozzles.

A-3.2 INSTRUMENTATION

Instrumentation stations for the calibration tests are indicated in Fig. A-3. Total temperatures were measured with single-shielded, self-aspirating, copper-constantan thermocouple probes using an ice bath reference junction. Pressures were measured with differential, strain-gage transducers which were referenced to atmospheric pressure.

The EPES inlet and exhaust total-pressure profiles were obtained with a twelve-probe and a twenty-one-probe fixed position rake, respectively. The exhaust pressure rake was installed downstream of the exhaust nozzle rather than in the mixing duct to minimize rake wake and blockage effects on EPES performance.

A-3.3 TEST PROCEDURES

Transducers and thermocouples were calibrated in place before and after each test period. Pressures applied during the calibration were measured with a multiple-turn, fused-quartz bourdon tube equipped with a servocontrolled optical transducer.

All data were obtained at steady-state conditions. Flow control parameters (secondary flow venturi inlet pressure and temperature, primary nozzle inlet pressure and temperature, and test cell exhaust pressure) were monitored continuously to verify that steady-state conditions did exist throughout the data acquisition process. Data acquisition was accomplished using a digital data acquisition system.

Total pressures deduced from the exhaust nozzle exit pitot pressure surveys were used to define the area weighted mixing duct exit total pressure (PT8A) used to compute SPR. Pumping characteristics for a given EPES configuration were obtained at a constant EPES inlet total pressure (corresponding to the wind tunnel stagnation conditions). By varying the primary nozzle total pressure, hence flow rate, a range of values of SPR could be obtained. Variations in the inlet corrected mass flux were obtained by varying the inlet outbleed flow rate.

The calibration test conditions selected were comparable to anticipated wind tunnel conditions. Additional calibration data were obtained at two lower inlet Reynolds number conditions to define any possible Reynolds number effects that might exist with the EPES units. Geometric parameters and general test matrix investigated are summarized in Table A-1.

A-3.4 PRECISION OF MEASUREMENTS

Uncertainties (bands which include 95 percent of the calibration data) of the basic experimental parameters were estimated from repeat calibrations of the instrumentation. Uncertainties of the instrumentation systems were estimated from repeat calibrations of the systems against secondary standards whose precisions were traceable to the National Bureau of Standards calibration equipment. The uncertainties were combined using the Taylor series method of error propagation (Ref. 7) to determine the precision of the experimental parameters presented in Table A-2.

A-4.0 RESULTS AND DISCUSSION

Initial calibration of the EPES units indicated inadequate performance by the EPES because of the design compromises caused by model constraints. During the course of the calibrations, several significant design modifications were made to the EPES units to increase overall performance to a level suitable for the wind tunnel evaluation. The scope of the more significant design modifications and the impact of the modifications on the performance results are discussed along with the final calibration results.

A-4.1 SUBSONIC CRUISE CONFIGURATION

The original design for the subsonic cruise EPES unit incorporated provisions for outbleed of a portion of the inlet mass flow through an annular slot surrounding the injector face. Initial testing with this configuration revealed that the outbleed flow rates obtainable through the annular slot were inadequate, being a maximum of approximately six percent of the inlet flow. The annular outbleed slot was removed and replaced with an inlet scoop configuration as shown in Fig. A-2. The scoop was located at an axial position relative to the ejector that was dictated by existing internal flow passages in the B-1 nacelle/wing root area. With the scoop configuration, outbleed flow rates of approximately 20 percent of the inlet flow were obtained. However, the scoop produced a wake that caused low duct centerline Mach numbers at the no bleed condition (Fig. A-4) with the subsonic cruise units. The initial supersonic dash units were calibrated with the scoops removed so ejector inlet Mach numbers were more uniform (Fig. A-5) for these cases.

The results of the subsonic cruise EPES calibration tests are presented in Figs. A-6 through A-10. Inlet mass fluxes (WEC) obtained with no inlet outbleed were five percent lower than the 50-lbm/sec/ft² estimate based on the EPES research experiments (Ref. 2). The maximum outbleed that could be obtained with choked flow at the exit of the outbleed scoop was approximately 20 percent of the corrected inlet mass flux. With maximum outbleed, the maximum obtainable corrected inlet mass flux was within approximately four percent of the design value (Fig. A-6), which was felt to be sufficiently close to demonstrate the viability of the EPES concept in the wind tunnel tests. Both of the subsonic cruise EPES units produced pumping characteristics that were within ± 0.5 percent of each other. Thus, no significant problem appears to exist with multiple units of the same design manufactured within reasonable shop tolerances producing essentially identical performance.

Variation of WEC with ejector driving pressure is presented in Fig. A-7. The data indicate a maximum value of WEC is obtained at ejector-to-inlet pressure ratio of 75, either with or without outbleed. As ejector pressure is increased, flow at the primary nozzle exits becomes increasingly underexpanded which in turn causes a reduction in the effective secondary flow area and WEC.

Exhaust flow pressure surveys (Fig. A-8) indicated relatively uniform flow conditions with ejector driving pressures corresponding to exhaust-to-inlet pressure ratios less than 1.8. With higher driving pressures, supersonic flow existed in the mixing duct which produced significant nonuniformities in the exhaust flow and relatively low mixing duct static pressures. The mixing duct exit static pressure for the supersonic condition is about 70 percent lower than the subsonic value (Fig. A-9). Furthermore, the change from subsonic to

supersonic mixing duct flow is an abrupt function of the primary nozzle driving pressure and is also sensitive to the exhaust pressure near the transition condition. Data obtained with the inboard unit near the subsonic/supersonic transition condition (PSP3/PT2A ~ 86) indicated (Fig. A-9) that an exhaust pressure about nine percent higher than the nominal calibration exhaust pressure maintained subsonic mixing duct conditions with about the same total-pressure distribution that was obtained with lower exhaust pressures (Fig. A-8). Supersonic mixing duct conditions were also evident from a comparison of average total pressures obtained from the mixing duct pitot probes (station 8) and the exhaust rake. With ejector pressure ratios less than 80, the mixing duct probes and the exhaust rake gave comparable results (Fig. A-10). At higher ejector pressures where nonuniform supersonic flow conditions existed, differences are more evident between the two measurements. For the wind tunnel tests, the area weighted exhaust total pressure deduced from the nozzle exit rake was used with PT2A to define simulator exhaust-to-inlet total-pressure ratio (SPR).

A-4.2 SUPERSONIC DASH CONFIGURATION

The initial calibration testing of the supersonic dash EPES units resulted in maximum corrected inlet mass flux rates 25 percent below the design value and an exhaust nozzle exit flow that was severely distorted and indicative of supersonic flow throughout the mixing duct. The source of both of these problems was attributable to the design constraints that arose from the large exhaust nozzle throat area for this engine operating condition. The relatively limited secondary flow passage around the primary nozzles resulted in the EPES inlet flow choking through the ejector unit, thereby limiting the inlet mass flux. Several modifications were subsequently made to alleviate these problems. First, the inlet flow was increased by (1) using a portion of the subsonic cruise outbleed system and (2) by removing some of the ejector struts. By removing the eight centermost nozzles and associated struts from the ejector unit, the inlet area was increased sufficiently to obtain the desired value of corrected inlet mass flux when operating with the outbleed system. A small additional increase in the inlet flow area was obtained by removal of excess material near the base of the remaining struts and around the inner wall of the injector unit between the struts (Fig. A-11). Exhaust flow uniformity was improved by (1) the addition of eleven nozzles in the remaining ejector struts and (2) the addition of a screen near the mixing duct exit (Fig. A-2).

The screen configuration required to completely eliminate the supersonic core in the exhaust flow (21-percent solidity) was choked, thereby limiting the inlet mass flow to approximately 70 percent of the flow with no screen installed. A compromise screen configuration with seven-percent solidity was selected that reduced the distortion in the exhaust flow (Fig. A-12) but did not restrict the inlet flow. Nozzle exit pitot pressure profiles obtained with the modified ejectors and the seven- percent solidity screens are presented in Fig. A-13.

Results of the calibration of the supersonic dash EPES units are shown in Figs. A-14 and A-15. Once again, SPR was defined on the basis of an area weighted exhaust total pressure deduced from the nozzle exit rake. Higher inlet flows were consistently obtained with the inboard unit (Fig. A-14) which is attributed to differences in material removed near the base of the struts (Fig. A-11). The maximum obtainable value of WEC for the outboard unit was within two percent of the design value (Fig. A-14) and corresponded to an outbleed flow rate of approximately ten percent of the inlet mass flow. For the inboard unit, the design value of corrected inlet mass flux was obtainable with an outbleed flow rate of approximately five percent of the inlet mass flow.

The corrected inlet mass flux is presented in Fig. A-15 as a function of ejector driving pressure ratioed to simulator inlet total pressure. The data indicate that the value of WEC is constant at values of injector-to-inlet pressure ratio between approximately 40 to 90. As injector pressure is increased beyond this value, WEC decreases significantly because of the underexpanded primary nozzle exit conditions.

Variation of the mixing duct exit static pressure with ejector driving pressure (Fig. A-16) also reflects geometry differences between the two units. However, area weighted total pressures from the nozzle exit rake that were used to define nozzle exit pressure in the wind tunnel tests (Fig. A-17) are in good agreement.

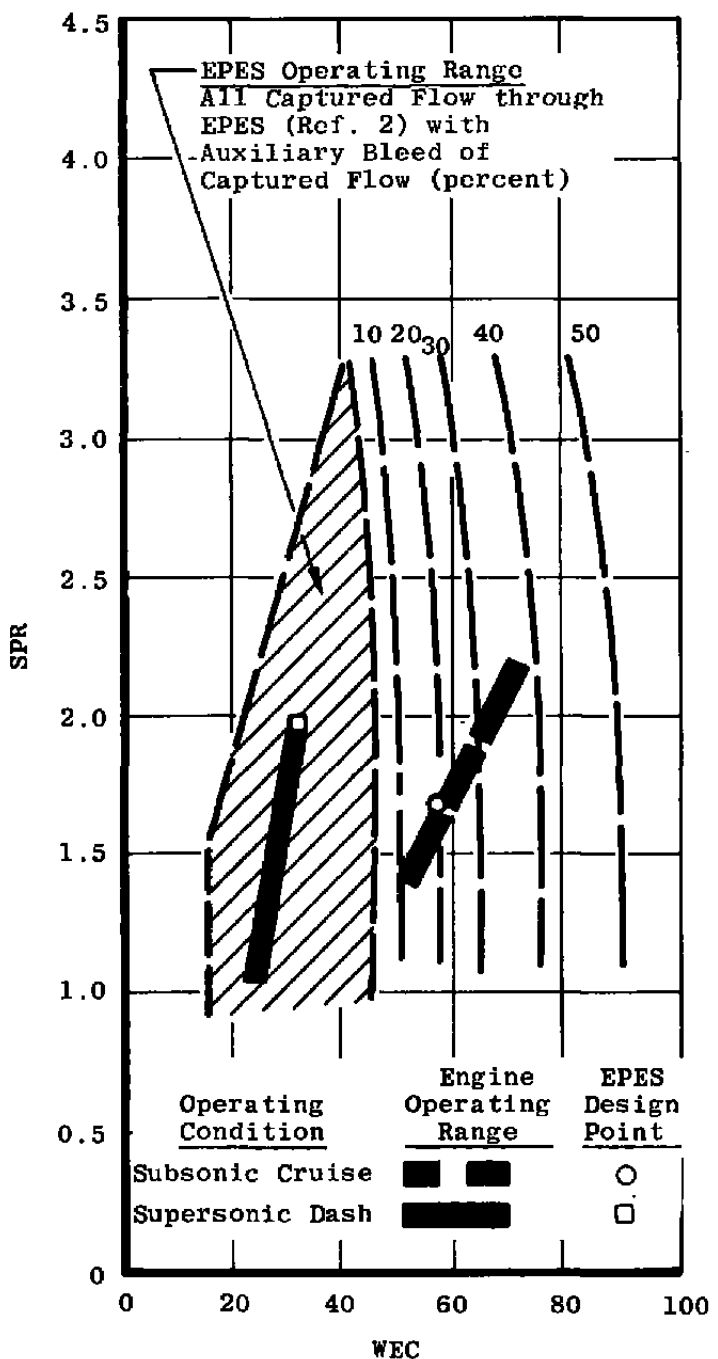
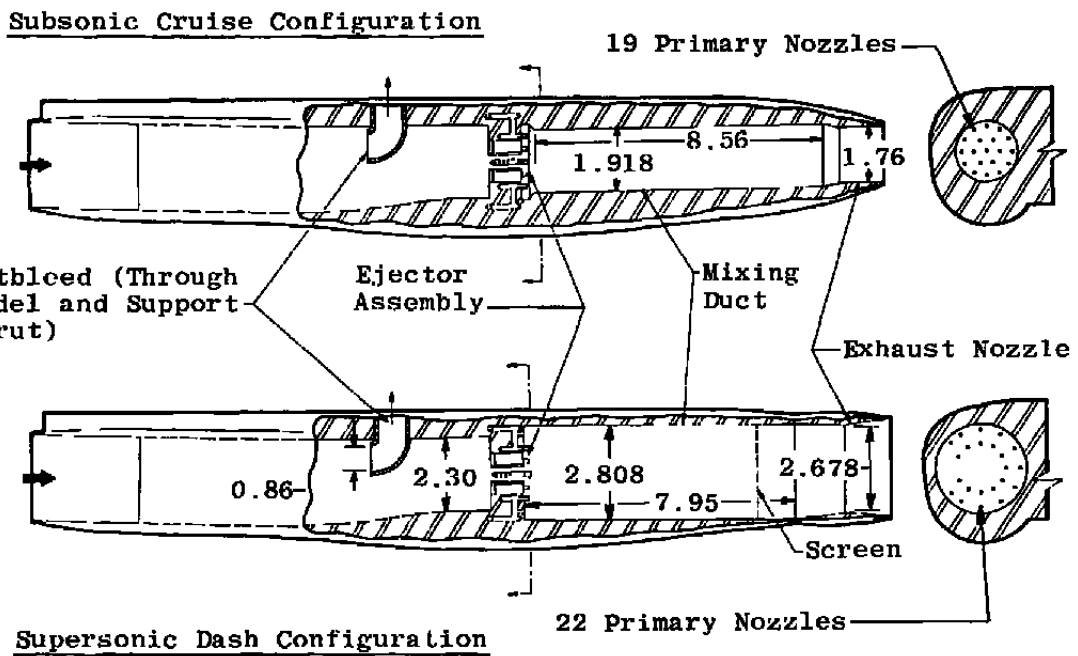
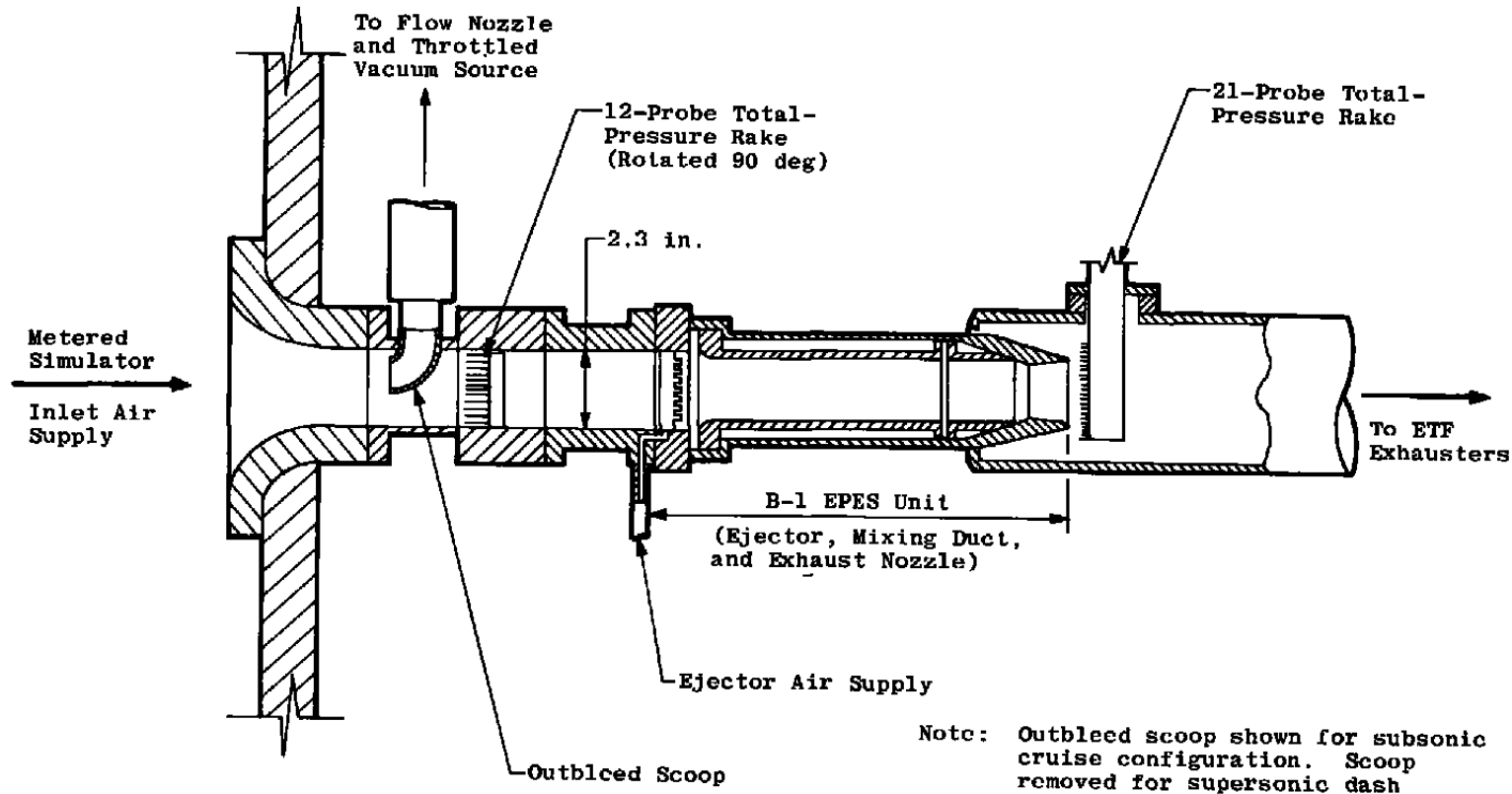


Figure A-1. Comparison of B-1 model EPES design condition and EPES operating limits.

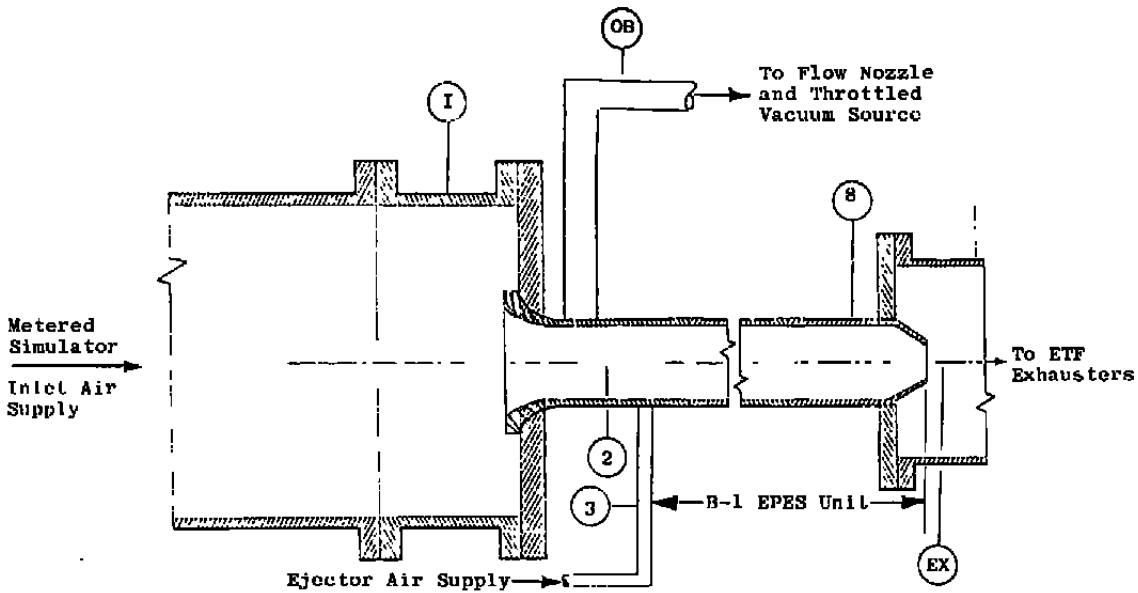


a. Final designs

Figure A-2. 0.06-scale B-1 EPES calibration details.



b. Test cell configuration
Figure A-2. Concluded.



Station	Nomenclature	PT	P	TT	Remarks
1	Inlet Plenum	1	1	1	
OB	Outbliced Line	--	2	1	Static Pressure Taps Upstream and Downstream of Venturi
2	EPES Inlet	12	4	--	Static Pressure Taps 90 deg Apart; Total Pressure, 12-Probe Rake
3	Ejector Air Supply	--	2	1	Static Pressure Taps 180 deg Apart on Ejector Manifold
8	Mixing Duct Exit	2	4	--	Static Pressure Taps 90 deg Apart; Total-Pressure Probes 180 deg Apart
EX	EPES Exhaust	21	2	1	Static Pressure Taps 180 deg Apart; Total Pressure, 21-Probe Rake

Figure A-3. Instrumentation stations for B-1 EPES calibration tests.

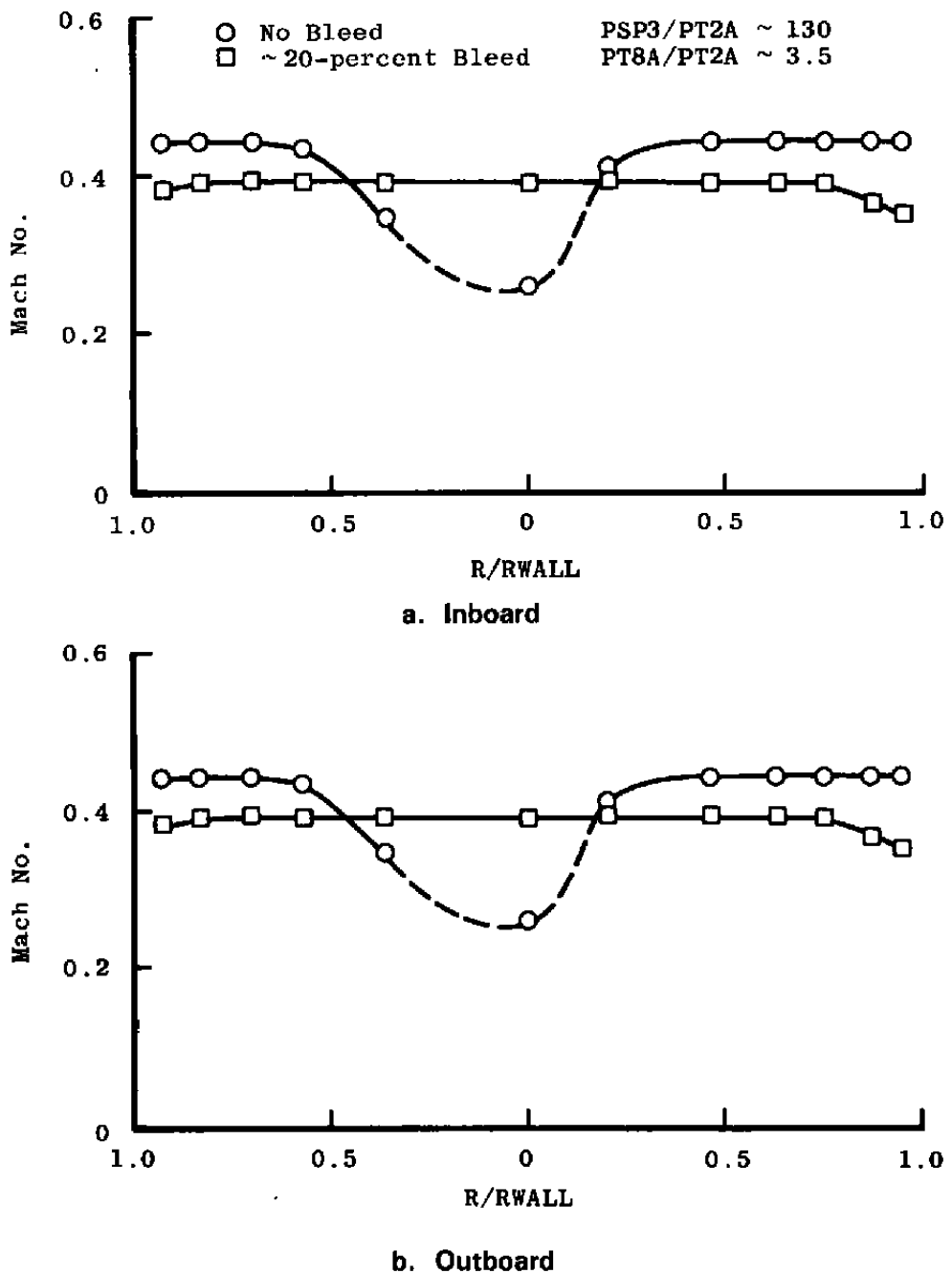


Figure A-4. Typical subsonic cruise EPES inlet Mach number distributions obtained during calibration.

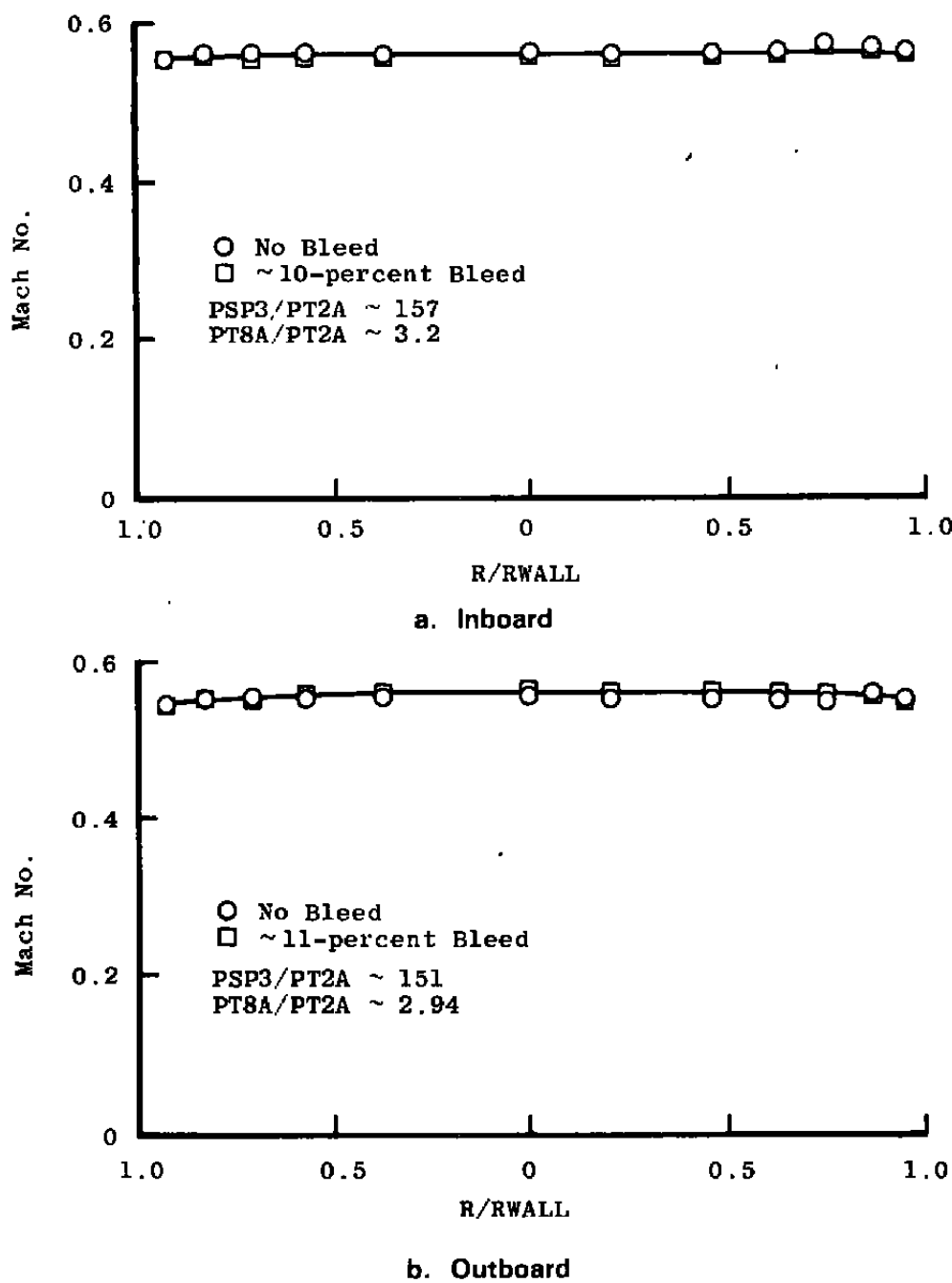


Figure A-5. Typical supersonic dash EPES inlet Mach number distributions obtained during calibration.

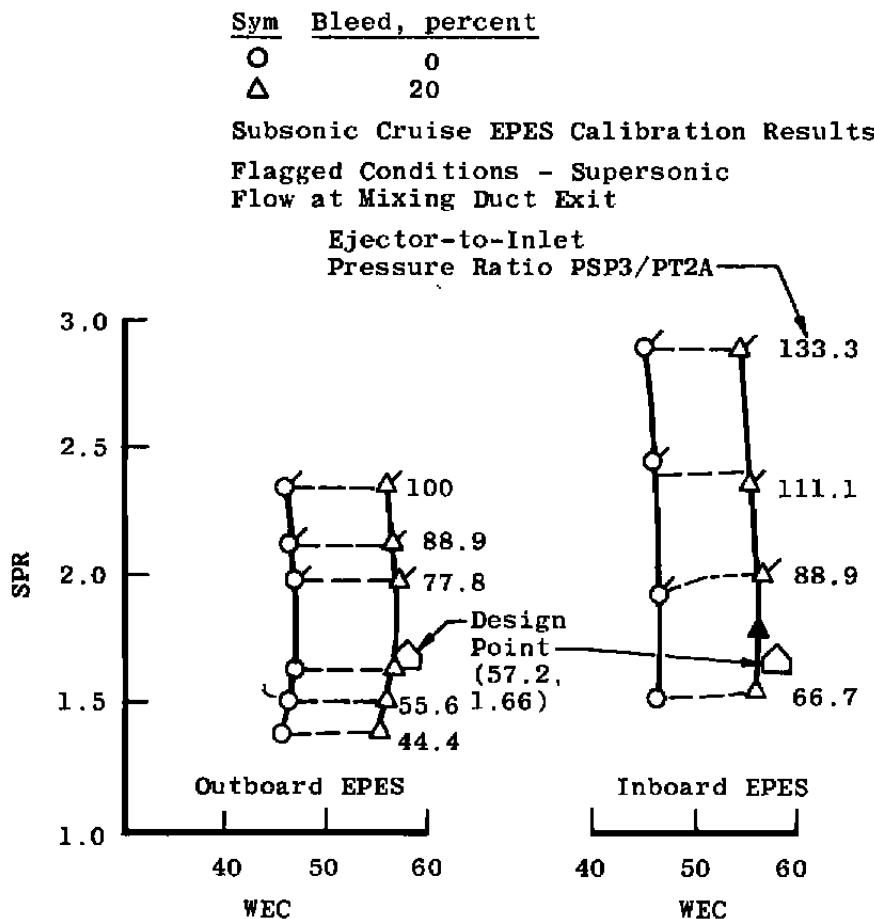


Figure A-6. Performance of 0.06-scale B-1 EPES (subsonic cruise configuration).

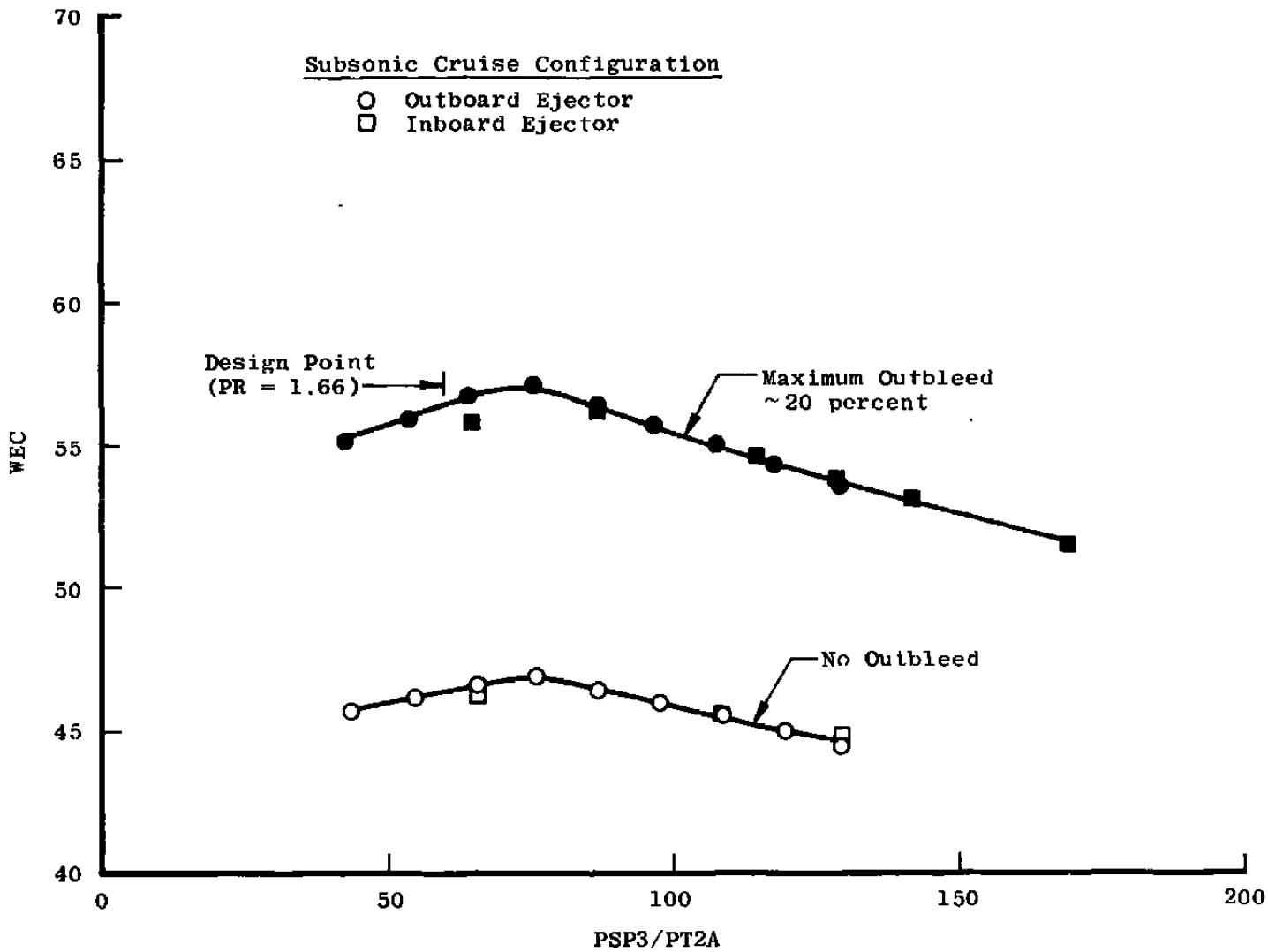
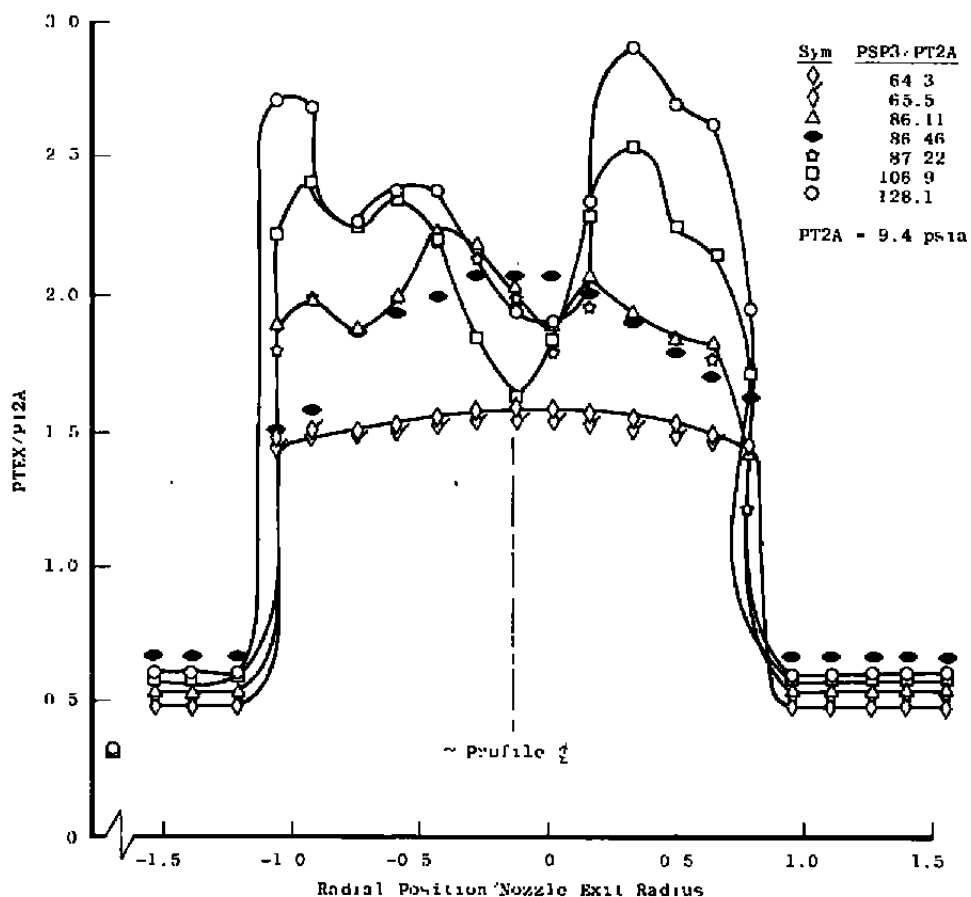
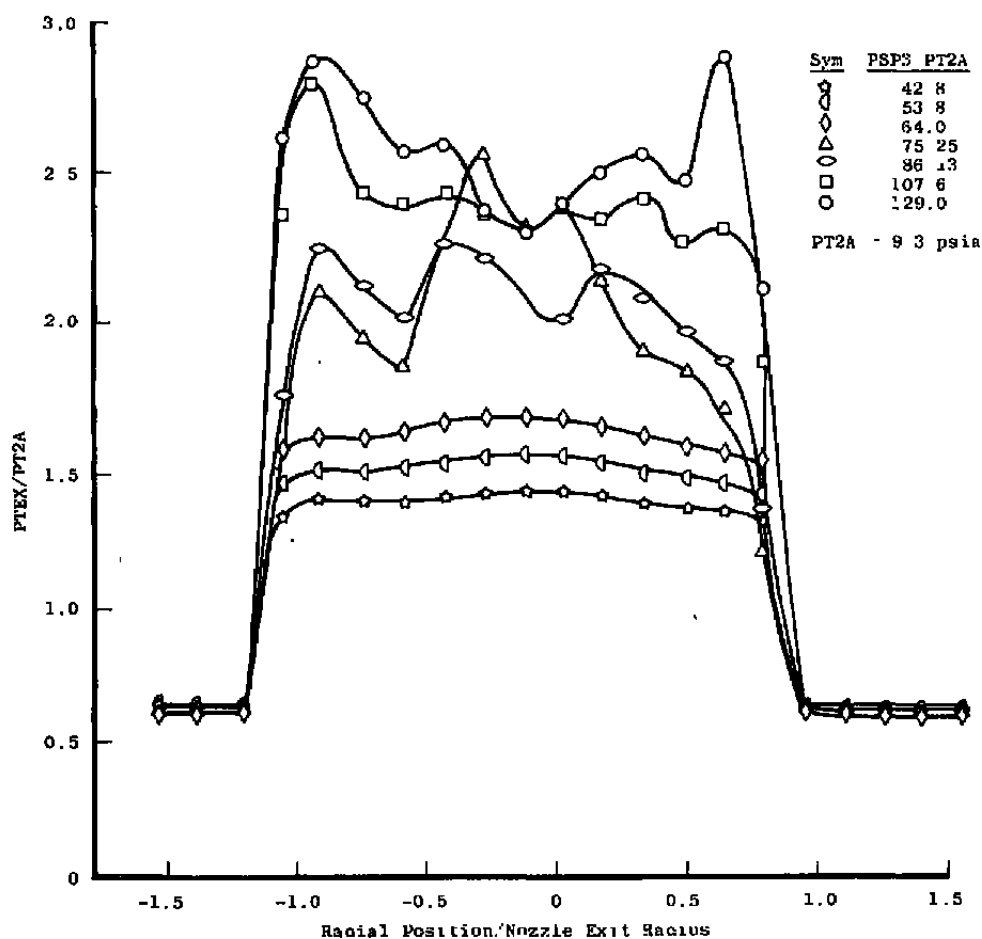


Figure A-7. Variation of WEC with ejector driving pressure (subsonic cruise).



a. Inboard

Figure A-8. Exhaust total-pressure distribution for subsonic cruise EPES.



b. Outboard
Figure A-8. Concluded.

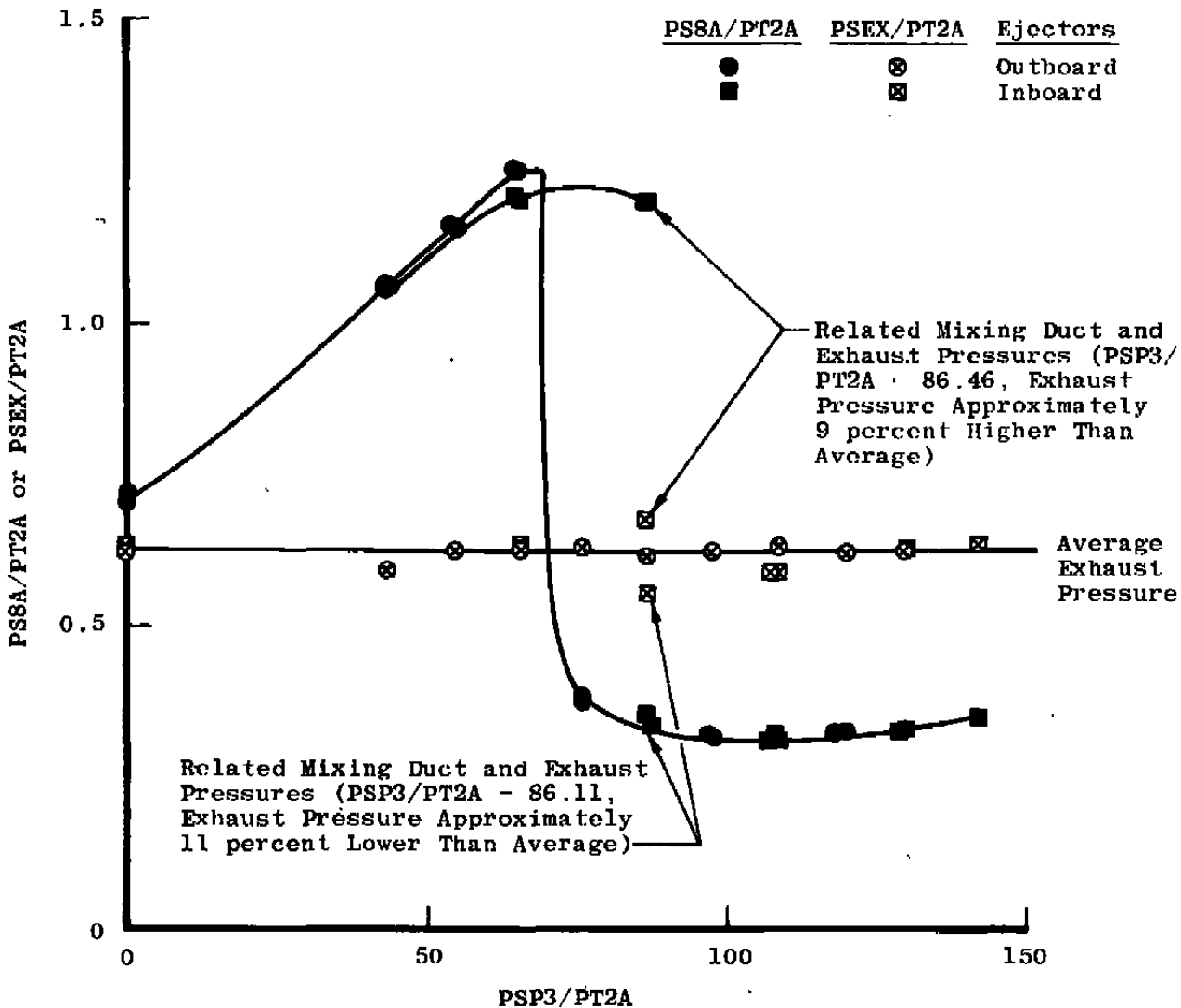
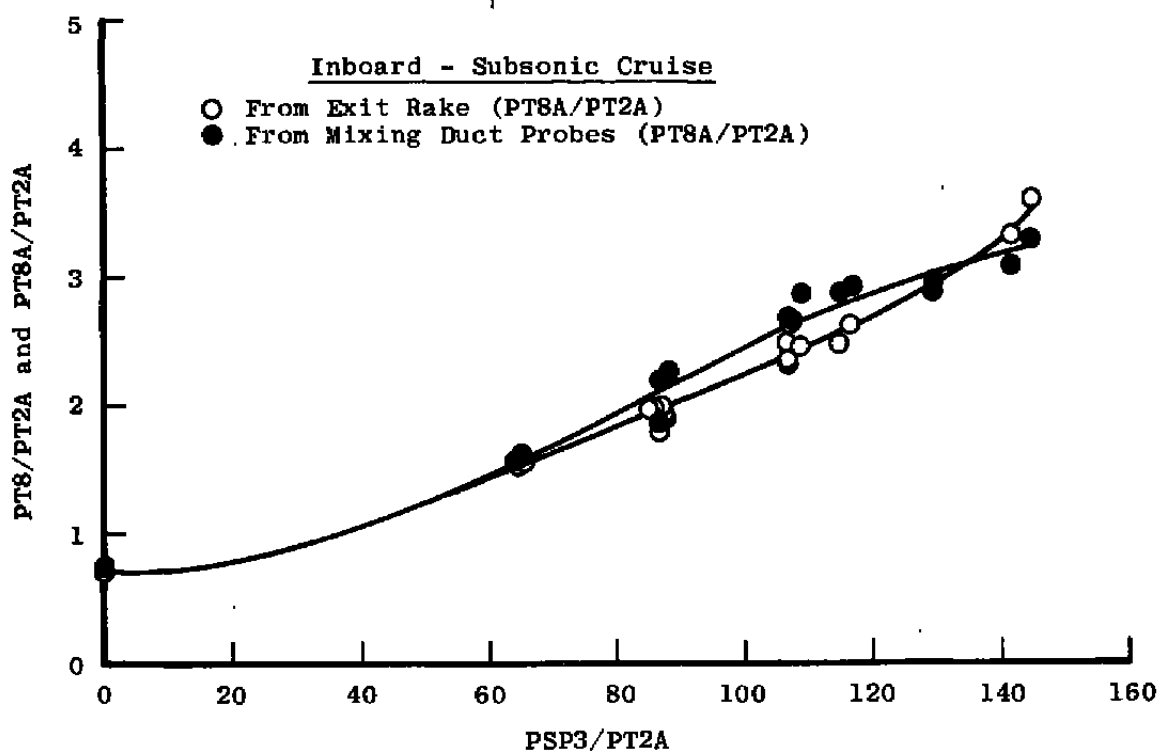
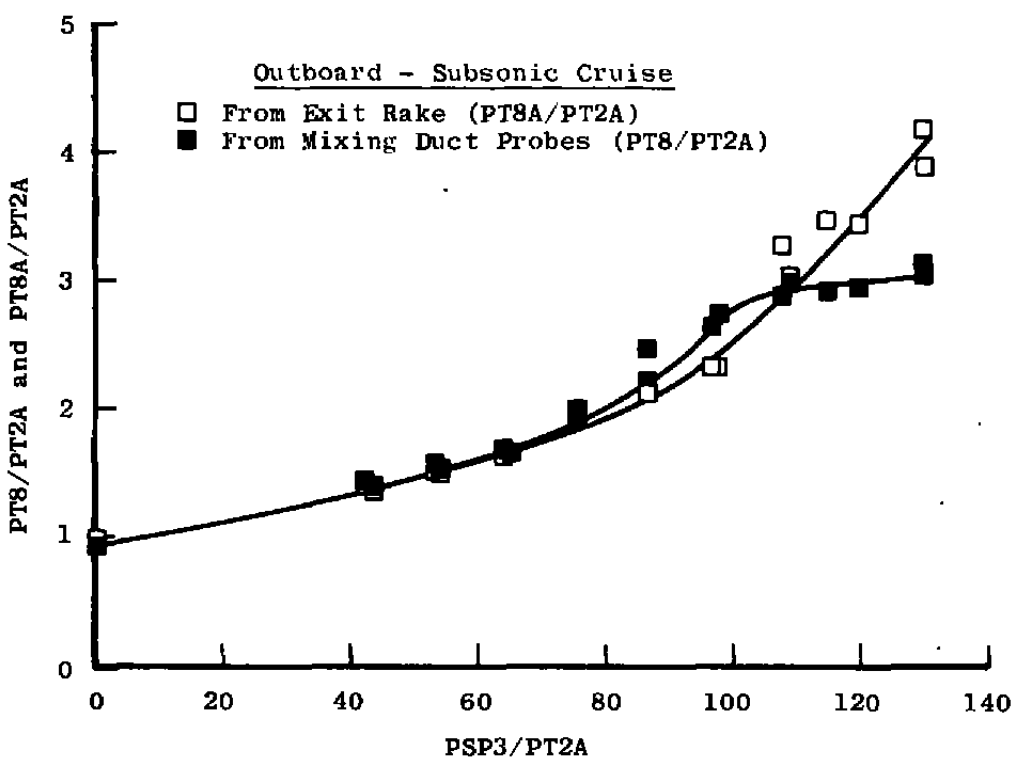


Figure A-9 Variation of mixing duct exit static pressure with ejector and exhaust pressure (subsonic cruise ejectors).



a. Inboard

Figure A-10. Comparison of mixing duct exit total pressures deduced from station 8 probes and the exhaust nozzle exit rake (subsonic cruise ejectors).



b. Outboard
Figure A-10. Concluded.

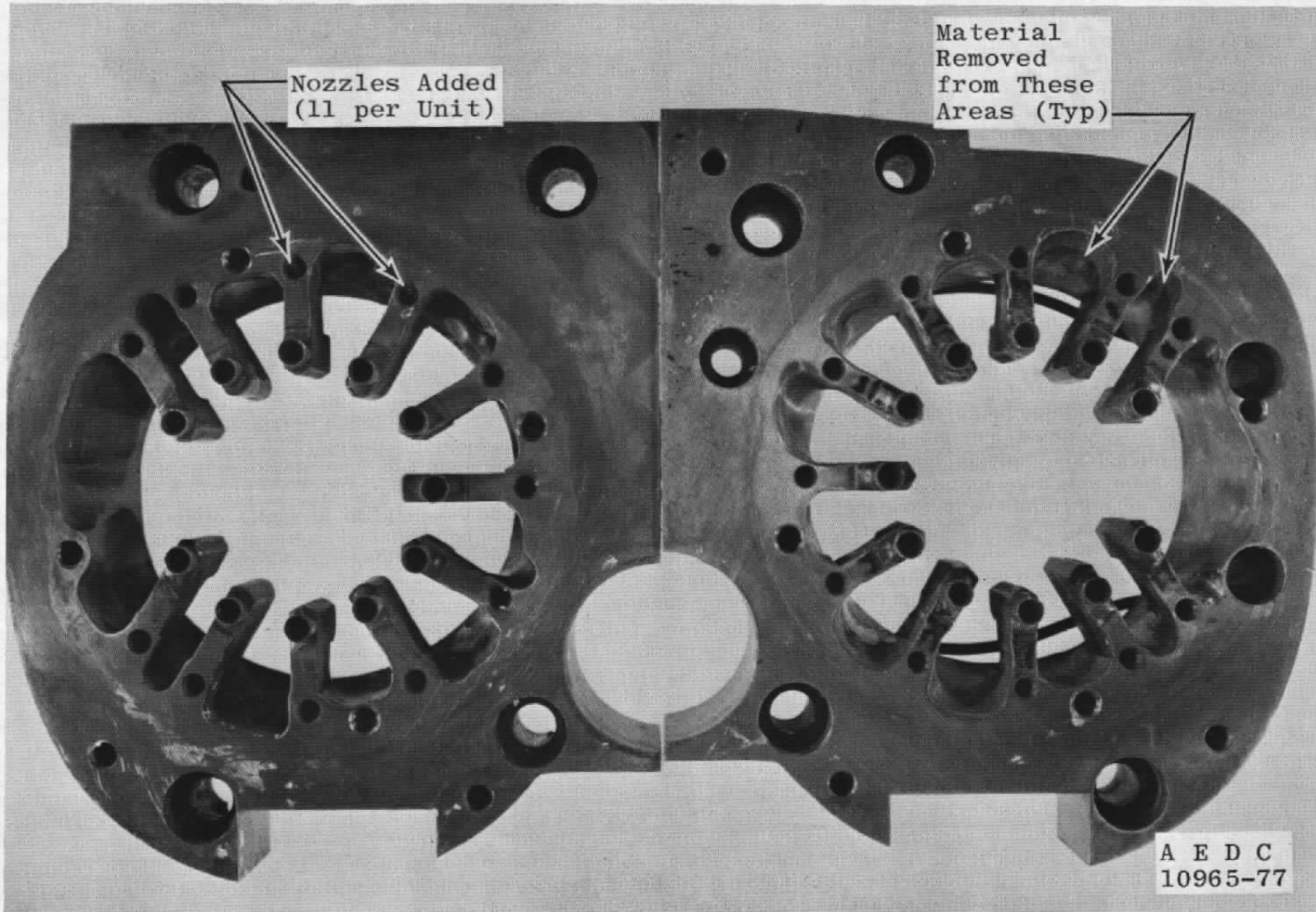


Figure A-11. Supersonic dash ejectors.

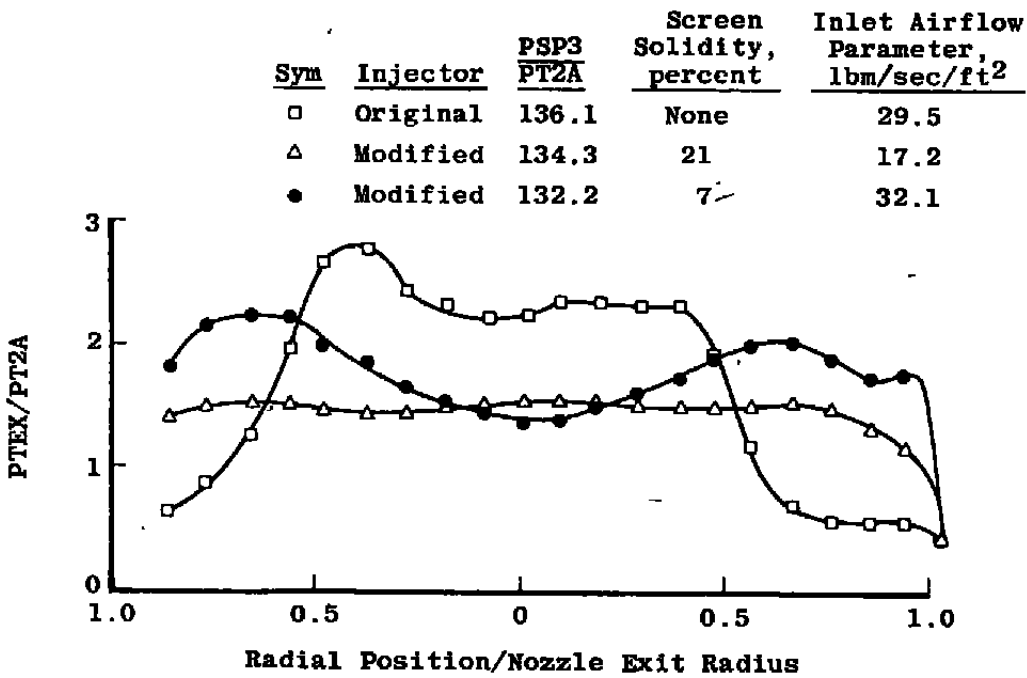
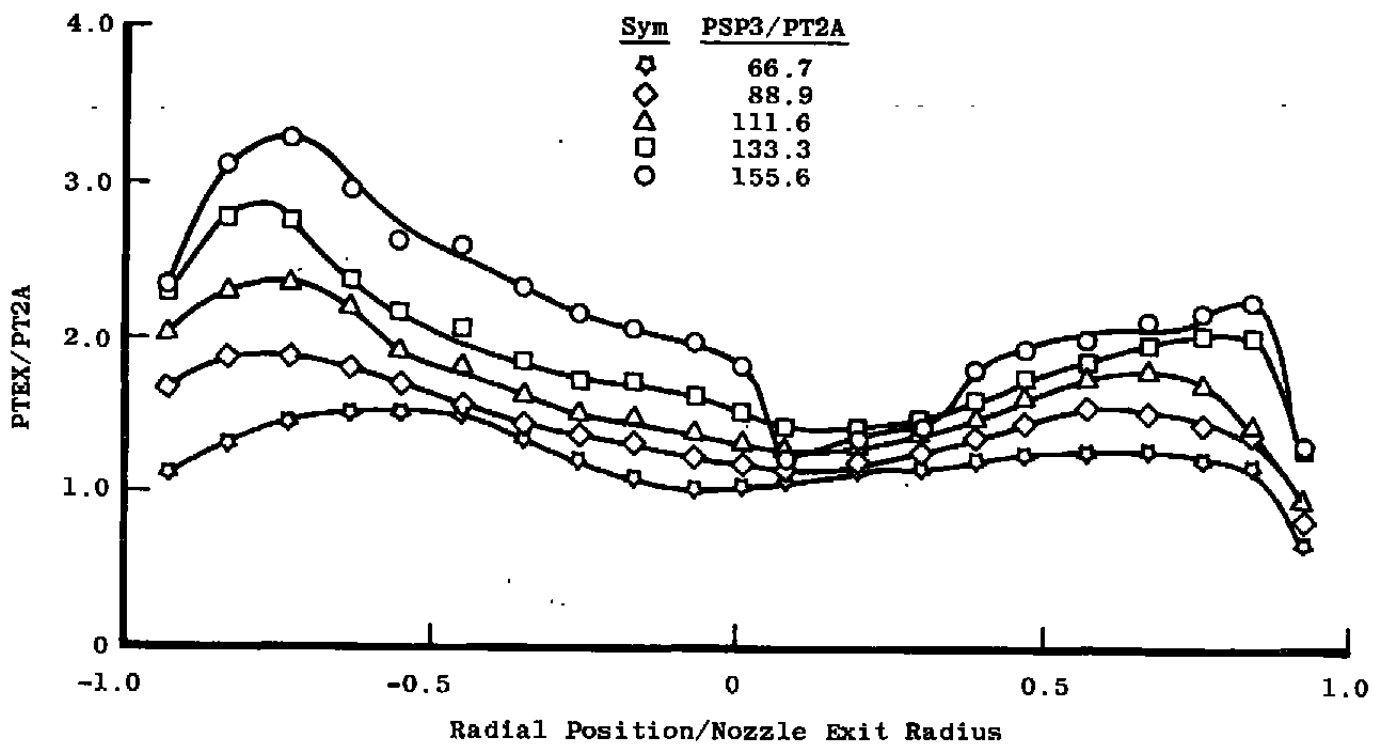
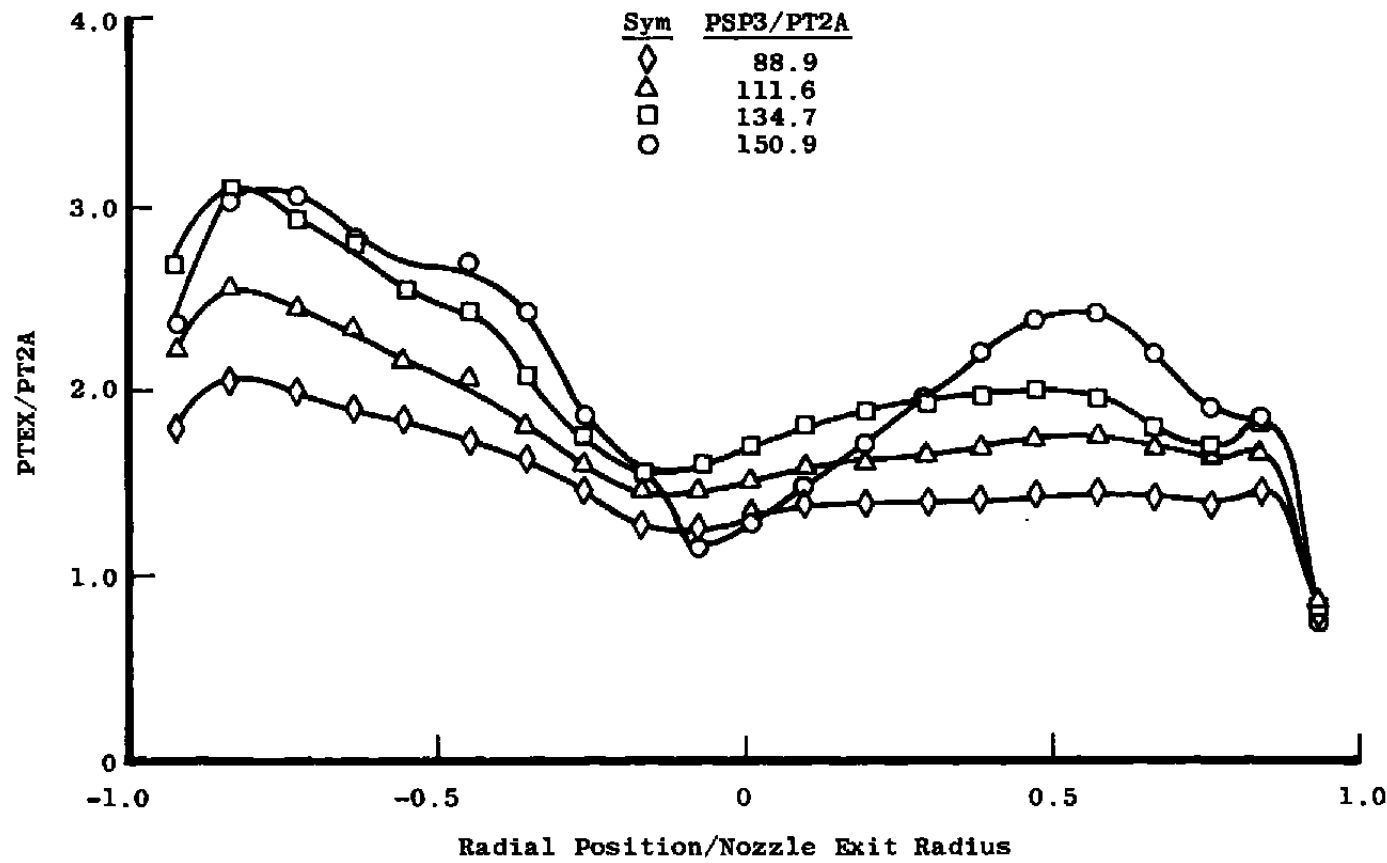


Figure A-12. Effect of screens and ejector modifications on supersonic dash EPES exhaust.



a. Inboard

Figure A-13. Exhaust total-pressure distribution for supersonic dash EPES with modified ejector and seven-percent solidity screen.



b. Outboard
Figure A-13. Concluded.

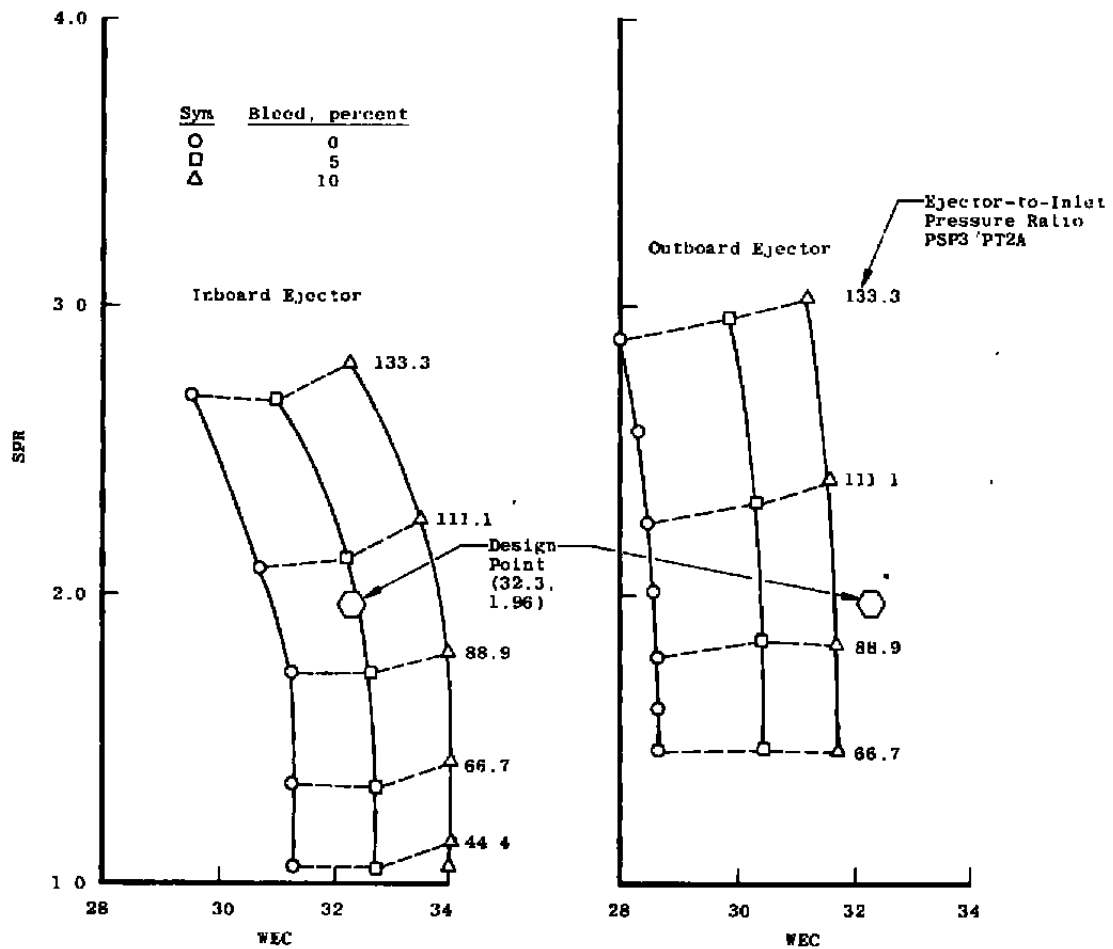


Figure A-14. Performance of 0.06-scale B-1 EPES (supersonic dash configuration).

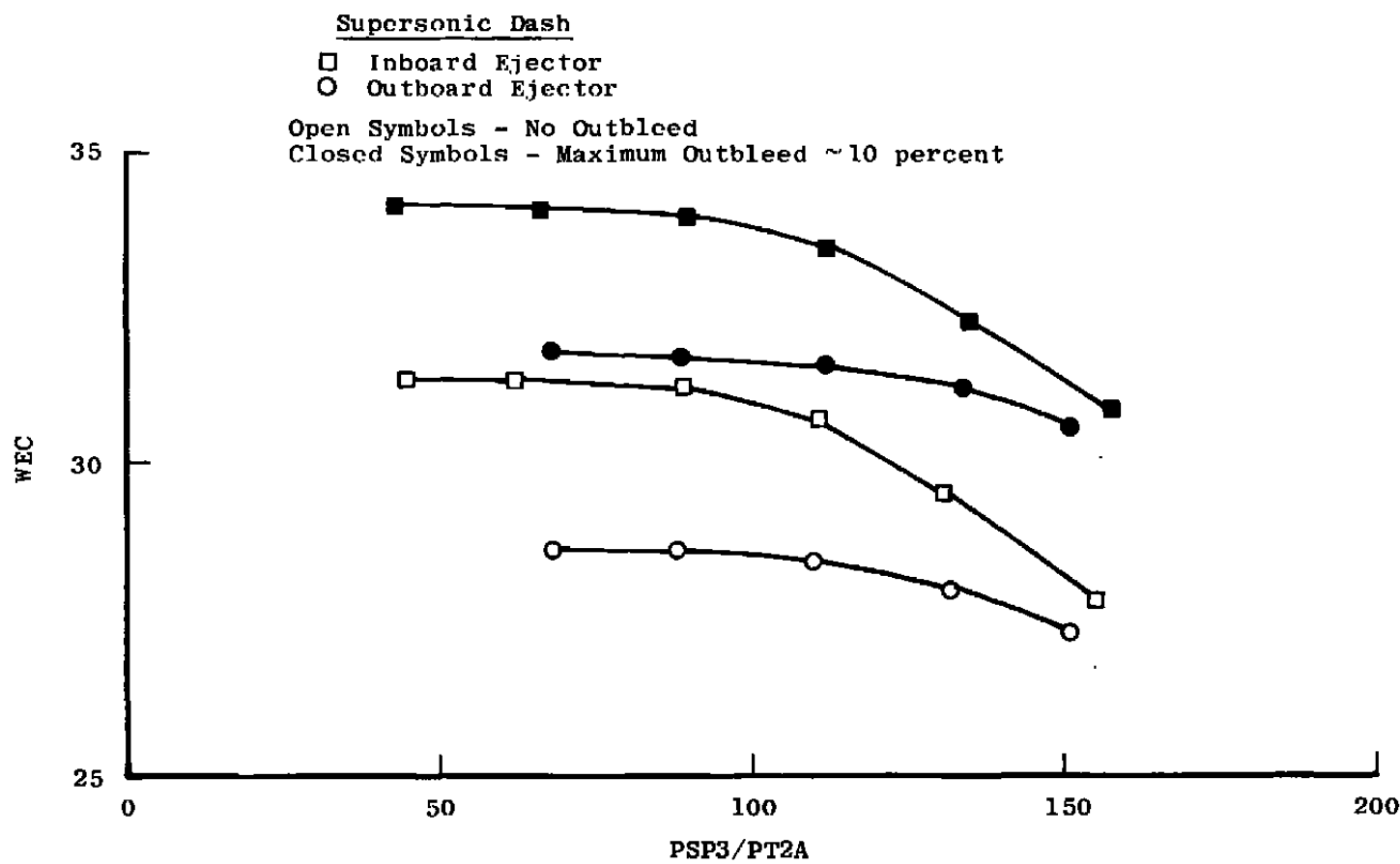


Figure A-15. Variation of WEC with ejector pressure (supersonic dash).

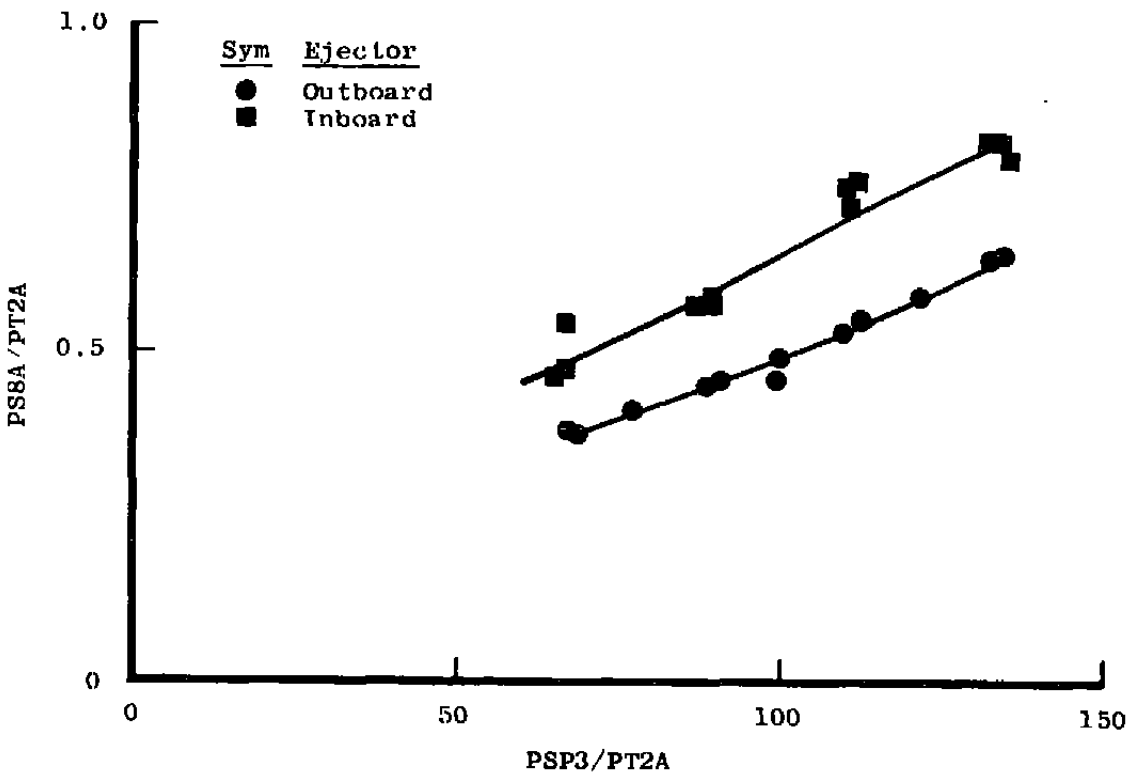


Figure A-16. Variation of mixing duct exit static pressure with ejector pressure (supersonic dash).

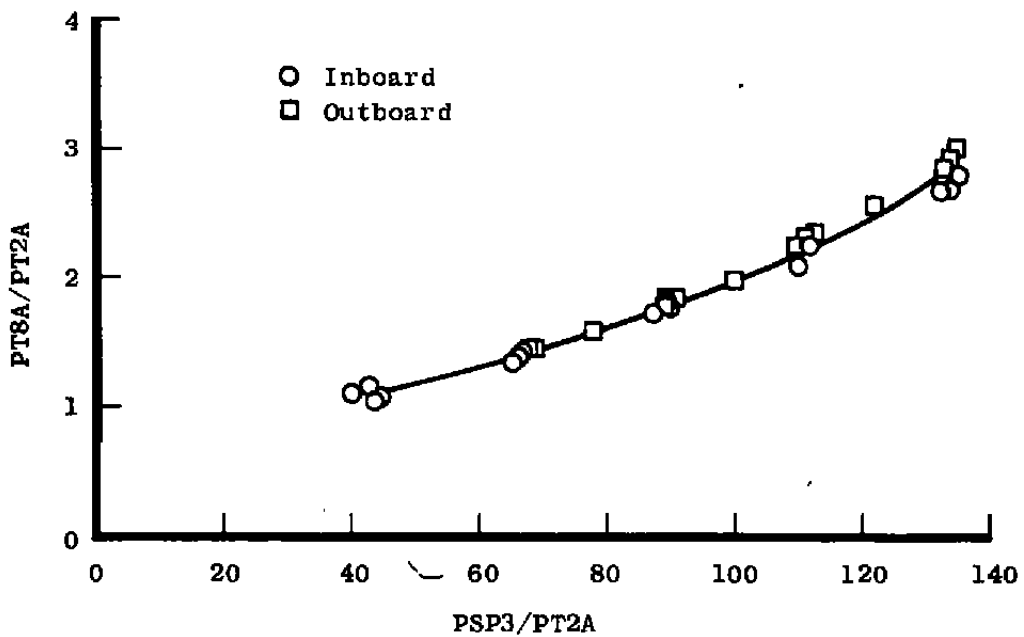


Figure A-17. Variation of mixing duct exit total pressure with ejector pressure (supersonic dash ejectors).

Table A-1. EPES Calibration Parameters

<u>Experimental Parameter</u>	<u>Subsonic Cruise</u>	<u>Supersonic Dash</u>
EPES Inlet Section Diameter	2.30	2.30
EPES Inlet Bleed Scoop Diameter	0.86	0.86*
Ejector Nozzle Throat Diameter (Nominal)	0.045	0.0293
Ejector Nozzle Area Ratio (Nominal)	9.316	25.0
Ejector Nozzle 1-D Mach Number	3.85	5.0
Mixing Duct Diameter	1.918	2.808
Mixing Duct Length	8.56	7.95
Exhaust Nozzle Throat Diameter	1.76	2.678
Exhaust Nozzle Exit Diameter	1.79	2.944
Mixing Duct Exit/Exhaust Nozzle Throat Contraction Ratio	1.188	1.099
Range of Outbleed Percent Experimentally Obtained	0-20	0-10
Range of Inlet Corrected Flow (WEC) Experimentally Obtained (Inboard)	43.5 to 56.2	29.5 to 34
Range of Inlet Corrected Flow (WEC) Experimentally Obtained (Outboard)	44.0 to 57.0	28.0 to 31.8
Range of SPR Experimentally Obtained (Inboard)	1.4 to 2.8	1.0 to 2.8
Range of SPR Experimentally Obtained (Outboard)	1.3 to 2.4	1.4 to 3.0

*Scoop Removed and Replaced with Orifice Flush Mounted to Wall.

Table A-2. Measurement Uncertainty

<u>Experimental Parameter</u>	<u>Uncertainty, percent of Value</u>	<u>Range</u>
Overall Pressure Ratio, SPR	±2.1	0 to 3.0
Mass Flow Parameter, WEC	±1.1	20 to 60 lbm/sec-ft ²
Mach Number, M	±2.0	0 to 1.0
Pressure, Ratio	±1.4	0 to 120

NOMENCLATURE

A	Area, ft ²
AC	Inlet capture area, ft ²
AREF	Wing reference area, ft ²
A2	Flow duct area at ejector face, ft ²
AEXT	Exhaust nozzle throat area, ft ²
CAL	EPES model calibration data
CDCOWL	Axial pressure force coefficient, inlet cowl
CDNOZ	Axial pressure force coefficient, combined nozzles
CDRAMP	Axial pressure force coefficient, inlet ramp
CF2	Inlet flow coefficient
C _p	Pressure coefficient
DELH	Horizontal tail deflection, deg
EPES	Ejector-powered engine simulator model (0.06-scale)
FLIGHT	Flight vehicle, B-1 aircraft number 2
g _c	Universal gravitational constant, lbf-lbm/sec ²
HL	Inlet throat height, in.
INLET	Inlet model (0.07-scale)
KBL	Inlet flow outbleed, percent
M	Free-stream Mach number

MFR	Mass flow ratio - actual/ideal
M2	Mach number at ejector face
NAB	Jet-effects nozzle afterbody model (0.06-scale)
NPR	Nozzle total-to-free-stream static pressure ratio
NS	Nacelle station, in.
P	Static pressure, psia
PSNB	Exhaust nozzle base static pressure, psia
PS2	Static pressure at ejector face, psia
PSP3	Ejector supply pressure, average, psia
PS8A	Mixing duct exit static pressure, average, psia
PTEX	Exhaust pitot pressure, psia
PT2A	Total pressure at ejector face, average, psia
PT8A	Area weighted simulator exit total pressure from calibration tests, psia
q	Dynamic pressure
R	Gas constant for air, ft-lb/lbm °R
Re	Reynolds number/ft
REX	Exhaust nozzle exit radius, in.
RN	Radius of nozzle external surface, in.
RWALL	Duct radius, in.
SPR	Simulator pressure ratio, PT8A/PT2A

T	Static temperature, °R
TT	Free-stream total temperature, °R
WA	Mass flow rate at ejector face, lbm/sec
WB	Outbleed mass flow rate, lbm/sec
WC	Ideal inlet capture area mass flow rate, lbm/sec
WEC	Simulator inlet corrected airflow parameter, lbm/sec/ft ²
WI	Inlet mass flow rate, lbm/sec
W.T.	EPES model wind tunnel data
X	Axial nozzle location measured from NS 23.195, in.
Y/L	Nacelle axial station-nondimensionalized by nacelle length, L, 446.27 in.
α ,ALPH	Angle of attack, deg
γ	Ratio of specific heats
δ^2	PT2A/14.69
θ^2	TT/518.7

SUBSCRIPTS

∞	Free-stream
i	Local pressure orifice identification, 351, 472, etc.

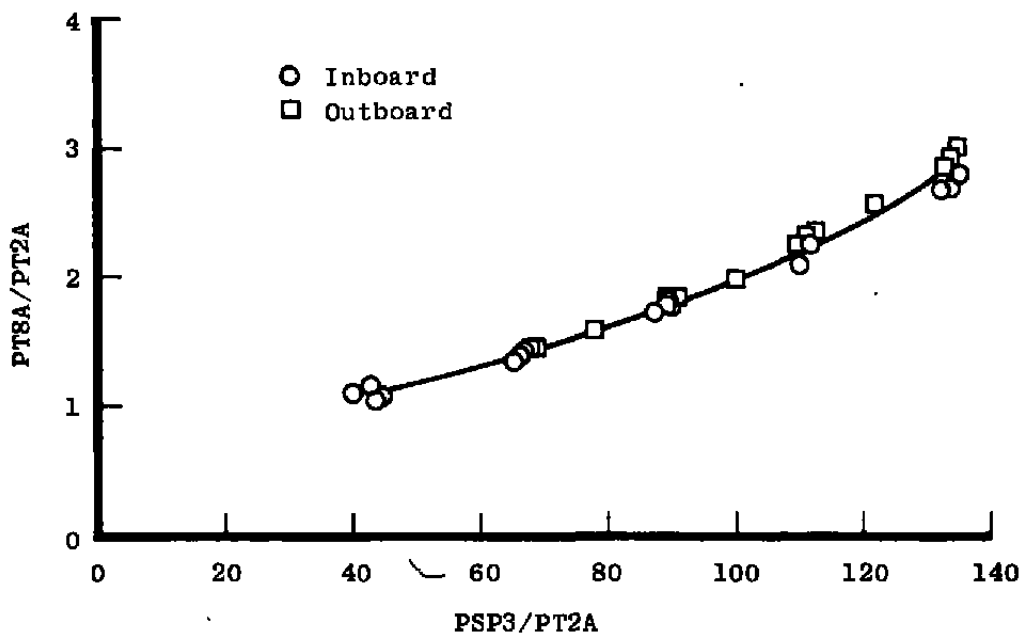


Figure A-17. Variation of mixing duct exit total pressure with ejector pressure (supersonic dash ejectors).

Table A-1. EPES Calibration Parameters

<u>Experimental Parameter</u>	<u>Subsonic Cruise</u>	<u>Supersonic Dash</u>
EPES Inlet Section Diameter	2.30	2.30
EPES Inlet Bleed Scoop Diameter	0.86	0.86*
Ejector Nozzle Throat Diameter (Nominal)	0.045	0.0293
Ejector Nozzle Area Ratio (Nominal)	9.316	25.0
Ejector Nozzle 1-D Mach Number	3.85	5.0
Mixing Duct Diameter	1.918	2.808
Mixing Duct Length	8.56	7.95
Exhaust Nozzle Throat Diameter	1.76	2.678
Exhaust Nozzle Exit Diameter	1.79	2.944
Mixing Duct Exit/Exhaust Nozzle Throat Contraction Ratio	1.188	1.099
Range of Outbleed Percent Experimentally Obtained	0-20	0-10
Range of Inlet Corrected Flow (WEC) Experimentally Obtained (Inboard)	43.5 to 56.2	29.5 to 34
Range of Inlet Corrected Flow (WEC) Experimentally Obtained (Outboard)	44.0 to 57.0	28.0 to 31.8
Range of SPR Experimentally Obtained (Inboard)	1.4 to 2.8	1.0 to 2.8
Range of SPR Experimentally Obtained (Outboard)	1.3 to 2.4	1.4 to 3.0

*Scoop Removed and Replaced with Orifice Flush Mounted to Wall.

Table A-2. Measurement Uncertainty

<u>Experimental Parameter</u>	<u>Uncertainty, percent of Value</u>	<u>Range</u>
Overall Pressure Ratio, SPR	±2.1	0 to 3.0
Mass Flow Parameter, WEC	±1.1	20 to 60 lbm/sec-ft ²
Mach Number, M	±2.0	0 to 1.0
Pressure, Ratio	±1.4	0 to 120

NOMENCLATURE

A	Area, ft ²
AC	Inlet capture area, ft ²
AREF	Wing reference area, ft ²
A2	Flow duct area at ejector face, ft ²
AEXT	Exhaust nozzle throat area, ft ²
CAL	EPES model calibration data
CDCOWL	Axial pressure force coefficient, inlet cowl
CDNOZ	Axial pressure force coefficient, combined nozzles
CDRAMP	Axial pressure force coefficient, inlet ramp
CF2	Inlet flow coefficient
C _p	Pressure coefficient
DELH	Horizontal tail deflection, deg
EPES	Ejector-powered engine simulator model (0.06-scale)
FLIGHT	Flight vehicle, B-1 aircraft number 2
g _c	Universal gravitational constant, lbf-lbm/sec ²
HL	Inlet throat height, in.
INLET	Inlet model (0.07-scale)
KBL	Inlet flow outbleed, percent
M	Free-stream Mach number

MFR	Mass flow ratio - actual/ideal
M2	Mach number at ejector face
NAB	Jet-effects nozzle afterbody model (0.06-scale)
NPR	Nozzle total-to-free-stream static pressure ratio
NS	Nacelle station, in.
P	Static pressure, psia
PSNB	Exhaust nozzle base static pressure, psia
PS2	Static pressure at ejector face, psia
PSP3	Ejector supply pressure, average, psia
PS8A	Mixing duct exit static pressure, average, psia
PTEX	Exhaust pitot pressure, psia
PT2A	Total pressure at ejector face, average, psia
PT8A	Area weighted simulator exit total pressure from calibration tests, psia
q	Dynamic pressure
R	Gas constant for air, ft-lb/lbm °R
Re	Reynolds number/ft
REX	Exhaust nozzle exit radius, in.
RN	Radius of nozzle external surface, in.
RWALL	Duct radius, in.
SPR	Simulator pressure ratio, PT8A/PT2A

T	Static temperature, °R
TT	Free-stream total temperature, °R
WA	Mass flow rate at ejector face, lbm/sec
WB	Outbleed mass flow rate, lbm/sec
WC	Ideal inlet capture area mass flow rate, lbm/sec
WEC	Simulator inlet corrected airflow parameter, lbm/sec/ft ²
WI	Inlet mass flow rate, lbm/sec
W.T.	EPES model wind tunnel data
X	Axial nozzle location measured from NS 23.195, in.
Y/L	Nacelle axial station-nondimensionalized by nacelle length, L, 446.27 in.
α , ALPH	Angle of attack, deg
γ	Ratio of specific heats
δ^2	PT2A/14.69
θ^2	TT/518.7

SUBSCRIPTS

∞	Free-stream
i	Local pressure orifice identification, 351, 472, etc.